PLANETARY SYSTEMS UNLIKE THE SOLAR SYSTEM

Georgina Dransfield



UNIVERSITY OF BIRMINGHAM

A thesis presented for the degree of
Doctor of Philosophy

School of Physics and Astronomy
College of Engineering and Physical Sciences
University of Birmingham
June 2023

UNIVERSITY OF
BIRMINGHAM

University of Birmingham Research Archive

e-theses repository

This unpublished thesis/dissertation is copyright of the author and/or third parties. The intellectual property rights of the author or third parties in respect of this work are as defined by The Copyright Designs and Patents Act 1988 or as modified by any successor legislation.

Any use made of information contained in this thesis/dissertation must be in accordance with that legislation and must be properly acknowledged. Further distribution or reproduction in any format is prohibited without the permission of the copyright holder.

Abstract

Planetary systems unlike the solar system

Georgina Dransfield

In the field of Exoplanetology, there is palpable excitement about the new era we have now entered: the era of in-depth atmospheric and orbital characterisation with a new generation of observatories. In space, these include the recently launched *JWST*, soon to be joined by *Ariel*, as well as the upcoming Extremely Large Telescopes (ELTs) on the ground. Such is the furor, that it might appear the remaining Big Unanswered Questions in the field could all be addressed simply by learning more about the existing planet sample. In this thesis, I seek to show that this is not the case.

The scene is set in Chapter 1, where I introduce the science of exoplanet detection and discovery. In this work, I focus primarily on detection using the transit method, so this technique is explored in the most detail. Discovering new planets via transit photometry requires access to telescopes blindly surveying the night sky, and I describe the main instruments used in this work (the space telescope *TESS*, ASTEP in Antarctica, and SPECULOOS in Chile, Spain and Mexico), as well as those with historical significance for the field. Finally, I describe some of the aforementioned Big Unanswered Questions that require ongoing active discovery efforts if they are to be settled.

Chapter 2 contains a detailed description of the methods used throughout this thesis. When going about the business of discovering new planets, there is a process that runs almost chronologically, provided there are no hiccups encountered along the way (which is rarely the case). I lay out the now well-choreographed progression from initial signal detection, through reduction of photometric observations and global Bayesian analysis, to the ways of checking if more can be learned about the new system. In this Chapter I also present the first paper of the thesis, which describes the scheduling systems and new automatic photometric analysis pipeline I produced for ASTEP.

The third chapter contains the first planet discoveries of the thesis. In the game of *TESS* follow-up, there is a distinction to be made between planet confirmations and validations. Here I introduce the second paper of my thesis, which presents the confirmation of a three-planet system orbiting the Solar-like star, HD 28109. These three transiting planets have radii $R_{\rm b} = 2.199^{+0.098}_{-0.10}\,{\rm R}_\oplus$, $R_{\rm c} = 4.23 \pm 0.11\,{\rm R}_\oplus$ and $R_{\rm d} = 3.25 \pm 0.11\,{\rm R}_\oplus$, and the outer two present large transit timing variations. This system is swiftly followed by my third published paper, a validation of a $R_{\rm b} = 1.55 \pm 0.06\,{\rm R}_\oplus$ planet in the habitable zone of its M-dwarf host, TOI-715. There is a lot to learn still about both systems, leaving large scope for future work. I additionally present a Work in Progress in Chapter 3: the now-validated AMY-1 system, consisting of at least one planet orbiting a mid M-dwarf.

In Chapter 4, I introduce an observation programme I have been leading within SPECULOOS for just over a year: MANGOs. MANGOs is an ambitious project of discovery, seeking out new giant objects (planets, Brown Dwarfs and M-dwarfs) orbiting low-mass stars, and I set out our goals and motivations. The project is still young, but the first paper in the series is already submitted and another is in the early preparatory stages. I present our submitted paper (on which I am second author) containing the confirmation of a short-period giant planet orbiting TOI-4860, followed by the Work in Progress of our second paper (to be led by me), which will include eight newly discovered MANGOs systems.

Chapter 5 is my concluding chapter. I summarise the impact of my thesis, and return to some of the Big Unanswered Questions from Chapter 1 to assess whether we are any closer to resolutions. I also describe some future avenues for continued investigation of some of the systems introduced in this thesis.

Dedication

*This work is dedicated to all dogs, everywhere. Every last one of them. Even chihuahuas. They are **all** good dogs.*

Acknowledgements

I swear there is no particular order to this. So nobody should read into anything.

My first thanks go to Amaury. While yes, it takes a village to raise a PhD student, I wouldn't have even got started had it not been for the fact that you gave me a shot. I came to you as a secondary school Physics teacher with no real research experience and asked for an opportunity, and you gave me one. I am constantly grateful that you saw enough in me to invest time and money into building a researcher - all the science I get to produce is because you gave someone with a non-traditional background a shot at their dream. My hope is that you'll continue to give people chances and fill the field with people who came at it in a non-linear fashion.

Aside from that one little detail, you've also genuinely been the best supervisor a PhD student could ask for. Thank you for your time, even at really unsociable hours. Thank you for the advice and the chats, even about totally non-science related stuff. Thank you for introducing me to people, even when I told you I was not great with strangers. Thank you for putting me on such cool projects, and letting me run with the ones I came up with. Thank you for letting me swear and rage and whine when the need took me. And thank you for the absolute humanity you showed me when I lost my dad three weeks into the PhD. With any other supervisor, I might not have found my way back into a work rhythm. Basically, I'm just kinda grateful it was you. So thanks.

The rest of the office ain't bad either, to be honest. What a lovely group of people you all are. I genuinely am anxious with groups of new people, but the folks who were there when I arrived made me feel included immediately. And now that I'm part of the furniture, I've loved welcoming new people too! Thanks Annelies and Guy for answering my questions (dumb and otherwise) and for always being super encouraging. Thanks Martin, Warrick, Daniel and Lalitha for helping me with anything I was stuck with, and never making me feel thick for asking. Thank you to Emily, Emma, Alex, other Alex, Matt, Vedad, Oli, Owen, Tom and Walter, for the help, the advice, the fun chats, the socials, and the general vibes. Our group really is the envy of all other research groups out there. Well done, everyone.

Chief among the office lads, thanks goes to my wonderful girl gang: the BADASS GODDESSES OF ASTRO. Alix, Yaz, Maddy and Daisy, you guys make me feel so damn loved and appreciated. Like

seriously, you hype me up so much that I almost believe it sometimes. You're such excellent friends and I feel disgustingly lucky to have you all in my life. How cool is it that now we will all be in the office together? I'm so damn proud of you all, and watching you guys become such incredible researchers is just an honour. I love you all.

The office also gave me Linds, to whom I'm grossly indebted. We were just instant friends, which doesn't happen often. Thank you for making me noodles in the days after It Happened, and for helping to encourage me back into work. Thank you for helping to fix my code, and sharing bottles of wine with me. Thank you for reading things I write, and giving me feedback. Thank you for sending me a `Pandas` binary over WhatsApp when I was in Antarctica so I could get my pipeline installed. Just thanks, dude. What a legend of a friend. I can't wait to sew together again.

It's been a real pleasure getting to work with the SPECULOOS consortium. There's such excellent science happening there and I'm grateful to everyone who heard me out, taught me new skills, and let me lead proposals. I'm especially grateful to Elsa and Lionel. You guys have taught me So. Much. Stuff. And had infinite patience for my endless questions. I love to learn things, but it's even better when you get to learn from friends.

My favourite SPECULOOS colleague (yes, I have favourites, get over it) by far is Mathilde. My beloved Timmy. To think that we started our friendship over Slack during the pandemic by working late into the night on ESO and HST proposals together. It's wild to think that the first time we met in person was to go on holiday together for three weeks, but when you know, you know. And we just knew. You're not only an outstandingly smart researcher, you are a gothic queen and a wonderful friend. I love our chats, our travels, and our earnest heart-to-hearts. You've taught me so much about the coolest shoes (Buffalo omg, how did I not know?), photometric reduction, and singing. I'm sorry my singing hasn't improved. I promise you it never will. Thank you for loving me anyway, and I can't wait for our next adventure together. Let's hope we don't run into any bears this time!

Another fabulous bunch of people I got to work with was the ASTEP team. I can't imagine what you all thought of me when I rocked up to Zoom meetings with the bright pink hair and the endlessly barking dog, but you all listened to me and let me do things. Thank you Tristan, Djamel, Lyu, Karim, Olga and Philippe for allowing me to run wild with my plans for organising our observations - I had a blast doing it. And thank you for the opportunity of a lifetime in giving me the task of producing a pipeline for our fantastic little telescope. How many PhD students get to go to Antarctica? Thanks to ASTEP, I will forever have the best trip photos to put in slides at every conference. Nobody can beat Antarctica. What, you have a picture of a volcano? BAM- here's a picture of me with a penguin! I win!

During a PhD, a lot of us suffer from some occasionally deteriorating mental health. It's a bit sub-optimal, but the pressure can be a lot at times so it happens. I'm therefore massively grateful to my excellent running club, the Malvern Joggers. Every run with you guys helps keep me sane, from the Wednesday club nights, to the long marathon training runs in the depths of winter - I love them all. Even when I complain, I love the runs. Even cross country. No, that one was a lie. I hate cross country, but I loved captaining the team and I loved when it was over. So thank you all for the runs,

the chats and the support.

To my family: Ma, Vicky and my dad. Each of you helped shape me into whatever it is I am today. And allegedly I'm not the worst, which must mean that you guys contributed to that. I'm grateful for the love and support you have shown me over the years, and for believing in me and my dreams. Thank you ma for helping look after Amy so I could go into the office when Ian was away. Thank you Vicky for always bigging up my achievements. And to my dad... well, the timing of your death sucked. But in life, you were often proud of me and I appreciated it. I reckon you would've loved seeing me on TV.

I have to say, my friendship with the Bells has also been instrumental in getting this far in my PhD. Liz, our runs and chats and board games just fill me with joy. Thank you for always being there to dissect stuff with me, and for supporting me through some of the most challenging bits I've lived through in the last few years. Mark, I don't know what I would've done without your coding advice and insights - thank you so much for always having some time to help me out with things. And James, even on the dreariest of days, when I hear you say my name it just lights up my world. All the Bells, you're excellent friends and I'm grateful to have you all in my life.

Wendy, my one and only sunshine. You are my favourite waistcoat. Indubitably. You know the little up-down shade thingys on airplane windows? I love you more than them. More than nuns with guns. Thank you for always, unconditionally supporting me. Thank you for crossing an ocean to be by my side when I got married. Thank you for listening to me endlessly talk about planets. Thank you for watching me on TV (illegally). You tell me I can do hard things and then push me to do them. Thank you for being my best friend.

Ian... who even is Ian? Ah yes, the husbutt. You made this PhD possible. By agreeing to move to the other side of the country with me so I could pursue it. By staying home alone and looking after the dog while I spent months abroad for my research. By spending countless evenings alone while I worked late into the night on code or proposals. By letting me describe whatever I was working on whether or not you understood it, just so I could talk about it during evening dog walks. By crying with pride whenever I achieved something big, and making me feel proud of myself too. By making me take breaks when I was frustrated and getting nowhere. By making me coffee every single morning. Without you, life would be garbage and I would not be doing research. Thank you for making my dreams possible with your support and your love. Your farts didn't help, but they happened and that should be documented. I love you embarrassing amounts. Bzzt.

Then there's Shiggy. You're not a full person yet, but it was hilarious that you chose to start existing at the exact time I needed to write my thesis. Someone once told me I like to live life on 'hard mode', so thank you Shiggy for ensuring that thesis-writing was on the hardest mode possible: pregnant mode. I can't wait to meet you.

And finally, Amy. My whole life I dreamed of you, and when you finally came into my life I learned what the purest love feels like. You are the **best dog**. Thank you for sticking your head under my arm when I've been working too long and you want me to take a break to stroke you. Thank you for welcoming me home from long trips abroad with more love and excitement than anyone's ever shown

at the sight of me. Nothing beats the love of a dog, and no other dog will ever beat you.

Contents

Abstract iii

Dedication v

Acknowledgements vii

Contents xi

List of Publications xv

List of Figures xviii

List of Tables xxv

1 Exoplanetology in 2023 1
- 1.1 What's left to find out? . . . 1
- 1.2 Exoplanet detection methods . . . 2
  - 1.2.1 A Keplerian orbit . . . 3
  - 1.2.2 Transit photometry . . . 5
  - 1.2.3 Radial velocities for planet detection . . . 11
  - 1.2.4 The importance of stellar characterisation . . . 14
- 1.3 Blind transit surveys . . . 16
  - 1.3.1 From Space . . . 16
  - 1.3.2 From the ground . . . 19
- 1.4 What we [think we] know about exoplanets . . . 24
  - 1.4.1 Planet flavours . . . 24
  - 1.4.2 Patterns arising from statistics . . . 26
- 1.5 What's left to find out? . . . 30

2 Methods Used in This Thesis 31
- 2.1 Searching for planet candidates . . . 31
  - 2.1.1 BLS and TLS searches . . . 32
  - 2.1.2 SHERLOCK . . . 33
- 2.2 Photometry . . . 33
  - 2.2.1 Photometric reduction . . . 34
- 2.3 Vetting and Validation . . . 38

2.3.1 Vetting . . . 38
2.3.2 Validation . . . 38
2.4 Transit modelling . . . 39
2.4.1 Bayesian statistics . . . 40
2.4.2 `exoplanet`: single transit modelling via MCMC . . . 41
2.4.3 `allesfitter`: global analysis via nested sampling . . . 42
2.5 Can we study the planet's atmosphere? . . . 43
2.5.1 Handy metrics . . . 43
2.5.2 A step further: simulating atmospheric investigations . . . 44
2.6 Paper: Scheduling and data analysis software for ASTEP . . . 45
2.7 Observation Scheduling and Automatic Data Reduction for the Antarctic telescope, ASTEP+ . . . 47
2.7.1 Introduction . . . 47
2.7.2 Sensitivity to long period planets and long duration transits . . . 48
2.7.3 Observation scheduling . . . 50
2.7.4 Data analysis pipeline . . . 55
2.7.5 ASTEP+ in the future . . . 60
2.7.6 Conclusions . . . 60

3 Validation and Confirmation of Candidates from *TESS* 67
3.1 Introduction . . . 67
3.2 Paper: Confirmation of the HD 28109 (TOI-282) 3-planet system . . . 67
3.3 HD 28109 hosts a trio of transiting Neptunian planets including a near-resonant pair, confirmed by ASTEP from Antarctica . . . 69
3.3.1 Introduction . . . 69
3.3.2 Stellar Characterisation . . . 70
3.3.3 Identification of planetary candidates . . . 71
3.3.4 Vetting and validation of candidates . . . 73
3.3.5 Analysis . . . 76
3.3.6 System discussion . . . 81
3.3.7 Conclusions . . . 83
3.4 Paper: Validation of the TOI-715 system . . . 87
3.5 A 1.55 $R_\oplus$ habitable-zone planet hosted by TOI-715, an M4 star near the ecliptic South Pole . . . 88
3.5.1 Introduction . . . 88
3.5.2 Stellar Characterisation . . . 89
3.5.3 Identification of planetary candidates . . . 91
3.5.4 Vetting and validation . . . 93
3.5.5 Global photometric analysis . . . 95
3.5.6 Discussion . . . 97
3.5.7 Conclusions . . . 102
3.6 Work in progress: Validation of the Nemesis-12/AMY-1 system . . . 106

4 MANGOs in Space 113
4.1 World: meet MANGOs . . . 113
4.2 Paper: MANGOs I - Validation of the TOI-4860 system . . . 114
4.3 An M dwarf accompanied by a close-in giant orbiter . . . 116
4.3.1 Observations collected and their analysis . . . 117
4.3.2 Results & discussion . . . 119
4.3.3 Appendix A: Online supplementary material . . . 123

4.4 Work in progress: MANGOs II - Programme introduction and multi-flavour validation . 126

5 In Conclusion **135**
5.1 Concluding remarks 135
5.1.1 The conundrum of Hot and Warm Jupiter formation 136
5.1.2 Peas in a pod: yay or nay? 138
5.1.3 The M-dwarf radius valley... or not 139
5.1.4 How common are MANGOs in space? 140
5.2 Future work 141
5.3 The End 142

Bibliography **143**

List of publications

38) Standing, M. R., Sairam, L., Martin, D. V., et al. - Radial-velocity discovery of a second planet in the TOI-1338/BEBOP-1 circumbinary system. Nature Astronomy 2023; 7: 702-714

37) Brahm, R., Ulmer-Moll, S., Hobson, M. J., et al. - Three Long-period Transiting Giant Planets from TESS. The Astronomical Journal 2023; 165: 227

36) Barkaoui, K., Timmermans, M., Soubkiou, A., et al. - TOI-2084 b and TOI-4184 b: two new sub-Neptunes around M dwarf stars. arXiv e-prints 2023;: arXiv:2306.15095

35) Duck, A., Martin, D. V., Gill, S., et al. - The EBLM project X. Benchmark masses, radii, and temperatures for two fully convective M-dwarfs using K2. Monthly Notices of the Royal Astronomical Society 2023; 521: 6305-6317

34) **Dransfield, G., Timmermans, M., Triaud, A. H. M. J., et al. - A $1.55\ R_\oplus$ habitable-zone planet hosted by TOI-715, an M4 star near the ecliptic South Pole. Monthly Notices of the Royal Astronomical Society 2023; 2023MNRAS.tmp.1463D**

33) Trifonov, T., Brahm, R., Jordán, A., et al. - TOI-2525 b and c: A Pair of Massive Warm Giant Planets with Strong Transit Timing Variations Revealed by TESS. The Astronomical Journal 2023; 165: 179

32) Hawthorn, F., Bayliss, D., Wilson, T. G., et al. - TOI-836: A super-Earth and mini-Neptune transiting a nearby K-dwarf. Monthly Notices of the Royal Astronomical Society 2023; 520: 3649-3668

31) Pozuelos, F. J., Timmermans, M., Rackham, B. V., et al. - A super-Earth and a mini-Neptune near the 2:1 MMR straddling the radius valley around the nearby mid-M dwarf TOI-2096. Astronomy and Astrophysics 2023; 672: A70

30) Sebastian, D., Swayne, M. I., Maxted, P. F. L., et al. - The EBLM project - IX. Five fully convective M-dwarfs, precisely measured with CHEOPS and TESS light curves. Monthly Notices of the Royal Astronomical Society 2023; 519: 3546-3563

29) Kokori, A., Tsiaras, A., Edwards, B., et al. - ExoClock Project. III. 450 New Exoplanet Ephemerides from Ground and Space Observations. The Astrophysical Journal Supplement Series 2023; 265: 4

28) Pedersen, P. P., Murray, C. A., Queloz, D., et al. - Precise near-infrared photometry, accounting for precipitable water vapour at SPECULOOS Southern Observatory. Monthly Notices of the Royal Astronomical Society 2023; 518: 2661-2670

27) Delrez, L., Murray, C. A., Pozuelos, F. J., et al. - Two temperate super-Earths transiting a nearby late-type M dwarf. Astronomy and Astrophysics 2022; 667: A59

26) **Dransfield, G., Triaud, A. H. M. J., Guillot, T., et al. - HD 28109 hosts a trio of transiting Neptunian planets including a near-resonant pair, confirmed by ASTEP from Antarctica. Monthly Notices of the Royal Astronomical Society 2022; 515: 1328-1345**

25) Vach, S., Quinn, S. N., Vanderburg, A., et al. - TOI-712: A System of Adolescent Mini-Neptunes Extending to the Habitable Zone. The Astronomical Journal 2022; 164: 71

24) Schmider, F.-X., Abe, L., Agabi, A., et al. - Observing exoplanets from Antarctica in two colours: set-up and operation of ASTEP+. Ground-based and Airborne Telescopes IX 2022; 12182: 121822O

23) **Dransfield, G., Mékarnia, D., Triaud, A. H. M. J., et al. - Observation scheduling and automatic data reduction for the Antarctic Telescope, ASTEP+. Observatory Operations: Strategies, Processes, and Systems IX 2022; 12186: 121861F**

22) Gan, T., Soubkiou, A., Wang, S. X., et al. - TESS discovery of a sub-Neptune orbiting a mid-M dwarf TOI-2136. Monthly Notices of the Royal Astronomical Society 2022; 514: 4120-4139

21) Timmermans, M., Dransfield, G., Ducrot, E., et al. - TOI-4336.01: A mini-Neptune ripe for atmospheric characterization in a nearby triple M-dwarf system. Bulletin of the American Astronomical Society 2022; 54: 102.204

20) Murray, C. A., Queloz, D., Gillon, M., et al. - A study of flares in the ultra-cool regime from SPECULOOS-South. Monthly Notices of the Royal Astronomical Society 2022; 513: 2615-2634

19) Christian, S., Vanderburg, A., Becker, J., et al. - A Possible Alignment Between the Orbits of Planetary Systems and their Visual Binary Companions. The Astronomical Journal 2022; 163: 207

18) Standing, M. R., Triaud, A. H. M. J., Faria, J. P., et al. - BEBOP II: sensitivity to sub-Saturn circumbinary planets using radial-velocities. Monthly Notices of the Royal Astronomical Society 2022; 511: 3571-3583

17) Triaud, A. H. M. J., Standing, M. R., Heidari, N., et al. - BEBOP III. Observations and an independent mass measurement of Kepler-16 (AB) b - the first circumbinary planet detected with radial velocities. Monthly Notices of the Royal Astronomical Society 2022; 511: 3561-3570

16) Wilson, T. G., Goffo, E., Alibert, Y., et al. - A pair of sub-Neptunes transiting the bright K-dwarf TOI-1064 characterized with CHEOPS. Monthly Notices of the Royal Astronomical Society 2022; 511: 1043-1071

15) Kaye, L., Vissapragada, S., Günther, M. N., et al. - Transit timings variations in the three-planet system: TOI-270. Monthly Notices of the Royal Astronomical Society 2022; 510: 5464-5485

14) Schanche, N., Pozuelos, F. J., Günther, M. N., et al. - TOI-2257 b: A highly eccentric long-period sub-Neptune transiting a nearby M dwarf. Astronomy and Astrophysics 2022; 657: A45

13) Smith, G. D., Gillen, E., Queloz, D., et al. - NGTS clusters survey - III. A low-mass eclipsing binary in the Blanco 1 open cluster spanning the fully convective boundary. Monthly Notices of the Royal Astronomical Society 2021; 507: 5991-6011

12) Dong, J., Huang, C. X., Zhou, G., et al. - TOI-3362b: A Proto Hot Jupiter Undergoing High-eccentricity Tidal Migration. The Astrophysical Journal 2021; 920: L16

11) Swayne, M. I., Maxted, P. F. L., Triaud, A. H. M. J., et al. - The EBLM project - VIII. First results for M-dwarf mass, radius, and effective temperature measurements using CHEOPS light curves. Monthly Notices of the Royal Astronomical Society 2021; 506: 306-322

10) Burt, J. A., Dragomir, D., Mollière, P., et al. - TOI-1231 b: A Temperate, Neptune-sized Planet Transiting the Nearby M3 Dwarf NLTT 24399. The Astronomical Journal 2021; 162: 87

9) Wells, R. D., Rackham, B. V., Schanche, N., et al. - A large sub-Neptune transiting the thick-disk M4 V TOI-2406. Astronomy and Astrophysics 2021; 653: A97

8) Grieves, N., Bouchy, F., Lendl, M., et al. - Populating the brown dwarf and stellar boundary: Five stars with transiting companions near the hydrogen-burning mass limit. Astronomy and Astrophysics 2021; 652: A127

7) Dong, J., Huang, C. X., Dawson, R. I., et al. - Warm Jupiters in TESS Full-frame Images: A Catalog and Observed Eccentricity Distribution for Year 1. The Astrophysical Journal Supplement Series 2021; 255: 6

6) Dawson, R. I., Huang, C. X., Brahm, R., et al. - Precise Transit and Radial-velocity Characterization of a Resonant Pair: The Warm Jupiter TOI-216c and Eccentric Warm Neptune TOI-216b. The Astronomical Journal 2021; 161: 161

5) Tinetti, G., Eccleston, P., Haswell, C., et al. - Ariel: Enabling planetary science across light-years. arXiv e-prints 2021;: arXiv:2104.04824

4) Sebastian, D., Gillon, M., Ducrot, E., et al. - SPECULOOS: Ultracool dwarf transit survey. Target list and strategy. Astronomy and Astrophysics 2021; 645: A100

3) Sebastian, D., Pedersen, P. P., Murray, C. A., et al. - Development of the SPECULOOS exoplanet search project. Ground-based and Airborne Telescopes VIII 2020; 11445: 1144521

2) Bouma, L. G., Hartman, J. D., Brahm, R., et al. - Cluster Difference Imaging Photometric Survey. II. TOI 837: A Young Validated Planet in IC 2602. The Astronomical Journal 2020; 160: 239

1) **Dransfield, G., & Triaud, A. H. M. J. - Colour-magnitude diagrams of transiting exoplanets - III. A public code, nine strange planets, and the role of phosphine. Monthly Notices of the Royal Astronomical Society 2020; 499: 505-519**

List of Figures

1.1 Planetary mass as a function of orbital separation, with each panel highlighting the contribution of one of the four main detection methods to the known planetary population. 'Other' methods include Astrometry, Disk Kinematics, Eclipse Timing Variations, Orbital Brightness Modulation, Pulsar Timing, Pulsation Timing Variations, and Transit Timing Variations - the 63 planets discovered via these methods are over-plotted as small white hexagons in each panel to highlight their positions. 3

1.2 **Upper panel:** geometry of elliptical orbits as viewed from above. **Lower panel:** elliptical orbit in three dimensions. Both panels are inspired by Figures 2.1 and 2.2 from Perryman (2018) 4

1.3 Geometry of planetary transits. The black circles represent a transiting exoplanet as it moves across the limb-darkened stellar disc. Below, the black solid line is a limb-darkened lightcurve while the grey line shows the lightcurve for the same planet and star but without the limb-darkening. The planet positions marked 1,2,3, and 4 indicate first, second, third and fourth contact points. 6

1.4 Transit lightcurves of HD 209458 b spanning bandpasses from the blue to the near-infrared, with the colours corresponding the the spectral region of the bandpass. From Knutson et al. (2007). 7

1.5 Side and front view of planetary transit geometry, showing that as orbital inclination i decreases from $90°$, the planet transits further up the stellar disc. We also see that if $a\ \cos i\ > R_\star + R_\mathrm{p}$, the planet will not transit along our line of sight. 11

1.6 How has detection by transit photometry evolved? The four panels above demonstrate the widening of the parameter space explored by the transit method year-on-year since the first detection in 2000. All planets shown here were discovered using the transit method; from left the panels show discoveries per year by transit probability, planet-to-star radius ratio, orbital separation, and host radius. One planet has been omitted from the sample (WD 1856+534 b, Vanderburg et al. 2020) as it orbits a white dwarf and significantly skews the plots. Point are coloured by their discovery year. 12

1.7 The trend in detected radial velocity semi-amplitudes over time, highlighting both planets discovered by RV, and those first detected in transit but later followed-up on by RV. Note: for planets discovered by the transit method, the year is their year of discovery, not the year they were first detected in the radial velocity data. This fact skews the plot slightly, as the smallest detected RV semi-amplitude of $< 0.25\mathrm{ms}^{-1}$ was for Kepler-37 b, a planet discovered in 2013 (Barclay et al. 2013); however its current mass was published this year (Bonomo et al. 2023) 13

1.8 Hertzsprung-Russell diagram showing the main groupings of stars. M dwarfs are the redder stars on the main sequence, and Hot Subdwarfs are on the extreme horizontal branch to the left of the main sequence. the position of the Sun is also shown. From Heber (2009). 15
1.9 *Kepler*'s field of view in the Cygnus-Lyra region of the sky, just above the galactic plane. Image credit: NASA/Ames/JPL-Caltech (downloaded from `Wikipedia.org`). 17
1.10 **Panel (a):** Field of view of all four *TESS* cameras combined. **Panel (b):** *TESS*'s 26 observing sectors, with the overlap of the northern sectors at the ecliptic poles visible. **Panel (c):** Observation timescales accounting for overlaps between sectors on the celestial sphere. The area in red is *TESS*'s continuous viewing zone (CVZ); *JWST*'s CVZ is also shown within it. Figure from Ricker et al. (2015), and caption adapted from the original. 18
1.11 ASTEP+ in its new dome at Concordia Station on the Antarctic Plateau. In the background on the right hand side, the telescope's previous dome can be seen. 21
1.12 The four telescopes of the SPECULOOS Southern Observatory at ESO Paranal. Photo credit: Mathilde Timmermans 23
1.13 Planet radius (left hand panel) and planet mass (right hand panel) as a function of orbital period. Only planets discovered by RV or transit are included in this figure. In the left hand panel, the population of warm Jupiters discovered by RV is missing as these have very low transit probabilities due to their large orbital separations. Likewise, most Super-Earths and Sub-Neptunes are missing from the right hand panel as they transit stars too faint for spectroscopic mass measurements. 24
1.14 Giant planet occurrence vs orbital period. The black circles are values from the *Kepler* sample (Santerne et al. 2016), while the blue squares and red triangles are from RV surveys (Cumming et al. 2008; Mayor et al. 2011). Arrows indicate upper limits. Figure from Winn (2018). 26
1.15 Histogram showing planet radii for objects with orbital periods < 100 days; the planet numbers have been corrected for completeness. The light red shaded area represents 'Super-Earths' while the light green area encapsulates 'Mini-Neptunes'. The red solid like is a model fit to the data, while the dashed turquoise line is a possible underlying occurrence. Figure from Fulton et al. (2017), and caption adapted from the original. 27

2.1 Sample output from a BLS search. The upper panel shows a noisy time-series, and the bottom left panel shows the periodogram from the search. The panel on the bottom right shows the phase-folded binned time-series with the box-shaped model over-plotted. From Kovács et al. (2002). 32
2.2 The calibration frames taken for an observation of AMY-1 on the night of 2022 Februrary 11 with Io, one of the four telescopes of the SPECULOOS Southern Observatory. **Left panel:** bias frame. **Middle panel:** dark frame. **Right panel:** flat frame taken with the *I+z'* filter to match the observation. 34
2.3 Sample `prose` output from an observation on the night of 2023 01 27, by SPECULOOS-South (Io) in *Sloan-i'*. **Left panel:** Example stack image with detected sources. The scales on the x- and y-axes refer to pixel positions. **Upper right panel**: Position of the target aperture and annulus. **Lower right panel:** target lightcurve following differential photometry. 36
2.4 Figure from the successful *HST* proposal for atmospheric reconnaissance of TOI-4336 b (Dransfield et al. 2021). The green and purple lines are simulated transmission spectra calculated with `ExoTransmit` and the points are simulated observations from `PandExo`. . . 45
2.5 Results of the observability simulation for our synthetic sample of 2500 long period/long duration transiting planets. In all panels points are coloured according to the percentage of transits observable in full. Top row: duration and period distribution of the sample. Bottom row: the distribution of the sample on the sky. 49

2.6 Which systems can never be observed? Having removed all systems north of -40°, we show the systems that ASTEP still cannot observe to check if they are observable by other telescopes. Green points in all panels are systems where ASTEP can observe at least one transit in full, while red points have zero transits observable by ASTEP in the next five years. Top row: observability in terms of duration; bottom row: observability and period distribution. 50
2.7 Schematic of the ASTEP+ scheduling toolkit, showing how the three elements are interconnected. The `Python` toolkit generates data, the Google Sheet holds the data, and the website both displays and updates the data. 51
2.8 Screenshot of the graphical user interface for the target selection toolkit. 52
2.9 Screenshot of the DataTables display of the schedule as it appears on the ASTEP website. 54
2.10 The graphical web schedule, showing user inputs and options. When the cursor is hovered over an observation bar, the tooltip shows the name of the target and the timing of the event, as well as the airmass and moon illumination during the event. 54
2.11 Screenshot of the `JavaScript` target selection toolkit as it appears on the website, with the layout adapted from Crouzet et al. (in prep). Interactive airmass plots are displayed on the left, and information for potential targets is shown on the right. Targets can be selected from the dropdown list and then scheduled with the 'schedule' button. 55
2.12 Comparison of lightcurves produced by the two pipelines. The upper panels show the lightcurves produced by the `IDL` pipeline, while the lower panels show the results of the `Python` pipeline. Grey points are normalised fluxes and black points are binned in 5 minute bins. The upper lightcurves are raw fluxes with the blue line indicating the systematics + transit model. The bottom lightcurves have had the systematics trend removed. Left panels: observation of TOI-1107.01 on 13 August 2020. Middle panels: observation of TOI-282.01 (now HD 28109 b) on 10 May 2021. Right panels: observation of TOI-270.02 (now TOI-270 d) on 21 May 2022. 58

3.1 Spectral energy distribution (SED) of TOI-282. Red symbols represent the observed photometric measurements, where the horizontal bars represent the effective width of the passband. Blue symbols are the model fluxes from the best-fit Kurucz atmosphere model (black). 70
3.2 PDCSAP lightcurves of TOI-282, as produced by the SPOC pipeline. The top panel shows the photometry for sectors 1-13, while the bottom panel contained sectors 27-37, with a gap where sector 32 was missing. Binned data with a cadence of 30 min are shown in purple. 72
3.3 Results of our search for additional candidates in the data, using `TransitLeastSquares` as implemented by `Sherlock`. **Upper panel:** Lomb-Scargle periodogram showing the detected period and its harmonics. **Lower panel:** *TESS* lightcurve phase-folded on this period, with a transit model overplotted. 72
3.4 Contrast curves for HD 28109/TOI-282. The top panel shows the results from Gemini South, the middle panel shows the results from SOAR, and the bottom panel shows results from VLT/NaCo. All three panels are inset with final reconstructed images; none of the observations revealed bound companions within 5 magnitudes of the target. 74

3.5 Images of the field of TOI-282/HD 28109, showing that the star does not have any bright contaminating sources nearby. **Left Panel:** Target pixel files showing TOI-282 as a red star and other nearby sources as orange circles. The size of the circles is representative of the source's brightness. **Middle Panel:** Sloan Digital Sky Survey (SDSS York et al. 2000) image of the surrounding field of TOI-282 (indicated by a red cross). **Right Panel:** *TESS* target pixel file of one of the 25 sectors in which TOI-282 was observed, created with `TPFPlotter` (Aller et al. 2020). The pipeline aperture is shown by the white shaded region, and all nearby sources from Gaia (Gaia Collaboration et al. 2018) down to a magnitude difference $\Delta M = 8$ are overplotted as red circles. 76
3.6 Detrended transits observed with ASTEP on the nights of 2020 June 08, 2021 March 15 and 2021 May 10. The green points are the detrended flux, while the white circles are binned. Curves superimposed are the best-fitting models for each transit. 78
3.7 Global fit of the *TESS* photometric data for each of the planets of HD 28109. Points in the background are the phase-folded 2-minute cadence data, while white circles are the binned points. Curves are 20 samples drawn from the posterior. 79
3.8 Transit timing variations (in minutes) for each of the planets of HD 28109 spanning two years of *TESS* data plus ground-based photometric monitoring of planet c. The points show the difference between the fitted midtimes and the linear predictions, while the lines show the model predictions from our dynamical analysis in Section 3.3.5. 79
3.9 The 3:2 resonance structure diagram following Nesvorný & Vokrouhlický (2016). Systems with $\alpha = a_c/a_d < \alpha_{res}$ ($\alpha > \alpha_{res}$), where $\alpha = 0.763$ corresponds to the exact resonance, have orbits just wide (narrow) of the resonance. The resonance region where ψ librates is shaded. The separatrices and stable point are solid. Three planetary systems are plotted: HD 28109 (this work), TOI-216 (Dawson et al. 2021; Nesvorny et al. 2021) and KOI-142 (Nesvorný et al. 2013). TOI-216 is firmly in the resonance and KOI-142 is firmly outside the resonance. For HD 28109, the blue dots show a sample of 500 posterior solutions from our dynamical 3-planet fit, of which roughly two-thirds are non-resonant and roughly one-third are resonant. 80
3.10 Model predictions of the transit timings variations for the planets of HD 28109 for the next $11\,000$ days, spanning more than one full TTV period for the two outer planets. 80
3.11 Phased radial velocity measurements for each of the three planets. Triangles are points from ESPRESSO, while circles are points from HARPS; the curves are 20 model samples from the posterior. The data uncertainties include the RV jitter. 81
3.12 Distribution of known multi-planetary systems exhibiting transit timing variations. The planets of HD 28109 are shown as hexagons in violet (planet b), green (planet c) and pink (planet d); other planets are either shown in dark grey if they have a measured mass (by RV or TTV) or light grey if they do not. In the upper panel we show the distribution in planet radius according to host star *V* mag, while in the bottom panel we show the distribution in orbital period. 82
3.13 Mass-radius diagram showing the positions of HD 28109 b, c and d. Planets c and d are plotted as squares with their masses as estimated from TTVs. As the mass of planet b is still poorly constrained, we plot its position using its RV estimated mass as a hexagon, while the average mass for planets of its radius (estimated mass following Chen & Kipping (2017)) is plotted as a cross. 83
3.14 Model transmission spectra of HD 28109 b, c and d with simulated *HST* observations. Each point corresponds to a single transit depth with no offset; the curves represent the simulated transmission spectra. 83

3.15 LDSS-3C red optical spectrum of TOI-715 (black line), compared to its best-fit M4 template (Kesseli et al. 2017, magenta line). Spectra are normalized in the 7400–7500 Å region, and major absorption features are labeled, including regions of strong telluric absorption (⊕). The inset box shows a close-up of the region encompassing Hα (6563 Å) and Li I (6708 Å) features, neither of which is detected in the data. 90
3.16 Spectral energy distribution of TOI-715. Red symbols represent the observed photometric measurements, where the horizontal bars represent the effective width of the passband. Blue symbols are the model fluxes from the best-fit NextGen atmosphere model (black). . 90
3.17 Distribution of ages for all sources in GALAH Data Release 3 (light grey histogram) and those GALAH sources that match the UVW velocities and metallicity of TOI-715 (dark grey histogram). The latter distribution is consistent with a median age of $6.6^{+3.2}_{-2.2}$ Gyr (green shaded region, 25% and 75% quantiles), which we adopt as the age of TOI-715. 91
3.18 PDCSAP flux extracted from the short (2 minute) cadence data of the 24 sectors (1–13, 27, 29–37, 39) in which TOI-715 was observed. Light grey point show the $120\,\mathrm{s}$ exposures and the purple line shows the flux in $3\,\mathrm{minute}$ bins. The transit events of TOI-715.01 are shown with the dark pink arrows and the locations of possible transits of TIC 271971130.02 are indicated with green arrows; we note that individual transits are not readily apparent by eye. 92
3.19 Results of our search for additional candidates in the data, using `TransitLeastSquares` as implemented by `SHERLOCK`. **Upper panel:** `TLS` periodogram showing the detected 25.61 day period of TIC 271971130.02 and its harmonics. **Lower panel:** *TESS* PDCSAP lightcurve phase-folded on this period, with a transit model overplotted. We note that the errorbars on the binned points are smaller than the markers, and that the lightcurve shown here is the one treated with the SG Filter. 93
3.20 Plot showing the 5σ speckle imaging contrast curves in both filters as a function of the angular separation out to $1.2''$, the end of speckle coherence. The inset shows the reconstructed $832\,\mathrm{nm}$ image with a $1''$ scale bar. The star, TOI-715, was found to have no close companions to within the angular and brightness contrast levels achieved. 94
3.21 Photometry of TOI-715 b along with best fitting models. Grey points are raw flux and dark pink circles are 15-minute binned points. The dark pink lines are 20 fair draws from the posterior transit model. The flux and the transit models have been corrected by subtracting the baseline models. The *TESS*, ExTrA 2 and ExTrA 3 photometry are phase-folded, while the others are single transits. 98
3.22 Photometry of TOI-715 b along with best fitting models. Grey points are raw flux and dark pink circles are 15-minute binned points. The dark pink lines are 20 fair draws from the posterior transit model. The flux and the transit models have been corrected by subtracting the baseline models. All transits shown here are single transits. For the TRAPPIST lightcurves, the number in the figure titles denotes the visit number. These are treated as single transits due to the different exposure times of each visit. Increased scatter during the transit observed by SSO-Io (bottom right panel) cause the middle binned point to have a large errorbar. 99
3.23 Measured transit depths vs. wavelength. The dark grey horizontal line indicates the depth of the *TESS* transits, while other depths are highlighted with circles for comparison. . . . 100
3.24 Phase folded *TESS* photometry of TIC 271971130.02. Grey points are raw flux and green circles are 15-minute binned points. The green lines are 20 fair draws from the posterior transit model. The flux and the transit models have been corrected by subtracting the baseline models. 100

3.25 Plot of the current sample of planets orbiting hosts cooler than 4000 K in radius-period space. The grey circles are confirmed planets with radii measured to better than 10% precision, and the dark pink and green circles are TOI-715 b and TIC 271971130.02 respectively. We note that some errorbars are smaller than the markers. The blue line indicates the measured radius valley according to Van Eylen et al. (2021) for hosts cooler than 4000 K. The black dashed line is the low-mass star radius valley as measured by Cloutier & Menou (2020) for hosts cooler than 4700 K, while the dotted black line indicates the radius valley for Sun-like stars as measured by Martinez et al. (2019). The yellow shaded area indicates where planets referred to as 'keystone planets' can be found. The histogram in the right-hand panel does not include TOI-715 b or TIC 271971130.02. . . . 100
3.26 Transmission spectroscopy metric vs. instellation for transiting planets orbiting hosts cooler than 4000 K. The blue shaded area shows the conservative habitable zone as defined by Kopparapu et al. (2013). The two dark pink circles highlight the positions of TOI-715 b in the rocky and water world scenarios, while the green circle indicates the position of TIC 271971130.02. We highlight in yellow the positions of the seven planets of TRAPPIST-1. The sizes of the circles are scaled with planetary radius. 101
3.27 TESS-SPOC photometry of Nemesis-12/AMY-1. The light grey points are raw while the purple line indicates the $5\mathrm{min}$ binned points. The transit times are indicated with light green arrows. The upper panel contains the $1800\mathrm{s}$ photometry from sectors 5 and 6, and the lower panel has the $600\mathrm{s}$ photometry from sectors 32 and 33. 107
3.28 Spectral energy distribution of Nemesis-12/AMY-1. Red symbols are observed photometric measurements, with the horizontal bars representing the width of the bandpasses. The blue points are the model fluxes from the best-fit NextGen atmosphere model (black line). (Caption adapted from previous captions provided by Keivan Stassun.) 107
3.29 LDSS-3C red optical spectrum of Nemesis-12/AMY-1 compared to its best fitting M5 template. (Caption adapted from previous captions provided by Adam Burgasser.) 109
3.30 Plot showing the $5-\sigma$ speckly imaging contrast curve in the blue and red filters as a function of angular separation. The inset image shows the reconstructed speckle image. (Caption adapted from other captions provided by Steve Howell). 110
3.31 Phase-folded and detrended ground- and space-based photometry for AMY-1 b. Overplotted on each lightcurve are 20 models randomly drawn from the posterior distribution. 112

4.1 This figure shows all of the photometric data we use in this paper. On the left hand side we show each lightcurve and 20 models obtained from the posterior. On the top right, we plot photometry obtained around the time of secondary eclipse and 20 models from the posterior for each of the 14 lightcurves. The *TESS* data are not used to determine planetary parameters in this paper. Instead, they were used to corroborate the other observations we obtained. The middle right panels shows that when transit depths $R_{\mathrm{b}}^2/R_{\star}^2$ are fitted independently in each wavelength, they demonstrate that the transit signal is achromatic. The bottom right panel draws the density of posterior samples for solutions including secondary eclipse depths parameters (arbitrary unit), assuming the orbit of the planet is circular. All are consistent with no loss of light. All colours are chosen to depict the wavelength of the observations. 118
4.2 Radial-velocities measured by IRD as a function of orbital phase. We show 20 models randomly drawn from the posterior. 119
4.3 This diagram highlights TOI-4860 b's uniqueness amongst transiting giant exoplanets as being hosted by the lowest mass star yet. The purple dot corresponds to TOI-4860 b. All other grey dots correspond to planets with radius $> 0.6\ \mathrm{R_{Jup}}$ and a measured mass $< 25\ \mathrm{M_{Jup}}$. Data from TEPCAT (Southworth 2011). 119

4.4 MagE optical spectrum of TOI-4860 (black lines) compared to M3, M4, and M5 spectral templates (colored lines from top to bottom) from Bochanski et al. (2007). All spectra are normalized at 7400–7500 Å. Primary atomic and molecular absorption features in the 4500-9000 Å spectra of M dwarfs are labeled, as are regions of strong telluric absorption (⊕). The inset box displays a close-up of the 6500–6800 Å region that hosts the 6563 Å Hα and 6708 Å Li I lines (vertical dashed lines), neither of which are detected. 123
4.5 SpeX SXD spectrum of TOI-4860 (blue) and the M5 standard Wolf 47 (grey). Prominent M-dwarf spectral features are highlighted, and regions of strong telluric absorption are shaded in grey. The grey lines at the bottom of the plot show the measurement uncertainties for the target and comparison star (higher and lower, respectively). 123
4.6 Cross-correlated IRD spectrum for on 2023-02-01, when TOI-4860 b was at orbital phase 0.69 (i.e. close to maximum velocity). This profile shows TOI-4860 is a single-lined system and unlikely to be an unresolved binary. 123
4.7 Images of the field of TOI-4860. In both images, the yellow cross-hairs are positioned on the current location of the target. **Left panel:** 1954 red image from the Digitised Sky Survey (DSS). **Right panel:** *Sloan-z'* image taken by SSO Europa in 2023. 123
4.8 View of the Google Sheet used to track observations and reports submitted to TFOP. . . 127
4.9 View of the Google Sheet used for tracking progress on the MANGOs II paper. 128
4.10 Photometric observations of TOI-234 b. Plotted on each lightcurve there 20 models randomly drawn from the posterior. 129
4.11 Photometric observations of TOI-4666 b. Plotted on each lightcurve there 20 models randomly drawn from the posterior. 131
4.12 Photometric observations of TOI-734 B. Plotted on each lightcurve there 20 models randomly drawn from the posterior. 132
4.13 Photometric observations of TOI-2415 B. Plotted on each lightcurve there 20 models randomly drawn from the posterior. 134

5.1 The impact of my thesis on the field of exoplanets. The yellow and orange stars are planet discoveries published or in preparation, led by me. Purple hexagons are discoveries that made use of ASTEP photometry, to which I contributed. Dark pink triangles are SPECULOOS-led discoveries which I co-authored. The large collection of crosses at the top are all validated MANGOs. 136
5.2 Four of us travelled to Concordia for our 2021/22 summer service mission; pictured here from left to right are Djamel Mekarnia, myself, Olivier Lai, and Karim Agabi. Behind us is ASTEP in its new dome, and in the background are the two towers that make up the main quarters of the station. 137
5.3 Photos from my 2022 service mission to the SPECULOOS Southern Observatory at ESO Paranal in Chile. **Left panel:** here I am preparing to dismount the camera from one of the telescopes for cleaning. **Right panel:** sitting comfortably in the slit of one of the domes. My colleagues preferred not having to touch the chain grease for the slit motors if they could avoid it - I had no such reservations which meant I got to climb up and enjoy the views. 140

List of Tables

3.1 Stellar parameters adopted for this work. 71
3.2 Summary of ground-based follow-up observations carried out for the validation of TOI-282.01, .03 and .04. 73
3.3 Priors used in our fit, along with fitted and derived parameters. Uniform priors are indicated as $\mathcal{U}(\text{lower bound, upper bound})$ and normal priors are indicated as $\mathcal{N}(\text{mean, standard deviation})$. 77
3.4 Stellar parameters adopted for this work. 90
3.5 Summary of ground-based follow-up observations carried out for the validation of TOI-715.01 and TIC 271971130.02 94
3.6 Priors used in our fit, along with fitted and derived parameters. Uniform priors are indicated as $\mathcal{U}(\text{lower bound, upper bound})$ and normal priors are indicated as $\mathcal{N}(\text{mean, standard deviation})$. ⋆Equillibrium temperature is calculated assuming an albedo of 0.3 and emissivity of 1. . . 96
3.7 Stellar parameters adopted for this work. 108
3.8 Fitted parameters from AMY-1 b. 110
3.9 Derived parameters for AMY-1 b. 111

4.1 Fitted and derived parameters after performing a global analysis of the data. *TESS* photometry is not included in the analysis. Parameters denoted with * were estimated by letting the eccentricity to be set by two free parameters. All other parameters assume a circular orbit. The equilibrium temperature is calculated assuming an albedo of 0.3 and emissivity of 1. 119
4.2 Summary of photometric ground-based observations table for TOI-4860.01. 124
4.3 Stellar parameter estimates. 124
4.4 Radial velocity measurements with IRD at Subaru Telescope. 124
4.5 Table containing other fitted and derived parameters from our analysis and complementing Table 4.1 125
4.6 Dispositions used to classify MANGOs in our target list. 126
4.7 Fitted and derived parameters for TOI-234 b. 130
4.8 Fitted and derived parameters for TOI-4666 b. 130
4.9 Fitted and derived parameters for TOI-734 B. 133
4.10 Fitted and derived parameters for TOI-2415 B. 133

1

Exoplanetology in 2023

1.1 What's left to find out?

Some of the earliest records of systematic arithmetic Astronomy can be found in the British Museum, where they tell the story of 'omen watching' in ancient Mesopotamia (Jones 2000). A collection of around 70 clay tablets documents the links made by early astronomers between celestial phenomena and meteorological activities (Reiner & Pingree 1985); these exquisitely preserved artifacts allow us to look back on over four millennia of documented astronomical observations.

The above opening remarks really are just to say the following: people have been doing Astronomy for a while now. The salient question is therefore, what truly **big** things are left to learn? Fortunately, the answer is a resounding 'loads', evident in the fact that the astronomical sub-field of Exoplanets, wherein this thesis sits, is roughly as old as I am.

One of the ways a field with the mammoth scope of Astronomy can continue to grow is by identifying gaps, either in our understanding or in what we think is a well known parameter space. Until January 1992 we only knew of one planet-hosting star, so essentially the entire parameter space of star-planet possibilities was a gap. But the discovery of at least two planet-mass objects orbiting the pulsar PSR1257+12 (Wolszczan & Frail 1992) opened up a planetary can of worms, birthing a new world of possibilities for exploration.

The extreme environment of these planets orbiting a long-dead star could not be less like our own Solar System, and it wasn't until a few years later that a planet was first discovered orbiting another Sun-like star. But while 51 Pegasi b (Mayor & Queloz 1995) may orbit a star that's more familiar to us, its blisteringly short orbit represented another extreme discovery. And so, the plot thickens.

I could list fascinating firsts all day, but I'll stop at two as there have been too many to do the field any justice. As of today, there are 5338 confirmed extrasolar planets[a], so suffice it to say that it's going well. So well that the field is now shifting its focus away from detection and discovery towards in-depth characterisation of what we've got.

[a] According to the NASA Exoplanet Archive: https://exoplanetarchive.ipac.caltech.edu, but that number will undoubtedly be out of date by the time anyone reads this thesis.

And yet, here I present what is ostensibly a thesis focused on detection and discovery. Bold move.

Throughout the pages of this work, I aim to convince my readers of the continued importance of searching for new planets. There are some planet-star combinations we still haven't found any examples of, such as any planet orbiting a Hot Subdwarf (Thuillier et al. 2022), or small planets in circumbinary systems (Martin & Fitzmaurice 2022). There are also some flavour pairings with too few known examples to discern whether they are flukes or common occurrences, such as planets around white dwarfs (Vanderburg et al. 2020). Ongoing discovery and detection therefore serves not only to fill but also broaden the parameter space.

There is also statistics to consider. Remarkable new results can often emerge from studies of statistically large samples, one of the best examples being the curious paucity of planets with radii between $1.5 - 2\,\mathrm{R}_{\oplus}$ which became evident following examination of the full *Kepler* sample (Fulton et al. 2017). Continued efforts to find new planets enable the community to assemble large enough samples for this type of groundbreaking science to happen.

But I'm getting ahead of myself. In thesis lore, you don't even know what words like *Kepler* and Hot Subdwarf mean. From Section 1.2 onward, writing will be in proper full thesis mode and (hopefully), all will be explained. No need to buckle in - this should be the smoothest of rides.

1.2 Exoplanet detection methods

The first planet discovered orbiting a star other than the Sun was found using variations in the timings of the radio pulses detected from a rapidly rotating neutron star (Wolszczan & Frail 1992). In the three decades since, this method has only yielded five more planetary discoveries (Kramer 2018), one of which was a third planet in that original system (Wolszczan 1994).

With the exception of direct imaging (for a review: Pueyo 2018), all exoplanet discovery methods rely on planets having a detectable effect on their host star[b] or their planetary siblings. Figure 1.1 presents the distribution of confirmed exoplanets in mass - orbital separation space, with each of the four panels highlighting the contribution of a different detection method; pulsar timing falls under 'Other' due to its minute contribution.

In Figure 1.1 we can see that there are four detection methods that have had the most significant impact on the known sample: transits, radial velocities (RV), microlensing and direct imaging. We can also see the parameter space that each method typically probes. It is clear that the transit and RV methods have the largest overlap in parameter space, which is why they are such complementary techniques (e.g. Léger et al. 2009; Rauer et al. 2014). Direct imaging, on the other hand, can so far only find very massive planets at large orbital separations, as these can be spatially resolved with current instrumentation (Traub & Oppenheimer 2010). Most of the systems discovered so far are also young, as the planets still retain formation heat allowing them to be brighter in the infrared (e.g. Marois et al. 2008; Macintosh et al. 2015).

[b] The other exception being free-floating planets, sometimes detectable via microlensing. In these cases we detect the planet's gravitational effect on other unrelated stars (Gaudi 2012), rather than on their non-existent host.

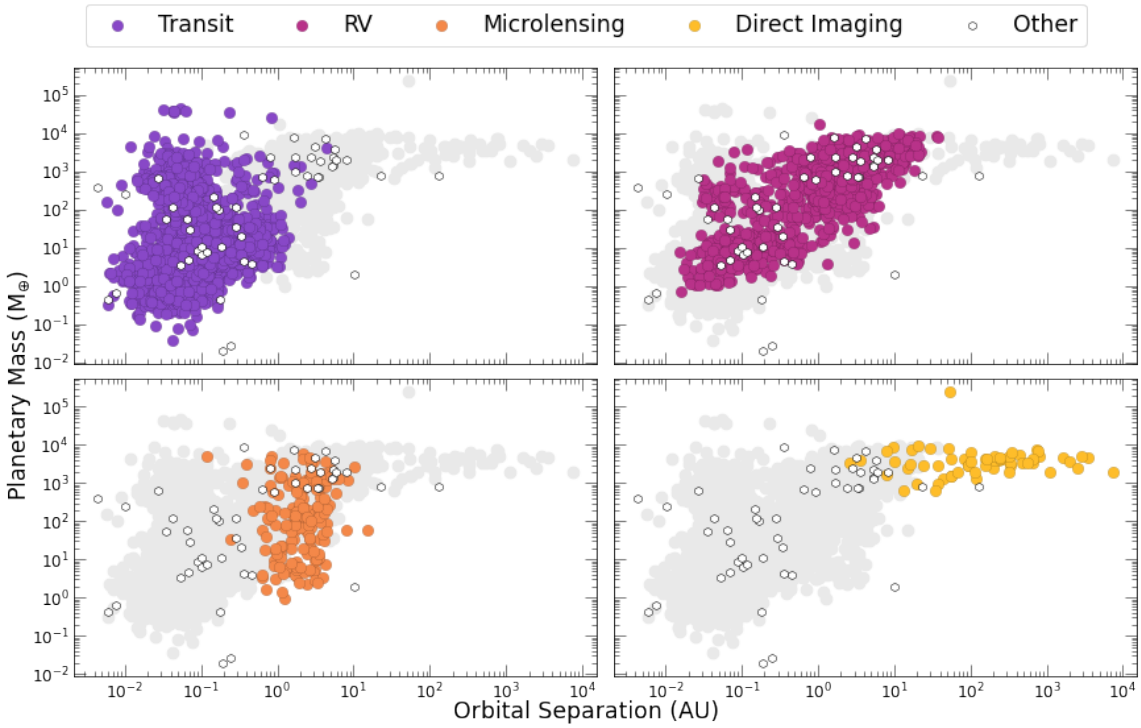


Figure 1.1: Planetary mass as a function of orbital separation, with each panel highlighting the contribution of one of the four main detection methods to the known planetary population. 'Other' methods include Astrometry, Disk Kinematics, Eclipse Timing Variations, Orbital Brightness Modulation, Pulsar Timing, Pulsation Timing Variations, and Transit Timing Variations - the 63 planets discovered via these methods are over-plotted as small white hexagons in each panel to highlight their positions.

Microlensing planets do appear at first look to also have a large overlap with both transits and RV in Figure 1.1; however, most of these systems are much further away than other known systems, making them incompatible with photometric or spectroscopic detections (Griest & Safizadeh 1998). However, one of the great benefits of microlensing is its ability to detect low-mass planets at relatively large orbital separations (Gaudi 2010); this is a parameter space as yet out of reach to the other most successful detection methods.

Of the various methods used to discover exoplanets, only one is truly pertinent to this work: transits. However, the other biggest contributor to our current sample of known planets, namely radial velocity, also warrants some description. Each of these two methods of planetary detection can also be used as a tool for detailed follow-up of a planet discovered by another method. In the sections that follow, I will describe the quantities directly observable from transit and radial velocity observations, as well as the physical parameters we can derive from them.

1.2.1 A Keplerian orbit

Before launching into discovery methods, I will describe in brief the key elements that make up a Keplerian orbit, as described in Murray & Correia (2010); Winn (2010); Perryman (2018).

A Keplerian orbit is one that obeys Kepler's three laws of planetary motion (Kepler 1609), the first

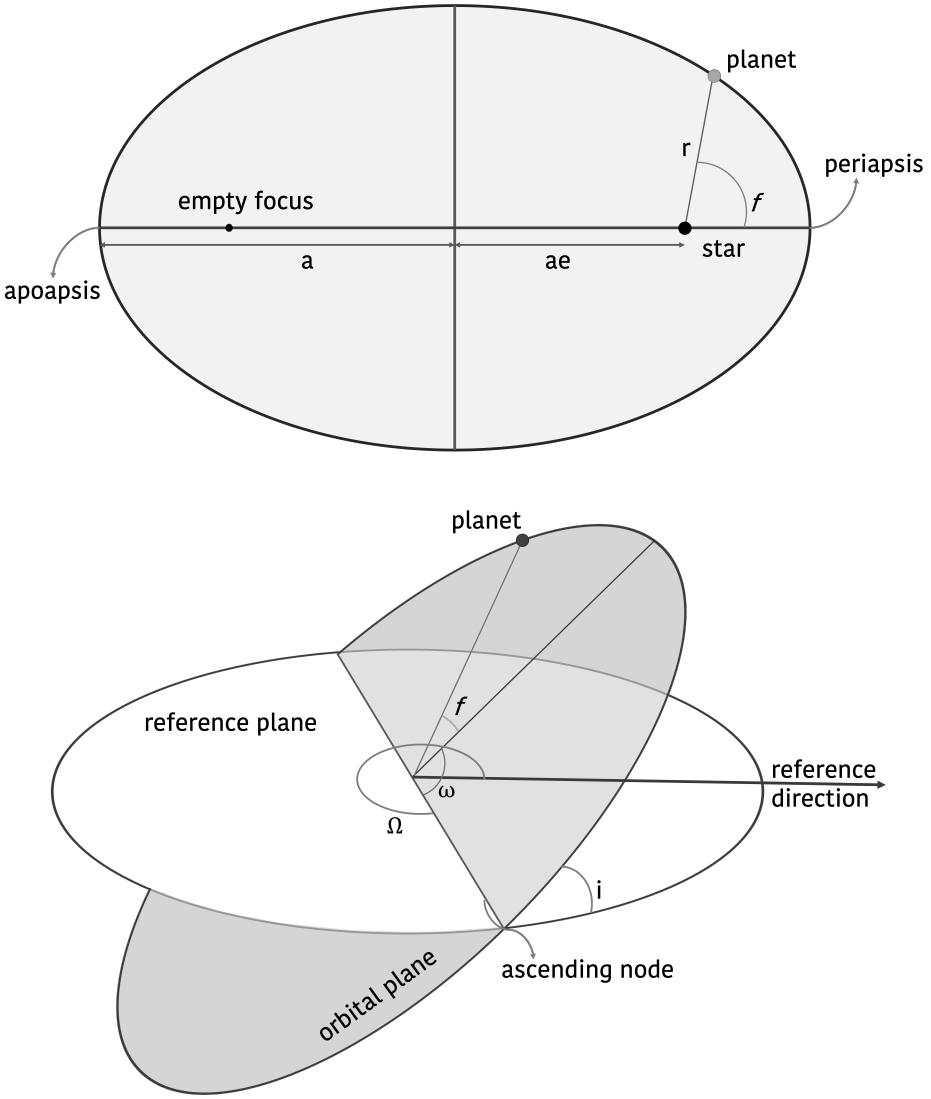


Figure 1.2: Upper panel: geometry of elliptical orbits as viewed from above. **Lower panel:** elliptical orbit in three dimensions. Both panels are inspired by Figures 2.1 and 2.2 from Perryman (2018)

of which states that planets orbit their stars in elliptical orbits with the host star at one of the two foci. The shape and size of the elliptical orbit are described by two quantities: the semi-major axis a, and the eccentricity e. Two further quantities are required to describe the orientation of the orbital plane; they are the orbital inclination i, the angle between the orbital and reference planes; and the longitude of the ascending node Ω, the angle between the reference direction and the ascending node (the point where the planet crosses from below to above the reference plane).

There are two final orbital elements which describe the orbit. The argument of periastron ω is the angle between the ascending node and the periapsis, and serves to orient the orbit within the orbital plane. Finally, the true anomaly f is an angle which is a function of time, and tells us the current angle between the planet's location and the periapsis.

The distance between the planet and star r at any time is given by

$$r = \frac{a(1-e^2)}{1+e\ \cos\ f}\ . \tag{1.1}$$

All orbital elements described above are represented in Figure 1.2.

Kepler's second law is a consequence of conservation of angular momentum, and states that a line joining the star and the planet will sweep out equal areas in equal times. Kepler's third and final law tells us that the square of the orbital period is directly proportional to the cube of the semi-major axis. While this law was originally derived empirically, it can now also be derived from first principles, and it can be simply shown in the case of a circular orbit that

$$P^2 = \frac{4\pi^2}{GM_\star}a^3\ , \tag{1.2}$$

where P is the orbital period, G is the gravitational constant, and $M_\star$ is the mass of the central star. This result assumes that the planets mass is significantly smaller than the host mass ($M_p << M_\star$); in cases where this is not true, $M_\star$ is replaced in Equation 1.2 with $M_\star + M_p$.

1.2.2 Transit photometry

When a planet passes in front of its host star along our line of sight, a small portion of the stellar disc is temporarily obscured resulting in a decrease in flux. This event is known as a transit, and by taking repeated measurements of stellar brightness and plotting a lightcurve we can detect a planetary transit *if* the planet-to-star radius ratio is favourable.

1.2.2.1 Observable parameters from transit lightcurves

Figure 1.3 presents a schematic of the transit geometry and a corresponding lightcurve. There are four quantities directly measurable from transit lightcurves: the transit depth (ΔF), the total and full transit durations (T_T and T_F respectively), and the orbital period (P) (Seager & Mallén-Ornelas 2003).

The transit depth is the fractional drop in flux observed during a transit (Deeg & Alonso 2018). It is approximately given by the ratio of the areas of the discs of the planet and star, which reduces to:

$$\Delta F\ \approx\ \left(\frac{R_\mathrm{p}}{R_\star}\right)^2\ . \tag{1.3}$$

As can be seen in Figure 1.3, these quantities are not exactly equal to each other as stellar limb-darkening causes an overshoot (Seager & Mallén-Ornelas 2003; Csizmadia et al. 2013; Heller 2019), which leads us into 'limb-darkening'.

Limb-darkening: Limb-darkening is the observed effect where the stellar disc gradually darkens radially towards the limb (Winn 2010). This is caused by the geometry of observing a spherical object which appears to us as a disc; closer to the limb of the disc we are looking a thicker slice of the stellar atmosphere than at the centre of the disc. Therefore, if our observations are sensitive to a particular optical depth, we will probe a hotter layer of the star at the centre of the disc than at the limb.

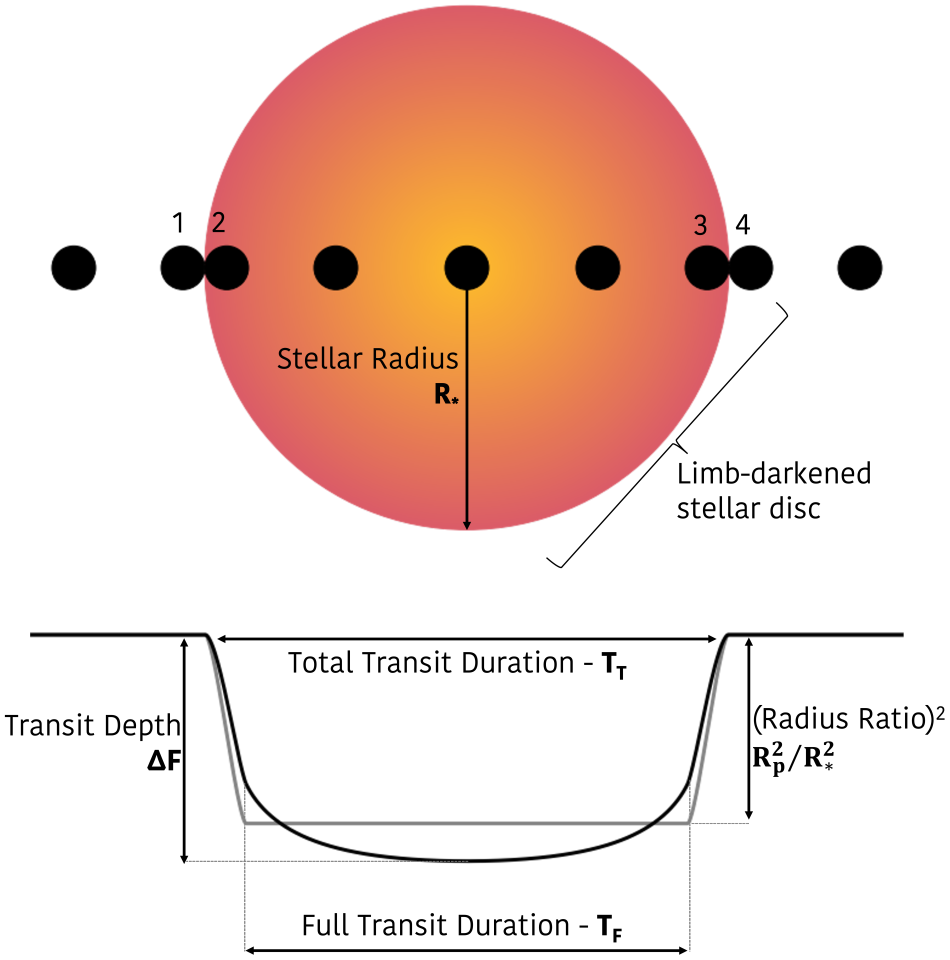


Figure 1.3: Geometry of planetary transits. The black circles represent a transiting exoplanet as it moves across the limb-darkened stellar disc. Below, the black solid line is a limb-darkened lightcurve while the grey line shows the lightcurve for the same planet and star but without the limb-darkening. The planet positions marked 1,2,3, and 4 indicate first, second, third and fourth contact points.

As a planet transits across the disc of a star, it is therefore obscuring regions of different intensity, which will have an effect on the shape of the transit lightcurve. The effect is wavelength dependent; lightcurves observed in shorter wavelengths have more rounded bottoms while longer, redder wavelength lightcurves have flatter bottoms (e.g. Knutson et al. 2007), as can be seen in Figure 1.4. Thus the planet-to-star radius ratio, often denoted as 'k', cannot be inferred directly from a single transit lightcurve without modeling.

On Figure 1.3 four points of contact between the planetary and stellar discs are highlighted. The time between the first and fourth contacts is the total transit duration ($T_{\rm T}$), and the time between second and third contacts is the full transit duration ($T_{\rm F}$). The latter is therefore the time of totality, when the disc of the planet is completely within the disc of the star. For grazing geometries, where the disc of the planet is never fully encapsulated in the disc of the star, there are no second and third contacts

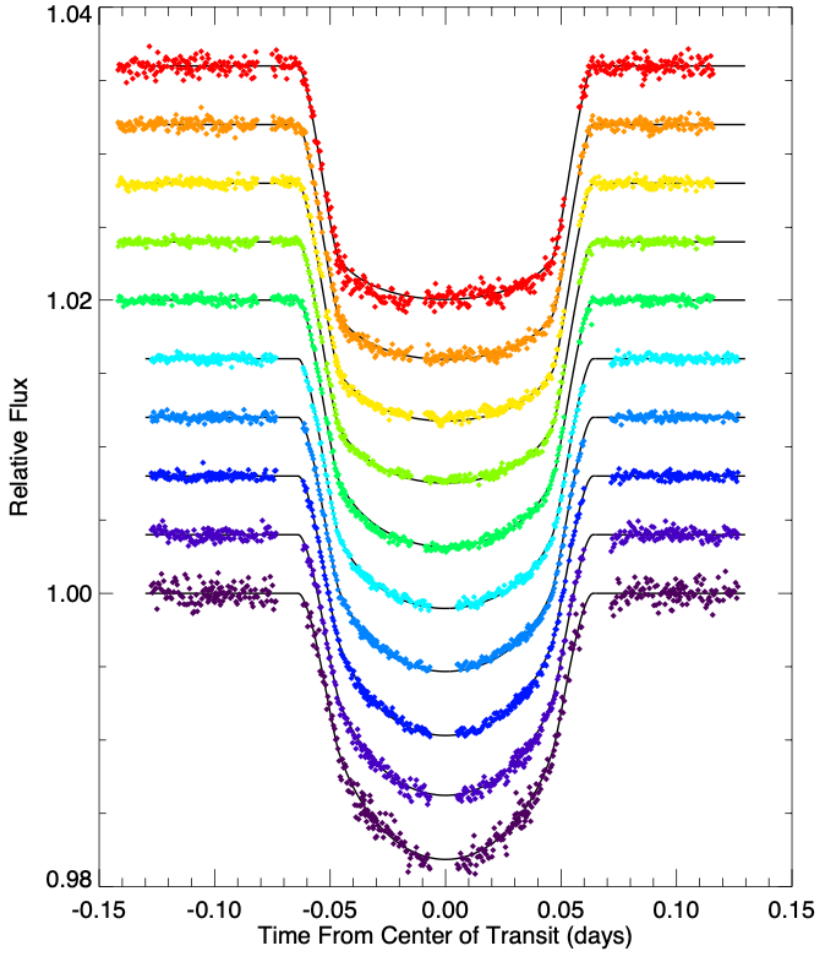


Figure 1.4: Transit lightcurves of HD 209458 b spanning bandpasses from the blue to the near-infrared, with the colours corresponding the the spectral region of the bandpass. From Knutson et al. (2007).

and the full transit duration is thus zero (Winn 2010).

Sackett (1999) demonstrated that it is possible to estimate a planet's orbital period from a single transit lightcurve, given knowledge of the stellar spectral type. However, by observing at least two consecutive transits and measuring the time of inferior conjunction (t_0 - the time at which the planet lies between host star and observer (Pepe et al. 2010a)) and calculating the time between them, we can measure the period directly. In Winn (2010), this is given as:

$$t_0[n] = t_0[0] + nP \,, \tag{1.4}$$

where $t_0[n]$ is the time of inferior conjunction of the nth event.

1.2.2.2 Physical system parameters from transit lightcurves

With the four quantities directly measurable from transit observations now described, we can move onto physical parameters of interest; these are the planetary radius R_p, the orbital inclination i, the

semi-major axis (or orbital separation) a, the host star's density $\rho_\star$, and the orbital eccentricity e. A sixth parameter that relates to the orbital inclination is the impact parameter b, defined as the projected distance between the centres of the stellar and planetary discs during transit. b is measured as a fraction of $R_\star$ and is a dimensionless quantity (Deeg & Alonso 2018). In Figure 1.5 we can see that b can be expressed as

$$b = \frac{a \cos i}{R_\star} . \tag{1.5}$$

Seager & Mallén-Ornelas (2003) demonstrated that it is possible to derive an estimate of the host star's density from the four transit observables, using the following expression:

$$\frac{\rho_\star}{\rho_\odot} = \frac{32}{G\pi} P \frac{\Delta F^{3/4}}{\left(T_\mathrm{T}^2 - T_\mathrm{F}^2\right)^{3/2}} , \tag{1.6}$$

where $\rho_\star$ is the host star's density and G is the gravitational constant. Equation 1.6 assumes a non-grazing transit and a circular orbit, and negates the effects of limb darkening. This expression is so widely accepted that it is often used in combination with an independently measured stellar density to assess the validity of transit signals or the completeness of a lightcurve model (Kipping 2014). However, Kipping (2010) carried out numerical investigations to assess the impact of assuming $e = 0$ and found that neglecting eccentricities of just ~ 0.1 can vary the measured stellar density by 30%.

To extract a value for the orbital separation a, we can use Kepler's third law (Equation 1.2), although this requires the assumption that $M_\mathrm{p} << M_\star$, as well as an estimate of the host mass. It is possible to use stellar mass-radius relations to estimate the host mass from the density derived using Equation 1.6 (Seager & Mallén-Ornelas 2003), although in many cases we will have an independent measure of the stellar parameters as described in Section 1.2.4. In a similar vein, the planetary radius can be estimated from Equation 1.3, requiring once again an external estimate for the host radius, or the use of the stellar mass-radius relations as described above.

The orbital inclination, and hence the impact parameter, are related to the transit shape, which is parametrised as the ratio of the full transit duration T_F to the total transit duration T_T. In Seager & Mallén-Ornelas (2003) the expression for this is presented as

$$\frac{T_\mathrm{F}}{T_\mathrm{T}} = \frac{\arcsin\left(\frac{R_\star}{a}\left[\frac{\left(1-\sqrt{\Delta F}\right)^2 - \left(\frac{a\cos i}{R_\star}\right)^2}{1-\cos^2 i}\right]^{1/2}\right)}{\arcsin\left(\frac{R_\star}{a}\left[\frac{\left(1+\sqrt{\Delta F}\right)^2 - \left(\frac{a\cos i}{R_\star}\right)^2}{1-\cos^2 i}\right]^{1/2}\right)} . \tag{1.7}$$

This expression then allows us to extract the orbital inclination from the transit observables, once the other physical parameters have also been derived.

1.2.2.3 A possible second loss of light: planetary occultations

In some cases, a transiting planet may also pass behind the central star along our line of sight becoming completely hidden from view. This event is known as an occultation (or sometimes a secondary eclipse), and may result in a second decrease in flux (Winn 2010).

When the decrease in flux during occultation is caused mostly by thermal emission from the planet, the occultation depth gives us a measure of the planet-to-star flux ratio (Alonso 2018). This is because the occultation depth is given by

$$\Delta F_{\rm occ} = \frac{F_{\rm p}}{F_\star} = \left(\frac{R_{\rm p}}{R_\star}\right)^2 \frac{S_{\rm p}}{S_\star} \,, \tag{1.8}$$

where $F_{\rm p}$ and $F_\star$ are the planet and stellar fluxes respectively, and $S_{\rm p}$ and $S_\star$ are the surface brightnesses of the planet and star respectively (adapted from Winn 2010). The quantity $S_{\rm p}/S_\star$ is known as the surface brightness ratio.

If the drop in flux is dominated by reflection of stellar flux, then the occultation depth is instead given by

$$\Delta F_{\rm occ} = A_{\rm g} \left(\frac{R_{\rm p}}{a}\right)^2 \phi(\alpha) \,, \tag{1.9}$$

where $A_{\rm g}$ is the planet's geometric albedo and $\phi(\alpha)$ is a phase function which tells us when in the orbital phase the secondary eclipse happens (Alonso 2018) (a and $R_{\rm p}$ maintain their usual meanings).

The detection of a planetary occultation can also help to constrain the eccentricity of the orbit (Alonso 2018) using both the measured midtimes and the full durations of each event. The midtimes are used to find the tangential component of the eccentricity $e\ \cos\ \omega$ using

$$e\ \cos\ \omega = \frac{\pi}{P} \frac{t_{0,\rm occ} - t_{0,\rm tra} - \frac{P}{2}}{1 + \cos^2 i} \,, \tag{1.10}$$

where $t_{0,\rm tra}$ and $t_{0,\rm occ}$ are the transit and occultation midtimes respectively. The radial component of the eccentricity $e\ \sin\ \omega$ can then be derived from the durations of the events using the following approximate expression from Winn (2010):

$$e\ \sin\ \omega \approx \frac{T_{\rm F,tra}}{T_{\rm F,occ}} - 1 \,, \tag{1.11}$$

where $T_{\rm F,tra}$ and $T_{\rm F,occ}$ are the full transit and occultation durations. As event durations are harder to constrain precisely than their midtimes, both Winn (2010) and Alonso (2018) note that the constraint on the tangential component of the eccentricity from photometry is stronger than that of the radial component.

1.2.2.4 When is an orbit non-Keplerian?

In a two-body orbiting system, the expectation is that Kepler's three laws will be obeyed, as described in Section 1.2.1. However, in systems where at least one additional body is present, mutual gravita-

tional interactions can lead to non-Keplerian behaviour. This is especially the case in multi-planetary systems where two or more planets find themselves in or close to a mean-motion-resonance (MMR), where orbital periods are integer multiples of each other (Lithwick et al. 2012). In particular, this deviation from Kepler's laws can lead to transit midtimes arriving early or late compared with linear predictions - these deviations are known as Transit Timing Variations (TTVs) (Agol & Fabrycky 2018).

For each individual transit, the magnitude of the TTV is given by the difference between the observed transit midtime and the time calculated from the linear model (Agol & Fabrycky 2018). The TTVs for each planet can then be plotted as a function of time; this allows a sinusoidal model to be fitted in order to measure the amplitude of the TTV signal. Lithwick et al. (2012) demonstrated how the amplitude of the TTV signal can be used to measure the dynamical masses of the planets, provided they are close to but not exactly in a MMR. This method of extracting mass measurements has been widely used for multi-planetary systems where follow-up with precise radial velocities is not possible (e.g. Hadden & Lithwick 2014, 2017; Lopez et al. 2019; Agol et al. 2021; Greklek-McKeon et al. 2023).

Crucially, this method can only reveal the planet-to-star mass ratios; to transform this to a true mass measurement, we require knowledge of the host star's parameters.

1.2.2.5 Transit probabilities

The transit method of detecting exoplanets now accounts for over 75% of discoveries, an astounding achievement considering that detection of exoplanet transits is inherently unlikely (Borucki & Summers 1984; Perryman 2018). In Winn (2010), the transit probability for a system is given as:

$$P_{\rm tr} = \left(\frac{R_\star \pm R_{\rm p}}{a}\right)\left(\frac{1 + e\ \sin\omega}{1 - e^2}\right), \tag{1.12}$$

where $R_\star$ is the stellar radius, $R_{\rm p}$ is the planetary radius, a is the orbital semi-major axis, ω is the argument of periastron, and e is the orbital eccentricity. In the numerator of the above expression, the '+' allows for eclipses with grazing geometry, while using the '-' sign excludes them.

In equation 1.12, the orbital inclination (i) must satisfy $a\ \cos\ i \leq R_\star + R_{\rm p}$ (Sackett 1999), and in cases where the small planet approximation applies ($R_\star >> R_{\rm p}$) and the eccentricity is small, the geometric transit probability reduces to the familiar $P_{\rm tr} = R_\star/a$ (Borucki & Summers 1984).

In Figure 1.5 we can see an illustration of the orbital inclination condition for the transit probability formula: should $a\ \cos i > R_\star + R_{\rm p}$, there is no transit as the planetary disc would pass above the stellar disc, hence not producing a planetary transit along our line of sight.

When is it useful to calculate the transit probability of a planet? If the planet has been discovered with another method (in most cases, by radial velocity), then we may be curious to know if this planet also transits. Stevens & Gaudi (2013) demonstrate that in these cases the *a posteriori* transit probability is often different from the *a priori* probability (found using Equation 1.12) due to the dependence of a on the planetary mass. In particular, they showed that for Super-Earth and Neptune mass planets, the posterior transit probability can be higher than expected, making them more optimistic candidates for transit follow-up after discovery via RV.

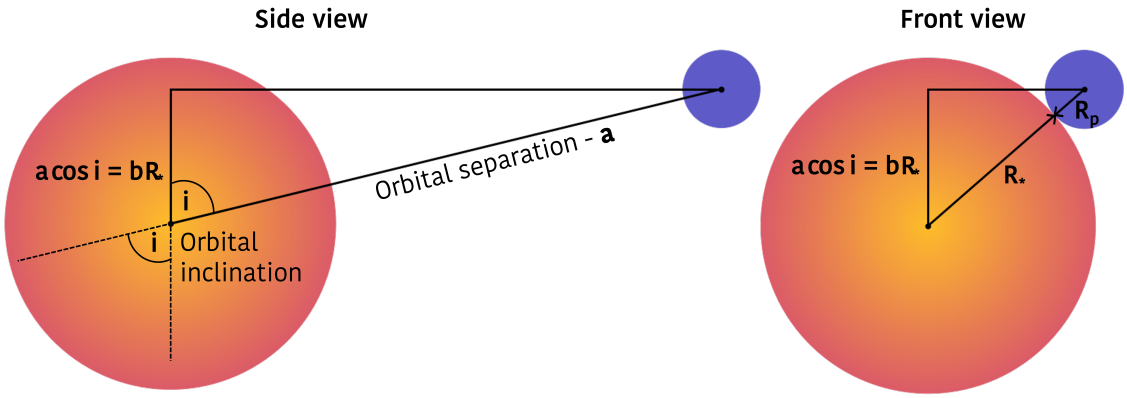


Figure 1.5: Side and front view of planetary transit geometry, showing that as orbital inclination i decreases from $90°$, the planet transits further up the stellar disc. We also see that if $a\ \cos i\ > R_\star + R_\mathrm{p}$, the planet will not transit along our line of sight.

The first planet detected in transit was HD 209458 b (Charbonneau et al. 2000), a planet which had already been previously detected by RV (Mazeh et al. 2000). The first planet to be discovered using the transit method was also only the second planet to be detected in transit: OGLE-TR-56 b (Konacki et al. 2003). Compared with RVs, transits got off to a slow start, but this discovery method has more than compensated and now accounts for >75% of known planets[c].

In Figure 1.6 we can see how discoveries by the transit method have evolved since that first discovery 30 years ago by looking at the widening of the parameter space. Overall, the transit method can now detect smaller planets, planets around smaller stars, and planets with far wider orbital separations, resulting in the detection of planets with lower transit probabilities. The biggest step forward in the field came with the launch of *Kepler* (Borucki et al. 2010) (see Section 1.3.1), but improved instrumentation overall has also been key in enabling these detections, and the next generation of ground- and space-based telescopes is set to widen the transit parameter space even further.

1.2.3 Radial velocities for planet detection

This thesis does not contain any discoveries made with radial velocities; however, the field of transit detections owes its existence in part to the early RV detections. When Borucki & Summers (1984) first examined possible transit probabilities, the numbers were very pessimistic: working on the assumption that giant planets would all have long periods (i.e. they would be true Jupiter analogs), the expectation was that one year of monitoring $\sim 10\,000$ stars would produce one planet detection. The discovery of 51 Peg b (Mayor & Queloz 1995) revealed the unexpected existence of giant planets on very short orbits, which suddenly made transit photometry appear more plausible (Borucki et al. 1997).

When a planet orbits a star it causes a reflex motion in its host, resulting in both objects orbiting a common barycentre. Provided the orbital plane is not at $90°$ to our line of sight, this will cause variations in the line-of-sight velocity, i.e. the radial velocity (RV), of the host star (Wright 2018). These

[c] According to the records of the NASA Exoplanet Archive: https://exoplanetarchive.ipac.caltech.edu.

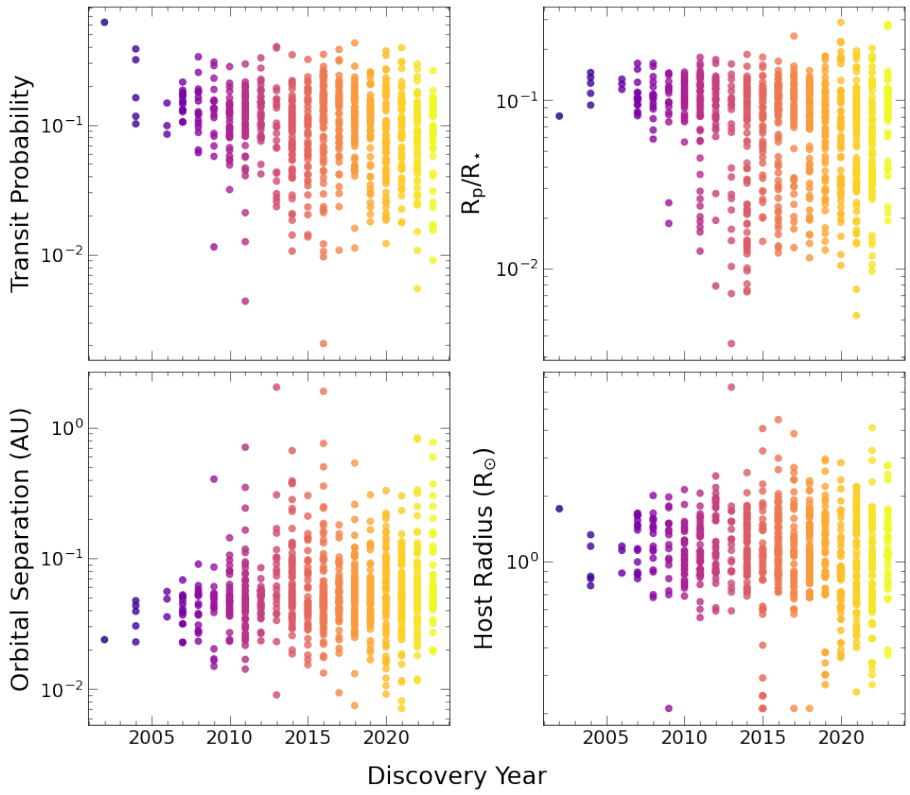


Figure 1.6: How has detection by transit photometry evolved? The four panels above demonstrate the widening of the parameter space explored by the transit method year-on-year since the first detection in 2000. All planets shown here were discovered using the transit method; from left the panels show discoveries per year by transit probability, planet-to-star radius ratio, orbital separation, and host radius. One planet has been omitted from the sample (WD 1856+534 b, Vanderburg et al. 2020) as it orbits a white dwarf and significantly skews the plots. Point are coloured by their discovery year.

variations can be detected by the technique of Doppler spectroscopy: measuring periodic redshifts and blueshifts of stellar spectral lines (Mayor et al. 2014).

RV measurements produced the first confirmed exoplanet detection around a Solar-type star with the discovery of 51 Peg b (Mayor & Queloz 1995), but the technique in fact predates the existence of the field of Exoplanets by over a century; Vogel (1890) first used RV variations to show that the star Algol has an unseen solar-mass companion. It is only with vastly improved instrument stability leading to exceptional precisions, that we can now also detect planet mass companions (e.g. Queloz et al. 2001; Pepe et al. 2010a, 2014).

Unlike transit detections, radial velocity discoveries require repeated observations covering the entire orbital phase of a planet, with a cadence appropriate to the system (Perryman 2018). Once this has been achieved, there are three orbital parameters directly observable from the radial velocity technique: the RV semi-amplitude K, the orbital period P, and the orbital eccentricity e.

The magnitude of the radial velocity variations depends on the system parameters. Wright (2018) presents this relationship as:

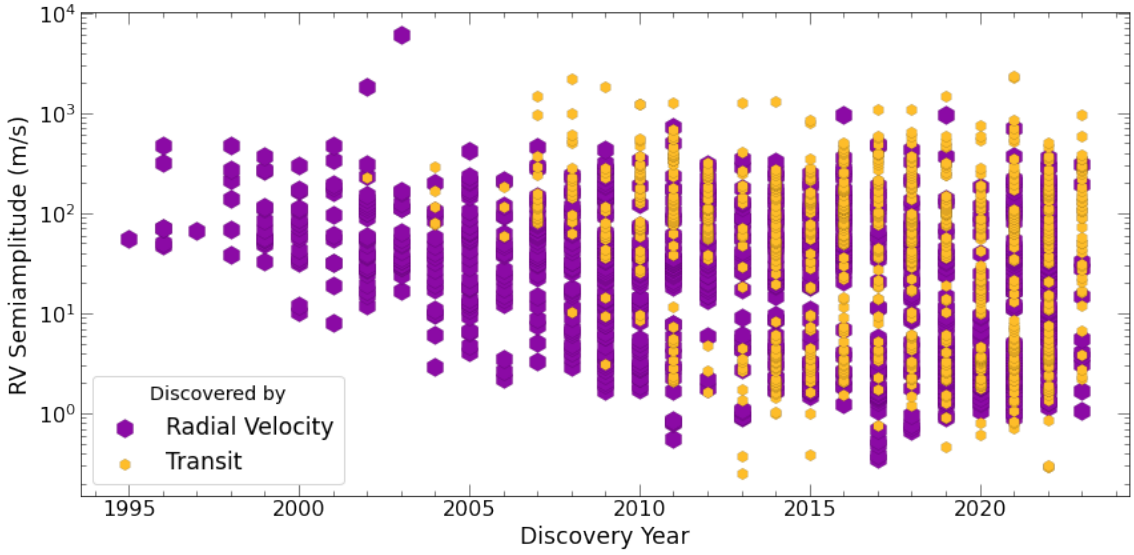


Figure 1.7: The trend in detected radial velocity semi-amplitudes over time, highlighting both planets discovered by RV, and those first detected in transit but later followed-up on by RV. Note: for planets discovered by the transit method, the year is their year of discovery, not the year they were first detected in the radial velocity data. This fact skews the plot slightly, as the smallest detected RV semi-amplitude of $< 0.25\mathrm{ms}^{-1}$ was for Kepler-37 b, a planet discovered in 2013 (Barclay et al. 2013); however its current mass was published this year (Bonomo et al. 2023)

$$K \approx \left(\frac{2\pi G}{P {M_\star}^2}\right)^{\frac{1}{3}} \frac{M_\mathrm{p} \sin i}{\sqrt{1-e^2}}, \tag{1.13}$$

where K is the semi-amplitude of the changes in radial velocity over the course of one orbital period P, G is the gravitational constant, $M_\star$ is the mass of the parent star, M_p is the mass of the planet, i is the orbital inclination, and e is once again the orbital eccentricity. The quantity $M_\mathrm{p} \sin i$ is often referred to as the 'minimum mass', as the true mass will be larger by a factor $1/\sin i$. As the orbital inclination cannot be derived from radial velocity observations alone, only the minimum mass of a planet can be extracted from RV measurements.

RV measurements are most sensitive to the planet's minimum mass, but it is also clear from Equation 1.13 that there is a dependence on the host star's mass $M_\star$. This makes low-mass stars (described in Section 1.2.4) excellent candidates for RV planet searches, as planets will produce a larger radial velocity variation in them than their Solar-mass counterparts. The dependence on orbital period is weak, indicating that the key limitation for detecting long-period planets is not the amplitude of the RV variation, but the long baseline of observations required to cover a full orbit (Wright 2018).

In Figure 1.7 we can see how the field of RV discovery and follow-up has evolved since the first detection in 1995. Between 1995 and 2013 there was a clear trend demonstrating the improving precision of instruments, as progressively smaller RV semi-amplitudes were detected year on year. This trend has since plateaued due to the challenge of disentangling small RV signals from stellar activity (e.g. Mortier & Collier Cameron 2017). However, the new generation of ultra-stable spectrographs

(e.g. ESPRESSO, Pepe et al. 2010b), along with improved modelling of stellar activity (e.g. Faria et al. 2022), may soon lead to precisions down to $< 10\ \mathrm{cm\ s^{-1}}$.

1.2.4 The importance of stellar characterisation

In the previous sections, one proviso that has arisen repeatedly is the need for some knowledge of the parameters of the host star in the system. In Section 1.2.2.1, I described how an estimate can be gained from the stellar density combined with empirical mass-radius relations; in practice, however, the norm is to extract stellar parameters from external information.

Throughout the chapters of this thesis, I have called upon the expertise of my colleagues to learn fundamental parameters of the stars that host the planets I have investigated. These parameters include the stellar mass and radius ($M_\star$ and $R_\star$ respectively), metallicity [Fe/H], surface gravity $\log\ g$, effective temperature $T_{\rm eff}$, and even an estimate of the stellar age where possible. In fact, for each discovery in Chapters 3 and 4, stellar parameters were provided for me via multiple methods, including spectral energy distribution and reconnaissance spectroscopy. A description of these methods is far beyond the scope of this work, but suffice it to say that stellar characterisation is a crucial part of the field of exoplanets. As we have seen above, the precision with which we know our planetary parameters depends entirely on how well we know the central star.

As well as discerning fundamental parameters of the host star (such as radius $R_\star$, mass $M_\star$, and effective temperature $T_{\rm eff}$), stellar characterisation can reveal the spectral type of the host in question. In this thesis, there are three flavours of host star investigated, each of which I will describe in brief.

1.2.4.1 Solar-like stars

The Sun is a main sequence star with an effective temperature $\sim\ 5700\ \mathrm{K}$ and spectral type G2V. Definitions of the boundaries of what makes a star 'Solar-like' abound, but in the context of exoplanet hosts, I will adopt the definition from Bryson et al. (2021): main sequence stars with effective temperatures between $4800 - 6300\ \mathrm{K}$ will be described as 'Solar-like'. This definition then includes main sequence dwarfs with spectral types including F, G and K; these stars typically have masses in the range $0.45 - 1.4\ \mathrm{M_\odot}$ and radii in the range $0.7 - 1.4\ \mathrm{R_\odot}$ (Habets & Heintze 1981). As the full effective temperature range of FGK stars typically spans $3700 - 7500\mathrm{K}$, not all stars of these spectral types would be classed as 'Solar-like'.

In Figure 1.8 we can see a Hertzsprung-Russell Diagram (H-R Diagram) showing the main spectral types, with the location of the Sun highlighted for clarity.

1.2.4.2 M dwarfs

Stars of spectral type M, often referred to as M dwarfs or low-mass stars, are the most abundant stars in the galaxy, representing in excess of 75% of the galactic population (Winters et al. 2015). They are significantly less massive than the sun, with masses in the range $0.1 - 0.6\ \mathrm{M_\odot}$, and they represent the

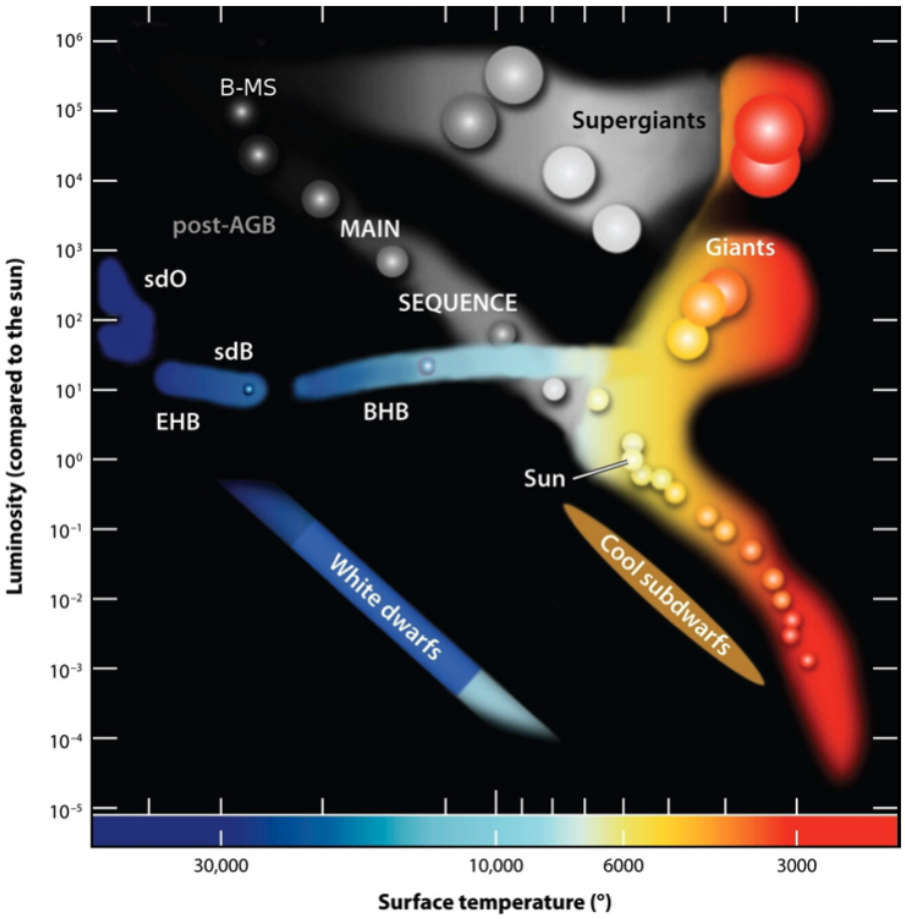


Figure 1.8: Hertzsprung-Russell diagram showing the main groupings of stars. M dwarfs are the redder stars on the main sequence, and Hot Subdwarfs are on the extreme horizontal branch to the left of the main sequence. the position of the Sun is also shown. From Heber (2009).

coolest and faintest stars on the main sequence (Mann et al. 2015). The reduced masses of M dwarfs cause their rate of fusion to be lower than other main sequence spectral types, leading to exceptionally long lifetimes (Laughlin et al. 1997).

M dwarfs are found in the bottom right of the H-R diagram in Figure 1.8 at the coolest and faintest end of the main sequence.

1.2.4.3 Brown Dwarfs

The H-R diagram in Figure 1.8 does not extend quite far enough to include Brown Dwarfs, but if it did, they would be in the bottom right hand corner: cooler and fainter than M dwarfs. Brown dwarfs lack the mass to sustain nuclear fusion of Hydrogen, and hence never make it onto the main sequence (Kumar 1963), although some of the more massive objects can fuse deuterium in their cores (Kirkpatrick 2005). Their masses typically range from $10 - 80\ \mathrm{M_J}$ (Chabrier et al. 2000), creating a somewhat blurred boundary between Brown Dwarfs and giant planets (Showman et al. 2020).

1.3 Blind transit surveys

The expected transit detection rates presented in Borucki & Summers (1984) were unduly conservative owing to an incomplete picture of planetary diversity. However, one key idea that also stemmed from that work was that the most efficient way of detecting planets using the transit method would involve observing a large number of stars for a long time.

As described above, RV discoveries paved the way for transit detections by showing the unlikely existence of short-period giant planets (so-called Hot Jupiters) (Mayor & Queloz 1995; Butler et al. 1997; Cochran et al. 1997; Fischer et al. 1999). The first transit searches were then carried out from the ground using small telescopes: the very first detected transit, that of HD 209458 b, was in fact observed with a $10\ \mathrm{cm}$ telescope (Charbonneau et al. 2000).

These early successes encouraged the setup of dedicated ground-based transit surveys, as described in Horne (2003). A key motivator in these transit searches was the ability to extract additional planetary parameters from transit observations, such as the radius R_p and orbital inclination i (Winn 2010; Deeg & Alonso 2018) as described in Section 1.2.2.1.

In this section, I will describe the key players in the field of transit surveys from space and from the ground. For each, I will highlight the most historically important surveys and their contributions, followed by a description of the current surveys that are most relevant to this work.

1.3.1 From Space

Borucki & Summers (1984) described how planets beyond the Solar System could be detected using transit photometry; in that work they also raised that in order to detect small terrestrial planets, a 'space-based platform' would be required. The benefits of observing from space include avoiding perturbations caused by Earth's atmosphere and removing interruptions caused by the day/night cycle (Stapelfeldt et al. 2021).

The first space telescope to carry out a blind transit survey was in fact not designed for this purpose. *CoRoT* (Convection, Rotation and planetary Transits) was originally conceived as a mission to observe the oscillations of Solar-type stars (Baglin et al. 1993), but several delays to the mission meant that, following the discovery of the first exoplanet, the mission objectives could be extended to include the first space based transit survey (Baglin 2003).

CoRoT was launched close to the end of 2006, and within three months it had discovered its first exoplanet (Barge et al. 2008). In its lifetime CoRoT discovered 34 exoplanets (Stapelfeldt et al. 2021), including the first Super-Earth, CoRoT-7 b (Léger et al. 2009; Charbonneau et al. 2009). And crucially, it launched the era of big space based exoplanet surveys.

1.3.1.1 Kepler

Kepler was first proposed in 1992 under the name FRESIP (FRequency of Earth-Size Inner Planets) (Borucki et al. 2009), and as the name suggests, its primary mission objective was to reveal how

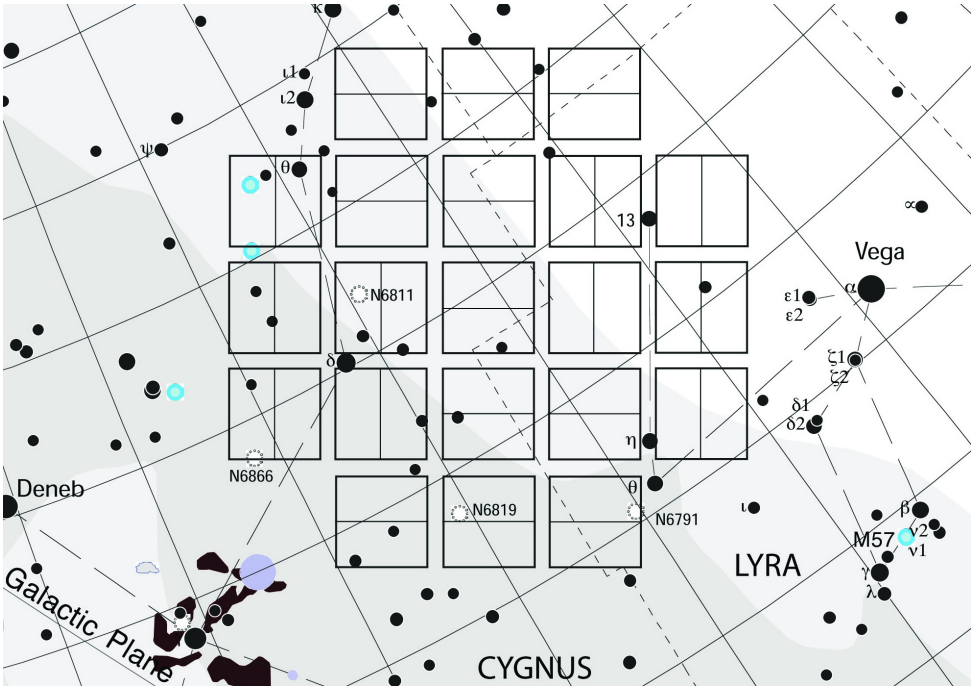


Figure 1.9: *Kepler*'s field of view in the Cygnus-Lyra region of the sky, just above the galactic plane. Image credit: NASA/Ames/JPL-Caltech (downloaded from Wikipedia.org).

common Earth-like planets are in our solar neighbourhood (Borucki et al. 2003, 2010). The initial proposal was rejected on the basis that the stated goals weren't demonstrably feasible yet. It took ten years and five proposals for the *Kepler* mission to eventually be accepted in 2001 (Borucki et al. 2009).

The telescope was based on a classic Schmidt design with a $95\mathrm{cm}$ correcting aperture, a $1.4\mathrm{m\,f/1}$ primary mirror, and 42 back-illuminated science CCDs with 1024×2200 pixels each. *Kepler*'s field of view was $115°$ squared with a pixel scale of 3.98"px^{-1} (Borucki et al. 2008, 2010). In order to achieve its goal of detecting Earth-like planets around Sun-like stars, *Kepler's* photometers were designed to achieve 20ppm (parts per million) precision on a 6.5 hr transit[d] of an Earth-sized planet orbiting a G-type star similar to the Sun (Borucki et al. 2010). In order to detect at least three transits of such a planet, a long baseline mission duration of three years was required. Because of this, a fixed field of view of was chosen in the Cygnus-Lyra region of the sky as it contains at least 100 000 dwarf stars (Borucki et al. 2008). In Figure 1.9 we can see the *Kepler* field of view, with the CCD array overlaid on the sky region of observation.

Kepler was launched in March 2009 on an Earth-trailing orbit, and in its first six weeks of observations it discovered five new exoplanets (Borucki et al. 2010; Koch et al. 2010). At the end of the 3-year mission, it became clear that the 20 ppm precision had not been achieved and other Solar-like stars showed more variability than observations of the Sun had implied was the norm (Borucki 2016).

[d] An Earth-like planet on a 1AU orbit around a Sun-like star would actually produce a ~ 13 hr transit if it transits the centre of the star with impact parameter $\mathrm{b} = 0$. However, this configuration is the least likely and therefore the design was based on a transit with a higher, non-zero impact parameter (Borucki et al. 2003).

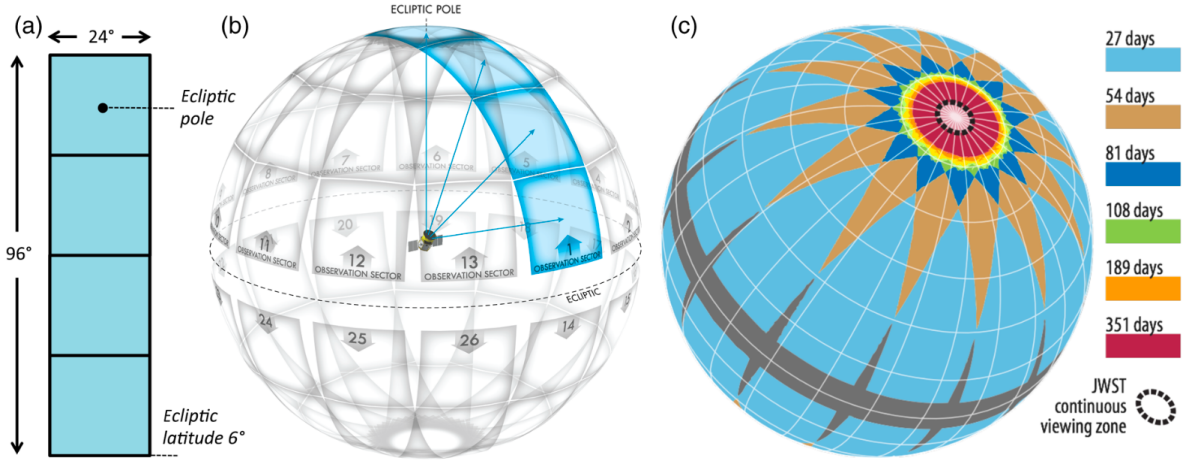


Figure 1.10: Panel (a): Field of view of all four *TESS* cameras combined. **Panel (b):** *TESS*'s 26 observing sectors, with the overlap of the northern sectors at the ecliptic poles visible. **Panel (c):** Observation timescales accounting for overlaps between sectors on the celestial sphere. The area in red is *TESS*'s continuous viewing zone (CVZ); *JWST*'s CVZ is also shown within it. Figure from Ricker et al. (2015), and caption adapted from the original.

These shortcomings meant that three transits were not sufficient to detect an Earth-analog at $8-\sigma$, so the mission was given funding for a two-year extension. Unfortunately, before the extension could complete, two of the reaction wheels failed in 2013 leaving *Kepler* unable to point at its field. Following a search for alternative uses for the instrument, the *K2* mission was selected, with *Kepler* observing various fields along the ecliptic (Howell et al. 2014).

Kepler and *K2* combined discovered 3255 confirmed planets, and there are another 3030 candidates from the two missions still awaiting confirmation[e]. These numbers demonstrate that over 60% of known exoplanets were discovered by a single instrument – the impact of the *Kepler* mission cannot be overstated. In Section 1.4 I discuss some of the key lessons the field has learned from statistics on the large exoplanet populations; the majority of these results stem from statistical studies of the *Kepler* sample.

1.3.1.2 *TESS*

One of the key shortcomings of the *Kepler* mission was that the majority of planets discovered are hosted by stars too faint for precise mass determination with radial velocities. For this reason, NASA's current transit mission *TESS* (Transiting Exoplanet Survey Satellite) has as one of its prime mission objectives to discover small planets around stars bright enough for spectroscopic follow-up (Ricker et al. 2015).

TESS was first proposed in 2006, and went through several iterations before it was eventually adopted by NASA in 2011 (Ricker et al. 2015). In order to achieve the goal of detecting planets around brighter stars, *TESS* adopted a 'wide and shallow' approach over the 'narrow and deep' strategies of

[e]Retrieved from https://exoplanetarchive.ipac.caltech.edu/docs/counts_detail.html on the 5th of May, 2023

CoRoT and *Kepler*; that is to say that *TESS* was designed as an all-sky survey rather than having a small fixed field of view (Ricker et al. 2009). In Figure 1.10 we can see how this observing strategy worked in practice: the whole sky was divided into 26 sectors with *TESS* observing each for 27 days at a time before moving on. Centred around the ecliptic poles there are regions where 13 sectors overlap, called the continuous viewing zones. These allow for the detection of longer period planets and especially the probing of habitable zones, where water could exist in a liquid state on a planet's surface (Kopparapu et al. 2014).

The mission was launched in 2018 in a high-Earth elliptical orbit (Barclay et al. 2018) equipped with four cameras, each with a custom $f/1.4$ lens and a $2\mathrm{k} \times 2\mathrm{k}$ CCD (Ricker et al. 2015). The combined field of view of the four-camera array is $24^\circ \times 96^\circ$ (as shown in Figure 1.10) producing a pixel scale of $21'' \ \mathrm{px}^{-1}$. The prime mission duration for *TESS* was set to two years, with the first year spent observing the southern ecliptic hemisphere and the northern skies being observed during year two.

Early estimates of the planet detection rate for *TESS* by Sullivan et al. (2015) used a simulated sample of the $200\,000$ stars the mission was expecting to observe with its short $(2 \ \mathrm{min})$ cadence mode; they estimated that during the prime mission, *TESS* would discover approximately 1700 planets. Following the publication of the TESS Input Catalogue Candidate Target List (Stassun et al. 2018), a revised exoplanet yield was published by Barclay et al. (2018) predicting that *TESS* would discover 1250 ± 70 planets orbiting stars observed in short cadence during the prime mission.

TESS's first planet was discovered soon after launch: a Super-Earth orbiting π Mensae, a star already known to host a long-period giant planet (Huang et al. 2018). Five years after launch, *TESS* is back observing the southern skies as part of its third extended mission. The total number of confirmed planets discovered by the mission stands at 333[f], significantly lower than the estimates from Sullivan et al. (2015) and Barclay et al. (2018). However, there are currently 4359 candidate planets from *TESS* that are the subject of active follow-up[g], so it is possible that the expected number of planets *have* been detected, but are as yet unconfirmed.

1.3.2 From the ground

When Horne (2003) published his list of ground-based transit surveys, it contained 26 active or planned experiments searching for planets beyond the Solar System. The apertures ranged in size from $3.6\mathrm{cm}$ to $3.6\mathrm{m}$, and using fields of view, expected precisions, and the geometric transit probability, he estimated these projects would produce 191 transit detections per month between them. Despite the optimism, only 27 new transiting planets had been discovered from the ground by the end of 2007 (Deeg & Alonso 2018).

Among the early adopters, however, were two of the most productive ground-based surveys of the past two decades: SuperWASP (Pollacco et al. 2006) and HATNet (Bakos et al. 2004). In the

[f] Correct on 26 May 2023 according to https://exoplanetarchive.ipac.caltech.edu/docs/counts_detail.html.
[g] Correct on 26 May 2023 according to https://exoplanetarchive.ipac.caltech.edu/docs/counts_detail.html.

following subsections I will briefly describe these two pioneering surveys, followed by the two ground-based projects that have contributed the most data to this thesis: SPECULOOS and ASTEP.

1.3.2.1 SuperWASP

WASP (Wide Angle Search for Planets) is a UK-based project dedicated to the search for transiting exoplanets (Pollacco et al. 2006). The consortium's pilot project was the WASP0 camera, which was constructed from commercially available parts in order to decrease development time and be on-sky as soon as possible. The prototype was a resounding success (Kane et al. 2004, 2005b,a) and led to the development of the multi-detector SuperWASP cameras, to be installed in the northern and southern hemispheres at Observatorio del Roque de Los Muchachos on La Palma (SuperWASP-N) and Sutherland Station of the South African Astronomical Observatory (SuperWASP-S) respectively.

Each SuperWASP observatory consists of eight wide-field cameras mounted on robotic equatorial fork mounts (Pollacco et al. 2006). The cameras are manufactured by Andor and consist of back-illuminated 2048×2048 pixel CCDs, thermoelectrically cooled to $-50°C$. The principle apertures used by the telescopes are Canon 200mm f/1.8 telephoto lenses. This setup results in a field of view of $7.8° \times 7.8°$ and a pixel scale of 13.7”px^{-1} (Butters et al. 2010; Wilson et al. 2008).

In order to observe as many stars as possible WASP surveyed fields with large numbers of stars but avoided the Galactic plane where possible due to crowding (Christian et al. 2006). Several fields are surveyed per night by taking 30s exposures of each, slewing to the next, and then returning to the first to restart the sequence (Clarkson et al. 2007).

SuperWASP-North achieved first light in November 2003 (Pollacco et al. 2006) and published its first two discoveries, WASP-1 b and WASP-2 b three years later (Collier Cameron et al. 2007). SuperWASP-South on the other hand, saw its first light in April 2004 and had to wait almost four years for its first discovery (WASP-4 b Wilson et al. 2008). To date, the SuperWASP project has discovered 160 planets and another 27 planets have been discovered within some of those systems[h].

Among these discoveries are some of the most formidable planets known thus far. WASP-33 b is one of the hottest exoplanets known, with an equilibrium temperature of 2780K owing to its $1.2\,\text{day}$ orbit around its A5-type host (Collier Cameron et al. 2010; Chakrabarty & Sengupta 2019). WASP-12 b is not far behind in the temperature stakes but it is inflated to an even larger size, boasting a radius $> 1.9\times$ that of Jupiter and an even shorter orbital period of just over one day (Hebb et al. 2009; Chakrabarty & Sengupta 2019).

Due to their initial transit detections and radial velocity confirmations, the planets discovered by the SuperWASP project have become some of the best studied planets in the field.

1.3.2.2 HATNet

HATNet is the Hungarian-made Automated Telescope Network (Bakos et al. 2004), a multi-facility observatory network aimed at detecting exoplanets with the transit method. The first instrument was

[h] Figures retrieved from https://exoplanetarchive.ipac.caltech.edu/ on 2023 April 27.



Figure 1.11: ASTEP+ in its new dome at Concordia Station on the Antarctic Plateau. In the background on the right hand side, the telescope's previous dome can be seen.

completed in mid-2000 and consisted of a Meade Pictor 768×512 CCD camera with a Nikon 180mm $f/2.8$ lens on a horseshoe mount. This prototype (named HAT-1) was installed first in an observatory in Budapest, Hungary, but was later moved to Kitt Peak Observatory to be operated remotely. It remained operational at this site for almost two years.

As the experiment progressed, the network grew. HATNet now boasts two sub-networks: HAT-North, consisting of six automated telescopes at two sites with 0.11m aperture $f/1.8$ lenses, and $4\text{k} \times 4\text{k}$ CCDs providing a pixel scale of 9"px^{-1} (Perryman 2018); and HAT-South, which also includes six units across three sites. Each of the instruments of HAT-South holds four 0.18m $f/2.8$ telescope tubes on a common mount, with $4\text{k} \times 4\text{k}$ CCDs, resulting in a pixel scale of 3.7"px^{-1} (Bakos 2018).

HATNet announced its first discovery in 2007 (Bakos et al. 2007); HAT-P-1 b is a Hot Jupiter orbiting one star in a main sequence binary. At the time of publishing, it was the largest and least dense exoplanet known. In its years since, the telescopes of the HATNet have gone on to discover a further 139 planets[i].

1.3.2.3 ASTEP

ASTEP (Antarctic Search for Transiting Exoplanets) is a French-led photometric project hosted at the French-Italian Concordia Station on Dome C in Antarctica (Mékarnia et al. 2016). The project is now on its third incarnation. The first was known as ASTEP-South, and consisted of a $10\ \text{cm}$ refracting telescope that operated for four winters between 2008-2013 (Crouzet et al. 2010b, 2018). This first instrument served to survey the photometric conditions at the site to ensure a larger instrument was

[i] According to the NASA Exoplanet Archive; correct as of 2023 June 13.

appropriate (Crouzet et al. 2010a). The pilot mission demonstrated that photometric conditions could be achieved 74% of the time during the Austral winter, due to a combination of favourable conditions: elevation of 3250m, low wind speeds (Aristidi et al. 2005), a median seeing level of 0.27" above $30\mathrm{m}$ with a very stable atmosphere (Lawrence et al. 2004), and almost uninterrupted phase coverage during the polar night (Fressin et al. 2006).

The larger instrument, known as ASTEP 400, was installed on the site in 2009 and began operations in March 2010 (Daban et al. 2010). ASTEP 400 was a Newtonian design telescope equipped with an FLI-Proline camera with a $4\mathrm{k}\times4\mathrm{K}$ front-illuminated CCD. The field of view was $1^\circ\times1^\circ$ resulting in a pixel scale of $0.93\text{”}\ \mathrm{px}^{-1}$ (Mékarnia et al. 2016). The project was originally conceived as a ground-based successor to the *CoRoT* mission, and conducted a blind transit survey of its own until 2013, revealing several new transiting planet candidates. The instrument was then repatriated to France for analysis of the data, and returned to Concordia Station at the start of the 2016 observing season for long-term monitoring of the δ-Scuti pulsator β-Pictoris (Mékarnia et al. 2017).

At the start of the 2020 observing season, ASTEP 400 transitioned to follow-up operations as part of the *TESS* Follow-up Observing Programme. This has resulted in some unique contributions by observing planetary transits inaccessible to other instruments, as described in Chapter 2. The start of the 2022 observing season saw the launch of the newly upgraded instrument known as ASTEP+ - this consists of a two-colour photometer mounted on the same telescope, enabling simultaneous observations in two colours (Crouzet et al. 2020; Schmider et al. 2022).

1.3.2.4 SPECULOOS

SPECULOOS (Search for habitable Planets EClipsing ULtra-cOOl Stars) is a ground-based transit mission with four telescopes in the south (SPECULOOS Southern Observatory at European Southern Observatory, Paranal in Chile) and one in the north (SPECULOOS Northern Observatory at Teide Observatory in Tenerife, Spain) (Burdanov et al. 2018). SPECULOOS aims to harness the ‘small star opportunity’ by searching for small, potentially habitable planets around nearby low-mass stars. In particular, SPECULOOS is designed to survey a sub-population of low-mass stars known as ‘ultra-cool dwarfs’: stars with effective temperatures $< 2700\ \mathrm{K}$, encompassing spectral types M6 and later, including L, Y and T dwarfs.

The project was piloted with the proof-of-concept mission TRAPPIST (TRAnsiting Planets and PlanetesImals Small Telescope) (Gillon et al. 2011), which surveyed 50 nearby ultra-cool dwarf stars. TRAPPIST began its survey in 2011 with the goal of demonstrating the feasibility of the project; later M dwarfs are known to be active and it was not clear whether this would impede detection of small planets (Burdanov et al. 2018). The pilot mission yielded fruit in 2016 with the discovery of seven small planets orbiting the late M dwarf now known as TRAPPIST-1 (Gillon et al. 2017).

With the project concept now feasible, the telescopes of SSO and SNO were installed, with first light achieved for the first of the telescopes in early 2017; by the end of 2019 all telescopes were operational. All five telescopes are identical 1m-class Ritchey-Chrétein telescopes, equipped with



Figure 1.12: The four telescopes of the SPECULOOS Southern Observatory at ESO Paranal. Photo credit: Mathilde Timmermans

Andor iKon-L cameras. These are thermoelectrically cooled and the $2\mathrm{K} \times 2\mathrm{K}$ deep depletion CCDs are optimised for the near-infrared, where ultra-cool dwarf stars are the brightest. The field of view of each telescope is $12' \times 12'$ which gives a pixel scale of 0.35" px^{-1}.

The target list for SPECULOOS was published in Sebastian et al. (2021) and consists of 1657 ultra-cool dwarf stars. These are divided among three distinct observing programs. Programme 1 aims to find terrestrial-type planets that could be suitable for atmospheric characterisation with *JWST*, while programme 2 seeks to work in synergy with *TESS* by following up on small temperate planet candidates discovered from space. The final programme consists of a survey of all remaining ultra-cool dwarfs within 40 pc.

In addition to the main SPECULOOS survey, approximately 20% of telescope time is available for so-called 'annex' programmes, consisting of any non-survey observations in keeping with the core objectives of the mission (Sebastian et al. 2020). At the time of writing, SPECULOOS has not yet discovered any new planets from the core survey. However, as part of the annex observations the telescopes have had a huge impact by following up on candidate planets identified by space telescopes (e.g. Niraula et al. 2020; Schanche et al. 2022; Delrez et al. 2022), including the discovery of the small habitable-zone planet TOI-715 b, as described in Chapter 3.

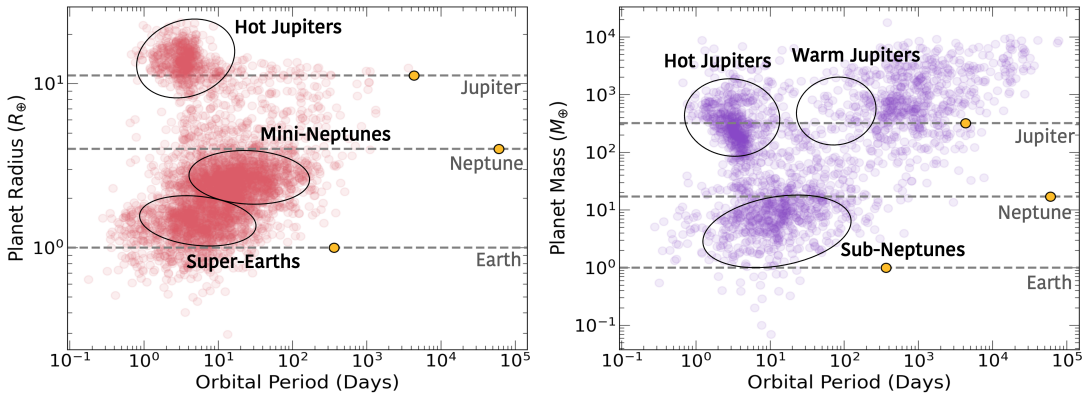


Figure 1.13: Planet radius (left hand panel) and planet mass (right hand panel) as a function of orbital period. Only planets discovered by RV or transit are included in this figure. In the left hand panel, the population of warm Jupiters discovered by RV is missing as these have very low transit probabilities due to their large orbital separations. Likewise, most Super-Earths and Sub-Neptunes are missing from the right hand panel as they transit stars too faint for spectroscopic mass measurements.

1.4 What we [think we] know about exoplanets

In the preceding sections I have discussed at length how we might find a new exoplanet and learn some of its system parameters. These methods have been in place, and constantly evolving, for over 20 years, resulting in a sample size in excess of 5000 exoplanets. In this section, I describe some of the most exciting results from demographics studies of the current population of exoplanets, starting with some nomenclature for the most common planet flavours.

1.4.1 Planet flavours

Mordasini (2018) wrote that what characterises the known sample of exoplanets is 'extreme diversity' - this is evident in Figure 1.1 where we see the wide parameter space already populated by planets. In Section 1.2 I also described how surprising the discovery of 51 Peg b was, as the planetary population in our own Solar System gave no clue that such a gas giant on a short orbit could exist (Mayor & Queloz 1995).

In Figure 1.13 we can see four distinct sub-populations of exoplanets that have emerged from transit and radial velocity surveys: Hot and Warm Jupiters, Mini-Neptunes, and Super-Earths.

1.4.1.1 Giant planets: Hot and Warm Jupiters

Hot Jupiters are defined as gas giant planets with masses ≥ 0.25 M_J and orbital periods ≤ 10 days (Dawson & Johnson 2018). Despite the community's collective shock at their existence, Struve (1952) had suggested that Hot Jupiters might be a possibility given the existence of very short period binaries.

Figure 1.13 appears to indicate that Hot Jupiters are common. However, this is a selection bias due to their high transit probabilities and large RV semi-amplitudes making them easy to discover,

leading to over-representation in the known population (Gaudi et al. 2021). In fact, occurrence rates studies have shown that only $\sim 0.6\%$ of solar-type stars host a Hot Jupiter, and they are even rarer among low mass stars and metal poor stars (Johnson et al. 2010).

Exoplanet formation theory had until 1995 been centered around explaining the present day architecture of the Solar System (Madhusudhan 2021). In the years since, the question of Hot Jupiter formation has not yet converged on a single solution, instead finding that formation may take place in-situ (Batygin et al. 2016) or at wider orbital separations followed by inward migration (Rasio & Ford 1996; Baruteau et al. 2014). In their review of Hot Jupiter formation, Dawson & Johnson (2018) demonstrate how individual observed characteristics of Hot Jupiters are consistent with a range of mechanisms for formation, migration, and eccentricity excitation, but no single mechanism can thus far explain all observations.

Warm Jupiters, unlike their 'hot' counterparts, are defined as having orbital periods $10 - 200$ days (Huang et al. 2016). The first two planets of this flavour were both discovered shortly after 51 Peg b: 55-Cnc b (Butler et al. 1997) and 70 Vir b (Naef et al. 2004)[j], and with periods of ~ 15 days and ~ 116 days respectively, they span the wide parameter space occupied by Warm Jupiters.

The population of Warm Jupiters is evident in the RV panel (right hand side) of Figure 1.13, but not the left; this is purely down to selection effects as their transit probabilities are very low, yet they can be discovered via RV provided there is a long baseline of observation (Gaudi et al. 2021). Transit discoveries are on the rise thanks to missions like *Kepler* and *TESS* (e.g. Grieves et al. 2022; Trifonov et al. 2023), although confirmation still often requires RV follow-up, as their long, and infrequent transits make them a challenge to photometrically validate from the ground. That is, of course, unless one has access to ASTEP, as will be discussed in Chapter 2.

Occurrence rates of Warm Jupiters are not trivial to find in the literature. Dong et al. (2021a) notes that they are inherently rarer than other planet types, yet Figure 3 from Winn (2018) (presented here in Figure 1.14) appears to suggest that on average, their occurrence may be similar to Hot Jupiters. There is a slight downturn between $10 - 100$ days, a region often referred to as the 'period valley' (Wittenmyer et al. 2010), with occurrence increasing again as we move toward longer periods and the 'Cold-Jupiter' regime (e.g. Santerne et al. 2016).

Formation of Warm Jupiters is as much a mystery as that of their hot counterparts (Dong et al. 2021a), and like Hot Jupiters much of the debate surrounding their origins is centered on whether they form in situ (e.g. Boley et al. 2016) or undergo some form of migration (e.g. Baruteau et al. 2014; Petrovich 2015). Another similarity with Hot Jupiters is that no one formation pathway can explain all observed properties of the Warm Jupiter population (Dawson & Johnson 2018).

1.4.1.2 Sub-Neptunes: Mini-Neptunes and Super-Earths

The *Kepler* sample confirmed that planets intermediate in size between Earth and Neptune with orbital periods < 100 days are the most common outcome of planet formation (Bean et al. 2021); this is

[j] 70 Vir b was first detected in 1996 but the original discovery citation has been omitted from this thesis.

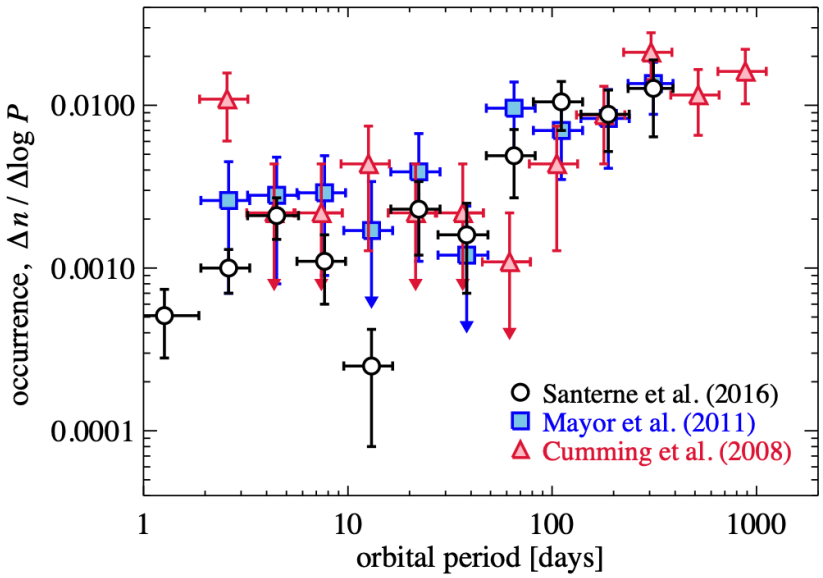


Figure 1.14: Giant planet occurrence vs orbital period. The black circles are values from the *Kepler* sample (Santerne et al. 2016), while the blue squares and red triangles are from RV surveys (Cumming et al. 2008; Mayor et al. 2011). Arrows indicate upper limits. Figure from Winn (2018).

evident in the left hand panel of Figure 1.13 where these so-called Sub-Neptunes are the densest population. The group is, however, less notable in the right hand panel as the majority of these planets were detected by *Kepler* and hence orbit stars too faint for precise mass measurements using radial velocities (Gaudi et al. 2021).

The nature and origin of sub-Neptunes is not yet well understood. An early interpretation of the population following discoveries via radial velocities was that they are terrestrial in nature and were therefore dubbed 'Super-Earths' (e.g. Rivera et al. 2005; Queloz et al. 2009; Howard et al. 2009). However, for planets that weren't yet known to transit only minimum masses were known, and for many of those where transits were detected the calculated densities seemed inconsistent with a rocky composition (Bean et al. 2021).

An alternative interpretation of this population was to call them 'Mini-Neptunes', i.e. more similar in nature to the ice giant planets of our own Solar System and containing a large mass fraction of ices and volatiles (e.g. Barnes et al. 2009; de Mooij et al. 2012). A third suggestion is that sub-Neptunes are in fact so-called 'Hycean Worlds': planets with a large mass fraction ($\sim 10\%$) of water (Léger et al. 2004; Sotin et al. 2007; Madhusudhan et al. 2021).

1.4.2 Patterns arising from statistics

As previously mentioned, the current size of the exoplanet sample, largely helped along by *Kepler*, puts the exoplanet community in an excellent position to look for patterns. In this Section, I will outline some of the key trends that have arisen from statistical studies of this sample.

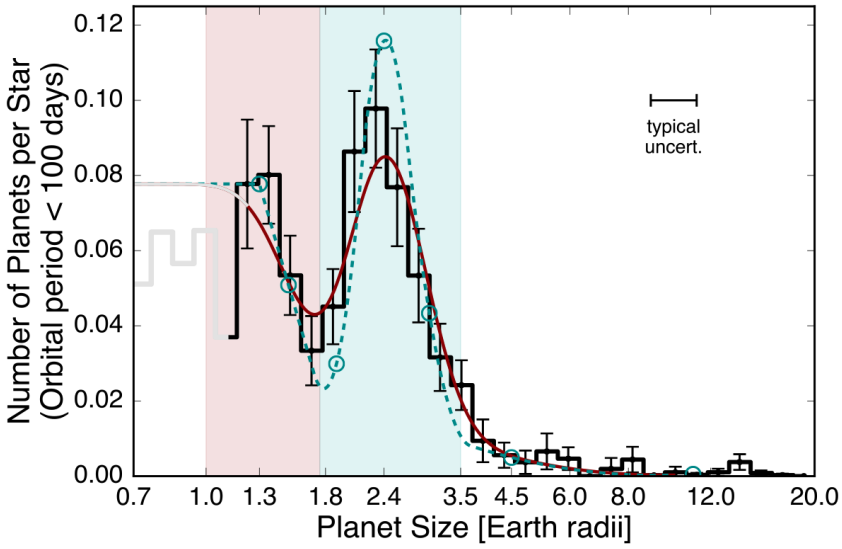


Figure 1.15: Histogram showing planet radii for objects with orbital periods < 100 days; the planet numbers have been corrected for completeness. The light red shaded area represents 'Super-Earths' while the light green area encapsulates 'Mini-Neptunes'. The red solid like is a model fit to the data, while the dashed turquoise line is a possible underlying occurrence. Figure from Fulton et al. (2017), and caption adapted from the original.

1.4.2.1 The Radius Valley

Large statistical studies of the *Kepler* sample shed some early light on the question of the nature of Sub-Neptunes: a radius bimodality emerged showing a clear distinction between Super-Earths and Mini-Neptunes, with a paucity of planets between $1.5 - 2$ $R_\oplus$ (Fulton et al. 2017; Van Eylen et al. 2018) (see Figure 1.15). The interpretation of this bimodality then is that planets below the gap are stripped of their primordial atmospheres, while planets above the gap retain them (Bean et al. 2021). Proposed mechanisms for the atmospheric loss include photo-evaporation (Owen & Wu 2013, 2017), core-powered mass-loss (Lopez & Fortney 2013; Ginzburg et al. 2018; Gupta & Schlichting 2019). Crucially, these explanations for the so-called 'radius valley' would indicate that both flavours of sub-Neptunes, Mini-Neptunes and Super-Earths, are one and the same: born as puffy volatile-rich rocky planets, with some fated to lose their atmospheres to evaporation (Bean et al. 2021). However, gas-poor formation has also emerged as a possible explanation for the observed radius distribution (Lee et al. 2014; Venturini & Helled 2017).

Several studies have investigated the factors that shape the radius valley, with a particular focus on stellar parameters such as mass and age (e.g. Fulton & Petigura 2018; Berger et al. 2020). Of particular relevance to this thesis is the dependence on host mass, as in Chapter 3 I present the discovery of a planet hosted by a low-mass star, whose size places it inside the bounds of the underpopulated parameter space. Fulton & Petigura (2018) found that the centre of the radius valley shifts toward larger radii with increasing stellar mass, but their sample bottomed out at 0.8 $M_\odot$ so we can only infer through extrapolation what the trend is for low-mass stars. This finding was reiterated by Berger et al. (2020) with a stellar sample that extended to 0.5 $M_\odot$. But what about later M dwarfs?

Several studies have attempted to determine the shape and location of the M-dwarf radius valley. Cloutier & Menou (2020) assessed the radius-period trend for planets hosted by stars with $T_{\rm eff} < 4700$ K and found a slope with opposite sign to FGK stars by using a sample of *Kepler* planets corrected for completeness. The second study was carried out by Van Eylen et al. (2021), looking at a selective sample of planets with precisely measured masses and radii; this work found a radius-period slope consistent in sign with FGK stars. Given the inconsistent methods, it remains unclear whether the radius valley exists for planets hosted by low-mass stars.

Another recent work that sought to bring clarity to this ongoing mystery was presented by Luque & Pallé (2022). They demonstrated that M-Dwarf planets instead may have a density bimodality, with some being consistent with rocky compositions and others belonging to a water-dominated population.

With this question still wide open, it is clear that continued efforts to discover and characterise Sub-Neptune-sized planets close to or within the radius valley are crucial to understand the origins of these worlds.

1.4.2.2 Planets around low-mass stars

All but one of the systems presented in this thesis orbit low-mass stars. As described in Section 1.3.2.4, their abundance, planet hosting rates, and small sizes make them ideal for hunting for other worlds. In this Section, I will describe the trends, both predicted and observed, in planetary characteristics around M dwarfs.

While *Kepler* was designed to hunt for Earth analogs around Sun-like stars, it also observed several thousand M dwarfs (e.g. Gaidos et al. 2016), allowing the community to once again observe statistically significant trends. Mulders et al. (2015a) measured occurrence rates as a function of stellar spectral type and planet size, and found that M dwarfs host planets in the size range $1 - 4$ R$_\oplus$ twice and three times as frequently as G and F type stars respectively. In another study of the same year, Mulders et al. (2015b) noted that specifically, M dwarfs host more small Sub-Neptunes ($1-2.8$ R$_\oplus$) than FGK stars, but fewer in the range $2.8 - 4$ R$_\oplus$. The finding is also supported by Morton & Swift (2014) who find that occurrence rates for M dwarfs continue to increase with decreasing radii. Similar results were reported by Sabotta et al. (2021) from an injection-recovery investigation into high precision spectra from low-mass stars; their study found that M dwarfs host at least twice as many small planets ($M_{\rm p} sin\ i < 10$ M$_\oplus$) than their G-type counterparts. The message then is clear: low mass stars are the most likely hosts of small planets, as well as being the hosts where we can most easily find these planets with current instrumentation.

Another valuable result comes from Dressing & Charbonneau (2015), reporting that M dwarfs host on average 2.5 ± 0.2 planets intermediate in size between Earth and Neptune with periods < 200 days per star. A more recent study by Hsu et al. (2020) found even more optimistic results, reporting that low-mass stars could host 4.2 ± 0.6 planets in the range $0.5 - 4$ R$_\oplus$ with periods up to 256 days. These results indicate that multiplicity in M-dwarf hosted planetary systems is the norm, which is a key motivator in the search for additional planets once a first detection is made.

But what of larger planets? How does the radius distribution behave at the giant planet end? An early RV survey of 90 M dwarfs reported no discoveries of giant exoplanets inside $1\mathrm{AU}$ (Endl et al. 2006); from their non-detection they derived an upper limit on the occurrence of close-in Jovian planets of 0.0127 planets per star. An RV survey on HARPS also measured giant planet occurrence for M dwarfs, reporting < 0.01 planets with masses $100\ \mathrm{M}_{\oplus} < \mathrm{M}_{\mathrm{p}} < 1000\ \mathrm{M}\oplus$ with periods < 10 days, and $0.02^{+0.03}_{-0.01}$ planets with periods $10 - 100$ days per star (Bonfils et al. 2013). Sabotta et al. (2021) measured an occurrence of $0.06^{+0.04}_{-0.03}$ planets per star in the same mass range with periods up to 1000 days, but place an upper limit on Hot Jupiter occurrence of 0.03 planets per star.

The most recent study of giant planet occurrence around M dwarfs comes from Bryant et al. (2023) using *TESS* photometry; they find for their full host mass range of $0.088 - 0.71\ \mathrm{M}_{\odot}$, a giant planet occurrence rate of 0.00194 ± 0.00072 planets per star with periods < 10 days. While this is significantly lower than other studies, this sample extends to significantly later spectral types than previous works that also used lightcurve data to measure giant planet occurrence (e.g. Gan et al. 2023, used hosts with masses $0.45 - 0.65\ \mathrm{M}_{\odot}$ and found 0.0027 ± 0.0009 planets per star).

The theory agrees with these lower frequencies of Hot Jupiters around low-mass stars – to an extent. The leading theory for planet formation, namely core accretion (for a review, D'Angelo & Lissauer 2018; Dawson & Johnson 2018), predicts that the formation of giant planets should get increasingly harder with decreasing stellar mass (Laughlin et al. 2004; Burn et al. 2021); this is due to the expected lower masses of protoplanetary discs (Pascucci et al. 2016; Kurtovic et al. 2021). However, the recent planetary population synthesis of Burn et al. (2021) cannot produce Hot Jupiters around hosts with masses $< 0.4\ \mathrm{M}_{\odot}$ at all; and yet, they exist.

To date only a handful of short period (< 10 days) giant planets have been discovered orbiting late M dwarfs, but enough to confirm that the occurrence is non-zero (e.g. Hobson et al. 2023; Kagetani et al. 2023). This could indicate that our understanding of core accretion is incomplete or that another pathway is responsible for giant planet formation around low-mass stars. Gravitational instability has been suggested as an alternative formation mechanism, although it's thought that this method would lead to significantly higher mass planets than those that have been detected so far (Schlecker et al. 2022).

Close-in giant planets around low-mass stars are a conundrum; this is explored further in Chapter 4, where I describe the **MANGOs** program that I've been leading to address the open mystery of the origins of **M**-dwarfs **A**ccompanied by close-i**N** **G**iant **O**rbiter**s**.

1.4.2.3 Planetary peas in a space pod

Another curious result to emerge from the *Kepler* sample was the apparent uniformity in size and period distribution of planets within multi-planetary systems (Weiss et al. 2018). This intra-system uniformity also applies to the planet mass, as deduced by Millholland et al. (2017); Goyal & Wang (2022); Otegi et al. (2022) using systems with TTV measured masses, RV measured masses, and a combination of both respectively.

There has been some debate surrounding whether the effect is astrophysical in origin or the result of detection biases caused by the signal-to-noise ratio limiting detections within a system (Zhu 2020). However, it appears that the result is too statistically significant to result from detection biases alone (Weiss & Petigura 2020). Another potential challenge to this result is the effect of undetected planets within a system, either because of small transit depths or large impact parameters (Zhu & Dong 2021). The uniformity of the period distribution evident in the original by Weiss et al. (2018) suggests that where there are large gaps between planets, there may be as yet undiscovered siblings lurking.

1.5 What's left to find out?

The field of exoplanets is riddled with big open questions yet to be answered, and the hope is that some of them will be addressed by in-depth characterisation with instruments such as *JWST* or the upcoming ELTs (Extremely Large Telescopes). For example, we are yet to discover a true Earth-analog: a terrestrial planet orbiting a Sun-like star, nor have we found evidence of life on any of the planets discovered thus far in the so-called 'habitable zones' of their host stars. The scene is set for a fascinating few decades of expansion for the field of exoplanets, but we are not there yet.

Throughout the last 30-odd pages, I have explored some gaping gaps in our understanding. How do close-in giant planets form around low-mass stars? Perhaps our understanding of core-accretion is incomplete, or perhaps another mechanism entirely leads to Hot Jupiter formation around M dwarfs. At present, the sample of such planets remains small, as I will describe in more detail in Chapter 4. But by systematically searching for planets in this parameter space and building up a statistically significant sample, we can begin to probe their formation histories and shed light on their origins.

Similarly, I opened up the question of the nature of Sub-Neptunes: are they all slightly different versions of the same planet flavour? Or are they distinct populations with unique formation histories? In the same vein, does the so-called radius valley extend to M dwarfs? Or is there instead a density gap, as proposed by Luque & Pallé (2022)? The planet discoveries presented in Chapter 3 add new stand-out members to the population of known planets, which will help us understand their true natures.

In Exoplanetology, like in the whole of Astronomy, there is plenty left to find out. Find out a tiny bit more, in the pages of this thesis.

2

Methods Used in This Thesis

A large portion of the science chapters in this thesis is presented in the form of journal papers, either peer-reviewed and published, or in preparation. As such, the level of detail for some of the methods used is minimal as these methods are common in the field. Throughout this chapter, I will give detailed descriptions of the methods implemented in this body of work, making references to where they are used. Where possible and conducive to pleasant reading, the steps are described in roughly the chronological order in which they might be used for the process of planetary discovery.

2.1 Searching for planet candidates

As described in Chapter 1, all discoveries in this thesis made use of transit photometry. As such, the process begins with a lightcurve.

The `Lightkurve` package (Lightkurve Collaboration et al. 2018) is an open-source `Python` package for accessing and manipulating lightcurve data from *Kepler* and *TESS*. Following the download of each sector of *TESS* data from the telescope, the data are processed by the Science Processing Operations Centre (SPOC) pipeline (Jenkins et al. 2016). Lightcurves can then be downloaded from the NASA Mikulski Archive for Space Telescopes (MAST) via `Lightkurve`.

As part of the data processing by SPOC, all lightcurves are searched for transit-like events; results of these searches are made available in reports of threshold crossing events (TCEs). By this process, the community is alerted to potential candidates. All *TESS* TCEs are then subjected to strict vetting tests (Twicken et al. 2018) and those that pass are given *TESS* Object of Interest (TOI) status. These are the most credible candidates for follow-up. The processes by which SPOC searches for transiting planet candidates is well documented and beyond the scope of this thesis to describe. However, at times planets have been missed by the *TESS* pipeline, so there is a need for exoplaneteers to also conduct our own searches on lightcurves where we suspect this may have been the case.

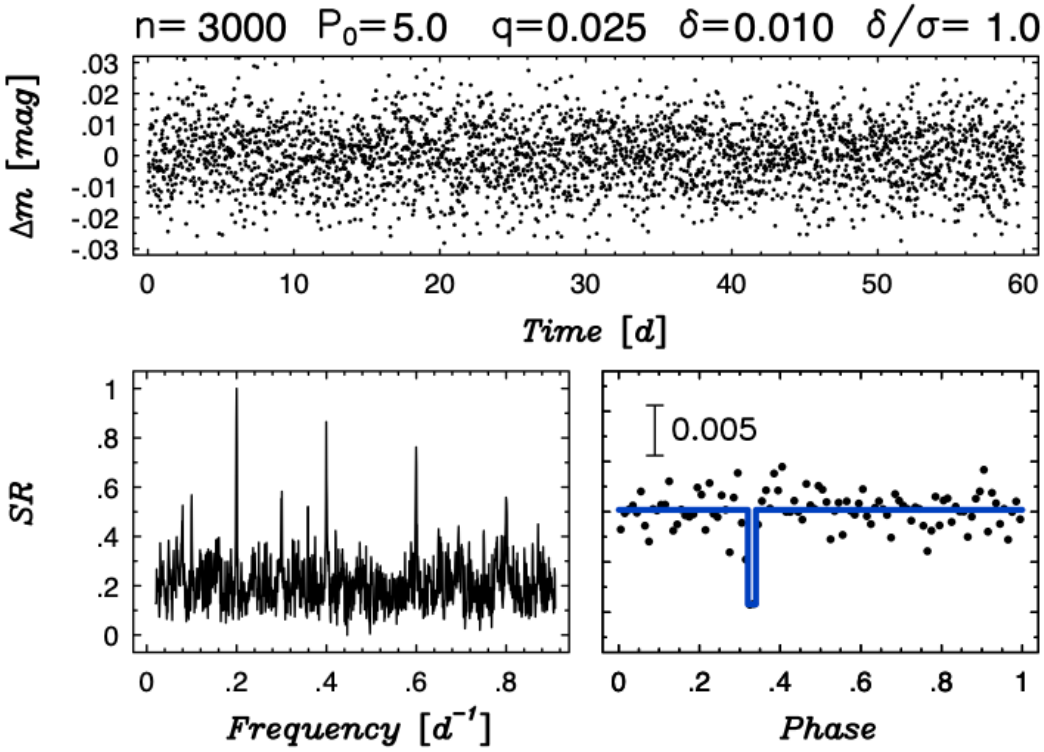


Figure 2.1: Sample output from a BLS search. The upper panel shows a noisy time-series, and the bottom left panel shows the periodogram from the search. The panel on the bottom right shows the phase-folded binned time-series with the box-shaped model over-plotted. From Kovács et al. (2002).

2.1.1 BLS and TLS searches

One of the most widely used algorithms to search for periodic transits in a lightcurve is the Box-fitting Least Squares (BLS) algorithm, presented in Kovács et al. (2002, 2016). With this method, a box-shaped transit is fitted on a lightcurve that has been phase-folded on various frequencies. At each frequency, the box model is fitted at various widths using least squares minimisation and a power spectrum is produced showing the detected frequencies.

In this work, the BLS algorithm is implemented via `astropy` (Astropy Collaboration et al. 2013, 2018, 2022) a broad and versatile `Python` package for astronomy. Alternatively, the BLS algorithm can be used via `Lightkurve` although under the hood `Lightkurve` also makes use of `astropy`'s implementation.

BLS has some limitations. The box-shaped model is not ideal for low signal-to-noise ratio (SNR) transits as the transit depth is too close to the level of instrumental noise. Enter TLS: `TransitLeastSquares` (Hippke & Heller 2019), a successor to the popular BLS algorithm that uses real transit shapes, complete with limb-darkening, ingresses and egresses. TLS is optimised for low SNR transits in large data sets, making it ideal to search for small planets in long time series. TLS is publicly available as a standalone `Python` package and can be used on any lightcurve.

While TLS is more sensitive than BLS, it is also more computationally intensive and takes longer

to run (Hippke & Heller 2019). This is especially the case when searching a wide parameter space over a lightcurve for a *TESS* target in the continuous viewing zone, as these time series can contain over two years of data.

2.1.2 SHERLOCK

When it comes to software, user-friendliness is key. Fortunately `SHERLOCK` (**S**earching for **H**ints of **E**xoplanets f**R**om **L**ightcurves **O**f spa**C**e-based see**K**ers, presented in Pozuelos et al. 2020; Demory et al. 2020) is a very good friend to all exoplanet hunters. While the acronym is reminiscent of many a shoehorn, the package is a superbly useful end-to-end pipeline to search for new exoplanet candidates.

`SHERLOCK` uses `Lightkurve` to download lightcurves from MAST and smooths the data if desired using a Savitzky-Golay filter (Savitzky & Golay 1964); this means that the precision of the data is artificially increased without affecting the trends in the data. Smoothing a noisy time-series in this way is sometimes helpful as it will artificially boost the SNR of weak signals, meaning they are more likely to pass a threshold so they get checked by eye. However, should signals be found and followed up on, the un-smoothed time-series should be analysed rather than the smoothed one to ensure the true SNR of the signal is known.

After the smoothing step, `SHERLOCK` then detrends the lightcurve using `Wotan` (Hippke et al. 2019), testing a broad range of window sizes for the bi-weight filter. The goal of detrending, unlike smoothing, is to remove unwanted trends in the data such as stellar variability caused by rotation. Each of the detrended lightcurves is then searched for transit-like signals using `TLS` iteratively until the user-defined SNR threshold is reached; planetary candidates are then conveniently reported in PDF files.

Once candidates of interest have been selected, `SHERLOCK` additionally has vetting, validation and fitting modules built in. In most cases in this thesis, these processes were carried out outside of `SHERLOCK`, so they are described separately in later sections.

`SHERLOCK` was developed by people with whom I've collaborated on the SPECULOOS project throughout my PhD research, so I was fortunate to be an early adopter and user of the software. I first used it when preparing my first planet confirmation paper for the HD 28109/TOI-282 system (see 3.2) and it then became a normal part of my workflow. As such, I also used it as standard for TOI-715 (3.4) and AMY-1 (3.6).

2.2 Photometry

As described in Chapter 1, *TESS* is currently the main provider of new exoplanet candidates for the community. Like *CoRoT* and *Kepler* before it, the *TESS* mission relies on a ground-based network of astronomers and observatories to follow-up on candidates, with the goal of confirming true planets and retiring false positives (Collins 2019).

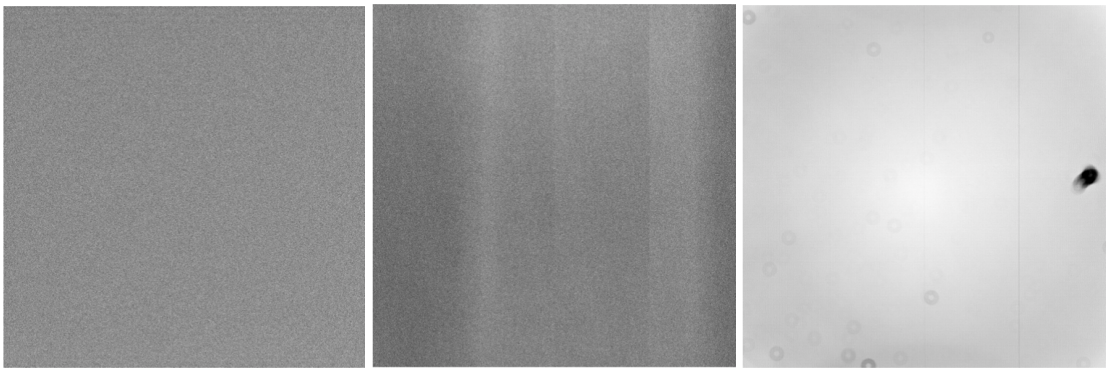


Figure 2.2: The calibration frames taken for an observation of AMY-1 on the night of 2022 Februrary 11 with Io, one of the four telescopes of the SPECULOOS Southern Observatory. **Left panel:** bias frame. **Middle panel:** dark frame. **Right panel:** flat frame taken with the *I+z'* filter to match the observation.

The discoveries presented in this thesis were all based on *TESS* photometry and involved intensive follow-up campaigns using ASTEP or the telescopes of the SPECULOOS network (supplemented by TRAPPIST), often making use of several different filters in order to probe different wavelengths. In this section, I describe the process of photometric reduction as carried out for the observations that I processed.

2.2.1 Photometric reduction

Photometry does it what it says on the tin: measuring light. And fittingly, the process of reducing raw photometric images is the journey we take from raw images of the sky to our desired end product, a lightcurve of one target star. The lightcurves used in this thesis were produced using several reduction methods (e.g. using `AstroImageJ` (Collins et al. 2017), using the automated SPECULOOS pipeline (Murray et al. 2020), or using the previous ASTEP automated pipeline (Mékarnia et al. 2016)); but the process I used involved `prose`.

`prose` is an open-source, pure-`python` framework for processing astronomical images, as presented in Garcia et al. (2022). In Section 2.6 I describe the new `Python`-based pipeline I built around `prose` for ASTEP, but in this section I will describe in more detail the process itself of image calibration and processing, as well as how these steps are implemented in `prose`.

2.2.1.1 Calibration

Raw images of the sky contain many sources of systematic errors (referred to as systematics) that lead them to be unusable without prior correction. These systematics stem from the instrument itself and the conditions during the observation. To correct the raw images, ground-based telescopes take three types of calibration frames during the night. Examples of each are presented in Figure 2.2.

Bias Frames - Bias frames are images taken with the shutter closed and zero exposure time, in order to measure the bias voltage. The bias voltage is a small constant voltage applied to the capacitor where the charge from the CCD is dumped, in order to account for readout noise. The

measured number of photoelectrons from each pixel is a gaussian distribution where the mean is the number of counts, and the standard deviation is the CCD readout noise. For low counts, this can lead to negative readings, which are not physically possible. The bias voltage then prevents these negative readings from occurring.

By collecting several bias frames at the start and end of the night, we can measure the bias voltage without any photoelectrons or thermally excited electrons. `prose` takes the median of all the bias frames from one night to create a master bias image - this is then subtracted from every raw image taken that night.

Dark Frames - As alluded to above, electrons can also be excited to the conduction band of the CCD thermally, known as a dark current. CCDs are usually cooled to minimise the dark current, although it can still be substantial at low temperatures. Dark frames are taken to correct for this; they are taken with the shutter closed to ensure there are no photoelectrons, and can be done with a range of exposure times.

Dark frames also need to be bias subtracted before creating a master dark image. `prose` creates the master dark by taking the median values from all the dark frames; the median is the best choice in this case as cosmic rays can also excite electrons during long exposures, and this is mitigated by not using the mean value. The master dark is then subtracted from bias-subtracted images.

The need for bias frames can be eliminated by taking dark frames at the same exposure times as the science images. This is because when the the master dark is subtracted, it will have the same bias voltage as the science frames and thus simplifies the process. For ASTEP, this method is often used instead of taking bias frames.

Flat Frames - An image taken of a perfectly uniform light source would not, in fact, be perfectly uniform. The non-uniformity can be caused by vignetting, intra-pixel variations, and dust on the filters or camera window. In order to measure these variations and correct for them, images are taken of the flattest sky possible during dawn and dusk twilights. In Figure 2.2 the third panel shows examples of these variations; what is particularly visible is the 'doughnutting' from small out-of-focus dust particles on the filter.

Because these effects can be filter specific, the flat frames must be taken with each science filter used during a given night. These frames must also be bias and dark subtracted before creating a master flat by taking the median of the images. `prose` then divides each bias- and dark-subtracted image by the master flat to normalise all frames.

The telescopes of the SPECULOOS observatories take daily dusk and dawn flats, however for ASTEP, this is more challenging. During the polar winters, there is often no twilight to speak of meaning that there isn't a flat enough sky to take flat frames. In some cases, dome flats are taken instead, or flats frames can be acquired at the start and end of the observing season and used throughout. This method is less robust though as the factors affecting non-uniformity of flats can vary significantly over time.

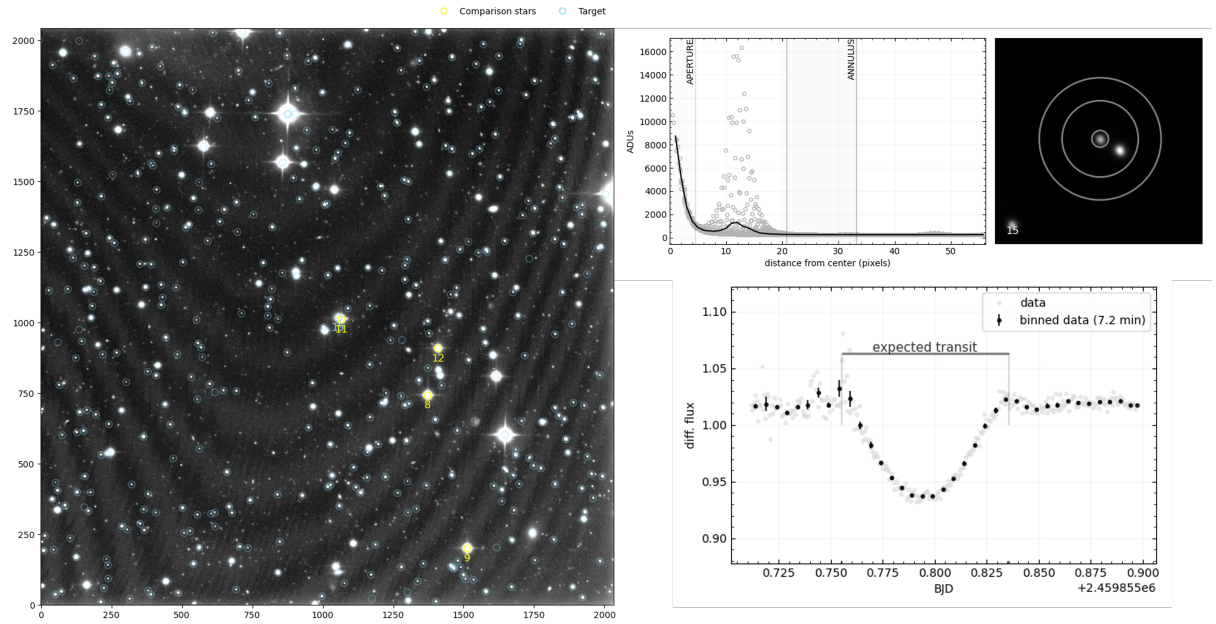


Figure 2.3: Sample `prose` output from an observation on the night of 2023 01 27, by SPECULOOS-South (Io) in *Sloan-i'*. **Left panel:** Example stack image with detected sources. The scales on the x- and y-axes refer to pixel positions. **Upper right panel**: Position of the target aperture and annulus. **Lower right panel:** target lightcurve following differential photometry.

2.2.1.2 Detection and alignment

Once each image has been calibrated as described above, the n brightest stars are detected in every image using the principles of image segmentation[a]. The positions of these sources are compared to a pre-selected reference image (in `prose`, this is by default the middle image), and an affine transformation is computed to align the images using `twirl`[b]. The aligned images are then combined to create a stack image, but the individual calibrated images are also stored to perform aperture photometry on each one. An example stack image is presented in Figure 2.3.

2.2.1.3 Aperture photometry

Aperture photometry consists of measuring the number of photons detected within a small portion of the image, known as the aperture. These apertures should be of a size appropriate to the spread of the point sources on the images, therefore the first step in this sequence is to fit a model to the effective PSF (point spread function) of the stack image. In the case of `prose`, an elliptical two-dimensional Moffat model (Moffat 1969) is fitted to the stack PSF, and the full width at half maximum of this model (FWHM) is then used to scale the photometric apertures used.

The next step consists of detecting stars in each image; for this, `prose` uses a `python` version of the `DAOPHOT` algorithm (Stetson 1987), implemented via `PhotUtils` (Bradley et al. 2016). This algorithm

[a] This is described in https://photutils.readthedocs.io/en/stable/segmentation.html
[b] https://github.com/lgrcia/twirl

is optimised for finding sources even in very crowded fields, and therefore gives the best chance of detecting the target of interest in the images.

Circular apertures are then placed on the detected sources to extract the flux. `prose` will by default use 40 apertures of several sizes in order to later on give the user choice of which aperture is the most appropriate for the target star. These are scaled using the FWHM of the fitted PSF model, and they range from $0.1 - 10$ times the FWHM. Aperture placement is computed by `prose` in the first instance using the inverse of the transformation matrix computed during the calibration for the affine transformation, but these positions are then refined using the centroiding algorithm `Ballet`[c]. A circular annulus is also placed around the aperture in order to measure the sky background in the region of each source. An example stack image with detected sources is presented in Figure 2.3, as well as a circular aperture.

Finally, the flux inside each aperture is extracted by `prose` using the `PhotUtils` classes `CircularAperture` and `CircularAnnulus`.

2.2.1.4 Differential photometry

As the goal of my photometric follow-up observations is to detect variations in the brightness of the target star over time (if they are present), I am not concerned with absolute photometric measurements. Instead, as is the norm in the field, I make use of differential photometry in order to construct a target lightcurve that shows the variations in normalised, relative brightness over the course of the observation.

Differential photometry is simple: the flux of the target star is divided by the averaged flux of a set of reference stars in each image, resulting in the relative flux measurements over time. One of the key benefits (and assumptions) of differential photometry is that all sources in the image will have been affected by the same systematics (e.g. variations in airmass, sky brightness, and FWHM of the PSF); therefore, these effects can be effectively divided out of the target lightcurve.

Choosing the reference stars can be challenging if the process is done manually. In `AstroImageJ` (Collins et al. 2017), for instance, bright comparison stars are selected by the user without prior knowledge; the best choices should present no variability of their own and lower the root-mean-squared variability (RMS) of the target star. In `prose`, this is simplified by implementing a customised pure `python` version of the differential photometry algorithm presented in Broeg et al. (2005). This step is described in the ASTEP pipeline paper in Section 2.6, so here I only summarise the process.

The Broeg et al. algorithm creates a single artificial comparison star by using all the detected sources in the image. Each source is given a weight depending on their signal-to-noise ratio and variability, so that quiet, high SNR stars are favoured and weighted the highest. This artificial comparison star is then used to compute the target lightcurve.

[c] https://github.com/lgrcia/ballet

2.3 Vetting and Validation

While vetting and validation are two distinct processes, I have grouped them here as both are concerned with the same challenge: ruling out false positive scenarios. False positives are astrophysical scenarios which produce lightcurves that mimic transit lightcurves.

Most astrophysical false positives involve eclipsing binary star systems (Santerne et al. 2013a); such a binary in the background of a *TESS* observation could produce a transit-like signal on the target star's lightcurve if its light is sufficiently blended. This is especially a problem for *TESS* lightcurves as the pixel scale is a mammoth $21'' \ \mathrm{px}^{-1}$ (Ricker et al. 2016). Another blend scenario can occur when an eclipsing binary is blended with the target star and unresolved even in high resolution images. Transit-like signals can also be the result of secondary eclipses of eccentric, inclined eclipsing binaries (Santerne et al. 2013b). A false positive involving a transiting planet can also arise, if the planet in question is orbiting a different star that is blended with the target (Sullivan et al. 2015). In this case the true host can be gravitationally bound to the target or simply blended in the line of sight.

In the following sections I will describe the processes of vetting and validation and how they allow us to rule out false positives.

2.3.1 Vetting

Vetting is the process of scrutinising all available photometric data and metadata to search for common indicators of false positives. The SPOC pipeline (Jenkins et al. 2016) produces data validation reports for each detected signal from *TESS* which includes standard vetting tests to rule out signals not produced by a transiting planet. For signals that are not detected by *TESS*, `python` packages such as `LATTE` (Eisner et al. 2020) or `WATSON`[d] allow users to create similar data validation reports for any detected signal.

The most common vetting tests to check for possible binarity include comparing odd and even transits to check for depth differences as every other transit could in fact be a secondary eclipse, as well as searching for weak secondary signals in the phase-folded lightcurves. Additionally, sudden variations in the background flux or centroid position are searched for, and the timing of momentum dumps[e] is checked against the timings of transits.

In general, the data validation reports would be scrutinised prior to initiating a follow-up campaign in order to ensure there is no prior evidence that the signal may not be planetary in nature.

2.3.2 Validation

In an ideal world, vetted planetary candidates would then have their planetary nature confirmed by measuring their masses with precise radial velocities. This procedure leaves almost no doubt as to

[d] https://github.com/PlanetHunters/watson

[e] Momentum dumps are described in the *TESS* mission handbook, available at https://archive.stsci.edu/files/live/sites/mast/files/home/missions-and-data/active-missions/tess/_documents/TESS_Instrument_Handbook_v0.1.pdf.

what has been discovered[f], and as such systems followed-up on in this way are considered 'confirmations'. However, three factors prevent this from being possible for all planetary candidates: the first is that not all host stars are bright enough for precise RV follow-up to be possible. Secondly, many of the planetary candidates around bright enough stars are small, and would therefore not produce a large enough RV signal for current instruments to detect. Finally, the number of candidates currently available for follow-up is simply astounding; there are not enough spectrographs available to confirm them all, even if they were all amenable.

All of the above reasons led to the development of a new method to promote candidate planets to full planetary status: probabilistic or statistical validation. Statistical validation was first introduced in the *Kepler* era with codes such as `BLENDER` (Torres et al. 2011), `PASTIS` (Díaz et al. 2014), and `VESPA` (Morton 2012; Montet et al. 2015). The process consists of using statistical methods to calculate a 'false positive probability' (FPP) for a given planetary candidate; if the FPP falls below a given threshold, then the planetary hypothesis is the most likely and therefore the planet is considered validated. Thus this leads to many systems being published as 'validations' rather than 'confirmations'.

In the era of *TESS*, the most widely used statistical validation software is `TRICERATOPS` (Giacalone et al. 2021), an open-source `python` package for calculating FPPs of *TESS* candidates. While the principle of all statistical validation algorithms is the same, they each have their nuances. `TRICERATOPS` examines 18 scenarios, including 16 astrophysical false positives and two true positive scenarios,[g] and calculates the probability for each one by fitting models to the phase-folded lightcurve. Lightcurves from ground-based follow up can also be folded in which help to lower the FPP, and contrast curves from high-resolution imaging can also be provided to help rule out blend scenarios.

In this thesis, I have made use of `TRICERATOPS` for several systems. In most cases I used the code directly, but `SHERLOCK` also has the possibility to implement the algorithm via its validation module. In the case of the HD-28109/TOI-282 system (3.2), I made use of the `SHERLOCK` implementation as described in the paper.

2.4 Transit modelling

Assuming that our vetted candidate has been the subject of successful follow-up and is now validated, the crucial next step is to extract the system parameters from the data set. This is done by fitting a transit model to the data. Before I venture into the specific methods used in this thesis, we will need to take a brief sidestep into the world of Bayesian inference. And I do mean *brief*.

[f] In most cases there is no doubt, however rare cases of spectroscopic blends could also muddy these waters. For instance, the case of WASP-9B which was first reported as a planetary candidate but was found to be an eclipsing binary in a hierarchical triple system (`http://exoplanet.eu/catalog/WASP-9_b/`)

[g] The true positives are transiting planet on the target star (TP), and diluted transiting planet on the target star (DTP). In the latter case, the planet may be bigger than previously thought, but it is still a true positive as the signal is planetary, and the host and orbital period are correct.

2.4.1 Bayesian statistics

Bayesian inference allows us to pose the following question: "how likely is it that this hypothetical planetary system produced the data set in front of me?". The assumption here is that we have some prior beliefs about the parameters of the planetary system, and the desire is to learn the posterior distribution of these parameters. These concepts are formalised in Bayes' Theorem, presented as follows in Parviainen (2018):

$$\Pr(H|D) = \frac{\Pr(H)\Pr(D|H)}{\Pr(D)} , \tag{2.1}$$

where H is the hypothesis about the system (the prior beliefs) and D is the data. Therefore $\Pr(H|D)$ is the posterior probability for the hypothesis given the data set at hand which is what we aim to find out. $\Pr(H)$ is the prior probability for the hypothesis, incorporating all our prior information about the system. Here we can include knowledge gained from different data sets and exclude non-physical areas of the parameter space. $\Pr(D|H)$ is known as the likelihood, and it is the probability of the data set being produced given the hypothesis. Finally, $\Pr(D)$ is the probability for the data, also known as the evidence; it is crucial to normalise over the evidence to extract absolute values for parameters from the posterior distribution.

For completeness, I include here the expression for the log-likelihood function as presented in Günther & Daylan (2021):

$$\log \mathcal{L} = -\frac{1}{2}\sum_{k=1}^{N}\left[\left(\frac{y_k - M(t_k)}{\sigma_k}\right)^2 + \log 2\pi\sigma_k^2\right] , \tag{2.2}$$

where N is the number of points in the time series, which contains data points y_k collected at times t_k. The data points have uncertainties σ_k (assumed to be Gaussian), and $M(t_k)$ is the model that represents the data set.

2.4.1.1 A note on priors

The prior information supplied will restrict the parameter space sampled for the posterior distributions; as such, subjective decisions must be made about how restrictive we want to be. In general, priors are supplied as either uniform or normal distributions. Uniform and log uniform priors, also known as uninformative priors[h], are used when our knowledge of a parameter is limited. Normal priors, often referred to as informative priors, are most suitable when there is robust prior information about the parameter in question. In the context of exoplanets, normal priors may be used for the stellar parameters of the host, as these are often extracted from external data sets.

[h] Although priors are never truly uninformative.

2.4.1.2 Sampling from the posterior

Having limited the parameter space to be explored by supplying our prior beliefs, the next step is to sample from the posterior distribution to find the areas of highest likelihood. This allows extraction of the posterior distributions for each of our parameters of interest. I have used the two most common methods of sampling throughout my work: Markov Chain Monte Carlo (MCMC) (e.g. Mackay 2003; Trotta 2008) and Nested Sampling (Skilling 2004).

MCMC has two parts: the 'Markov' Chain refers to the method having no memory, while the Monte Carlo element relates to randomness. In short, a set number of 'walkers' are given random starting positions within the parameter space to be explored; these walkers will explore the parameter space and find the areas of highest likelihood. The chain is constructed by walkers taking random steps; for each step to be accepted conditions need to be met, such as increasing the overall likelihood. As mentioned above, the Markov Chain has no memory of previous steps, so only the present state is known before taking the next random step. As the number of steps in the chain and the number of walkers launched are both set a priori, the chains will end regardless of whether the model has converged on a set of parameters or not. Convergence is therefore tested for using statistical tests, such as those described in Parviainen (2018).

Nested sampling does not directly sample from the posterior, although it does produce posterior distributions. One element that is completely ignored in MCMC is the Bayesian evidence $\Pr(\mathrm{D})$, the numerator in equation 2.1. In nested sampling however, calculation of the evidence at each step is the main goal. The process works by drawing a set number of live points from the prior distribution and then calculating the evidence ($\mathcal{Z}$). Then, the live point with the lowest likelihood is discarded and replaced with a new point drawn from the prior distribution; the condition for the new point is that the likelihood must be higher than before. This process continues iteratively until the stopping condition is reached: as we are calculating $\mathcal{Z}$ at each step or the iteration, and naturally it is increasing, the stopping condition used is when the gain in logarithmic evidence falls below a given threshold.

One of the key benefits of nested sampling over MCMC is that calculation of the Bayesian evidence allows us to effectively compare models. This is done by calculating the difference in logarithmic evidence for each model, known as the Bayes Factor (Kass & Raftery 1995).

2.4.2 `exoplanet`: single transit modelling via MCMC

`exoplanet` is a `python` toolkit for modelling exoplanet time-series data sets using MCMC (Foreman-Mackey et al. 2021). The inference package implemented for MCMC is `PyMC3` (Salvatier et al. 2016), and the `celerite` (Foreman-Mackey et al. 2017) library is used to model red and white noise using Gaussian Processes (GPs[i]).

`exoplanet` requires that users build their own models, which is trivial enough for a single time-series containing a single planet. Additional complexity is introduced if there are several data sets to

[i] A description of GPs is far beyond the scope of this work; for a review, see Rasmussen & Williams (2006).

include in the model, especially if there are independent systematics and limb-darkening coefficients due to differing instruments and filters respectively.

However, as `prose` works very well with `exoplanet` by design, the latter package is an ideal choice for modelling single transits after successful follow-up observations. As only the follow-up observation is being fitted, normal priors can be imposed on period, transit midtime, and depth from *TESS*. For simplicity, limb-darkening coefficients are left as uniform priors between $0-1$ by using the Kipping (2013) parametrisation. This setup generally takes between $2-4$ minutes to run on a 4-core MacBook Pro.

2.4.3 `allesfitter`: global analysis via nested sampling

Following an extensive, multi-facility, multi-band follow-up campaign, the goal is to extract the most precise system parameters possible. This is done this with a global analysis, which entails jointly fitting all available data sets. I will stress that this is possible with `exoplanet`, but it is not the most user-friendly experience.

This is where `allesfitter` (Günther & Daylan 2021, 2019) comes in. `allesfitter` is a flexible, `python`-based, open-source inference package for jointly modelling exoplanet time series, both photometric and radial velocity. Unlike `exoplanet` which produces its own lightcurve and RV models, `allesfitter` calls on `ellc` (Maxted 2016) for this task. Users can choose between MCMC sampling implemented via `emcee` (Foreman-Mackey et al. 2013), or nested sampling via `dynesty` (Speagle 2020)[j]. GP models are once again provided by `celerite`.

One key benefit of `allesfitter` for global analysis is that models do not have to be assembled by the user; instead, text files are prepared with all prior distributions and settings for the fit, and these are read in by the software. However, preparation of these files is cumbersome for simple single transit fits, which is why I opted to continue using `exoplanet` in those cases.

The outputs of `allesfitter` runs are convenient plots to assess the quality of fits, as well as detailed tables containing all fitted and derived parameters. The package additionally outputs tables in LaTeXto be used directly in publications.

Nested sampling is more computationally intensive than MCMC; additionally, a global analysis will involve several data sets, some of them very large. Therefore, the time taken to run these fits is significantly longer than the single-transit fits run with `exoplanet`. In fact, for systems in the *TESS* continuous viewing zone (CVZ) such as TOI-282 and TOI-715, the shear volume of data meant that I was not able to run these fits on my personal laptop. Instead, I offloaded them to the university's remote servers, where some runs took in excess of 80 hours to complete.

2.4.3.1 Side note: limb-darkening coefficients

Similar to single transit fits carried out with `exoplanet`, in `allesfitter` quadratic limb-darkening coefficients are provided in the Kipping (2013) parametrisation (q_1 and q_2) instead of the usual parameters

[j] All fits in this thesis were done using nested sampling to enable model comparison as described above.

(u_1 and u_2). One difference is that to help limit the parameter space of exploration to a useful area, I chose to calculate external priors for the coefficients using `PyLDTK` (Parviainen & Aigrain 2015).

`PyLDTK` is an open-source `python` package that used the Phoenix stellar atmosphere library (Husser et al. 2013) to calculate limb-darkening coefficients in different wavelength bands. Required inputs are stellar parameters (metallicity [Fe/H], surface gravity $\log\ g$, and effective temperature $T_{\rm eff}$) and the transmission profile of the filter used for each observation (these can be imported from the Spanish Virtual Observatory (Rodrigo et al. 2012; Rodrigo & Solano 2020)). The outputs are quadratic limb darkening coefficients for each filter (u_1 and u_2) which can be transformed into the Kipping (2013) parametrisation with the following equations:

$$q_1 \equiv (u_1 + u_2)^2 \tag{2.3}$$

$$q_2 \equiv \frac{u_1}{2\,(u_1 + u_2)}\ . \tag{2.4}$$

These are then provided to the fit as normal priors, as the stellar parameters used come from external data sets.

2.5 Can we study the planet's atmosphere?

The new generation of observatories in space, such as *JWST* (Gardner et al. 2006), *Ariel* (Tinetti et al. 2018), and on the ground, like the European Extremely Large Telescope (ELT, Gilmozzi & Spyromilio 2008), is set to revolutionise our understanding of exoplanet atmospsheres. In fact, *JWST* is already doing so, with its detections of CO_2 and SO_2 in the atmosphere of WASP-39 b (JWST Transiting Exoplanet Community Early Release Science Team et al. 2023; Tsai et al. 2023). Given the community's current collective excitement at this new era of detailed atmospheric investigation, a crucial step in an exoplanet discovery is to check whether the system is amenable for this flavour of follow-up.

2.5.1 Handy metrics

Atmospheric investigations currently come in two forms: transmission and emission spectroscopy (for a comprehensive review: Kreidberg 2018). Transmission spectroscopy is carried out by observing a planetary transit with a spectrograph, allowing us to look at the star's light through the planet's atmosphere in various wavelengths. Emission spectroscopy on the other hand, is carried out during a planetary occultation, enabling measurement of thermal emission from the planet.

The success or failure of these methods depends variously on the planet-to-star size ratio, the planet's temperature, the star's brightness, and the scale height of the putative atmosphere. The puffy atmospheres of inflated Hot Jupiters were some of the first successes of the field of exo-atmospheres (e.g. Charbonneau et al. 2002), but the compact atmospheres of Super-Earths, while of very high scientific value have thus far eluded us. There are therefore several factors to take into account when deciding whether to pursue these costly observations.

Rather conveniently, Kempton et al. (2018) introduced the Transmission and Emission Spectroscopy Metrics (TSM and ESM respectively) to assess a planet's amenability for these investigations with a simple formula for each. Along with the metrics, Kempton et al. provide cutoffs for each metric according the the planet type, to allow easy interpretation of the values. The TSM is calculated using the following formula:

$$\mathrm{TSM} = (\mathrm{Scale\,factor}) \times \frac{R_\mathrm{p}^3 T_\mathrm{eq}}{M_\mathrm{p} R_\star^2} \times 10^{-m_J/5} \,, \tag{2.5}$$

where the Scale Factor is a constant for each of four planet size categories, m_J is the *J*-band apparent magnitude of the host, T_eq is the planetary equilibrium temperature, and other symbols retain their usual meanings. The ESM is calculated using:

$$\mathrm{ESM} = 4.29 \times 10^6 \times \frac{B_{7.5}(T_\mathrm{day})}{B_{7.5}(T_\mathrm{eff})} \times \left(\frac{R_\mathrm{p}}{R_\star}\right)^2 \times 10^{-m_K/5} \,, \tag{2.6}$$

where $\mathrm{B}_{7.5}(T_\mathrm{day})$ and $\mathrm{B}_{7.5}(T_\mathrm{eff})$ are Planck functions evaluated for the planet dayside temperature and the host star effective temperature respectively, both at a representative wavelength of 7.5 μm, and m_K is the *K*-band apparent magnitude of the host.

These metrics are not designed to be exact, nor should they be used to rule out systems of very high scientific value if the TSM/ESM is found to be below the suggested cutoffs. However, they provide a simple metric for comparison between systems with otherwise similar parameters, and as such they have been widely adopted by the exoplanet community, featuring in hundreds of planet papers so far.

2.5.2 A step further: simulating atmospheric investigations

There are some circumstances where simply calculating the TSM or ESM for a planet is not enough. For instance, if a planet scores highly in the metrics and the goal is to demonstrate to a reader that the observations truly are feasible with current instrumentation. Or if a proposal is being prepared for *HST* or *JWST* and there is a need to demonstrate the detectability of a putative atmosphere with our proposed observation strategy. In these cases, there are other tools to take it a step further.

The tools available for this step split the process into two sub-steps: first, a simulated transmission or emission spectrum is calculated from the system parameters using (in my case) `ExoTransmit`[k] (Kempton et al. 2017); secondly, the simulated spectrum is input, together with transit ephemerides, to `PandExo` (Batalha et al. 2017) to generate simulated *HST* and/or *JWST* observations.

`ExoTransmit` is an open-source package written in `C` that takes into account atmospheric composition, clouds and hazes, and temperature-pressure profiles to calculate simulated spectra. For an unknown atmosphere, there is clearly a large element of assumption included in this step. Because of this, it is useful to simulate atmospheres with different compositions to see what changes are detectable. Additionally, it can be helpful to simulate atmospheres for a wide range of masses if the surface

[k] `ExoTransmit` can only calculate transmission spectra. Other packages are available, such as `PetitRadTrans` (Mollière et al. 2019), that can do both. However, in this thesis only transmission spectra were needed so `ExoTransmit suited my needs just fine.`

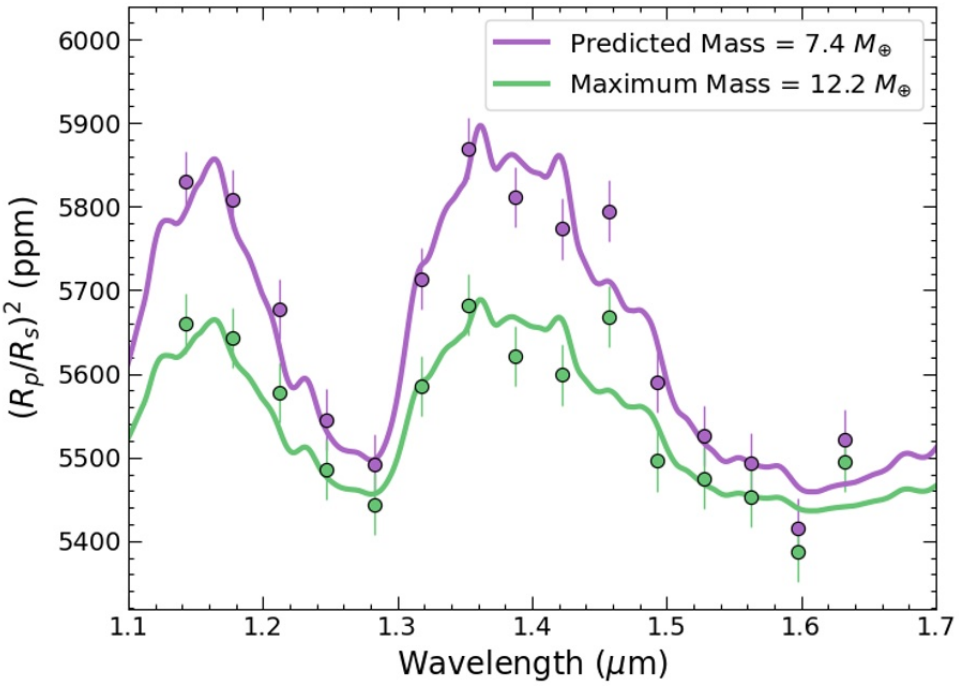


Figure 2.4: Figure from the successful *HST* proposal for atmospheric reconnaissance of TOI-4336 b (Dransfield et al. 2021). The green and purple lines are simulated transmission spectra calculated with `ExoTransmit` and the points are simulated observations from `PandExo`.

gravity of the planet is as yet unconstrained. This was the case when I calculated simulated spectra for TOI-715 b in Section 3.4, and also for my successful *HST* proposal for TOI-4336 b (Dransfield et al. 2021).

`PandExo` is also open-source software, available as a `python` package or as an online interface. It allows users to simulate time-series observations with both *HST* and *JWST*, crucially giving users an estimate of the expected noise in their observations. Together with the instruments' respective exposure time calculators (ETCs), `PandExo` is a vital step in testing whether the simulated atmospheric features are detectable with different instruments.

2.6 Paper: Scheduling and data analysis software for ASTEP

In July 2022, I presented the scheduling software and data analysis pipeline I developed for ASTEP at the SPIE Astronomical Telescopes and Instrumentation conference in Montreal. Presentations at SPIE conferences are accompanied by manuscripts presenting the work in additional detail, which afforded me the possibility to write a paper describing the work done in the first year of my PhD to support ASTEP's scheduling and data reduction needs.

The work for this paper includes observability simulations, development of scheduling software, development of a website, and construction of the new `python` pipeline; all of this work was done by me.

The scoring algorithms and layout of the scheduling page were inspired by the work of Nicolas

Crouzet, who generated PDF files with a similar look prior to the development of the current systems. The pipeline was built around `prose` - an ideal choice due to the software's flexibility and modular nature. The two main developers of `prose` (Lionel García and Mathilde Timmermans) both advised on the pipeline's construction and helped write the paper sections on calibration and photometry. Other co-authors contributed by writing small sections of the introduction and conclusions for the manuscript.

Observation Scheduling and Automatic Data Reduction for the Antarctic telescope, ASTEP+

Georgina Dransfield*[a], Djamel Mékarnia[b], Amaury H.M.J. Triaud[a], Tristan Guillot[b], Lyu Abe[b], Lionel J. Garcia[c], Mathilde Timmermans[c], Nicolas Crouzet*[,d,e], François-Xavier Schmider[b], Abdelkrim Agabi[b], Olga Suarez[b], Philippe Bendjoya[b], Maximilian N. Günther*[,e], Olivier Lai[b], Bruno Merín[e], and Philippe Stee[b]

[a]School of Physics & Astronomy, University of Birmingham, Edgbaston, B15 2TT, Birmingham, UK
[b]Université Côte d'Azur, Observatoire de la Côte d'Azur, CNRS, Lagrange Laboratory, Nice, France
[c]Astrobiology Research Unit, Université de Liège, 19C Allée du 6 Août, 4000 Liège, Belgium
[d]Leiden Observatory, Leiden University, Postbus 9513, 2300 RA Leiden, The Netherlands
[e]European Space Agency (ESA), European Space Research and Technology Centre (ESTEC), Keplerlaan 1, 2201 AZ Noordwijk, The Netherlands

ABSTRACT

The possibility to observe transiting exoplanets from Dome C in Antarctica provides immense benefits: stable weather conditions, limited atmospheric turbulence, and a night that lasts almost three months due to the austral winter. However, this site also presents significant limitations, such as limited access for maintenance and internet speeds of only a few KB/s. This latter factor means that the approximately 6 TB of data collected annually must be processed on site automatically, with only final data products being sent once a day to Europe. In this context, we present the current state of operations of ASTEP+, a 40 cm optical telescope located at Concordia Station in Antarctica. Following a successful summer campaign, ASTEP+ has begun the 2022 observing season with a brand-new two-colour photometer with increased sensitivity. A new `Python` data analysis pipeline installed on a dedicated server in Concordia will significantly improve the precision of the extracted photometry, enabling us to get higher signal-to-noise transit detections. The new pipeline additionally incorporates automatic transit modelling to reduce the amount of manual post-processing required. It also handles the automatic daily transfer of the photometric lightcurves and control data to Europe. Additionally, we present the `Python` and web-based systems used for selection and scheduling of transit observations; these systems have wide applicability for the scheduling of other astronomical observations with strong time constraints. We also review the type of science that ASTEP+ will be conducting and analyse how unique ASTEP+ is to exoplanet transit research.

Keywords: Exoplanets, Transit, TTV, Antarctica, TESS, ExoFOP, Photometry

1. INTRODUCTION

ASTEP (Antarctic Search for Transiting ExoPlanets) was initially conceived in 2006 as a photometric telescope to search for transiting exoplanets in dense fields of stars.[1] It was installed at the Concordia Station, located on Dome C in Antarctica, at the end of 2009, and successfully began its operations in 2010.[2,3] The telescope remained on site until 2013 exploiting the near-continuous winter polar nights and excellent weather conditions of the site.[4,5] It led to the first ground-based observation of a secondary eclipse of an exoplanet in the visible[6] and the discovery of tens of transiting planet candidates.[7] At that time, internet connection with the Concordia

Further author information: (Send correspondence to G. Dransfield)
G Dransfield: E-mail: gxg831@bham.ac.uk
* ESA Research Fellow (2018-2021)
* ESA Research Fellow

station was extremely limited, requiring the full-time presence of an astronomer on the site. Observations were saved on hard drives and fully analyzed in Europe the year after.

The return of ASTEP at the end of 2016 for a continuous observation of β Pictoris[8–10] required a different strategy, i.e., an automatic processing of the lightcurves and their transmission to Europe. Improvements in the internet connection with the Concordia station implied that an automatic transmission of limited amounts of data (of order 10 MB/day) was possible, using the HERMES system implemented by PNRA (*Programma Nazionale di Ricerche in Antartide*). A new server, adapted to the automatic processing of the ~ 6 TB of data per season, was sent to Concordia with a dedicated `IDL` pipeline, based on aperture photometry.[8] With the successful launch of *TESS* (Transiting Exoplanet Survey Satellite),[11] the ASTEP observation program naturally transitioned to a follow-up of transiting exoplanet candidates, focusing on those with long orbital periods (10-100+ days) and contributing to many discoveries.[12–21]

The geographic location of ASTEP is extremely interesting in complement to several key exoplanetary space missions. Of course, the Antarctic polar night is highly favorable for an efficient observation of transiting planets, in particular for those with long orbital periods and for those with long transit durations (the two being correlated). The combination of observations from mid-latitude sites in e.g., Chile, and Antarctica is particularly efficient.[22] However, the main asset is probably the fact that targets in the southern continuous viewing zones of the *TESS*, *JWST* and *Ariel* space missions are circumpolar and can be observed by ASTEP all the time. In counterpart, access to Antarctica is limited to about 3 months, between November and February, only a low-bandwidth internet connection is available, and the instrument must cope with temperatures ranging from about -10°C to -80°C. This makes operations with ASTEP intermediate between ground-based telescopes and space-based missions.

Starting in 2022, thanks to support from the University of Birmingham, ESA, INSU, and the Laboratoire Lagrange, a new camera box[23] could be installed, starting ASTEP+ observations in two colors. This required a new pipeline, but also an adaptation of the scheduling system to cope with the large number of potentially interesting targets to be observed.

In this paper we will describe the current status of ASTEP+. First we show how different ASTEP+'s sensitivity to transiting planets is to more traditional observatories in Section 2. In Section 3 we outline our current scheduling needs and how they are shaped by our team's science goals. We also describe the systems we have designed to meet these needs and our plans for further development. In Section 4 we provide a detailed description of our new automatic `Python` data analysis pipeline, as well as a quantitative comparison with the system it replaces. In Section 5 we map out in brief the possible future directions of the ASTEP+ project, and we conclude in Section 6.

2. SENSITIVITY TO LONG PERIOD PLANETS AND LONG DURATION TRANSITS

Prior to the start of the 2020 observing season, ASTEP had been dedicating its exquisite resources first to a blind exoplanet survey of its own,[7] and then to observations of the δ-Scuti pulsator β Pictoris.[8] In early 2020, ASTEP joined TFOP (*TESS* Follow-Up Observing Programs) Sub-Group 1 (SG1 hereafter) to support photometric follow-up and confirmation of *TESS* planet candidates.

In the context of *TESS* follow-up, ASTEP has a lot to offer; in particular, ASTEP can truly excel when it comes to observing long transits in full, as well as the transits of long-period planets. The current list of TOIs (*TESS* Objects of Interest) has 5767 targets, of which 3053 are observable from the South*. Of these, 285 have transits lasting at least five hours, and 186 have periods of at least 20 days. These 471 candidate planets fall perfectly in ASTEP's niche.

In order to quantitatively compare ASTEP's sensitivity to long transit/long period candidates, we created a synthetic sample of 2500 planet candidates. Each was given a transit epoch (t_0) drawn randomly from *TESS*'s first year, a period of between $20 - 200$ days, and a transit duration between $5 - 15$ hours. To keep the on-sky distribution of the sample as realistic as possible, we assigned to each a set of coordinates (right ascension,

*Taken from https://exofop.ipac.caltech.edu/tess/view_toi.php, correct on the 22th of June 2022.

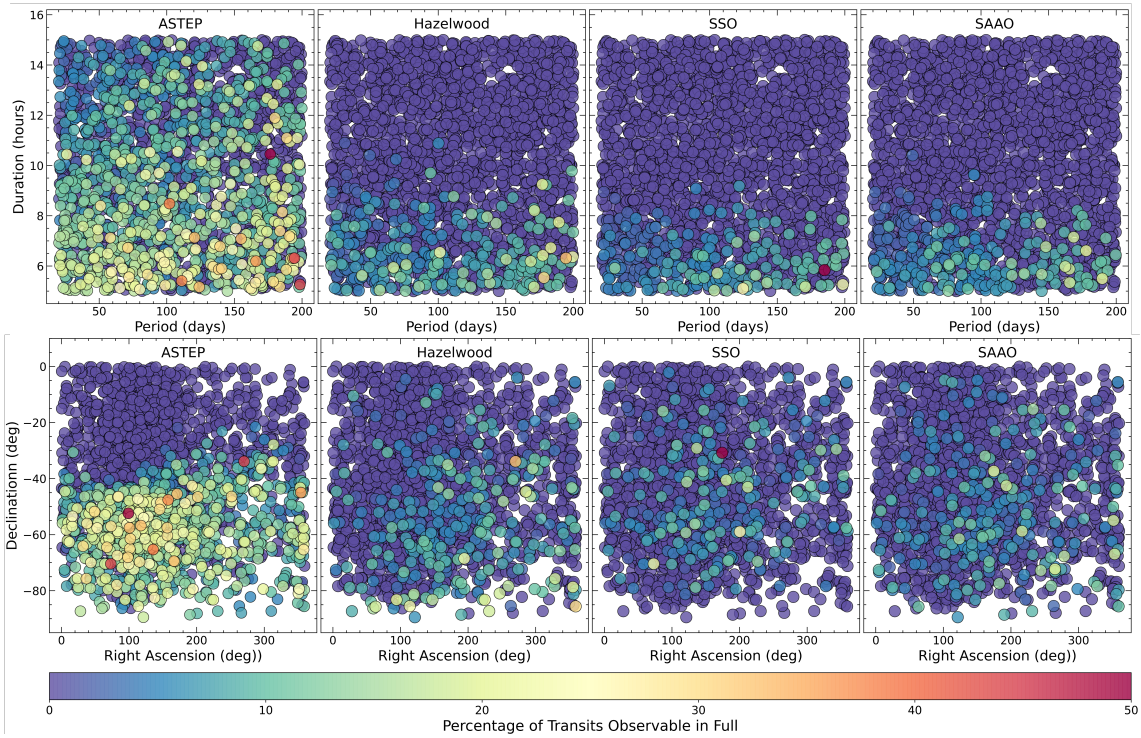


Figure 1. Results of the observability simulation for our synthetic sample of 2500 long period/long duration transiting planets. In all panels points are coloured according to the percentage of transits observable in full. Top row: duration and period distribution of the sample. Bottom row: the distribution of the sample on the sky.

declination) of real TOIs as taken from the current TOI list described above. Using this sample, we simulated observability of full transits by ASTEP and three other SG1 observatories: SPECULOOS-South (SSO)[24] in Chile, South African Astronomical Observatory (SAAO)[25] in South Africa, and Hazelwood Observatory[26] in Australia. The simulation was carried out using the `Python` package `astroplan`,[27] and observability was tested for a five-year period starting from the 01 January 2022.

The results of our simulation are presented in Fig. 1, with the top row of panels showing the distribution of planets according to period and duration and the bottom panel showing the planets' distribution on the sky. There are two very clear conclusions to be drawn from the top panels; firstly, we can see that ASTEP is the only observatory that can *consistently* observe full events for both infrequent and long duration transits. The other observatories have almost no observability above eight hours, while ASTEP maintains in excess of 20% for some transits lasting over 12 hours. Secondly, we can see that while all observatories can observe *some* long-period transits in full, their percentage observability is lower than ASTEP's, and where long periods intersect with long transits, there are no transits observable. We find that on average ASTEP is more than 8 times more likely to observe a full transit for long period planets, and for the duration bins where other telescopes have non-zero observability, ASTEP is almost 40 times more likely to catch a full event.

In the lower panels we can see how the sample of synthetic planets is spread on the sky, and we note that the bulk of ASTEP's zero-observability objects are concentrated in an area of the sky that is completely invisible to us. Circumpolar and very southern targets are high in the sky all year long, while more northern targets (above declinations of $-40°$) rise during the austral summer and set before ASTEP's observing season begins.

In Fig. 2 we filter out all objects north of $-40°$ and compare observability of the objects still invisible to ASTEP. In all panels, objects that ASTEP can observe at least one full transit for are plotted in green, while planets with zero observability are plotted as red circles. Crucially, we note that for all systems where ASTEP cannot observe a single transit in the next five years, only 2.3% can be observed by a different observatory.

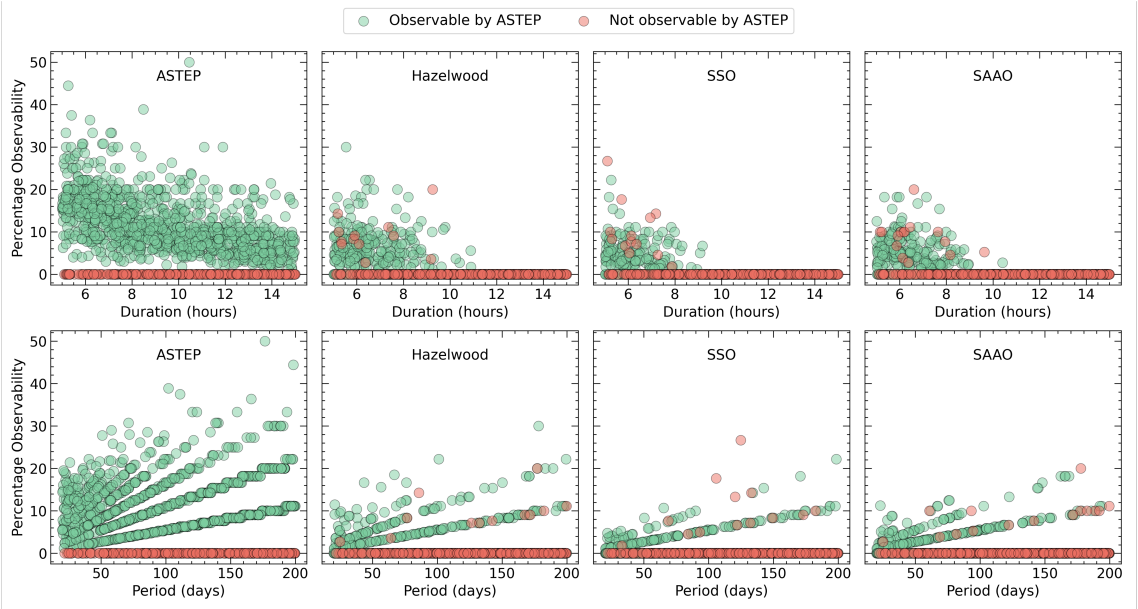


Figure 2. Which systems can never be observed? Having removed all systems north of $-40°$, we show the systems that ASTEP still cannot observe to check if they are observable by other telescopes. Green points in all panels are systems where ASTEP can observe at least one transit in full, while red points have zero transits observable by ASTEP in the next five years. Top row: observability in terms of duration; bottom row: observability and period distribution.

3. OBSERVATION SCHEDULING

The scheduling of our observations is heavily influenced by the type of observations we perform. At the moment, the main task of ASTEP+ is to confirm planetary candidates identified by ExoFOP (Exoplanet Follow-up Observing Programme), an international follow-up collaboration. Our lightcurves of transiting planets are necessary to validate *TESS*'s planetary candidates for the following reasons:

- *TESS* has a PSF (Point Spread Function) of about 30 arcseconds,[11] meaning that many transit events are in fact deep eclipse produced by faint background objects diluted by a foreground bright star (which is then usually identified as a transiting planet candidate by the *TESS* automated pipelines);
- Sometimes, transit events identified by *TESS* are false alarms, caused by instrumental systematics or an unlucky coincidence of stellar activity;
- We can check odd and even transit events and verify their depth are consistent with one another,[21] as a way to rule out blended eclipsing binaries (in non visually resolved binaries);
- We measure the transit depth and compare it to *TESS*'s and to other photometric bands in order to perform a *chromaticity check*,[21] another way to rule out blended eclipsing binaries, which works if the secondary component has a significantly different $T_{\rm eff}$ from the primary. For most of its operations ASTEP operated with a single filter, but recently we installed two cameras separated by a dichroic, allowing us to perform chromaticity check directly (see companion paper by Schmider et al.);
- We verify the transit ephemerides, notably the orbital period and time of transit;

Exoplanet transits are short compared to their orbital periods, and happen at specific times. This means that we need a scheduler able to handle those. In addition, new systems are identified by *TESS* with regularity, and some are removed (e.g. when we demonstrate the system is likely not a planet). Again here this forces our scheduler to adapt to new situations on a weekly basis.

While every night can be filled with observations of *TESS* Objects of Interests (TOIs), we remain scientists with interests in specific types of planets. This places further restrictions on the type of scheduler. First we

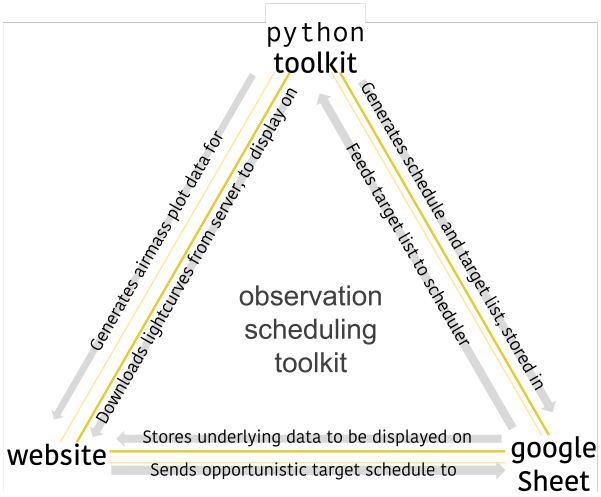


Figure 3. Schematic of the ASTEP+ scheduling toolkit, showing how the three elements are interconnected. The `Python` toolkit generates data, the Google Sheet holds the data, and the website both displays and updates the data.

prioritise systems aligned with our science goals (be they confirmed TOIs, non-confirmed TOIs, or unrelated systems altogether). Because this rarely fills the schedule, we also select TOIs opportunistically but also with a prioritisation that aligns with our preferences (see Section 2.)

In addition, we also perform filler observations for a few hours a night to create long timeseries. Typically this involves observing β Pictoris to search for a transit of the Hill sphere of its directly imaged planets,[28] monitoring J0600, a system with a candidate circumplanetary ring transiting a star (Kenworthy et al. in prep), and now some flaring stars.

Finally, our team is international, with partners in France, the United Kingdom and the Netherlands. We are not able to meet physically to decide targets, therefore requiring a web-based tool.

3.1 Early solutions

Upon joining ExoFOP at the start of 2020, ASTEP gained access to the *TESS* `Transit Finder`[29] (`TTF` hereafter), a web-based tool that allows observers to check for upcoming transits of targets of interest. It can also be used to search for all transits occurring in a given date range, which allowed the team to get a feel for the different categories of transiting candidates *TESS* was producing.

Throughout ASTEP's first observing season with *TESS*, the `TTF` output was saved to `.csv` files and then scored using an `IDL` routine according to how well they aligned with our niche (Crouzet et al. in prep). Airmass plots were then generated to highlight when in the night the transits would happen, and the information was saved to `.pdf` files which were then circulated to the team in advance of our weekly target selection meetings. Targets selected for observation each night were recorded in a Google Doc[30] which was shared with the team.

Both elements of this initial system were limited. The generation of the `.pdf` files required that each team member check the Google Drive for new files on a weekly basis. Our use of a Google Doc to record the upcoming schedule also rapidly became time consuming; additionally, the important information contained therein was vulnerable as the whole team had access. Finally, manual input of information meant that small inaccuracies could cause us to miss important observations.

The earliest incarnations of the system we use now harnessed the G-Suite[30] `Python` APIs (Application Programming Interfaces) to read and write information to a Google Sheet instead of a Google Doc. G-Suite provides excellent collaborative working tools for international teams such as ours, but limiting vulnerability of underlying data while ensuring everyone could access crucial information became a top priority. We also found that time could be saved generating the airmass plots by making use of the `TTF` API rather than manually downloading the output.

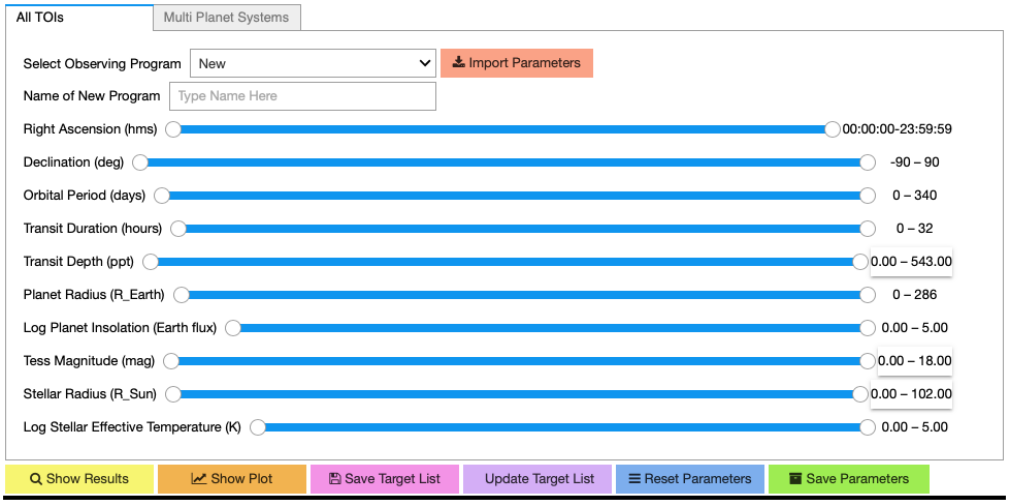


Figure 4. Screenshot of the graphical user interface for the target selection toolkit.

One final limitation we encountered was that most our transit observations were opportunistic. Moving forward, the ambition was to define cohesive observing programs of scientific interest to the team.

3.2 Current Systems

The system we have implemented since the start of the 2021 observing season consists of three components: a Google Sheet; a `Python` toolkit; and a website. Each of these elements and their key functions are described in the sections that follow. The interconnections between all three elements of the toolkit are summarised in Fig. 3.

3.2.1 Generating the data: `Python` toolkit

As described above, one of ASTEP's key goals that emerged from the 2020 observing season was to define a list of targets that were of particular scientific interest to us. With an ever-growing list of candidates emerging on a monthly basis from *TESS*, there was a need for a simple way to filter through the list of TOIs (*TESS* Objects of Interest) to find those best suited to our unique context. This motivated the development of our `TESS_target_list` tool, written in `Python` and used via a `Jupyter Notebook` with an `ipywidgets` GUI. This simple tool makes use of intuitive sliders and dropdown lists to make target lists based on user-selected parameters. We present a screenshot of the `TESS_target_list` tool in Fig. 4.

With pre-selected target lists now in place, a vast amount of scheduling can be done ahead of time. Computing the timings of upcoming transits using linear ephemerides is trivial, however the `Python` package `astroplan`[27] does this with elegance and simplicity. Not only can it compute the timings of upcoming events for eclipsing systems, both stellar and planetary in nature, but it will also output observability of said events for different observatories.

Leveraging both `astroplan` and the Google Sheets `Python` API, we developed the scheduler: `schedule_ahead`. This software reads the target list directly from a 'Master Target List' located on a Google Sheet (see Fig. 3) and imports the stellar coordinates and orbital ephemerides for each of the targets, provided they have an 'Observe' status of *'Active'*. User inputs are an observatory (ASTEP, in this case), a start date, and a number of days to schedule for; these are combined with the system parameters from the target list and fed into `astroplan`. Only events where at least one of ingress and egress are observable are then output. The user then has the option of pushing the outputs to the 'Schedule' Google Sheet and the 'Web Schedule'; the latter will be described in Section 3.2.3.

Before running the scheduler each week, there is the option to update the transit ephemerides of candidates in our target list by checking the `TTF`. This ensures that refinements resulting from other teams' observations are

included, but crucially it tells us if a candidate has been retired as a false positive, i.e. it has been conclusively shown not to be a planet.

Our nights are very seldom filled perfectly with pre-scheduled events; in fact there are often multiple events overlapping in one night and a decision has to be made about what should be observed (see Section 3.2.3). Additionally, the schedule often has large gaps (see Fig. 6) that can be filled with our pre-selected filler targets or opportunistic observations of transits. In order to facilitate the latter, we use a custom `Python` script to search the *TESS* `Transit Finder`[29] for transits of *TESS* candidates within a given date range. The results of the search are then scored according to how well each target suits our scientific interests, and airmass plot data are computed for the top 30 events using `astropy`.[31,32] These data, along with system parameters of interest, are stored in the Google Sheet. This script therefore completely replaces the `IDL` script which generated the `.pdf` files.

3.2.2 Holding the data: Google Sheet

The team's Google Sheet holds all the underlying data generated by the `Python` toolkit, and updated and read by the website, as shown in Fig. 3: the target list, the schedule, the airmass plot data, and the team's thoughts.

The Master Target List contains host star parameters, transit ephemerides and `TTF` meta-data (such as observing notes) for each target we have chosen to observe. The data for this sheet are generated by our `TESS_target_list` tool, and updated by the ephemerides checking script before running the scheduler each week. Targets are grouped into observing programs and are each given an 'Observe' status: *'Active'*, *'Standby'* or *'Retired'*. This flag is read by the scheduler and can be updated manually or programmatically.

The observation schedule is saved in two worksheets; one is human readable with observation and event timings in ISO format, while the other is intended to be read by the graphical web schedule and has timings in UNIX format. The former is also used to display the schedule in tabular form on the website.

As described above, the data for airmass plots of potentially interesting targets are generated via a `Python` script; these data are then stored in their own worksheet to be read by the website. The information contained therein is not intended to be human readable, therefore the worksheet is not formatted and has no headers. Data from previous weeks are cleared once observations have taken place to make the Google Sheet load quickly.

Once the data for the airmass plots have been generated in advance of a weekly meeting, the upcoming events can be viewed on the website on the target selection page. In order to facilitate fruitful discussions during the meeting, there is a box where team members can add their preferences and thoughts for upcoming scheduling. These thoughts are stored on the Google Sheet to be displayed in the appropriate place on the website.

3.2.3 Displaying the data: The website

For effective collaborative working in an international team, it is essential that everyone can access all the information in a convenient way. In addition, Google Sheets are handy but can be easily altered mistakenly. With this in mind, we developed a website for the ASTEP team using `HTML, CSS` and `JavaScript`.

The essential feature the website provides is access to data (see Fig. 3), and this is done via DataTables*, a `JavaScript` package for interactive `HTML` tables. Information from each of the Google Sheets is fed in as `JSON`. As a result team members can access fully paginated, searchable and sortable `HTML` tables. These tables can also be exported in four formats; a screenshot of the schedule as displayed in a DataTable is presented in Fig. 5.

In the hope of making the website experience as user-friendly as possible, we developed an interactive graphical view of the schedule using the `JavaScript` plotting package Highcharts†. In Fig. 6 we present a screenshot of this schedule view. The green bars represent the available observing time each night, defined as the time between the start of the evening civilian twilight and the end of the morning civilian twilight, where the sun is at 6° below the horizon. Scheduled events are shown as purple bars, which change to red for any portion of the event that is not during the night. Hovering over an event with the mouse displays the target name, the event timings,

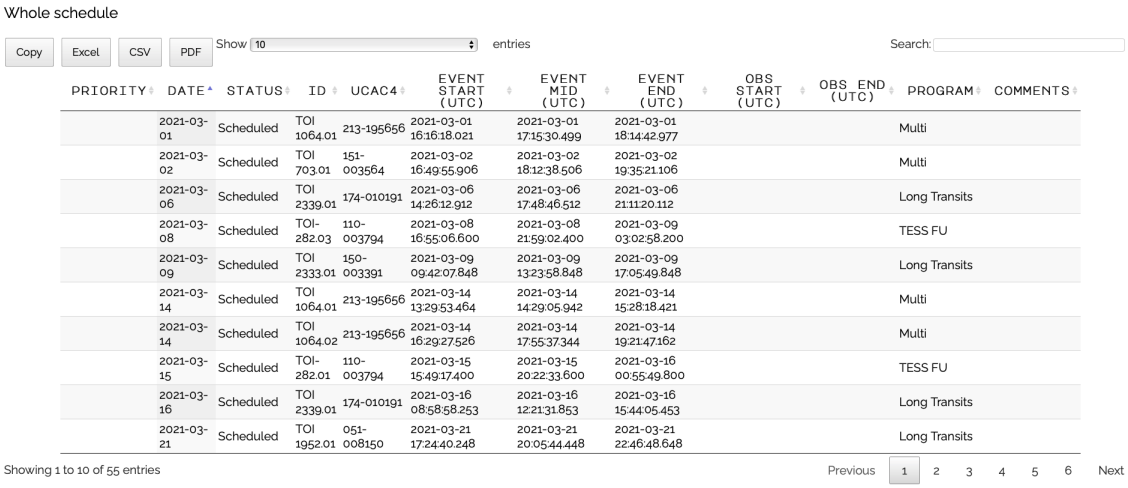


Figure 5. Screenshot of the DataTables display of the schedule as it appears on the ASTEP website.

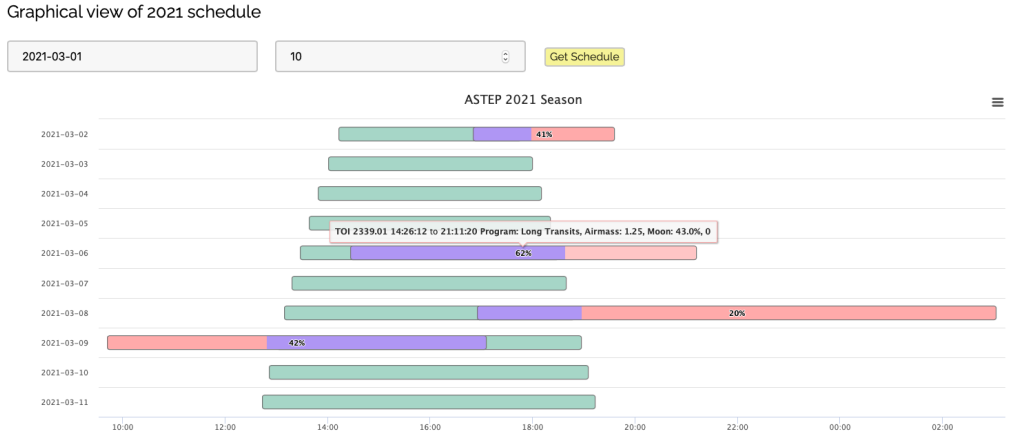


Figure 6. The graphical web schedule, showing user inputs and options. When the cursor is hovered over an observation bar, the tooltip shows the name of the target and the timing of the event, as well as the airmass and moon illumination during the event.

the observing program the target belongs to, the airmass at the time of mid-transit, and the percentage of moon illumination. All of these features allow for simple choices to be made when events clash.

As described in Sections 3.2.1 and 3.2.2, we sought to incorporate all the most useful elements of the airmass plot `.pdf` files into our new system. To this end, we included the Target Selection page in the website, which displays the airmass plots for the top 30 scored transiting candidates from the `TTF`. We also see all the pre-scheduled events, allowing us to choose which observations allow us to make best use of the available time each night. Opportunistic observations can then be scheduled directly from this page and sent to the Google Sheet, removing any need for manual input.

3.3 Future Direction

During the 2021 observing season the version of the Google Sheets API we were using was unexpectedly retired, causing our entire toolkit to stop working. Upgrading to the new version of the API took approximately two weeks, during which time we had to revert to manual target selection. With this in mind, we aspire to phase out our use of G-Suite in future. This will be achieved by storing our data in databases as they can be easily written

[*] https://datatables.net
[†] https://www.highcharts.com

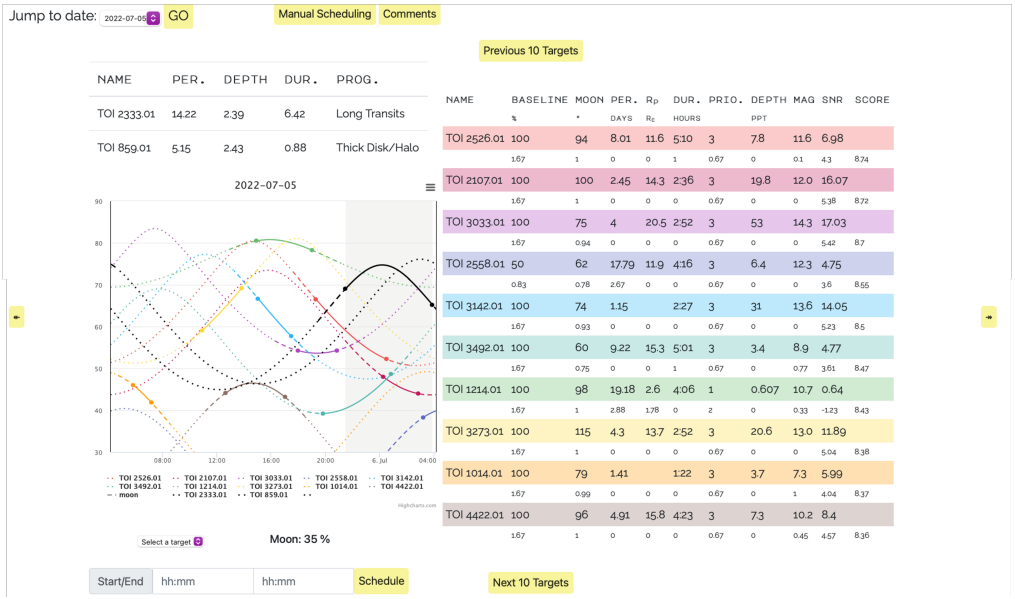


Figure 7. Screenshot of the `JavaScript` target selection toolkit as it appears on the website, with the layout adapted from Crouzet et al. (in prep). Interactive airmass plots are displayed on the left, and information for potential targets is shown on the right. Targets can be selected from the dropdown list and then scheduled with the 'schedule' button.

to and read by `Python` and web-based applications. The use of databases will therefore eliminate the need for a Google Sheet to store our data and the Sheets API to read/write information.

A further limitation which we will seek to address is that the full `Python` toolkit is locally stored and run on one team member's computer. This will be improved in future by using a `Python`-based web framework such as Django* or Flask† to fully embed the toolkit in the website. This will allow all of the scripts to be run by anyone, from anywhere, at any time.

4. DATA ANALYSIS PIPELINE

With our science goals shifting towards the competitive and fast-moving field of *TESS* follow-up, the need for a fast automatic pipeline has grown. It's especially important for the pipeline data products to be as close as possible to the format needed for submission to ExoFOP in order to minimise the time spent in post-processing. Additionally, we want our data products to be versatile enough that we are able to extract additional information from our images without the need for full reprocessing, such as lightcurves of other stars detected in the field. Finally, as our team has grown to include collaborators from other astronomical sub-fields, there has been a growing need to produce one flexible data product that can be handled by others without the need for context-specific coding experience.

In this section, we will first describe in brief the `IDL` pipeline that has served ASTEP for the past six years, followed by a detailed description of the new `Python` pipeline in Section 4.2.

4.1 `IDL` Pipeline

The `IDL` data process pipeline, only briefly described here (see Abe et al. 2013[6] for a complete description) is a custom `IDL` code using classical aperture photometry routines from the well-known `IDL` astronomical library. Each science exposure frame is bias subtracted, dark corrected and the astrometric solution is computed using reference stars from the UCAC4 catalogue. Photometric lightcurves of about 1,000 stars are then performed through 10 fixed circular apertures radii. The optimal calibrated lightcurve is then extracted using a set of

*https://www.djangoproject.com
†https://flask.palletsprojects.com/en/2.1.x/

comparison stars. This pipeline has served its purpose well and has allowed ASTEP to contribute to many publications since we joined TFOP in 2020[12,13,16,17] plus lead our own discovery paper[21] with several others in preparation (Abe et al.in prep., Schmider et al. in prep., Triaud et al. in prep.). However, the cost of `IDL` and its declining usage means that maintenance of the pipeline is becoming highly specialised knowledge. Thus the need for a pipeline which is fast, modular and in a popular programming language: `Python`.

4.2 `Python` Pipeline

Rather than starting to develop the pipeline from scratch, we chose to build the pipeline around an astronomical data processing package written with *TESS* follow-up in mind: `prose`.

`prose`* is an open-source `Python` package dedicated to astronomical image processing.[33] By featuring a wide range of pre-implemented processing blocks (from source detection to photometric extraction), it provides a framework to quickly assemble instrument-agnostic pipelines that are modular and easy to maintain. `prose` is supplemented by convenient tools to manage and share the products of astronomical observations, such as the automatic generation of *TESS* follow-up reports, making it an ideal base for the new ASTEP+ pipeline.

In the following sections, describe the blocks and functionalities that form the core of the ASTEP+ pipeline, including custom modifications from the base `prose` package. For a more comprehensive description of `prose`, we direct the reader to the work where the package was first presented[33] and its online documentation†

4.2.1 Image Calibration

We based ASTEP+'s pipeline on the `prose` default photometric pipeline, which can be decomposed in two steps: The calibration and alignment of all images to produce a high-SNR stack image of the complete observation; And the extraction of the fluxes from the brightest stars in the field, using a wide range of size-varying apertures. The calibration sequence starts with the selection of a reference image, on which n reference stars are detected, later used to align the rest of the science images on. Then, each raw image sequentially go through bias, dark and flat calibrations, before being trimmed for overscan pixels. For each image, the n brightest stars are detected and compared to the reference ones in order to compute the affine transformation to the reference image. This is done using `twirl` ‡ (a simplified `Python` implementation of `Astrometry.net`[34]). Finally, a stack image is created from the aligned images (transformed using bi-linear interpolation), while the unaligned calibrated images are saved to perform aperture photometry on.

4.2.2 Aperture Photometry

Two sequences are used in `prose` to perform aperture photometry on the calibrated images. The first sequence sets the number of stars to be detected on the stack image to 1000. This ensures the detection of the target star even in crowded fields using the DAOFindStars block based on a `photutils`§ implementation of DAOPHOT. An elliptical two-dimensional Moffat model of the stack effective PSF is fitted in order to scale the photometric aperture radii. A total of forty circular apertures is used to extract the flux of all the detected stars in the following sequence. The position of the apertures on each calibrated image is calculated using the inverse transformation matrix computed in the calibration step. To correct for possible errors in these coordinates, the positions of the apertures are recomputed using the centroiding algorithm `Ballet`¶, a convolutional neural network trained to predict accurately centroid positions. The flux is then extracted for each aperture and stored in a `.phot` file along with the values of systematic effects affecting the observation (position shifts on the detector, sky background, airmass and FWHM).

*https://github.com/lgrcia/prose
†https://lgrcia.github.io/prose-docs/build/html/index.html
‡https://github.com/lgrcia/twirl
§https://photutils.readthedocs.io/en/stable/index.html
¶https://github.com/lgrcia/ballet

4.2.3 Plate Solving and Target Identification

`prose` requires human intervention for the purpose of target selection on the stacked image; in order to automate this step we implement a local installation of `Astrometry.net`.[34] `Astrometry.net` is a robust and widely used system to provide blind plate solving of astronomical images. It works by extracting several patterns of four stars (asterisms) from query images, computing a hash code for each, and searching indexes for matching hash codes. The result is the WCS (World Coordinate System) header information providing the pointing, scale and orientation of the query image.

Index files have been produced for many astronomical surveys in various colours. To ensure the best coverage, providing the best chance of an astrometric solution, we use the full set of *Gaia* and *2MASS* index files.*

Unlike the `IDL` pipeline, the new pipeline only requires that we plate solve the stack image as the field rotation between each image is calculated by the `twirl` block by `prose` during the calibration stage of the pipeline.

ASTEP+'s images are centered on the guide star, and its coordinates, together with the image pixel scale determined by the astrometric solution, are used to define a search cone. Under normal operation a call would be made to MAST (Barbara A. Mikulski Archive for Space Telescopes) via `astroquery`[35] to find all stars in this cone for a given catalog. In order to remove this need, we instead make use of a local version of the *TESS* Input Catalog (TIC),[36] saved in an `SQLite` database, to perform the search. The WCS header information is then used to transform celestial coordinates into pixel coordinates, and the closest aperture to the target is selected.

The decision to move toward using the latest version of the TIC as our main reference catalog instead of UCAC4[37] was motivated by its completeness. Version 8 of the TIC includes all UCAC4 sources, as well as *Gaia* DR2 sources and several other large catalogs, making it the most complete catalog currently available.

4.2.4 Differential Photometry

Differential light curves are built from raw light curves using the algorithm presented in Broeg et al. 2005[38] (implemented in `Python` within `prose`). This method consists of building an artificial comparison light curve using the weighted sum of all available stars in the field. The weight attributed to each star is computed through an iterative process that favours stars displaying lower variability and higher signal-to-noise ratio, more likely to feature systematic signals. The optimal aperture is then chosen as the one minimising the white noise estimated using the median standard deviation of points per five minute bins. All the light curves for each aperture are also stored in the `.phot` file allowing for a manual check if needed.

4.2.5 Lightcurve Modelling

With the `IDL` pipeline, the biggest interaction required in post-processing has always been the modelling of lightcurves after they arrived in Europe. However, there are many simple cases where the detected transit matches the ephemerides well; to save time for these objects, we have written a new module for `prose`: `auto_modelling`.

All our lightcurves are correlated with airmass and background sky level. Additionally, variations in the FWHM (the full width at half maximum) can introduce spurious signals to the data. For this reason, all lightcurves are detrended by fitting an order two polynomial of time simultaneously to airmass, FWHM and the background sky level. This is done at the same time as the transit modelling. There are sometimes additional signals in the data caused by motion of the telescope in the night (dx and dy). Rather than detrend on these parameters, we reject any images where either of these parameters are greater than 5.

Transit fitting is implemented using `exoplanet`,[39] a flexible toolkit for modelling exoplanets using `PyMC3`[40] for MCMC (Markov Chain Monte Carlo) modelling. Priors on the transit parameters are taken from the image headers, while host star priors are drawn from the local TICv8 database. In cases where the stellar T_{eff}, [Fe/H] and logg are available, quadratic limb darkening coefficients are also calculated using `PyLDTK`.[41] These are then set as normal priors for the fit; where host data is not available, solar values of stellar mass and radius are used instead. In these cases uniform priors between $0 - 1$ are used for the limb darkening coefficients.

The automatic lightcurve modelling is not always successful. The most common reasons for failure are missing host star parameters, ambiguous detections and non-detections of transits, and transit timing variations (TTVs). In all these cases, manual post-processing is carried out after files have arrived on the server in Europe.

*Available for download from `http://data.astrometry.net`

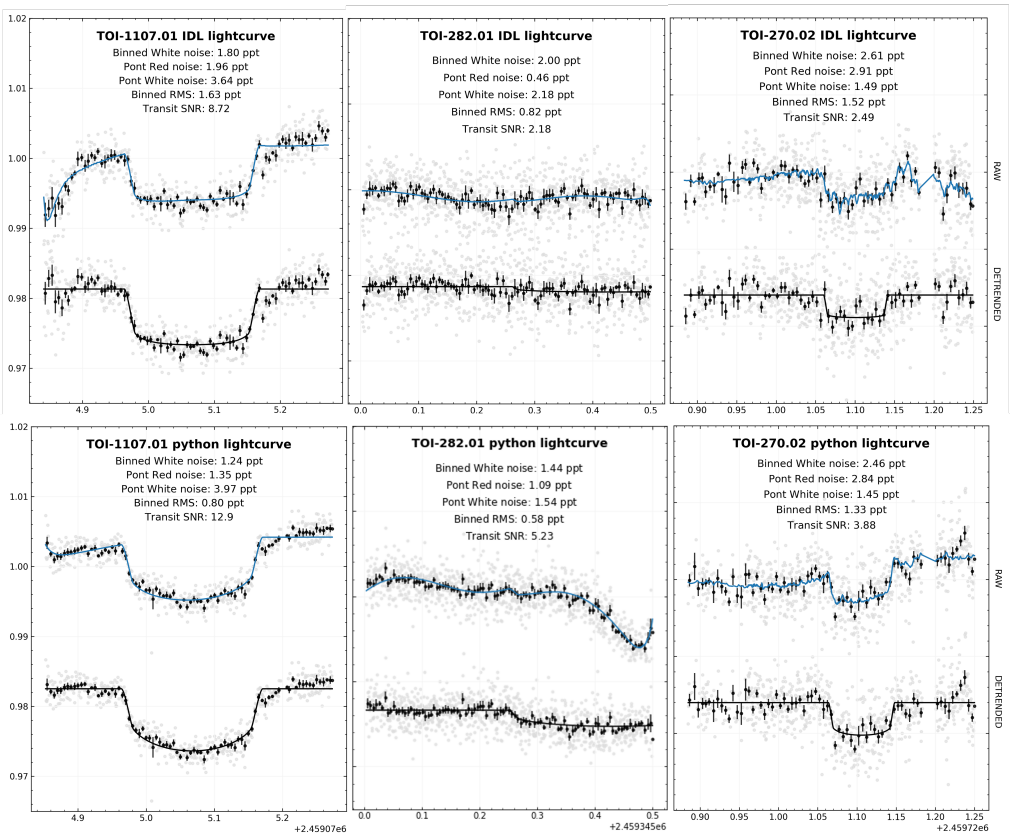


Figure 8. Comparison of lightcurves produced by the two pipelines. The upper panels show the lightcurves produced by the new `IDL` pipeline, while the lower panels show the results of the `Python` pipeline. Grey points are normalised fluxes and black points are binned in 5 minute bins. The upper lightcurves are raw fluxes with the blue line indicating the systematics + transit model. The bottom lightcurves have had the systematics trend removed. Left panels: observation of TOI-1107.01 on 13 August 2020. Middle panels: observation of TOI-282.01 (now HD 28109 b) on 10 May 2021. Right panels: observation of TOI-270.02 (now TOI-270 d) on 21 May 2022.

4.2.6 Delivery of Data Products

As described in Section 1, one of the biggest limitations that comes with an Antarctic telescope is the very limited internet connection. This is of course the motivation for our automatic data processing on-site, but it also limits how we access the data products output by the pipeline.

The data products produced by the pipeline fall into two categories: lightweight and heavyweight. Lightweight data products include a `.png` image of the target lightcurve and a `.csv` file containing the target flux and systematics. These products are emailed to all team members immediately after the pipeline finishes running to facilitate rapid inspection. In cases where the automatic lightcurve modelling and detrending has been successful, these two products are all that is needed.

The largest data products are the .phot files containing the aperture photometry for up to 1000 stars in the field as well as all the metadata for the observation, and the stack image produced during the reduction. These files are sent to a local server in Concordia using the `Python` package `paramiko`*; this server has a folder which synchronises with a corresponding folder on a server in Rome. Depending on the size of the files, they take between $12-24$ hours to arrive in Europe; they are then available for download for any necessary post-processing.

4.3 Results

In this section we compare the outcomes of the two pipelines, making quantitative comparisons where appropriate.

4.3.1 Noise and SNR comparison

Following the method described in Garcia et al. (2022),[33] we compare the automatic lightcurves produced by the `Python` and `IDL` pipelines using four metrics: the binned white noise, the white and red noise following Pont et al. (2006),[42] and the transit signal-to-noise ratio (SNR). All lightcurves used for the comparison were detrended by fitting a polynomial in time to the airmass and background sky level only; we then modelled each transit by fitting a simple Keplerian orbit using `exoplanet`. In all comparison cases, we placed uniform priors of $\mathcal{U}(0-1)$ on quadratic limb darkening coefficients. Using the resulting transit models, we also compare the binned root mean square (RMS) scatter of the lightcurves, calculated as the standard deviation of the binned residuals. The results of our comparison are presented in Fig. 8.

The left-hand panels of Fig. 8 show a deep (9 ppt) transit observed during the 2020 season. Upon visual inspection, we see that there is less scatter in the `prose` lightcurve than in the `IDL` plot, resulting in almost 1.5 x higher SNR detection. We also see the effects of the stellar limb darkening more clearly in the transit shape of the `prose` lightcurve.

In the middle two panels of Fig. 8 we present a detection of the shallow (0.85 ppt) transit of TOI-282.01 (now HD 28109 b[21]) observed during the 2021 observing season. This system has large TTVs (transit timing variations) and the detected transit ingress was $\sim$ 72 mins later than expected. We can see that while the `IDL` pipeline does not clearly detect the transit, the `prose` lightcurve has binned RMS scatter smaller than the transit depth, allowing for a conclusive detection of the event despite the large TTV.

In the right-hand panels of Fig. 8 we present the lightcurves of TOI-270.02, as observed in May of the current (2022) season. This planet is part of a three planet system where all planets find themselves in commensurate orbits leading once again to TTVs. As TTVs can be used to estimate planetary masses, ASTEP+ has a crucial role to play by measuring precise transit timings when systems are no longer visible from other southern observatories. Fig. 8 shows that the new pipeline can yield more precise timings through higher SNR detections of transits.

4.3.2 Processing time

One of the most important considerations for science carried out in Antarctica is energy usage. Concordia generates electricity using two diesel generators with a third available in case of emergencies or malfunctions. Fuel for the generators reaches the station by traverse: a convoy of tractors pulling containers on skis, which crosses $\sim$ 1300 km of ice over the course of $10-12$ days. Additionally, we must consider the greenhouse gas emissions resulting from computation. Each litre of diesel used by a generator emits $2.4-3.5$ kg of CO_2.[43]

On average, the `IDL` pipeline takes approximately 6 seconds per image to run in full, while the new `Python` pipeline takes 1.6 seconds. The addition of a second camera means that the pipeline will run for approximately twice as long, depending on the exposure times of the images in the respective colours. Even running the pipeline in full twice, our server will now spend half the time running intensive processes per day, therefore increasing CPU idle time. On average, power usage is increased threefold during computationally intensive processes when compared with idle time*, and with it the carbon footprint of the pipeline.

4.4 Limitations & Future Work

The biggest limitaiton we currently face with the `prose` pipeline is that we cannot yet process very defocused observations where the PSF (point spread function) is donut shaped. This does not present a huge problem in the current season as we have paused our observations of β Pictoris, but should we return to observing this very bright target it will become necessary to defocus the telescope once again. When the pipeline is updated during the next summer service mission, we intend to test new defocused PSF modelling blocks in order to ensure these observations can be processed in future.

*https://www.paramiko.org

*https://wccftech.com/review/intel-core-i9-9900k-8-core-cpu-z390-aorus-master-review/9/?beta=1

5. ASTEP+ IN THE FUTURE

At the moment ASTEP+ is mainly pursuing the validation of *TESS* transiting exoplanet candidates. Most of the easy pickings have been detected, and *TESS* will increasingly produce long period planets, candidates on fainter stars, or small planets producing weaker events. Whilst ASTEP+ is well geared towards the validation of longer orbital periods, there will be few targets and events are few and far in-between. This means that the ASTEP+ project will need to evolve. We are currently investigating photometric monitoring in coordination with X-ray satellites such as XMM, Chandra, AstroSat, for the study of flaring stars.[44] Of course, the monitoring of known transiting exoplanets will have to continue in order to refine the ephemerides and plan observations by programs such as JWST and Ariel as efficiently as possible.[45]

Another activity we are keen on pursuing is to repeatedly detect the transits of planetary systems where at least two planets have orbital periods near an integer ratio. This configuration means their gravitational interaction are detectable (producing Transit Timing Variations, TTVs), and would allow us to measure the planet's masses such as done already in papers where ASTEP observations were crucial.[17,21] In addition, ASTEP+ has produced the first ground-based detection of a circumbinary planet transit (Triaud et al. in prep). To support this science, measuring Eclipse Timing Variations (ETVs) produced by the eclipsing binary stars at centre of such system is also a source of information about the planets. In both science cases, all transits/eclipses are useful. Our unique position near the pole and opposite from Chile means we can collect a high yield of events using similar arguments to those described in Section 2.

In addition, we are currently developing a new dedicated direct-drive mount adapted to Antarctic conditions. This should maximize observation efficiency and pointing stability, thereby producing higher quality lightcurves. With this mount, we intend to check whether some transients are detectable, and test a rapid response mode to detect the electromagnetic counterparts of Gravitational Wave events, or be used has to follow up observations where a transient detected by the Vera Rubin telescope (in Chile) has set as seen from their location, but is still visible from our location thanks to our proximity to the South Pole. We are also investigating the possibility to search for and detect interstellar asteroids within the frames obtained during exoplanet transit observations. The idea is to leverage the fact that our field of view is mainly out of the ecliptic. Anything that moves is less likely to be from the Solar system.

The highest potential of Astronomy at Concordia however lies with observations in the infrared, particularly in the K band. As for the high plateaus of Antarctica in general, Concordia is characterized by a high sky transparency, low water content and low thermal background that makes it one of the best sites on Earth for infrared Astronomy.[46] Combining observations in the visible with ASTEP+ to observations in the infrared with a new telescope of a similar aperture could provide a real breakthrough for the monitoring of exoplanetary atmospheres and exoplanets around low-mass stars and for the study of counterparts of gravitational wave events.

6. CONCLUSIONS

In this work we have presented a suite of tools developed for scheduling time-domain astronomical observations. While these systems have been written with ASTEP+ in mind, they are easily adaptable for other observatories focused on observations with strong time constraints.

We have also presented a new automatic data analysis pipeline written in `Python` and built around `prose`. The new pipeline produces lightcurves that on average have lower red and white noise, lower scatter, and therefore allow for transits to be detected with higher SNR compared with the system it replaces. Additionally, as the pipeline runs significantly faster we will also decrease our energy usage and carbon footprint resulting from computationally intensive reductions. This remains true even taking into account the increase in data generated by having two cameras instead of one.

Finally, we have outlined the future directions for the ASTEP+ project, including new collaborations and synergies at the forefront of time-domain astronomy.

ACKNOWLEDGMENTS

This research is in part funded by the European Union's Horizon 2020 research and innovation programme (grants agreements n° 803193/BEBOP), and from the Science and Technology Facilities Council (STFC; grant n° ST/S00193X/1). We acknowledge support from the European Space Agency (ESA) through the Science Faculty of the European Space Research and Technology Centre (ESTEC). ASTEP and ASTEP+ have benefited from the support of the French and Italian polar agencies IPEV and PNRA, and from INSU, ESA through the Science Faculty of the European Space Research and Technology Centre (ESTEC), the University of Birmingham, the laboratoire Lagrange (CNRS UMR 7293) and the Université Côte d'Azur through Idex UCAJEDI (ANR-15-IDEX-01). This publication benefits from the support of the French Community of Belgium in the context of the FRIA Doctoral Grant awarded to Mathilde Timmermans and Lionel J. Garcia. MNG acknowledges support from the European Space Agency (ESA) as an ESA Research Fellow.

REFERENCES

[1] Fressin, F., Guillot, T., Schmider, F. X., Agabi, A., Moutou, C., Aigrain, S., Bouchy, F., Boer, M., Pont, F., Erikson, A., Rauer, H., and A Step Team, "A STEP: Towards a Large Photometric Survey for Exoplanets at Dome C," in [*EAS Publications Series*], Epchtein, N. and Candidi, M., eds., *EAS Publications Series* **25**, 225–232 (Jan. 2007).

[2] Daban, J.-B., Gouvret, C., Guillot, T., Agabi, A., Crouzet, N., Rivet, J.-P., Mekarnia, D., Abe, L., Bondoux, E., Fanteï-Caujolle, Y., Fressin, F., Schmider, F.-X., Valbousquet, F., Blanc, P.-E., Le van Suu, A., Rauer, H., Erikson, A., Pont, F., and Aigrain, S., "ASTEP 400: a telescope designed for exoplanet transit detection from Dome C, Antarctica," in [*Ground-based and Airborne Telescopes III*], Stepp, L. M., Gilmozzi, R., and Hall, H. J., eds., *Society of Photo-Optical Instrumentation Engineers (SPIE) Conference Series* **7733**, 77334T (July 2010).

[3] Guillot, T., Abe, L., Agabi, A., Rivet, J. P., Daban, J. B., Mékarnia, D., Aristidi, E., Schmider, F. X., Crouzet, N., Gonçalves, I., Gouvret, C., Ottogalli, S., Faradji, H., Blanc, P. E., Bondoux, E., and Valbousquet, F., "Thermalizing a telescope in Antarctica - analysis of ASTEP observations," *Astronomische Nachrichten* **336**, 638 (Sept. 2015).

[4] Crouzet, N., Guillot, T., Agabi, A., Rivet, J. P., Bondoux, E., Challita, Z., Fanteï-Caujolle, Y., Fressin, F., Mékarnia, D., Schmider, F. X., Valbousquet, F., Blazit, A., Bonhomme, S., Abe, L., Daban, J. B., Gouvret, C., Fruth, T., Rauer, H., Erikson, A., Barbieri, M., Aigrain, S., and Pont, F., "ASTEP South: an Antarctic Search for Transiting ExoPlanets around the celestial south pole," *Astronomy & Astrophysics* **511**, A36 (Feb. 2010).

[5] Crouzet, N., Chapellier, E., Guillot, T., Mékarnia, D., Agabi, A., Fanteï-Caujolle, Y., Abe, L., Rivet, J. P., Schmider, F. X., Fressin, F., Bondoux, E., Challita, Z., Pouzenc, C., Valbousquet, F., Bayliss, D., Bonhomme, S., Daban, J. B., Gouvret, C., and Blazit, A., "Four winters of photometry with ASTEP South at Dome C, Antarctica," *Astronomy & Astrophysics* **619**, A116 (Nov. 2018).

[6] Abe, L., Gonçalves, I., Agabi, A., Alapini, A., Guillot, T., Mékarnia, D., Rivet, J. P., Schmider, F. X., Crouzet, N., Fortney, J., Pont, F., Barbieri, M., Daban, J. B., Fanteï-Caujolle, Y., Gouvret, C., Bresson, Y., Roussel, A., Bonhomme, S., Robini, A., Dugué, M., Bondoux, E., Péron, S., Petit, P. Y., Szulágyi, J., Fruth, T., Erikson, A., Rauer, H., Fressin, F., Valbousquet, F., Blanc, P. E., Le van Suu, A., and Aigrain, S., "The secondary eclipses of WASP-19b as seen by the ASTEP 400 telescope from Antarctica," *Astronomy & Astrophysics* **553**, A49 (May 2013).

[7] Mékarnia, D., Guillot, T., Rivet, J. P., Schmider, F. X., Abe, L., Gonçalves, I., Agabi, A., Crouzet, N., Fruth, T., Barbieri, M., Bayliss, D. D. R., Zhou, G., Aristidi, E., Szulagyi, J., Daban, J. B., Fanteï-Caujolle, Y., Gouvret, C., Erikson, A., Rauer, H., Bouchy, F., Gerakis, J., and Bouchez, G., "Transiting planet candidates with ASTEP 400 at Dome C, Antarctica," *Monthly Notices of the Royal Astronomical Society* **463**, 45–62 (Nov. 2016).

[8] Mékarnia, D., Chapellier, E., Guillot, T., Abe, L., Agabi, A., De Pra, Y., Schmider, F. X., Zwintz, K., Stevenson, K. B., Wang, J. J., Lagrange, A. M., Bigot, L., Crouzet, N., Fanteï-Caujolle, Y., Christille, J. M., and Kalas, P., "The δ Scuti pulsations of β Pictoris as observed by ASTEP from Antarctica," *Astronomy & Astrophysics* **608**, L6 (Dec. 2017).

[9] Lagrange, A. M., Meunier, N., Rubini, P., Keppler, M., Galland, F., Chapellier, E., Michel, E., Balona, L., Beust, H., Guillot, T., Grandjean, A., Borgniet, S., Mékarnia, D., Wilson, P. A., Kiefer, F., Bonnefoy, M., Lillo-Box, J., Pantoja, B., Jones, M., Iglesias, D. P., Rodet, L., Diaz, M., Zapata, A., Abe, L., and Schmider, F.-X., "Evidence for an additional planet in the β Pictoris system," *Nature Astronomy* **3**, 1135–1142 (Aug. 2019).

[10] Kenworthy, M. A., Mellon, S. N., Bailey, J. I., Stuik, R., Dorval, P., Talens, G. J. J., Crawford, S. R., Mamajek, E. E., Laginja, I., Ireland, M., Lomberg, B., Kuhn, R. B., Snellen, I., Zwintz, K., Kuschnig, R., Kennedy, G. M., Abe, L., Agabi, A., Mekarnia, D., Guillot, T., Schmider, F., Stee, P., de Pra, Y., Buttu, M., Crouzet, N., Kalas, P., Wang, J. J., Stevenson, K., de Mooij, E., Lagrange, A. M., Lacour, S., Lecavelier des Etangs, A., Nowak, M., Strøm, P. A., Hui, Z., and Wang, L., "The β Pictoris b Hill sphere transit campaign. I. Photometric limits to dust and rings," *Astronomy & Astrophysics* **648**, A15 (Apr. 2021).

[11] Ricker, G. R., Winn, J. N., Vanderspek, R., Latham, D. W., Bakos, G. Á., Bean, J. L., Berta-Thompson, Z. K., Brown, T. M., Buchhave, L., Butler, N. R., Butler, R. P., Chaplin, W. J., Charbonneau, D., Christensen-Dalsgaard, J., Clampin, M., Deming, D., Doty, J., De Lee, N., Dressing, C., Dunham, E. W., Endl, M., Fressin, F., Ge, J., Henning, T., Holman, M. J., Howard, A. W., Ida, S., Jenkins, J. M., Jernigan, G., Johnson, J. A., Kaltenegger, L., Kawai, N., Kjeldsen, H., Laughlin, G., Levine, A. M., Lin, D., Lissauer, J. J., MacQueen, P., Marcy, G., McCullough, P. R., Morton, T. D., Narita, N., Paegert, M., Palle, E., Pepe, F., Pepper, J., Quirrenbach, A., Rinehart, S. A., Sasselov, D., Sato, B., Seager, S., Sozzetti, A., Stassun, K. G., Sullivan, P., Szentgyorgyi, A., Torres, G., Udry, S., and Villasenor, J., "Transiting Exoplanet Survey Satellite (TESS)," *Journal of Astronomical Telescopes, Instruments, and Systems* **1**, 014003 (Jan. 2015).

[12] Bouma, L. G., Hartman, J. D., Brahm, R., Evans, P., Collins, K. A., Zhou, G., Sarkis, P., Quinn, S. N., de Leon, J., Livingston, J., Bergmann, C., Stassun, K. G., Bhatti, W., Winn, J. N., Bakos, G. Á., Abe, L., Crouzet, N., Dransfield, G., Guillot, T., Marie-Sainte, W., Mékarnia, D., Triaud, A. H. M. J., Tinney, C. G., Henning, T., Espinoza, N., Jordán, A., Barbieri, M., Nandakumar, S., Trifonov, T., Vines, J. I., Vuckovic, M., Ziegler, C., Law, N., Mann, A. W., Ricker, G. R., Vanderspek, R., Seager, S., Jenkins, J. M., Burke, C. J., Dragomir, D., Levine, A. M., Quintana, E. V., Rodriguez, J. E., Smith, J. C., and Wohler, B., "Cluster Difference Imaging Photometric Survey. II. TOI 837: A Young Validated Planet in IC 2602," *The Astronomical Journal* **160**, 239 (Nov. 2020).

[13] Dawson, R. I., Huang, C. X., Brahm, R., Collins, K. A., Hobson, M. J., Jordán, A., Dong, J., Korth, J., Trifonov, T., Abe, L., Agabi, A., Bruni, I., Butler, R. P., Barbieri, M., Collins, K. I., Conti, D. M., Crane, J. D., Crouzet, N., Dransfield, G., Evans, P., Espinoza, N., Gan, T., Guillot, T., Henning, T., Lissauer, J. J., Jensen, E. L. N., Sainte, W. M., Mékarnia, D., Myers, G., Nandakumar, S., Relles, H. M., Sarkis, P., Torres, P., Shectman, S., Schmider, F.-X., Shporer, A., Stockdale, C., Teske, J., Triaud, A. H. M. J., Wang, S. X., Ziegler, C., Ricker, G., Vanderspek, R., Latham, D. W., Seager, S., Winn, J., Jenkins, J. M., Bouma, L. G., Burt, J. A., Charbonneau, D., Levine, A. M., McDermott, S., McLean, B., Rose, M. E., Vanderburg, A., and Wohler, B., "Precise Transit and Radial-velocity Characterization of a Resonant Pair: The Warm Jupiter TOI-216c and Eccentric Warm Neptune TOI-216b," *The Astronomical Journal* **161**, 161 (Apr. 2021).

[14] Dong, J., Huang, C. X., Dawson, R. I., Foreman-Mackey, D., Collins, K. A., Quinn, S. N., Lissauer, J. J., Beatty, T., Quarles, B., Sha, L., Shporer, A., Guo, Z., Kane, S. R., Abe, L., Barkaoui, K., Benkhaldoun, Z., Brahm, R., Bouchy, F., Carmichael, T. W., Collins, K. I., Conti, D. M., Crouzet, N., Dransfield, G., Evans, P., Gan, T., Ghachoui, M., Gillon, M., Grieves, N., Guillot, T., Hellier, C., Jehin, E., Jensen, E. L. N., Jordán, A., Kamler, J., Kielkopf, J. F., Mékarnia, D., Nielsen, L. D., Pozuelos, F. J., Radford, D. J., Schmider, F.-X., Schwarz, R. P., Stockdale, C., Tan, T.-G., Timmermans, M., Triaud, A. H. M. J., Wang, G., Ricker, G., Vanderspek, R., Latham, D. W., Seager, S., Winn, J. N., Jenkins, J. M., Mireles, I., Yahalomi, D. A., Morgan, E. H., Vezie, M., Quintana, E. V., Rose, M. E., Smith, J. C., and Shiao, B., "Warm Jupiters in TESS Full-frame Images: A Catalog and Observed Eccentricity Distribution for Year 1," *The Astrophysical Journal* **255**, 6 (July 2021).

[15] Grieves, N., Bouchy, F., Lendl, M., Carmichael, T., Mireles, I., Shporer, A., McLeod, K. K., Collins, K. A., Brahm, R., Stassun, K. G., Gill, S., Bouma, L. G., Guillot, T., Cointepas, M., Dos Santos, L. A., Casewell, S. L., Jenkins, J. M., Henning, T., Nielsen, L. D., Psaridi, A., Udry, S., Ségransan, D., Eastman, J. D., Zhou, G., Abe, L., Agabi, A., Bakos, G., Charbonneau, D., Collins, K. I., Colon, K. D., Crouzet, N.,

Dransfield, G., Evans, P., Goeke, R. F., Hart, R., Irwin, J. M., Jensen, E. L. N., Jordán, A., Kielkopf, J. F., Latham, D. W., Marie-Sainte, W., Mékarnia, D., Nelson, P., Quinn, S. N., Radford, D. J., Rodriguez, D. R., Rowden, P., Schmider, F.-X., Schwarz, R. P., Smith, J. C., Stockdale, C., Suarez, O., Tan, T.-G., Triaud, A. H. M. J., Waalkes, W., and Wingham, G., "Populating the brown dwarf and stellar boundary: Five stars with transiting companions near the hydrogen-burning mass limit," *Astronomy & Astrophysics* **652**, A127 (Aug. 2021).

[16] Burt, J. A., Dragomir, D., Mollière, P., Youngblood, A., García Muñoz, A., McCann, J., Kreidberg, L., Huang, C. X., Collins, K. A., Eastman, J. D., Abe, L., Almenara, J. M., Crossfield, I. J. M., Ziegler, C., Rodriguez, J. E., Mamajek, E. E., Stassun, K. G., Halverson, S. P., Villanueva, S., Butler, R. P., Wang, S. X., Schwarz, R. P., Ricker, G. R., Vanderspek, R., Latham, D. W., Seager, S., Winn, J. N., Jenkins, J. M., Agabi, A., Bonfils, X., Ciardi, D., Cointepas, M., Crane, J. D., Crouzet, N., Dransfield, G., Feng, F., Furlan, E., Guillot, T., Gupta, A. F., Howell, S. B., Jensen, E. L. N., Law, N., Mann, A. W., Marie-Sainte, W., Matson, R. A., Matthews, E. C., Mékarnia, D., Pepper, J., Scott, N., Shectman, S. A., Schlieder, J. E., Schmider, F.-X., Stevens, D. J., Teske, J. K., Triaud, A. H. M. J., Charbonneau, D., Berta-Thompson, Z. K., Burke, C. J., Daylan, T., Barclay, T., Wohler, B., and Brasseur, C. E., "TOI-1231 b: A Temperate, Neptune-sized Planet Transiting the Nearby M3 Dwarf NLTT 24399," *The Astronomical Journal* **162**, 87 (Sept. 2021).

[17] Kaye, L., Vissapragada, S., Günther, M. N., Aigrain, S., Mikal-Evans, T., Jensen, E. L. N., Parviainen, H., Pozuelos, F. J., Abe, L., Acton, J. S., Agabi, A., Alves, D. R., Anderson, D. R., Armstrong, D. J., Barkaoui, K., Barragán, O., Benneke, B., Boyd, P. T., Brahm, R., Bruni, I., Bryant, E. M., Burleigh, M. R., Casewell, S. L., Ciardi, D., Cloutier, R., Collins, K. A., Collins, K. I., Conti, D. M., Crossfield, I. J. M., Crouzet, N., Daylan, T., Dragomir, D., Dransfield, G., Fabrycky, D., Fausnaugh, M., Fűrész, G., Gan, T., Gill, S., Gillon, M., Goad, M. R., Gorjian, V., Greklek-McKeon, M., Guerrero, N., Guillot, T., Jehin, E., Jenkins, J. S., Lendl, M., Kamler, J., Kane, S. R., Kielkopf, J. F., Kunimoto, M., Marie-Sainte, W., McCormac, J., Mékarnia, D., Morales, F. Y., Moyano, M., Palle, E., Parmentier, V., Relles, H. M., Schmider, F.-X., Schwarz, R. P., Seager, S., Smith, A. M. S., Tan, T.-G., Taylor, J., Triaud, A. H. M. J., Twicken, J. D., Udry, S., Vines, J. I., Wang, G., Wheatley, P. J., and Winn, J. N., "Transit timings variations in the three-planet system: TOI-270," *Monthly Notices of the Royal Astronomical Society* **510**, 5464–5485 (Mar. 2022).

[18] Wilson, T. G., Goffo, E., Alibert, Y., Gandolfi, D., Bonfanti, A., Persson, C. M., Collier Cameron, A., Fridlund, M., Fossati, L., Korth, J., Benz, W., Deline, A., Florén, H.-G., Guterman, P., Adibekyan, V., Hooton, M. J., Hoyer, S., Leleu, A., Mustill, A. J., Salmon, S., Sousa, S. G., Suarez, O., Abe, L., Agabi, A., Alonso, R., Anglada, G., Asquier, J., Bárczy, T., Barrado Navascues, D., Barros, S. C. C., Baumjohann, W., Beck, M., Beck, T., Billot, N., Bonfils, X., Brandeker, A., Broeg, C., Bryant, E. M., Burleigh, M. R., Buttu, M., Cabrera, J., Charnoz, S., Ciardi, D. R., Cloutier, R., Cochran, W. D., Collins, K. A., Colón, K. D., Crouzet, N., Csizmadia, S., Davies, M. B., Deleuil, M., Delrez, L., Demangeon, O., Demory, B.-O., Dragomir, D., Dransfield, G., Ehrenreich, D., Erikson, A., Fortier, A., Gan, T., Gill, S., Gillon, M., Gnilka, C. L., Grieves, N., Grziwa, S., Güdel, M., Guillot, T., Haldemann, J., Heng, K., Horne, K., Howell, S. B., Isaak, K. G., Jenkins, J. M., Jensen, E. L. N., Kiss, L., Lacedelli, G., Lam, K., Laskar, J., Latham, D. W., Lecavelier des Etangs, A., Lendl, M., Lester, K. V., Levine, A. M., Livingston, J., Lovis, C., Luque, R., Magrin, D., Marie-Sainte, W., Maxted, P. F. L., Mayo, A. W., McLean, B., Mecina, M., Mékarnia, D., Nascimbeni, V., Nielsen, L. D., Olofsson, G., Osborn, H. P., Osborne, H. L. M., Ottensamer, R., Pagano, I., Pallé, E., Peter, G., Piotto, G., Pollacco, D., Queloz, D., Ragazzoni, R., Rando, N., Rauer, H., Redfield, S., Ribas, I., Ricker, G. R., Rieder, M., Santos, N. C., Scandariato, G., Schmider, F.-X., Schwarz, R. P., Scott, N. J., Seager, S., Ségransan, D., Serrano, L. M., Simon, A. E., Smith, A. M. S., Steller, M., Stockdale, C., Szabó, G., Thomas, N., Ting, E. B., Triaud, A. H. M. J., Udry, S., Van Eylen, V., Van Grootel, V., Vanderspek, R. K., Viotto, V., Walton, N., and Winn, J. N., "A pair of sub-Neptunes transiting the bright K-dwarf TOI-1064 characterized with CHEOPS," *Monthly Notices of the Royal Astronomical Society* **511**, 1043–1071 (Mar. 2022).

[19] Mann, A. W., Wood, M. L., Schmidt, S. P., Barber, M. G., Owen, J. E., Tofflemire, B. M., Newton, E. R., Mamajek, E. E., Bush, J. L., Mace, G. N., Kraus, A. L., Thao, P. C., Vanderburg, A., Llama, J., Johns-Krull, C. M., Prato, L., Stahl, A. G., Tang, S.-Y., Fields, M. J., Collins, K. A., Collins, K. I., Gan,

T., Jensen, E. L. N., Kamler, J., Schwarz, R. P., Furlan, E., Gnilka, C. L., Howell, S. B., Lester, K. V., Owens, D. A., Suarez, O., Mekarnia, D., Guillot, T., Abe, L., Triaud, A. H. M. J., Johnson, M. C., Milburn, R. P., Rizzuto, A. C., Quinn, S. N., Kerr, R., Ricker, G. R., Vanderspek, R., Latham, D. W., Seager, S., Winn, J. N., Jenkins, J. M., Guerrero, N. M., Shporer, A., Schlieder, J. E., McLean, B., and Wohler, B., "TESS Hunt for Young and Maturing Exoplanets (THYME). VI. An 11 Myr Giant Planet Transiting a Very-low-mass Star in Lower Centaurus Crux," *The Astronomical Journal* **163**, 156 (Apr. 2022).

[20] Christian, S., Vanderburg, A., Becker, J., Yahalomi, D. A., Pearce, L., Zhou, G., Collins, K. A., Kraus, A. L., Stassun, K. G., de Beurs, Z., Ricker, G. R., Vanderspek, R. K., Latham, D. W., Winn, J. N., Seager, S., Jenkins, J. M., Abe, L., Agabi, K., Amado, P. J., Baker, D., Barkaoui, K., Benkhaldoun, Z., Benni, P., Berberian, J., Berlind, P., Bieryla, A., Esparza-Borges, E., Bowen, M., Brown, P., Buchhave, L. A., Burke, C. J., Buttu, M., Cadieux, C., Caldwell, D. A., Charbonneau, D., Chazov, N., Chimaladinne, S., Collins, K. I., Combs, D., Conti, D. M., Crouzet, N., de Leon, J. P., Deljookorani, S., Diamond, B., Doyon, R., Dragomir, D., Dransfield, G., Essack, Z., Evans, P., Fukui, A., Gan, T., Esquerdo, G. A., Gillon, M., Girardin, E., Guerra, P., Guillot, T., K. Habich, E. K., Henriksen, A., Hoch, N., Isogai, K. I., Jehin, E., Jensen, E. L. N., Johnson, M. C., Livingston, J. H., Kielkopf, J. F., Kim, K., Kawauchi, K., Krushinsky, V., Kunzle, V., Laloum, D., Leger, D., Lewin, P., Mallia, F., Massey, B., Mori, M., McLeod, K. K., Mékarnia, D., Mireles, I., Mishevskiy, N., Tamura, M., Murgas, F., Narita, N., Naves, R., Nelson, P., Osborn, H. P., Palle, E., Parviainen, H., Plavchan, P., Pozuelos, F. J., Rabus, M., Relles, H. M., Rodríguez López, C., Quinn, S. N., Schmider, F.-X., Schlieder, J. E., Schwarz, R. P., Shporer, A., Sibbald, L., Srdoc, G., Stibbards, C., Stickler, H., Suarez, O., Stockdale, C., Tan, T.-G., Terada, Y., Triaud, A., Tronsgaard, R., Waalkes, W. C., Wang, G., Watanabe, N., Wenceslas, M.-S., Wingham, G., Wittrock, J., and Ziegler, C., "A Possible Alignment Between the Orbits of Planetary Systems and their Visual Binary Companions," *The Astronomical Journal* **163**, 207 (May 2022).

[21] Dransfield, G., Triaud, A. H. M. J., Guillot, T., Mekarnia, D., Nesvorný, D., Crouzet, N., Abe, L., Agabi, K., Buttu, M., Cabrera, J., Gandolfi, D., Günther, M. N., Rodler, F., Schmider, F.-X., Stee, P., Suarez, O., Collins, K. A., Dévora-Pajares, M., Howell, S. B., Matthews, E. C., Standing, M. R., Stassun, K. G., Stockdale, C., Quinn, S. N., Ziegler, C., Crossfield, I. J. M., Lissauer, J. J., Mann, A. W., Matson, R., Schlieder, J., and Zhou, G., "HD 28109 hosts a trio of transiting Neptunian planets including a near-resonant pair, confirmed by ASTEP from Antarctica," *Monthly Notices of the Royal Astronomical Society* (May 2022).

[22] Fruth, T., Cabrera, J., Csizmadia, S., Dreyer, C., Eigmüller, P., Erikson, A., Kabath, P., Pasternacki, T., Rauer, H., Titz-Weider, R., Abe, L., Agabi, A., Gonçalves, I., Guillot, T., Mékarnia, D., Rivet, J. P., Crouzet, N., Chini, R., Lemke, R., and Murphy, M., "Transit Search from Antarctica and Chile—Comparison and Combination," *Publications of the Astronomical Society of the Pacific* **126**, 227 (Mar. 2014).

[23] Crouzet, N., Agabi, A., Guillot, T., Abe, L., Schmider, F.-X., Mékarnia, D., Triaud, A. H. M. J., Bresson, Y., Mauclert, N., Bailet, C., Breeveld, D., Blommaert, S., Shortt, B., Daban, J.-B., Lagrange, A.-M., Touzé, R., Dufour, J., Stee, V., and Caruana, J., "Towards ASTEP+, a two-color photometric telescope at Dome C, Antarctica," in [*Society of Photo-Optical Instrumentation Engineers (SPIE) Conference Series*], *Society of Photo-Optical Instrumentation Engineers (SPIE) Conference Series* **11447**, 114470O (Dec. 2020).

[24] Delrez, L., Gillon, M., Queloz, D., Demory, B.-O., Almleaky, Y., de Wit, J., Jehin, E., Triaud, A. H. M. J., Barkaoui, K., Burdanov, A., Burgasser, A. J., Ducrot, E., McCormac, J., Murray, C., Silva Fernandes, C., Sohy, S., Thompson, S. J., Van Grootel, V., Alonso, R., Benkhaldoun, Z., and Rebolo, R., "SPECULOOS: a network of robotic telescopes to hunt for terrestrial planets around the nearest ultracool dwarfs," in [*Ground-based and Airborne Telescopes VII*], Marshall, H. K. and Spyromilio, J., eds., *Society of Photo-Optical Instrumentation Engineers (SPIE) Conference Series* **10700**, 107001I (July 2018).

[25] Brown, T. M., Becker, M., Burleson, B., De Vera, J., Dragomir, D., Dubberley, M., Eastman, J., Graham, M., Haldeman, B., Hawkins, E., Haynes, R., Hjelstrom, A., Howell, D. A., Hygelund, J., Lister, T., Lobdill, R., Norbury, M., Petry, D., Pickles, A., Posner, V., Rosing, W., Sand, D., Street, R., Tsapras, Y., Tufts, J., and Valenti, S., "LCOGT's New Telescopes and Instruments," in [*American Astronomical Society Meeting Abstracts #221*], *American Astronomical Society Meeting Abstracts* **221**, 345.23 (Jan. 2013).

[26] Kossakowski, D., Espinoza, N., Brahm, R., Jordán, A., Henning, T., Rojas, F., Kürster, M., Sarkis, P., Schlecker, M., Pozuelos, F. J., Barkaoui, K., Jehin, E., Gillon, M., Matthews, E., Horch, E. P., Ciardi, D. R.,

Crossfield, I. J. M., Gonzales, E., Howell, S. B., Matson, R., Schlieder, J., Jenkins, J., Ricker, G., Seager, S., Winn, J. N., Li, J., Rose, M. E., Smith, J. C., Dynes, S., Morgan, E., Villasenor, J. N., Charbonneau, D., Jaffe, T., Yu, L., Bakos, G., Bhatti, W., Bouchy, F., Collins, K. A., Collins, K. I., Csubry, Z., Evans, P., Jensen, E. L. N., Lovis, C., Marmier, M., Nielsen, L. D., Osip, D., Pepe, F., Relles, H. M., Ségransan, D., Shporer, A., Stockdale, C., Suc, V., Turner, O., and Udry, S., "TOI-150b and TOI-163b: two transiting hot Jupiters, one eccentric and one inflated, revealed by TESS near and at the edge of the JWST CVZ," *Monthly Notices of the Royal Astronomical Society* **490**, 1094–1110 (Nov. 2019).

[27] Morris, B. M., Tollerud, E., Sipőcz, B., Deil, C., Douglas, S. T., Berlanga Medina, J., Vyhmeister, K., Smith, T. R., Littlefair, S., Price-Whelan, A. M., Gee, W. T., and Jeschke, E., "astroplan: An Open Source Observation Planning Package in Python," *The Astronomical Journal* **155**, 128 (Mar. 2018).

[28] Kenworthy, M. A., Mellon, S. N., Bailey, J. I., Stuik, R., Dorval, P., Talens, G. J. J., Crawford, S. R., Mamajek, E. E., Laginja, I., Ireland, M., Lomberg, B., Kuhn, R. B., Snellen, I., Zwintz, K., Kuschnig, R., Kennedy, G. M., Abe, L., Agabi, A., Mekarnia, D., Guillot, T., Schmider, F., Stee, P., de Pra, Y., Buttu, M., Crouzet, N., Kalas, P., Wang, J. J., Stevenson, K., de Mooij, E., Lagrange, A. M., Lacour, S., Lecavelier des Etangs, A., Nowak, M., Strøm, P. A., Hui, Z., and Wang, L., "The β Pictoris b Hill sphere transit campaign. I. Photometric limits to dust and rings," *Astronomy & Astrophysics* **648**, A15 (Apr. 2021).

[29] Jensen, E., "Tapir: A web interface for transit/eclipse observability," (June 2013).

[30] Google LLC , "G suite."

[31] Astropy Collaboration, Robitaille, T. P., Tollerud, E. J., Greenfield, P., Droettboom, M., Bray, E., Aldcroft, T., Davis, M., Ginsburg, A., Price-Whelan, A. M., Kerzendorf, W. E., Conley, A., Crighton, N., Barbary, K., Muna, D., Ferguson, H., Grollier, F., Parikh, M. M., Nair, P. H., Unther, H. M., Deil, C., Woillez, J., Conseil, S., Kramer, R., Turner, J. E. H., Singer, L., Fox, R., Weaver, B. A., Zabalza, V., Edwards, Z. I., Azalee Bostroem, K., Burke, D. J., Casey, A. R., Crawford, S. M., Dencheva, N., Ely, J., Jenness, T., Labrie, K., Lim, P. L., Pierfederici, F., Pontzen, A., Ptak, A., Refsdal, B., Servillat, M., and Streicher, O., "Astropy: A community Python package for astronomy," *Astronomy & Astrophysics* **558**, A33 (Oct. 2013).

[32] Astropy Collaboration, Price-Whelan, A. M., Sipőcz, B. M., Günther, H. M., Lim, P. L., Crawford, S. M., Conseil, S., Shupe, D. L., Craig, M. W., Dencheva, N., Ginsburg, A., Vand erPlas, J. T., Bradley, L. D., Pérez-Suárez, D., de Val-Borro, M., Aldcroft, T. L., Cruz, K. L., Robitaille, T. P., Tollerud, E. J., Ardelean, C., Babej, T., Bach, Y. P., Bachetti, M., Bakanov, A. V., Bamford, S. P., Barentsen, G., Barmby, P., Baumbach, A., Berry, K. L., Biscani, F., Boquien, M., Bostroem, K. A., Bouma, L. G., Brammer, G. B., Bray, E. M., Breytenbach, H., Buddelmeijer, H., Burke, D. J., Calderone, G., Cano Rodríguez, J. L., Cara, M., Cardoso, J. V. M., Cheedella, S., Copin, Y., Corrales, L., Crichton, D., D'Avella, D., Deil, C., Depagne, É., Dietrich, J. P., Donath, A., Droettboom, M., Earl, N., Erben, T., Fabbro, S., Ferreira, L. A., Finethy, T., Fox, R. T., Garrison, L. H., Gibbons, S. L. J., Goldstein, D. A., Gommers, R., Greco, J. P., Greenfield, P., Groener, A. M., Grollier, F., Hagen, A., Hirst, P., Homeier, D., Horton, A. J., Hosseinzadeh, G., Hu, L., Hunkeler, J. S., Ivezić, Ž., Jain, A., Jenness, T., Kanarek, G., Kendrew, S., Kern, N. S., Kerzendorf, W. E., Khvalko, A., King, J., Kirkby, D., Kulkarni, A. M., Kumar, A., Lee, A., Lenz, D., Littlefair, S. P., Ma, Z., Macleod, D. M., Mastropietro, M., McCully, C., Montagnac, S., Morris, B. M., Mueller, M., Mumford, S. J., Muna, D., Murphy, N. A., Nelson, S., Nguyen, G. H., Ninan, J. P., Nöthe, M., Ogaz, S., Oh, S., Parejko, J. K., Parley, N., Pascual, S., Patil, R., Patil, A. A., Plunkett, A. L., Prochaska, J. X., Rastogi, T., Reddy Janga, V., Sabater, J., Sakurikar, P., Seifert, M., Sherbert, L. E., Sherwood-Taylor, H., Shih, A. Y., Sick, J., Silbiger, M. T., Singanamalla, S., Singer, L. P., Sladen, P. H., Sooley, K. A., Sornarajah, S., Streicher, O., Teuben, P., Thomas, S. W., Tremblay, G. R., Turner, J. E. H., Terrón, V., van Kerkwijk, M. H., de la Vega, A., Watkins, L. L., Weaver, B. A., Whitmore, J. B., Woillez, J., Zabalza, V., and Astropy Contributors, "The Astropy Project: Building an Open-science Project and Status of the v2.0 Core Package," *The Astronomical Journal* **156**, 123 (Sept. 2018).

[33] Garcia, L. J., Timmermans, M., Pozuelos, F. J., Ducrot, E., Gillon, M., Delrez, L., Wells, R. D., and Jehin, E., "PROSE: a PYTHON framework for modular astronomical images processing," *Monthly Notices of the Royal Astronomical Society* **509**, 4817–4828 (Feb. 2022).

[34] Lang, D., Hogg, D. W., Mierle, K., Blanton, M., and Roweis, S., "Astrometry.net: Blind Astrometric Calibration of Arbitrary Astronomical Images," *The Astronomical Journal* **139**, 1782–1800 (May 2010).

[35] Ginsburg, A., Sipőcz, B. M., Brasseur, C. E., Cowperthwaite, P. S., Craig, M. W., Deil, C., Guillochon, J., Guzman, G., Liedtke, S., Lian Lim, P., Lockhart, K. E., Mommert, M., Morris, B. M., Norman, H., Parikh, M., Persson, M. V., Robitaille, T. P., Segovia, J.-C., Singer, L. P., Tollerud, E. J., de Val-Borro, M., Valtchanov, I., Woillez, J., The Astroquery collaboration, and a subset of the astropy collaboration, "astroquery: An Astronomical Web-querying Package in Python," *The Astronomical Journal* **157**, 98 (Mar. 2019).

[36] Stassun, K. G., Oelkers, R. J., Paegert, M., Torres, G., Pepper, J., De Lee, N., Collins, K., Latham, D. W., Muirhead, P. S., Chittidi, J., Rojas-Ayala, B., Fleming, S. W., Rose, M. E., Tenenbaum, P., Ting, E. B., Kane, S. R., Barclay, T., Bean, J. L., Brassuer, C. E., Charbonneau, D., Ge, J., Lissauer, J. J., Mann, A. W., McLean, B., Mullally, S., Narita, N., Plavchan, P., Ricker, G. R., Sasselov, D., Seager, S., Sharma, S., Shiao, B., Sozzetti, A., Stello, D., Vanderspek, R., Wallace, G., and Winn, J. N., "The Revised TESS Input Catalog and Candidate Target List," *The Astronomical Journal* **158**, 138 (Oct. 2019).

[37] Zacharias, N., Finch, C. T., Girard, T. M., Henden, A., Bartlett, J. L., Monet, D. G., and Zacharias, M. I., "The Fourth US Naval Observatory CCD Astrograph Catalog (UCAC4)," *The Astronomical Journal* **145**, 44 (Feb. 2013).

[38] Broeg, C., Fernández, M., and Neuhäuser, R., "A new algorithm for differential photometry: computing an optimum artificial comparison star," *Astronomische Nachrichten* **326**, 134–142 (Feb. 2005).

[39] Foreman-Mackey, D., Czekala, I., Agol, E., Luger, R., and Barclay, T., "dfm/exoplanet: exoplanet v0.2.4," (Dec. 2019).

[40] Coyle, P., "Probabilistic Programming and PyMC3," *arXiv e-prints* , arXiv:1607.00379 (July 2016).

[41] Parviainen, H. and Aigrain, S., "LDTK: Limb Darkening Toolkit," *Monthly Notices of the Royal Astronomical Society* **453**, 3821–3826 (Nov. 2015).

[42] Pont, F., Zucker, S., and Queloz, D., "The effect of red noise on planetary transit detection," *Monthly Notices of the Royal Astronomical Society* **373**, 231–242 (Nov. 2006).

[43] Jakhrani, A., Rigit, A., Othman, A.-K., Samo, S., and Kamboh, S., "Estimation of carbon footprints from diesel generator emissions," *Proceedings of the 2012 International Conference in Green and Ubiquitous Technology, GUT 2012* (07 2012).

[44] Lalitha, S., Schmitt, J. H. M. M., Singh, K. P., Schneider, P. C., Parke Loyd, R. O., France, K., Predehl, P., Burwitz, V., and Robrade, J., "Proxima Centauri - the nearest planet host observed simultaneously with AstroSat, Chandra, and HST," *Monthly Notices of the Royal Astronomical Society* **498**, 3658–3663 (Nov. 2020).

[45] Kokori, A., Tsiaras, A., Edwards, B., Rocchetto, M., Tinetti, G., Bewersdorff, L., Jongen, Y., Lekkas, G., Pantelidou, G., Poultourtzidis, E., Wünsche, A., Aggelis, C., Agnihotri, V. K., Arena, C., Bachschmidt, M., Bennett, D., Benni, P., Bernacki, K., Besson, E., Betti, L., Biagini, A., Brandebourg, P., Bretton, M., Brincat, S. M., Caló, M., Campos, F., Casali, R., Ciantini, R., Crow, M. V., Dauchet, B., Dawes, S., Deldem, M., Deligeorgopoulos, D., Dymock, R., Eenmäe, T., Evans, P., Esseiva, N., Falco, C., Ferratfiat, S., Fowler, M., Futcher, S. R., Gaitan, J., Horta, F. G., Guerra, P., Hurter, F., Jones, A., Kang, W., Kiiskinen, H., Kim, T., Laloum, D., Lee, R., Lomoz, F., Lopresti, C., Mallonn, M., Mannucci, M., Marino, A., Mario, J. C., Marquette, J. B., Michelet, J., Miller, M., Mollier, T., Molina, D., Montigiani, N., Mortari, F., Morvan, M., Mugnai, L. V., Naponiello, L., Nastasi, A., Neito, R., Pace, E., Papadeas, P., Paschalis, N., Pereira, C., Perroud, V., Phillips, M., Pintr, P., Pioppa, J. B., Popowicz, A., Raetz, M., Regembal, F., Rickard, K., Roberts, M., Rousselot, L., Rubia, X., Savage, J., Sedita, D., Shave-Wall, D., Sioulas, N., Školník, V., Smith, M., St-Gelais, D., Stouraitis, D., Strikis, I., Thurston, G., Tomacelli, A., Tomatis, A., Trevan, B., Valeau, P., Vignes, J. P., Vora, K., Vrašťák, M., Walter, F., Wenzel, B., Wright, D. E., and Zíbar, M., "ExoClock Project. II. A Large-scale Integrated Study with 180 Updated Exoplanet Ephemerides," *The Astrophysical Journal* **258**, 40 (Feb. 2022).

[46] Burton, M. G., Zheng, J., Mould, J., Cooke, J., Ireland, M., Uddin, S. A., Zhang, H., Yuan, X., Lawrence, J., Ashley, M. C. B., Wu, X., Curtin, C., and Wang, L., "Scientific Goals of the Kunlun Infrared Sky Survey (KISS)," *Publications of the Astronomical Society of Australia* **33**, e047 (Sept. 2016).

3

Validation and Confirmation of Candidates from *TESS*

3.1 Introduction

Here lies some of the real meat of this thesis: validation and confirmation of planets identified in the *TESS* data. In Chapter 2.3.2 I touched on the emergence of planet validations during the *Kepler* era, for cases where confirmation is not possible. With that in mind, in this chapter I present two new planetary systems I published during my PhD: the first is a confirmation as mass limits were available, while the second is a validation.

3.2 Paper: Confirmation of the HD 28109 (TOI-282) 3-planet system

This is somewhat a chronological order, as the HD 28109/TOI-282 system was the first one where I took the lead. As you will read in the paper, the system was the subject of an observation by ASTEP during our 2020 observing season. The transit was so shallow that we initially believed the observation was inconclusive. Following the end of the season I was tasked with sorting through the year's observations to search for interesting systems to re-observe in 2021. In doing so, I found that by squinting I could just about see the transit of TOI-282.01, a ~ 56 day planet around a Solar-like star. This led to me submitting an abstract to the *TESS* Wiki on behalf of the ASTEP team to alert the community that we were now preparing a publication on the system. Over the course of the following season, we observed the system on every possible occasion to monitor transit timings.

As is the case with many *TESS* planet papers, there were contributions from several collaborators. The high-resolution imaging used for the validation section was collected by Steve Howell, Elisabeth Matthews and Carl Zeigler, and they each wrote in the corresponding text and supplied figures. Keivan Stassun carried out the spectral energy distribution (SED) analysis to provide stellar parameters, and Samuel Quinn provided reconnaissance spectroscopy which gave us spectroscopic stellar parameters. Additional ground-based photometry was provided by Chris Stockdale and Karen Collins.

Our collaborators collected radial velocity points with HARPS and ESPRESSO, and kindly sup-

plied a subset of these data for the paper. They also contributed some text in the discussion describing the ongoing observation campaign with ESPRESSO.

The vetting of the planets identified by *TESS* was done by me, following the methods described in Chapter 2.3.1. I also used SHERLOCK to search for additional candidates in the system, which revealed the inner planet. I had support from the main SHERLOCK developer, Martín Devora-Pajares, to implement the validation module in order to statistically validate the system using SHERLOCK's implementation of TRICERATOPS.

I personally carried out the global analysis of all the photometric data using `allesfitter`. However, the resulting transit times were then analysed by our collaborator David Nesvorný, who carried out a dynamical analysis of the system in order to provide estimates of the planetary masses. I then used these mass estimates as priors for a fit of the RV data to gain an estimate of the inner planet's mass.

Several members of the ASTEP team contributed by writing small sub-sections of the paper, in particular in the introduction and discussion, although the MEGNO analysis and simulations of atmospheric observations were both done entirely by me.

This work is published in MNRAS (Dransfield et al. 2022a).

Monthly Notices of the ROYAL ASTRONOMICAL SOCIETY

MNRAS **515,** 1328–1345 (2022) https://doi.org/10.1093/mnras/stac1383

HD 28109 hosts a trio of transiting Neptunian planets including a near-resonant pair, confirmed by ASTEP from Antarctica

Georgina Dransfield [1★] Amaury H. M. J. Triaud [1] Tristan Guillot,[2] Djamel Mekarnia,[2] David Nesvorný,[3] Nicolas Crouzet,[4,5] Lyu Abe,[2] Karim Agabi,[2] Marco Buttu,[6] Juan Cabrera,[7] Davide Gandolfi [8] Maximilian N. Günther [4†] Florian Rodler,[9] François-Xavier Schmider,[2] Philippe Stee,[2] Olga Suarez,[2] Karen A. Collins [10] Martín Dévora-Pajares,[11] Steve B. Howell,[12] Elisabeth C. Matthews,[13] Matthew R. Standing,[1] Keivan G. Stassun [14] Chris Stockdale,[15] Samuel N. Quinn,[10] Carl Ziegler,[16] Ian J. M. Crossfield,[17] Jack J. Lissauer,[11] Andrew W. Mann,[18] Rachel Matson [19] Joshua Schlieder[20] and George Zhou[21]

Affiliations are listed at the end of the paper

Accepted 2022 May 5. Received 2022 April 11; in original form 2021 November 12

ABSTRACT

We report on the discovery and characterization of three planets orbiting the F8 star HD 28109, which sits comfortably in *TESS*'s continuous viewing zone. The two outer planets have periods of 56.0067 ± 0.0003 d and $84.2597^{+0.0010}_{-0.0008}$ d, which implies a period ratio very close to that of the first-order 3:2 mean motion resonance, exciting transit timing variations (TTVs) of up to 60 min. These two planets were first identified by *TESS*, and we identified a third planet in the *TESS*photometry with a period of 22.8911 ± 0.0004 d. We confirm the planetary nature of all three planetary candidates using ground-based photometry from *Hazelwood*, *ASTEP*, and *LCO*, including a full detection of the ~ 9 h transit of HD 28109 c from Antarctica. The radii of the three planets are $R_b = 2.199^{+0.098}_{-0.10}$ $R_\oplus$, $R_c = 4.23 \pm 0.11$ $R_\oplus$, and $R_d = 3.25 \pm 0.11$ $R_\oplus$; we characterize their masses using TTVs and precise radial velocities from ESPRESSO and HARPS, and find them to be $M_b = 18.5^{+9.1}_{-7.6}$ $M_\oplus$, $M_c = 7.9^{+4.2}_{-3.0}$ $M_\oplus$, and $M_d = 5.7^{+2.7}_{-2.1}$ $M_\oplus$, making planet *b* a dense, massive planet while *c* and *d* are both underdense. We also demonstrate that the two outer planets are ripe for atmospheric characterization using transmission spectroscopy, especially given their position in the CVZ of *James Webb Space Telescope*. The data obtained to date are consistent with resonant (librating) and non-resonant (circulating) solutions; additional observations will show whether the pair is actually locked in resonance or just near-resonant.

Key words: planets and satellites: detection – planets and satellites: dynamical evolution and stability – planets and satellites: fundamental parameters.

1 INTRODUCTION

The discovery of over 4500 extrasolar planets has in no way diminished our curiosity regarding our place in the universe; if anything, we have more questions than ever.

Following early results by Doppler surveys (e.g. Mayor et al. 2011; Howard et al. 2010b), the *Kepler*survey (Borucki et al. 2010) revealed an abundant population of planets comparable in size to Neptune (Fressin et al. 2013), the majority occupying periods shorter than a few hundred days (Howard et al. 2010a). The formation of these Neptune-size worlds remains debated; one possible pathway is that 'pebbles' (large dust particles) separate from the gas in the planet-forming disc and drift inwards (Johansen & Lambrechts 2017). Another possibility is that the pebbles are accreted into cores before migrating inwards (Coleman & Nelson 2016); thus, both models predict that most of the mass growth takes place *in situ* (e.g. Lambrechts et al. 2019; Bean, Raymond & Owen 2021).

Both the 'drift' and 'migration' formation pathways predict the formation of resonant chains, where adjacent planets find themselves in a mean-motion resonance with their neighbours (Bean et al. 2021). However, most planets are not found with commensurate orbital periods (Fabrycky et al. 2014). Studies show that in ∼95 per cent of cases the resonance chain becomes unstable following the dispersal of the gas disc (Matsumura et al. 2010; Pu & Wu 2015; Izidoro et al. 2021). Alternatively, the migratory pathway might be more chaotic (Rein 2012; Lee & Chiang 2015).

Statistical studies of the large samples of known planets have shown that multiplicity is common, i.e. many planets are in multiplanet systems (Fabrycky et al. 2014). Those planets that find themselves close to a mean-motion resonance with their neighbours allow for masses to be constrained without spectroscopic follow-up, by monitoring transit timing variations (TTVs) in the system (e.g. Agol et al. 2005; Holman & Murray 2005; Holman et al. 2010; Lithwick, Xie & Wu 2012).

Neptune-sized planets orbiting bright stars provide excellent dynamical laboratories to further investigate these exciting systems. The *Transiting Exoplanet Survey Satellite* (*TESS*; Ricker et al. 2015)

★ E-mail: gxg831@student.bham.ac.uk
† ESA Research Fellow.

© 2022 The Author(s)
Published by Oxford University Press on behalf of Royal Astronomical Society

Downloaded from https://academic.oup.com/mnras/article/515/1/1328/6590833 by University of Birmingham user on 22 June 2023

launched in 2018 to search for exoplanet candidates; one of its primary mission aims is to deliver to the community 50 planets smaller than 4 $R_\oplus$, with masses measured by high precision radial velocity (RV). Not all systems are suitable for RV mass measurements, but it is predicted that *TESS*will also observe ∼30 systems with TTVs, with approximately a third of those being suitable for dynamical mass measurements (Hadden et al. 2019). Another of *TESS*'s goals is the identification of planets orbiting bright stars, to permit detailed investigations into the dynamics and chemical composition of exoplanetary atmospheres. The discovery and analysis of HD 28109 (TOI-282) fulfils two of those primary objectives.

Stars within *TESS*'s northern and southern continuous viewing zones (CVZ) are continuously observed for a year, allowing for the discovery of long period planets (>20 d). These planets are likely to be favourable candidates for *JWST*, as its CVZ falls within *TESS*'s; however, they are challenging to confirm with ground-based photometry, especially if TTVs introduce large timing uncertainties.

Unless, of course, one is observing from Antarctica. *ASTEP*(**A**ntarctic **S**earch for **T**ransiting **E**xo**P**lanets; Guillot et al. 2015; Mékarnia et al. 2016) is a 40 cm telescope located on the Antarctic Plateau at a latitude of −75.1 deg an elevation of 3233 m. This unique location has a thin atmosphere, completely dry air, and virtually uninterrupted observing between late May and late July (Crouzet et al. 2010a,b). The visibility covers *TESS*'s CVZ and the area where Low-Earth Orbit telescopes have trouble reaching (e.g. CHEOPS; Broeg et al. 2013). For this reason, *ASTEP*is the observatory (ground or space) best suited for the photometric confirmation and follow-up of long-period transiting systems.

In this work, we present the discovery, validation, and characterization of three sub-Neptunes orbiting HD 28109. We begin by characterizing the host in Section 2, followed by Sections 3 and 4 where we describe the identification and validation of planetary candidates in the system. In Section 5, we describe our global analysis of all available photometric and radial velocity data to characterize the planets. We then place the three planets in the context of the field, including potential for atmospheric characterization of the system and further high precision radial velocity follow-up in Section 6. Finally, we summarize our findings and conclude in Section 7.

2 STELLAR CHARACTERIZATION

HD 28109 (TOI-282) is a bright ($V = 9.42$; $J = 8.476$) main-sequence star of spectral type F8/G0V. Its right ascension and declination are 04:20:57.19 −68:06:09.68, and it has a parallax of 7.13 mas (Gaia Collaboration et al. 2021, 2016), placing it at a distance of 140 pc (Bailer-Jones et al. 2021).

All planetary measurements are derived from our knowledge of the star; we therefore begin by characterizing the radius, mass, effective temperature and spectral type of the star.

2.1 Reconnaissance spectroscopy

We observed TOI-282 on three nights spanning 2019 February 14 to 2021 January 07 with the CHIRON spectrograph on the 1.5 m SMARTS telescope. CHIRON is a high-resolution echelle spectrograph fed by an image slicer and a fibre bundle, located at Cerro Tololo Inter-American Observatory (CTIO), Chile. The spectra have a resolution of $R = 80\,000$ with a wavelength coverage of 4500–8900 Å (Tokovinin et al. 2013). The wavelength solution is provided by bracketing Thorium-Argon cathode-ray lamp observations, and the spectra are extracted and wavelength calibrated with the official CHIRON pipeline (Paredes et al. 2021). We extracted the RVs by fitting the spectral-line profiles, which were measured via least-squares deconvolution of the observed spectra using synthetic templates (Donati et al. 1997). The three RVs exhibit a root mean square scatter of 58 m s^{-1}, which is not significant given the 44 m s^{-1} mean per-point uncertainty. With these data, we cannot place strong limits on the presence of additional companions, but the 2-yr time span of the observations does allow us to measure long-term trends that might be indicative of very massive outer companions. The best-fitting linear trend (0.076 ± 0.091 m s^{-1} d^{-1}) is consistent with zero, which suggests it is unlikely that there is a stellar companion in the system, but the precise radial velocities described in Section 4.3 can provide tighter constraints on the masses of the transiting planets and limits on the presence of other bound companions.

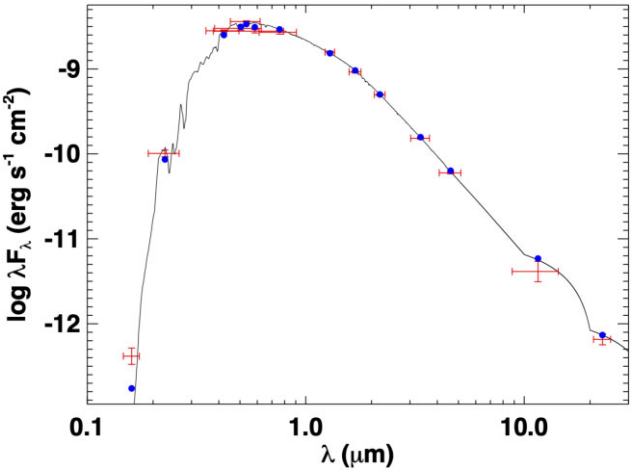


Figure 1. SED of TOI-282. Red symbols represent the observed photometric measurements, where the horizontal bars represent the effective width of the passband. Blue symbols are the model fluxes from the best-fitting Kurucz atmosphere model (black).

We also use the CHIRON spectra to determine the effective temperature, surface gravity, and metallicity of the host star by matching against observed spectra that have previously been classified using SPC (Buchhave et al. 2012). Interpolation to the final parameters is performed with a gradient-boosting regressor implemented in the SCIKIT-LEARN PYTHON module. We measure $T_{\rm eff} = 6120 \pm 50$ K, $\log g_\star = 4.13 \pm 0.10$, and [Fe/H] $= 0.0 \pm 0.10$. Following Gray (2005) and Zhou et al. (2018), we derive $v \sin i_\star$ by fitting broadening kernels to the instrumental, macroturbulent, and rotational line profiles, and estimate $v \sin i_\star = 7.7 \pm 0.5$ km s^{-1}.

2.2 Spectral energy distribution

As an independent check on the derived stellar parameters, and in order to determine an estimate for stellar age, we perform an analysis of the broad-band spectral energy distribution (SED). Together with the *Gaia* EDR3 parallax, we determine an empirical measurement of the stellar radius following the procedures described in Stassun & Torres (2016), Stassun, Collins & Gaudi (2017), and Stassun et al. (2018). We pulled the $B_T V_T$ magnitudes from *Tycho-2*, the JHK_S magnitudes from *2MASS*, the *W*1–*W*4 magnitudes from *WISE*, and the $GG_{\rm RP}G_{\rm BP}$ magnitudes from *Gaia*. In addition, we pulled the FUV and NUV fluxes from *GALEX* in order to assess the level of chromospheric activity, if any. Together, the available photometry spans the full stellar SED over the wavelength range of 0.2–22 μm (see Fig. 1).

Downloaded from https://academic.oup.com/mnras/article/515/1/1328/6590833 by University of Birmingham user on 22 June 2023

We perform a fit using Kurucz stellar atmosphere models (Kurucz 1979), with the effective temperature ($T_{\rm eff}$) and metallicity ([Fe/H]) adopted from the spectroscopic analysis. The remaining free parameter is the extinction, A_V, which was limited to the maximum line-of-sight value from the dust maps of Schlegel, Finkbeiner & Davis (1998). The resulting fit is very good (Fig. 1) with a best-fitting $A_V = 0.01 \pm 0.01$ and a reduced χ^2 of 2.8 (excluding the *GALEX* FUV flux, which is consistent with a modest level of chromospheric activity; see below). Integrating the (unreddened) model SED gives the bolometric flux at Earth of $F_{\rm bol} = 4.37 \pm 0.15 \times 10^{-9}$ erg s^{-1} cm^{-2}. Taking the $F_{\rm bol}$ and $T_{\rm eff}$ together with the *Gaia* EDR3 parallax, with no systematic offset applied (see e.g. Stassun & Torres 2021), gives the stellar radius as $R_\star = 1.446 \pm 0.035$ R$_\odot$. Finally, estimating the stellar mass from the empirical relations of Torres, Andersen & Giménez (2010) and a 6 per cent error from the empirical relation itself gives $M_\star = 1.26 \pm 0.08$ M$_\odot$, consistent with the mass estimated empirically from the stellar radius together with the spectroscopic $\log g$ that gives $M_\star = 1.03 \pm 0.24$ M$_\odot$.

We can also estimate the stellar age by taking advantage of the observed modest chromospheric activity in the UV together with empirical age–activity–rotation relations. For example, we can estimate the $\log R'_{\rm HK} = -4.56 \pm 0.05$ via the *GALEX* FUV excess and the empirical relations of Findeisen, Hillenbrand & Soderblom (2011). That implies an age of $\tau = 0.9 \pm 0.3$ Gyr via the empirical activity–age relations of Mamajek & Hillenbrand (2008). Finally, we can further corroborate the activity-based age estimate by also using empirical relations to predict the stellar rotation period from the activity. For example, the empirical relation between $R'_{\rm HK}$ and rotation period from Mamajek & Hillenbrand (2008) predicts a rotation period for this star of 7.2 ± 1.1 d, which is compatible with the (projected) rotation period $P_{\rm rot}/\sin i_\star = 9.51 \pm 0.62$ d inferred from the stellar radius above together with the spectroscopic $v \sin i_\star$.

We present the adopted stellar parameters in Table 1.

Table 1. Stellar parameters adopted for this work.

Designations	HD 28109, TIC 29781292, TOI-282, 2MASS J04205712-6806095, UCAC4 110-003794, WISE J042057.17-680609.5, Gaia DR2 4668163021600295552, HIP 20295, TYC 9154-01248-1	
Parameter	Value	Source
$T_{\rm mag}$	8.9387 ± 0.006	Stassun et al. (2019)
$B_{\rm mag}$	9.91 ± 0.03	Høg et al. (2000)
$V_{\rm mag}$	9.38 ± 0.02	Høg et al. (2000)
$G_{\rm mag}$	9.3063 ± 0.0028	Gaia Collaboration et al. (2021)
$J_{\rm mag}$	8.476 ± 0.020	Cutri et al. (2003)
$H_{\rm mag}$	8.256 ± 0.024	Cutri et al. (2003)
$K_{\rm mag}$	8.175 ± 0.023	Cutri et al. (2003)
$W1_{\rm mag}$	8.136 ± 0.023	Wright et al. (2010)
$W2_{\rm mag}$	8.175 ± 0.020	Wright et al. (2010)
$W3_{\rm mag}$	8.155 ± 0.020	Wright et al. (2010)
$W4_{\rm mag}$	7.997 ± 0.161	Wright et al. (2010)
Distance	140.087 ± 0.194	Bailer-Jones et al. (2021)
SpT	F8/G0V	Houk & Cowley (1975)
$R_\star$	1.446 ± 0.035R$_\odot$	This work
$M_\star$	1.26 ± 0.08M$_\odot$	This work
Age	1.1 ± 0.1 Gyr	This work
$T_{\rm eff}$	6120 ± 50 K	This work
$\log g_\star$	4.13 ± 0.10	This work
[Fe/H]	0.0 ± 0.1	This work
$v \sin i_\star$	7.7 ± 0.5 km s^{-1}	This work

3 IDENTIFICATION OF PLANETARY CANDIDATES

HD 28109 (TOI-282) is in the southern CVZ for *TESS*that means it is observed in all southern sectors, the only exception being sector 32 where the target was off the edge of the CCD by 3 pixels. At the time of writing, the star has been observed in 25 sectors at 2-min cadence.

In the following sections, we describe the identification of candidates by *TESS*, as well as our own search for further candidates in the data.

3.1 Note on nomenclature

Throughout Section 3, we refer to the host (HD 28109) using its *TESS*alias: TOI-282, where TOI is *TESS*object of interest. When referring to candidate planets, we also use the *TESS*nomenclature and add numeric suffixes in the order that candidates were identified. Once the candidates are confirmed we change their names. Thus, TOI-282.01 becomes HD 28109 c; TOI-282.03 becomes HD 28109 d; and TOI-282.04 is HD 28109 b, with letters indicating the order from closest to farthest from the host star.

3.2 *TESS*data

All 2-min cadence *TESS*data is reduced by the SPOC (Science Processing Operations Center) pipeline (Jenkins et al. 2016) and the photometry data products are delivered in the form of simple aperture photometry (SAP) or Presearch Data Conditioning Simple Aperture Photometry (PDCSAP), where the latter has been corrected for instrument systematics. The light curves are then searched for transit-like signals; candidates that have a signal-to-noise ratio ≥7 are reported as threshold crossing events (TCEs).

The first TCE on TOI-282 was detected in Sector 1, and a second was detected in Sector 2. The multisector data validation report for Sectors 1–2 showed this as a planetary candidate with a period of ∼18 d. It was not until Sectors 1–6 were available that the individual candidates could be disentangled. The one to six multisector validation report reported three planet candidates on TOI-282: candidate 0.01 with a period of ≈56 d, 0.02 with a period of ≈31 d, and finally 0.03 with a period of ≈84 d. Candidate 0.02 was later retired as a false alarm.[1]

The PDCSAP light curves for Sectors 1–13 and Sectors 27–39 can be found in Fig. 2, where transits of TOI-282.01 are highlighted in yellow, while the transits of TOI-282.03 are in green.

3.3 Search for additional transiting candidates

We made use of the custom SHERLOCK[2] pipeline presented in Pozuelos et al. (2020) and Demory et al. (2020) to perform a search for additional transiting candidates in the *TESS*data. SHERLOCK uses the LIGHTKURVE package (Lightkurve Collaboration et al. 2018) to download *TESS*PDCSAP data from NASA Mikulski Archive for Space Telescope (MAST); any outliers, defined as any points over 3σ above the running mean, are then removed. The pipeline then uses WOTAN (Hippke et al. 2019) to detrend the data using the biweight method testing several window lengths. In this case, we used six window sizes between 0.64 and 3.55 days in order to optimise signal detection efficiency (SDE). To aid in the detection of low SNR signals, SHERLOCK also optionally applies a a Savitzky–Golay filter (Savitzky & Golay 1964) to smooth the data and increase precision.

[1]The 31-d transit event was caused by a combination of noise and confusion with the 84-d transit events in early TESS data.
[2]SHERLOCK is publicly available at https://github.com/franpoz/SHERLOCK.

Downloaded from https://academic.oup.com/mnras/article/515/1/1328/6590833 by University of Birmingham user on 22 June 2023

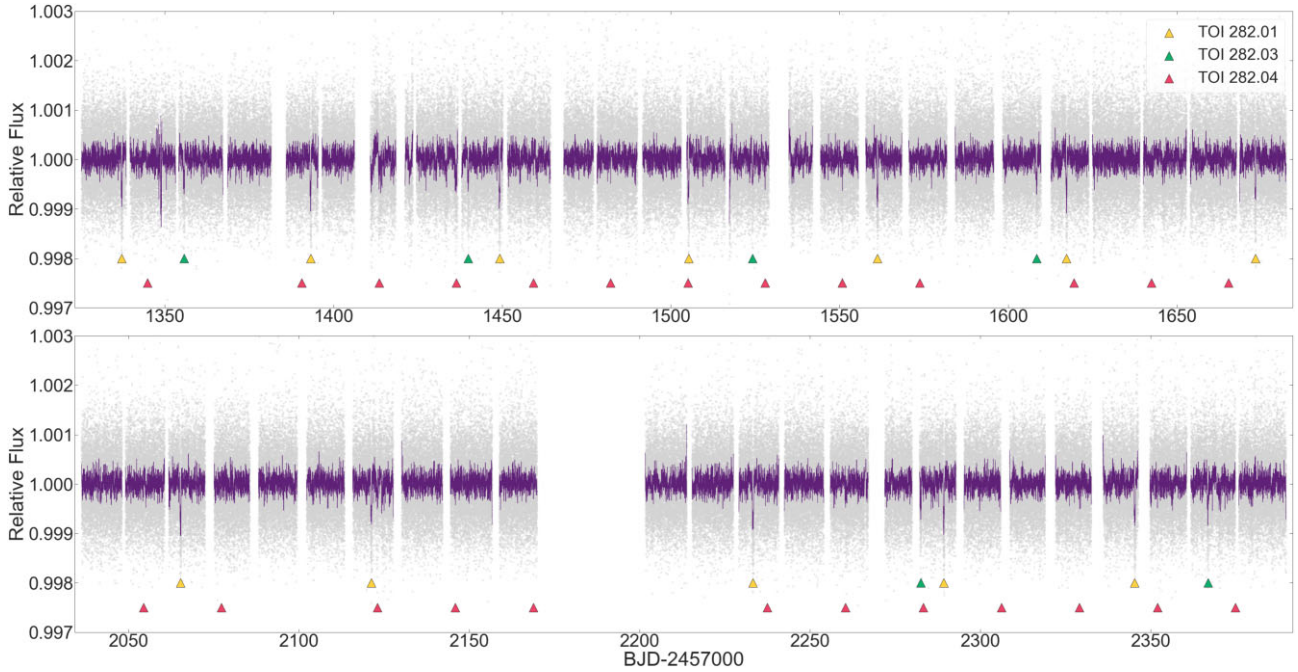


Figure 2. PDCSAP light curves of TOI-282, as produced by the SPOC pipeline. The top panel shows the photometry for Sectors 1–13, while the bottom panel contained Sectors 27–37, with a gap where Sector 32 was missing. Binned data with a cadence of 30 min are shown in purple.

The search for periodic signals is carried out using the TRANSIT LEAST SQUARE (TLS) package (Hippke & Heller 2019), as it is optimized to search for periodic signals with transit-like shapes. We searched a wide parameter space, with periods ranging from 5 to 100 d setting the minimum signal-to-noise ratio (SNR) to 5. This is in contrast to the SPOC pipeline, which sets the minimum SNR to 7.

We recover both candidates 0.01 and 0.03 in the first instance and find that the SDE is consistent across all window sizes, although the SNR and transit depths are at their highest using a window size of 2.8259 d. We also find a third significant signal at a period of 22.89 ± 0.01 d. This signal has an SNR of 23.8 and SDE of 13.1 using the same window-size as for the first two candidates; its depth of just 0.14ppt (parts per thousand) would make it extremely challenging to detect from the ground. Nevertheless, if this is indeed a third planet in the system, its size would be classed as a mini-Neptune just beyond the so-called radius valley (Fulton et al. 2017; Van Eylen et al. 2018), and its period would place it within $\sim$ 5 per cent of a 5:2 third-order resonance with candidate 0.01. The *TESS*light curve folded on this signal is presented in Fig. 3, along with the Lomb–Scargle periodogram.

While this signal does not match any of the TOIs on ExoFOP, further scrutiny reveals that this might have been the period originally associated with TOI-282.02. Dietrich & Apai (2020) include the candidates of TOI-282 in their sample, and cite the orbital period for the innermost candidate as $\sim$ 22.89 d. Additionally, when we scrutinize some of the first multisector data validation reports produced by the SPOC pipeline, we find that Candidate 2 has a period of $\sim$ 22.89 d.[3]

We now adopt this re-identified candidate as TOI-282.04 and indicate in dark pink the detected transits on Fig. 2.

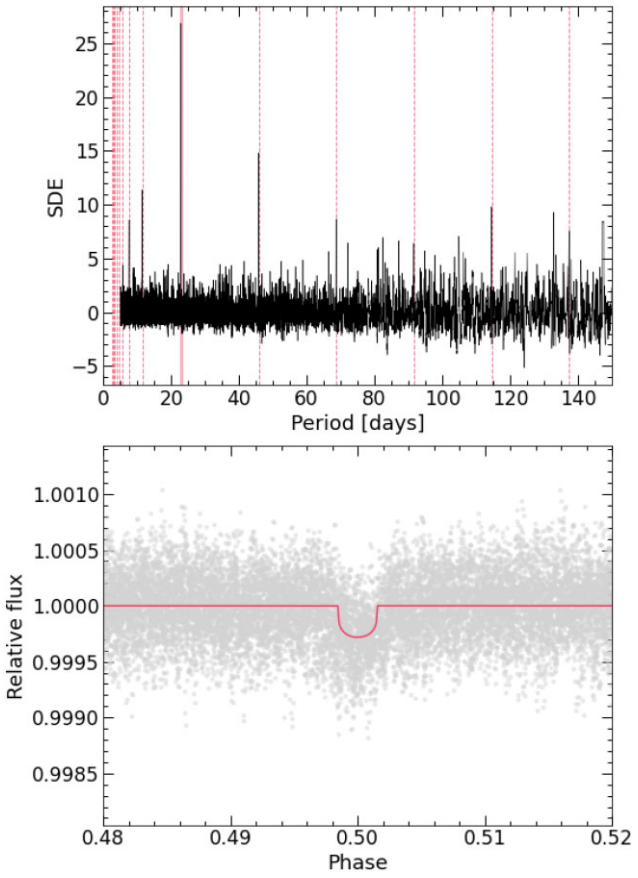


Figure 3. Results of our search for additional candidates in the data, using TRANSITLEASTSQUARES as implemented by SHERLOCK. Upper panel: Lomb–Scargle periodogram showing the detected period and its harmonics. Lower panel: *TESS*light curve phase-folded on this period, with a transit model overplotted.

[3]All data validation reports for TOI-282 are publicly available at https://exofop.ipac.caltech.edu/tess/target.php?id = 29781292.

Downloaded from https://academic.oup.com/mnras/article/515/1/1328/6590833 by University of Birmingham user on 22 June 2023

Table 2. Summary of ground-based follow-up observations carried out for the validation of TOI-282.01, 0.03, and 0.04.

Follow-up observations				
High resolution imaging				
Observatory	Filter	Date	Sensitivity limit	Result
VLT	K_s	2019 January 25	$\Delta m = 5$ at 0.23−4.5 arcsec	No sources detected
SOAR	I_c	2019 February 02	$\Delta m = 7.3$ at 1−3 arcsec	No sources detected
Gemini South	562 nm	2020 December 23	$\Delta m = 5$ at 0.1−1.2 arcsec	No sources detected
Gemini South	832 nm	2020 December 23	$\Delta m = 8$ at 0.1−1.2 arcsec	No sources detected
Photometric follow-up				
Observatory	**Filter**	**Date**	**Coverage**	**Result**
TOI-282.01 / HD 28109 c				
Hazelwood	I_c	2019 January 19	Ingress +50 per cent	Field cleared of NEBs within 2.5 arcsec
ASTEP	R_c	2020 June 08	Full	Detection
ASTEP	R_c	2021 March 15	Ingress +50 per cent	Detection
ASTEP	R_c	2021 May 10	Ingress +90 per cent	Detection
ASTEP	R_c	2021 July 05	Full	Non-detection
ASTEP	R_c	2021 August 30	Full	Non-detection
LCO	z_s	2021 August 30	Full	Field cleared of NEBs within 2.5 arcsec
TOI-282.03 / HD 28109 d				
ASTEP	R_c	2021 March 08	Ingress +30 per cent	Field cleared of NEBs within 2.5 arcsec
ASTEP	R_c	2021 August 23	Ingress +40 per cent	Field cleared of NEBs within 2.5 arcsec
TOI-282.04 / HD 28109 b				
Hazelwood	I_c	2019 January 19	Ingress +50 per cent	Field cleared of NEBs within 2.5 arcsec
Spectroscopic observations				
Instrument	Wavelength range	Date range	Number of spectra	Use
CHIRON	450–890 nm	2019 February 14–2021 January 07	3	Stellar characterization
ESPRESSO	380–788 nm	UT 2019 October 15–UT 2019 December 27	8	Rule out stellar companion
HARPS	383−693 nm	UT 2019 May 24–UT 2021 January 29	7	Rule out stellar companion

Two other periodic signals with low significance were also recovered which did not pass our vetting tests and are therefore attributed to instrument systematics.

4 VETTING AND VALIDATION OF CANDIDATES

In this section, we describe first the ground-based follow-up observations we conducted, staring with high-resolution imaging of the host to search for blended companions. We then describe the photometric observations conducted from several sites between 2019 January and 2021 August. In the first instance, the purpose of ground-based follow-up is to validate the planetary nature of the candidates; in Section 4.4, we describe how we used the available data on this system to rule out all feasible false-positive scenarios.

We note that while the validation tests described here allowed us to confirm the planetary nature of TOI-282.01, 0.03, and 0.04 initially, the analysis we describe in Section 5.2 reveals anticorrelated TTVs between planets 0.01 and 0.03. Therefore, many of the tests here described are not necessary to validate these two objects as planets, since TTVs are not known to have astrophysical false positives. We nevertheless kept the validation steps here for completeness.

All follow-up observations are summarized in Table 2.

4.1 High resolution imaging

If an exoplanet star has a close companion (bound or line of sight), 'third-light' flux from the companion can lead to an underestimated planetary radius if not accounted for in the transit modelling (Ciardi et al. 2015; Furlan & Howell 2017; Matson et al. 2018).

4.1.1 Gemini South Telescope

To search for close-in (bound) companions unresolved in other follow-up observations, we obtained high-resolution imaging observations from Gemini South's Zorro speckle interferometric instrument.[4]

TOI-282 was observed using Zorro on UT 2020 December 23. Zorro provides simultaneous high-resolution speckle imaging in two optical bands, 562/54 and 832/40 nm, with output data products including a reconstructed image, and robust limits on companion detections (Howell et al. 2011, 2021). Fig. 4 (upper panel) shows our 5σ detection limit contrast curves and the corresponding reconstructed speckle image in 832 nm. We find that TOI-282 is a single star with no companions detected in our observations down to a contrast level of 5–8 mag from the Gemini 8-m diffraction limit out to 1.2 arcsec. At the distance of TOI-282 ($d = 140$ pc) these angular limits correspond to spatial limits of 2.8–168 au.

4.1.2 Southern Astrophysical Research Telescope

We also searched for stellar companions to TOI-282 with speckle imaging on the 4.1-m Southern Astrophysical Research (SOAR) telescope (Tokovinin 2018) on UT 2019 February 2, observing in Cousins I-band, a similar visible bandpass as *TESS*. This observation was sensitive to a 7.3-mag fainter star at an angular distance of 1 arcsec from the target. More details of the observation are available in Ziegler et al. (2020). The 5σ detection sensitivity and speckle autocorrelation functions from the observations are shown in Fig. 4

[4] https://www.gemini.edu/sciops/instruments/alopeke-zorro/

Downloaded from https://academic.oup.com/mnras/article/515/1/1328/6590833 by University of Birmingham user on 22 June 2023

(middle panel). No nearby stars were detected within 3 arcsec of TOI-282 in the SOAR observations.

4.1.3 VLT NaCo

We collected high-resolution AO images of TOI-282 with VLT/NaCo (Lenzen et al. 2003; Rousset et al. 2003) on UT 2019 January 25, using the K_s filter. We collected 9 frames, each with exposure time 20s, and dithered the telescope by 2 arcsec in a grid-like pattern between each frame, and constructed a sky background frame by median combining the science images. We processed the data using a custom pipeline which corrects bad pixels, subtracts the sky frame and applies a flat-field correction, and then aligns the stellar position between each frame and co-adds the images. To test the sensitivity of these images, we injected faint fake PSFs into the data, and scaled them such that they could be redetected at 5σ. Significances are averaged radially and presented in Fig. 4 (lower panel); the data are sensitive to companions 5 mag fainter than the star beyond 230 mas, and to companions 7 mag fainter than the star in the background limited regime. We searched for companions in the reduced images by eye. Detector persistence at the dither positions causes a faint point source 2 arcsec directly to the south of the companion, but by inspecting the individual images we confirm that this is not a true visual companion. Apart from this persistence, no point sources are seen anywhere in the field of view (FoV), and we confirm that the star is single to the limit of our resolution.

4.2 Photometric follow-up

Both candidates identified by *TESS*(TOI-282.01 and 0.03) have long periods ($\sim$ 56 d and $\sim$ 84 d), long transit durations ($>$ 8 h), and their transits are shallow. These constraints combined made TOI-282 a challenging system to follow-up from the ground, accounting for why the 0.01 only has seven photometric follow-up observations to date with three detections, while the.03 candidate has two observations with no transit detections.

Below we describe first the observations carried out by *Hazelwood*, followed by the observations taken by *ASTEP*and *LCO*.

4.2.1 Hazelwood

The *Hazelwood* Observatory is a backyard observatory with a 0.32 m Planewave CDK telescope working at f/8, a SBIG STT3200 2.2k $\times$ 1.5k CCD, giving a 20 arcmin $\times$ 13 arcmin FoV and 0.55 arcsec per pixel. The camera is equipped with *B*, *V*, *Rc*, *Ic*, g', r', i', and z' filters. Typical FWHM is 2.2 arcsec to 2.7 arcsec. The Hazelwood Observatory, operated by Chris Stockdale in Victoria, Australia, observed an ingress of TOI-282.01 in Ic on UT 2019 January 21; the transit was below the detection threshold, resulting in a flat light curve, but a nearby eclipsing binary (NEB) check cleared the field within 2.5 arcmin.

Coincidentally, this observation spanned a rare double transit that included the innermost candidate (TOI-282.04) as well. The successful NEB check therefore also applies to this candidate, ruling out nearby stars as the source of the event.

4.2.2 ASTEP

*ASTEP*is a custom 0.4 m Newtonian telescope equipped with a 5-lens Wynne coma corrector and a 4k $\times$ 4k front-illuminated FLI Proline KAF-16801E CCD. The camera has an image scale of 0.93

[h!]

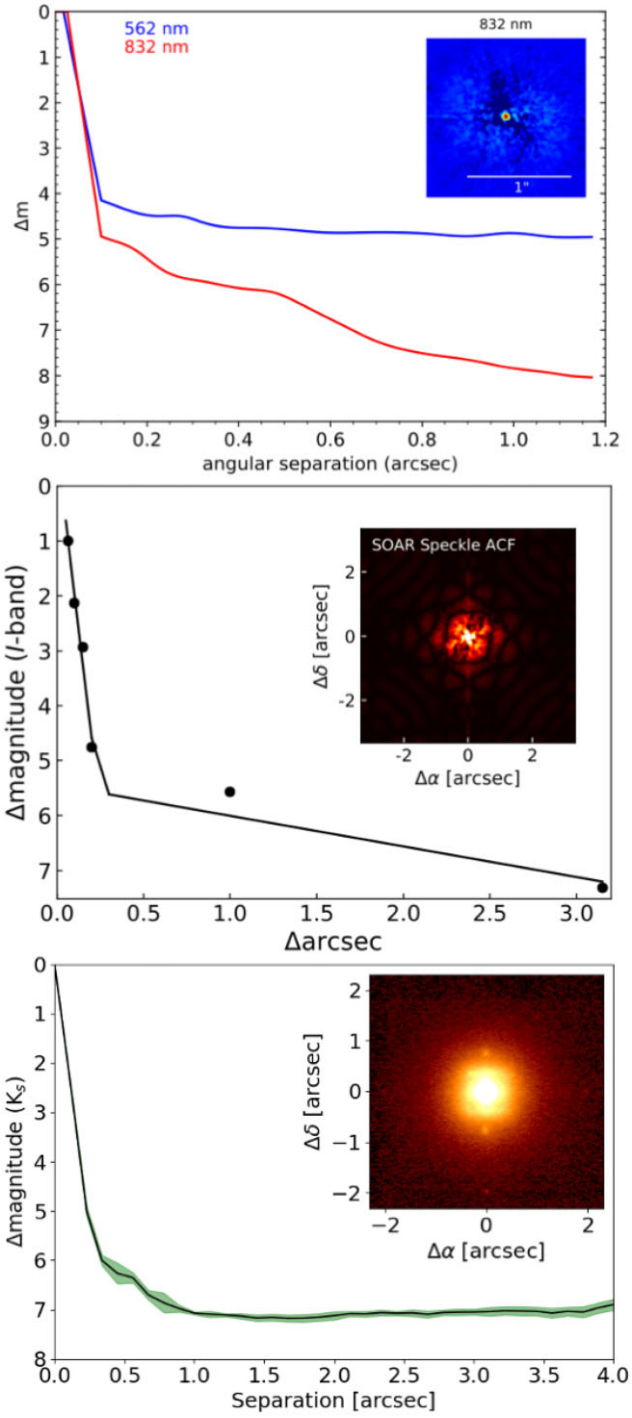


Figure 4. Contrast curves for HD 28109/TOI-282. The top panel shows the results from Gemini South, the middle panel shows the results from SOAR, and the bottom panel shows results from VLT/NaCo. All three panels are inset with final reconstructed images; none of the observations revealed bound companions within 5 mag of the target.

arcmin pixel^{-1}, resulting in a $1^\circ \times 1^\circ$ corrected FoV. The focal instrument dichroic plate splits the beam into a blue wavelength channel for guiding, and a non-filtered red science channel roughly matching an R_c transmission curve (Abe et al. 2013; Guillot et al. 2015). The telescope is automated or remotely operated when needed. Due to the extremely low data transmission rate at the

Downloaded from https://academic.oup.com/mnras/article/515/1/1328/6590833 by University of Birmingham user on 22 June 2023

Concordia Station, the data are processed on-site using an automated IDL-based aperture photometry pipeline (Mékarnia et al. 2016). The calibrated light curve is reported via email and the raw light curves of about 1000 stars of the field are transferred to Europe on a server in Roma, Italy, and are then available for deeper analysis. These data files contain each star's flux computed through 10 fixed circular apertures radii, so that optimal light curves can be extracted.

The *ASTEP*location at Dome C, on the Antarctic plateau, means that it enjoys excellent photometric conditions and exceptionally long nights (Crouzet et al. 2018). *ASTEP*is therefore well placed to observe targets with long orbital periods and transit durations.

We observed a transit of the candidate TOI-282.01 with *ASTEP*on the night of UT 2020 June 08 following our interest to confirm planets with long transits that we were particularly well able to observe during the austral winter. TOI-282.01 was identified by searching the TESS Transit Finder (Jensen 2013). Our detection of the full transit, the first of its kind as part of the photometric follow-up effort of TFOP (*TESS*Follow-up Observing Program) Sub-Group 1, prompted us to follow the system and look more closely at the available *TESS*data.

TOI-282.01 was observed on four further occasions by *ASTEP*(UT 2021 March 15, UT 2021 May 10, UT 2021 July 05, UT 2021 August 30), resulting in two partial transits and two non-detections due to poor weather.

TOI-282.03 was observed on the UT 2021 March 08 and again on the UT 2021 August 23. Both observations resulted in non-detections of the shallow event, but the field was cleared of NEBs within 2.5 arcsec.

4.2.3 LCO

We observed TOI-282 in Pan-STARRS z-short band on UTC 2021 August 30 from the Las Cumbres Observatory Global Telescope (LCOGT; Brown et al. 2013) 1.0 m network node at Siding Spring Observatory. The 1 m telescopes are equipped with 4096 × 4096 SINISTRO cameras having an image scale of 0.389 arcsec per pixel, resulting in a 26 arcmin × 26 arcmin FoV. The images were calibrated by the standard LCOGT BANZAI pipeline (McCully et al. 2018), and photometric data were extracted using AstroImageJ (Collins et al. 2017). The target star was saturated to provide higher photometric precision for fainter stars nears within 2.5 arcsec of the target star. The observations were scheduled to include ingress coverage for a transit of TOI-282.03 with more than $\pm 3\sigma$ ephemeris coverage according to a public ephemeris from the SPOC pipeline. However, according to the linear ephemeris extracted in Section 5.1 of this work, the observations covered from the time of nominal ingress to 90 min later. According to the TTV analysis of Section 5.2, the ingress would have happened 45 min earlier than the linear ephemeris from this work on this epoch, resulting in all in-transit coverage. Although these data do not rule out NEBs due to the ingress timing, we do not find an obvious deep event in any star within 2.5 arcsec of the target star that could be the source of the TESS signal.

4.3 Radial velocity follow-up

We acquired 8 high-resolution spectra ($R \approx 140\,000$) with the Echelle SPectrograph for Rocky Exoplanets and Stable Spectroscopic Observations (ESPRESSO; Pepe et al. 2021) on the 8.2 m ESO Very Large Telescope (VLT; Paranal observatory, Chile). The observations were performed in service mode between UT 2019 October 15 and UT 2019 December 27 as part of our programme 0104.C-0003 (PI: Rodler). The exposure time was set to 1115 s, leading to a mean signal-to-noise ratio (S/N) of ∼160 per pixel at 550 nm. We reduced the ESPRESSO data and extracted the radial velocity measurements by employing ESO's ESPRESSO data reduction pipeline, version 2.2.1,[5] reaching a mean RV precision of 1.1 m s^{-1}.

We also gathered 7 high-resolution spectra ($R \approx 115\,000$) with the High Accuracy Radial Velocity Planet Searcher (HARPS; Mayor et al. 2003) spectrograph mounted at the 3.6 m ESO telescope (La Silla observatory, Chile), as part of ESO programmes 60.A-9700 and 60.A-9707. The spectra were collected between UT 2019 May 24 and UT 2021 January 29, setting the exposure time to 1800 s, which led to a mean S/N ratio of ∼100 per pixel at 550 nm. We reduced the spectra using the dedicated HARPS data reduction software (DRS) and extracted the radial velocity (RV) measurements by cross-correlating the Echelle spectra with a G2 numerical mask (Baranne et al. 1996; Pepe et al. 2002; Lovis & Pepe 2007). The resulting radial velocity measurements have a mean precision of 3.58 m s^{-1}.

4.4 Validation

In this section, we make use of data validation reports combined with our ground-based follow-up observations to validate the planetary nature of the three candidates orbiting TOI-282. The tests we describe here are standard procedure for the discovery of *TESS*planets, but we note again that for the two outer candidates the presence of anticorrelated TTVs render these steps somewhat redundant.

4.4.1 Vetting Tests

The *TESS*data validation report contains several tests to check the validity of the candidates (Twicken et al. 2018). These tests include checking for a difference in depth between odd and even transits, the presence of a potential secondary eclipse implying possible binarity, and any centroid offsets to ensure the event is on target. Both TOI-282.01 and 0.03 passed these tests successfully and were given false alarm probabilities of 2.14×10^{-162} and 2.21×10^{-34}, respectively, indicating that these events are highly unlikely to be instrumental in nature. Having passed these tests, these candidates were ripe for follow-up observations to validate their planetary nature.

The false alarm probability for TOI-282.04 was calculated by Sherlock as 8×10^{-5}; Sherlock also provides a vetting stage for promising signals, where FOV plots are generated through the internal usage of TPFPlotter (Fig. 5; Aller et al. 2020) to check for possible contamination sources; it also injects the search results into Latte (Eisner, Lintott & Aigrain 2020), which is used as the main vetting engine. Sherlock also provides folded light curves to check for even/odd transits and discard the detection of harmonics or subharmonics of the real signal. We scrutinize the data validation report produced by Latte and note no centroid offsets at the time of transits, nor were there any sharp changes in background flux.

4.4.2 Ruling Out False Positives

NEB scenarios were ruled out for all three candidates by the photometric observations, as described in Section 4.2.1. Subsequent observations of TOI-282.01 by *ASTEP*later further confirmed the events on target with clear detections of the transits.

[5] https://www.eso.org/sci/software/pipelines/espresso/espresso-pipe-recipes.html

Downloaded from https://academic.oup.com/mnras/article/515/1/1328/6590833 by University of Birmingham user on 22 June 2023

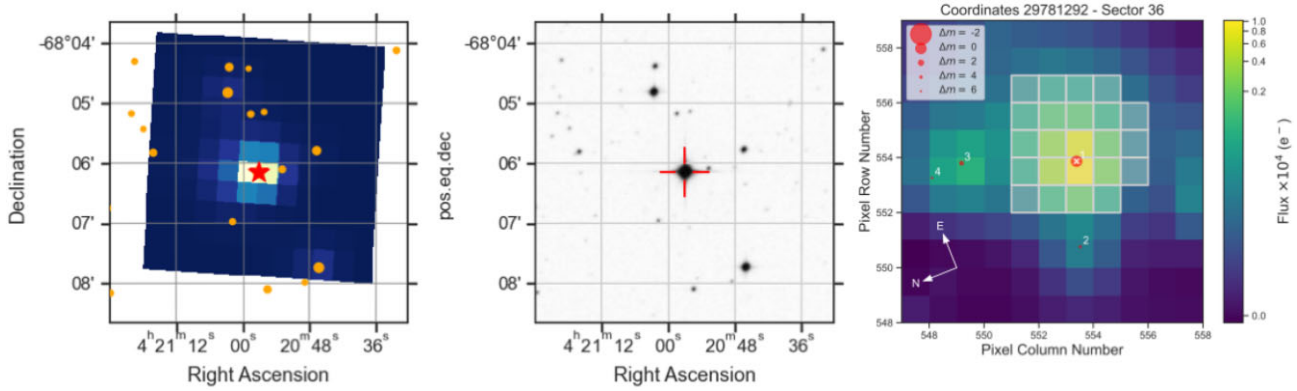


Figure 5. Images of the field of TOI-282/HD 28109, showing that the star does not have any bright contaminating sources nearby. Left-hand panel: Target pixel files showing TOI-282 as a red star and other nearby sources as orange circles. The size of the circles is representative of the source's brightness. Middle panel: Sloan Digital Sky Survey (SDSS; York et al. 2000) image of the surrounding field of TOI-282 (indicated by a red cross). Right-hand panel: *TESS*target pixel file of one of the 25 sectors in which TOI-282 was observed, created with TPFPLOTTER (Aller et al. 2020). The pipeline aperture is shown by the white shaded region, and all nearby sources from Gaia (Gaia Collaboration et al. 2018) down to a magnitude difference $\Delta M = 8$ are overplotted as red circles.

Additionally, our high-resolution observations described in Section 4.1 rule out any blended bound companions down to a projected orbital separation of 2.8 au. A 0.1 $M_\odot$ companion at this orbital separation would produce an RV variation of ~ 1.6 km/s. The very low scatter in our radial velocity measurements described in Section 4.3 rules out the presence of any bound stellar-mass companions in the system.

4.4.3 Statistical Validation with SHERLOCK and TRICERATPOS

SHERLOCK uses the statistical validation package TRICERATPOS presented in Giacalone et al. (2021) to calculate the false positive probability (FPP) for each of the candidates. TRICERATPOS queries the *TESS*Input Catalog (TIC) for stars within 10 pixels of the target and calculates the probability that the transits detected are caused by false positive scenarios. In all, 18 scenarios are tested, including that the signal is caused by a transiting planet on the target star with the input orbital period. SHERLOCK automates the preparation stage for TRICERATOPS by preparing the light curves and apertures; the statistical validation is then carried out five times to produce mean probabilities for each scenario.

The criteria for statistical validation of a planetary candidate is stated as FPP < 0.015; we compute FPPs of 0.0075, 0.035, and 0.203 for TOI-282.01, 0.03, and 0.04, respectively. This immediately places TOI-282.01 well below the threshold for validation, although the probability remains too high for TOI-282.03 and 0.04.

However, we are able to add further to this body of evidence by returning to the fact that this is a multiplanet system. Lissauer et al. (2012) derived an expression for a 'multiplicity boost', where the presence of additional planets in the same aperture increases the probability that the signals are planetary in nature:

$$P_3 \approx \frac{50\,P_1}{50\,P_1 + (1 - P_1)} \quad (1)$$

Where P_1 is the probability of planethood without taking the additional planets into account, and P_3 if the probability with the three-planet multiplicity boost. This decreased the FPP for TOI-282.01, 0.03, and 0.04–0.00015, 0.0007, and 0.005, respectively. All three planets now meet the criteria for statistical validation showing that overwhelmingly, the planet hypothesis is the most favoured. We note that while the multiplicity boost described about was developed for *Kepler*candidates, a similar boost for *TESS*candidates is described in Guerrero et al. (2021) which for small planets ($R < 6R_\oplus$) decreases the FPP by a factor of ≈54. We choose to apply the boost described in Lissauer et al. (2012) as it is more conservative.

4.5 Validation conclusions

Having ruled out all astrophysical false positive scenarios, calculated false positive probabilities and taken into account multiplicity we can now consider the system validated.

From this point on we refer to the three validated planets by their formal names in order of increasing semi-major axis:

(i) TOI-282.04 → HD 28109 b
(ii) TOI-282.01 → HD 28109 c
(iii) TOI-282.03 → HD 28109 d

5 ANALYSIS

With the planetary nature of the signals validated, we now present our analysis of all available data for HD 28109 b, c and d. We begin by describing our global analysis of the available photometry for the system in Section 5.1, followed by our dynamical analysis in Section 5.2. In Section 5.3, we make use of priors from our photometric and dynamical fits to fit the available radial velocity data.

5.1 Global photometric analysis

We carried out a global photometric analysis of the data sets described in Section 4 using ALLESFITTER (Günther & Daylan 2021, 2019). ALLESFITTER is a publicly available versatile inference package capable of jointly fitting photometric and radial velocity data sets from different instruments using ELLC (Maxted 2016) for light curve and RV models, EMCEE (Foreman-Mackey et al. 2013) for MCMC, DYNESTY (Speagle 2020) for dynamic nested sampling, and CELERITE (Foreman-Mackey et al. 2017) for Gaussian Process (GP) models. We chose to use this package, as it can simultaneously fit for white (uncorrelated) noise and red (correlated) noise for different instruments, while offering a wide selection of models to choose from and compare evidence.

We adopted the signal parameters found in Section 3.3 as uniform priors, and the stellar parameters derived in Section 2 as Gaussian

Downloaded from https://academic.oup.com/mnras/article/515/1/1328/6590833 by University of Birmingham user on 22 June 2023

Table 3. Priors used in our fit, along with fitted and derived parameters. Uniform priors are indicated as $\mathcal{U}$(lower bound, upper bound) and normal priors are indicated as $\mathcal{N}$(mean, standard deviation).

	HD 28109 b	HD 28109 c	HD 28109 d	Source
		Fit parametrization and priors		
Transit depth $R_p/R_\star$	$\mathcal{U}(0.008, 0.015)$	$\mathcal{U}(0.023, 0.035)$	$\mathcal{U}(0.017, 0.037)$	
Inverse scaled semimajor axis $(R_\star + R_p)/a$	$\mathcal{U}(0.05, 0.06)$	$\mathcal{U}(0.015, 0.035)$	$\mathcal{U}(0.015, 0.03)$	
Orbital Inclination cos i	$\mathcal{U}(0.000, 0.04)$	$\mathcal{U}(0.000, 0.04)$	$\mathcal{U}(0.000, 0.04)$	
Transit Epoch T_0	$\mathcal{U}(2458344.7, 2458344.9)$	$\mathcal{U}(2458337.12, 2458337.32)$	$\mathcal{U}(2458355.58, 2458355.98)$	
Planet Mass $M_p/M_\star$	$\mathcal{U}(0.0, 0.000026)$	$\mathcal{U}(0.0, 0.0005)$	$\mathcal{U}(0.0, 0.0005)$	
Period P	$\mathcal{U}(22.8, 23.0)$	$\mathcal{U}(55.6, 56.6)$	$\mathcal{U}(84.2, 86.0)$	
Eccentricity e	$\mathcal{U}(0.0, 0.5)$	$\mathcal{U}(0.0, 0.5)$	$\mathcal{U}(0.0, 0.5)$	
Longitude of periapsis ϖ	$\mathcal{U}(0, 360)$	$\mathcal{U}(0, 360)$	$\mathcal{U}(0, 360)$	
		Limb darkening coefficients		
TESSu_1	0.4041 ± 0.0007	*ASTEP*u_1	0.4758 ± 0.0009	
TESSu_2	0.1324 ± 0.0018	*ASTEP*u_2	0.1392 ± 0.0022	
TESSq_1	$\mathcal{N}(0.2878, 0.0024)$	*ASTEP*q_1	$\mathcal{N}(0.3782, 0.0034)$	
TESSq_2	$\mathcal{N}(0.3766, 0.0013)$	*ASTEP*q_2	$\mathcal{N}(0.3868, 0.0014)$	
External priors		**GP priors**		
Stellar mass $M_\star$	$\mathcal{N}(1.26, 0.08)$	Amplitude scale gp ln S_0(flux)	$\mathcal{U}(-15, 5)$	
Stellar radius $R_\star$	$\mathcal{N}(1.446, 0.035)$	Damping gp ln Q(flux)	$\mathcal{U}(-10, 10)$	
Stellar effective temperature $T_{\rm eff}$	$\mathcal{N}(6120, 50)$	Frequency gp ln ω_0(flux)	$\mathcal{U}(-10, 10)$	
		Fitted parameters		
$R_p/R_\star$	$0.01441^{+0.00031}_{-0.00037}$	0.02632 ± 0.00027	$0.01999^{+0.00035}_{-0.00037}$	Fixed Lin. Ephem. Fit
$(R_\star + R_p)/a$	$0.05017^{+0.00022}_{-0.00012}$	$0.02231^{+0.00073}_{-0.00066}$	$0.01688^{+0.00053}_{-0.00047}$	Fixed Lin. Ephem. Fit
cos i	$0.03964^{+0.00024}_{-0.00040}$	$0.0081^{+0.0018}_{-0.0021}$	$0.0064^{+0.0013}_{-0.0015}$	Fixed Lin. Ephem. Fit
T_0 (BJD)	$2458344.81772 \pm 0.00757$	$2458377.80109^{+0.00724}_{-0.00733}$	$2458355.67324 \pm 0.00432$	Dynamical Fit
P (d)	$22.89104^{+0.00035}_{-0.00036}$	$56.00819^{+0.00194}_{-0.00202}$	$84.25999^{+0.00744}_{-0.00662}$	Dynamical Fit
e	<0.3307	<0.1203	<0.0864	Dynamical Fit
Fitted RV Jitter		**Fitted GP hyperparameters**		
ln $\sigma_{\rm jitter;\ HARPS}$ (km s^{-1})	$-7.8^{+1.6}_{-2.8}$	gp ln S_0(flux)	$-19.72^{+0.20}_{-0.19}$	Fixed Lin. Ephem. Fit
ln $\sigma_{\rm jitter;\ espresso}$ (km s^{-1})	$-5.99^{+0.38}_{-0.36}$	gp ln Q(flux)	$-4.9^{+1.9}_{-2.2}$	Fixed Lin. Ephem. Fit
		gp ln ω_0(flux)	$6.0^{+2.2}_{-1.9}$	Fixed Lin. Ephem. Fit
		Derived parameters		
Companion radius; R_p ($R_\oplus$)	$2.199^{+0.098}_{-0.10}$	4.23 ± 0.11	3.25 ± 0.11	Fixed Lin. Ephem. Fit
Semimajor axis; a (au)	0.1357 ± 0.0034	0.308 ± 0.011	0.411 ± 0.016	Fixed Lin. Ephem. Fit
Inclination; i (deg)	$87.725^{+0.023}_{-0.012}$	$89.543^{+0.093}_{-0.086}$	$89.682^{+0.093}_{-0.082}$	Fixed Lin. Ephem. Fit
Impact parameter; b	$0.8007^{+0.0055}_{-0.0084}$	$0.365^{+0.058}_{-0.068}$	$0.339^{+0.075}_{-0.093}$	Fixed Lin. Ephem. Fit
Total transit duration; $T_{\rm tot}$ (h)	$5.392^{+0.10}_{-0.073}$	8.973 ± 0.060	$10.13^{+0.14}_{-0.11}$	Fixed Lin. Ephem. Fit
Full-transit duration; $T_{\rm full}$ (h)	$4.997^{+0.11}_{-0.081}$	8.425 ± 0.070	$9.66^{+0.14}_{-0.12}$	Fixed Lin. Ephem. Fit
Equilibrium temperature; $T_{\rm eq}$ (K)	881.2 ± 7.5	$585.2^{+8.7}_{-8.3}$	$506.5^{+8.7}_{-8.0}$	Fixed Lin. Ephem. Fit
Transit depth *TESS*; $\delta_{\rm tr;TESS}$ (ppt)	$0.188^{+0.013}_{-0.016}$	$0.834^{+0.015}_{-0.017}$	$0.489^{+0.021}_{-0.024}$	Fixed Lin. Ephem. Fit
Transit depth *ASTEP*; $\delta_{\rm tr;ASTEP}$ (ppt)	–	$0.854^{+0.016}_{-0.018}$	–	Fixed Lin. Ephem. Fit
Companion TTV mass; $M_{\rm p;TTV}$ ($M_\oplus$)	–	$7.943^{+4.227}_{-3.046}$	$5.681^{+2.738}_{-2.110}$	Dynamical Fit
Companion RV mass; $M_{\rm p;RV}$ ($M_\oplus$)	$18.496^{+9.120}_{-7.609}$	–	–	RV Fit

priors and we fit using the nested sampling algorithm. Nested sampling (Skilling 2004) works by drawing a number of live points from the prior distribution, and then removing the point with the lowest likelihood. Another point is then drawn from the prior while requiring that the overall likelihood now be higher than before. This process then repeats until the change in Bayesian evidence, parametrized as $\Delta \ln Z$, falls below a certain threshold. We begin the algorithm with 1500 live points and set the threshold to $\Delta \ln Z < 0.01$ as recommended by the ALLESFITTER documentation.

We computed quadratic limb darkening coefficients u_1 and u_2 for HD 28109 in *TESS*and R_c filters using PYLDTK (Parviainen & Aigrain 2015) and the PHOENIX stellar atmosphere library provided by Husser et al. (2013). The resulting coefficients are presented in Table 3; these are also input to our global fit as Gaussian priors.

We initially fit for a two-planet model using only HD 28109 c and HD 28109 d, and then for a three-planet model incorporating HD 28109 b. One of the key advantages of nested sampling over Markov chain Monte Carlo (MCMC) is the calculation of the Bayesian evidence at each stage of the algorithm; this allows us to determine which model is statistically favoured by calculating the Bayes' factor (Kass & Raftery 1995). In both cases, we fit simultaneously for all transit parameters, quadratic stellar limb-darkening coefficients in the Kipping (2013) parametrization, as well as the baseline model and the white noise scaling for each instrument. These latter two ensure that uncertainties arising from instrument systematics are appropriately propagated to derived physical parameters.

Downloaded from https://academic.oup.com/mnras/article/515/1/1328/6590833 by University of Birmingham user on 22 June 2023

In Section 3.3, we found that all three planets had the highest SNR in *TESS*when the flux was detrended; to detrend the data for semi-periodic stellar variability (red noise) present in all instruments, we simultaneously fit a GP using a Simple Harmonic Oscillating (SHO) kernel. The parametrization used in the fit is summarized in Table 3.

We find that the three-planet model is vastly statistically favoured over the two-planet model, with a Bayes Factor in excess of 60 000. A $BF > 150$ is usually considered strong enough statistical evidence to confirm a more complex model (Kass & Raftery 1995). The fit's result further confirms the existence of HD 28109 b in our data.

In both the two- and three-planet model fits, eccentricity and argument of periastron were set as free parameters. We note that the resulting derived orbital parameters suggest that the two outer planets could have small to moderate eccentricities ($e_c = 0.116^{+0.30}_{-0.079}$ and $e_d = 0.19^{+0.34}_{-0.15}$) and yield calculated host densities within 1σ of the prior, while the inner planet yields a very large eccentricity of $e_b = 0.809^{+0.049}_{-0.083}$ and a calculated host density 5σ below the prior. The host density is calculated from the transit parameters of each planet individually by ALLESFITTER using the expression presented in Seager & Mallén-Ornelas (2003):

$$\rho_{\star,\mathrm{obs}} \equiv \frac{3\pi(a/R_\star)^3_{\mathrm{obs}}}{GP^2}, \tag{2}$$

where $\rho_{\star,\mathrm{obs}}$ is the host density derived from transit parameters assuming a Keplerian circular orbit. The manner and extent of the discrepancy between $\rho_{\star,\mathrm{obs}}$ and the external prior on stellar density can be indicative of erroneous assumptions made regarding the orbits (Kipping 2014). In particular, for such an eccentric orbit we would expect the ratio $\rho_{\mathrm{obs}}/\rho_{\mathrm{true}}$ to be much greater than unity.

We therefore repeat the two- and three-planet fits constraining eccentricities to zero and then compare the evidence for each of the models to see which is statistically most likely. We find that all three-planet models are preferred over all two-planet models, with Bayes Factors in excess of 50 000. We also find that all circular models are preferred over models with non-zero eccentricities. In the case of the three-planet circular model versus the three-planet eccentric model, we find a Bayes Factor of almost 3000, indicating that a more complex light curve modelling with eccentric orbits is not preferred.

The results of the global fit, including derived parameters, are presented in Table 3. In Fig. 6, we present the three individual *ASTEP*transits for planet c along with the best-fitting model, and in Fig. 7, we present the *TESS*phase folded light curves for each planet along with the best-fitting model.

5.2 Dynamical analysis

In this section, we consider a non-Keplerian model for the planets of HD 28109; we first fit individual transit times and then use these timings to infer dynamical masses for the planets.

5.2.1 Transit timing variations

Given the proximity of the two outer planets to a first order 3:2 mean-motion resonance (within ~ 0.3 per cent), we would expect these planets to experience some mutual gravitational influence leading to TTVs. This is supported by visual inspection of the individual transit fits resulting from the nested sampling, as several appear to have noticeable offsets in time between the model and the data.

We therefore re-fit the photometry once again using ALLESFITTER, this time allowing the midtime of each individual transit to vary about a linear ephemeris for all three planets.

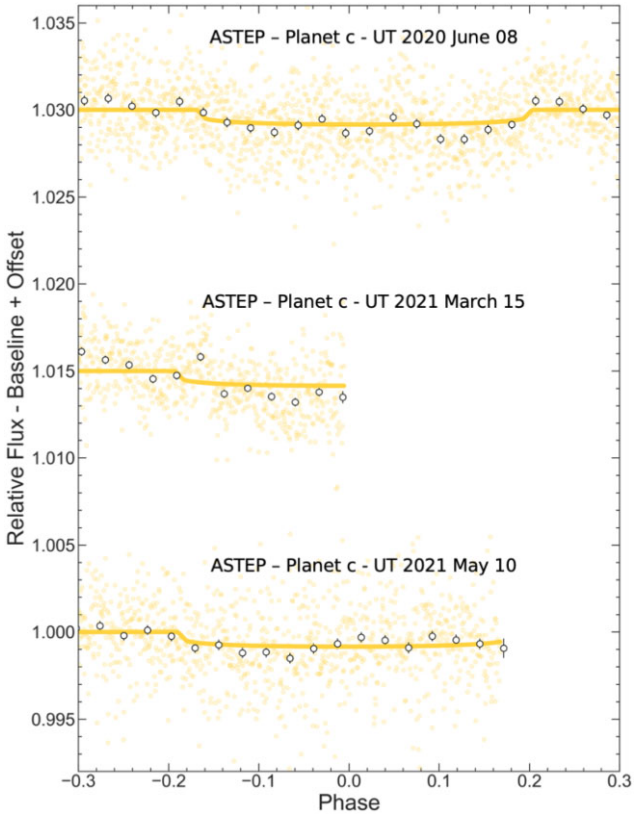


Figure 6. Detrended transits observed with *ASTEP*on the nights of 2020 June 08, 2021 March 15, and 2021 May 10. The green points are the detrended flux, while the white circles are binned. Curves superimposed are the best-fitting models for each transit.

When allowing for TTVs, we fit for all the same parameters as in the linear fit, except that we now fix the linear ephemeris using the values derived from the most statistically favoured fit in Section 5.1. We also constrain eccentricities to zero for all three planets and once again apply Gaussian priors on the stellar density and quadratic limb darkening coefficients.

In preparation for a TTV fit, ALLESFITTER attempts to guess the location of the flux minimum during each transit present in the data, with these guesses then used as uniform priors for the fit. However, we find that almost all of the guesses for planet b are affected by local stellar variability or nearby transits of other planets biasing the fit; instead, for each transit's mid-time, we impose a uniform prior defined as the linear predictions ± 120 minutes for all planets. Once again we simultaneously fit a GP with a SHO kernel to account for stellar variability.

The results of this fit are presented in Fig. 8. HD 28109 c and d present very clear and significant anticorrelated TTVs with peak to peak amplitudes of ~ 50 and ~ 100 min, respectively. While the shifts in timing do appear to show a sinusoidal variation between early and late, it is most likely that what we see here is the shorter term 'chopping' part of the signal (Deck & Agol 2015), given that the 'Super-Period' for these planets is expected to be in excess of 9000 d.

For HD 28109 b, the errors on the timings are very large due to how shallow individual events are (≈ 0.19ppt) and therefore our results are consistent with no TTVs. We note that for some individual events the errors were significantly smaller than average. Visual inspection of each transit fit showed that this is probably caused by artefacts in

Downloaded from https://academic.oup.com/mnras/article/515/1/1328/6590833 by University of Birmingham user on 22 June 2023

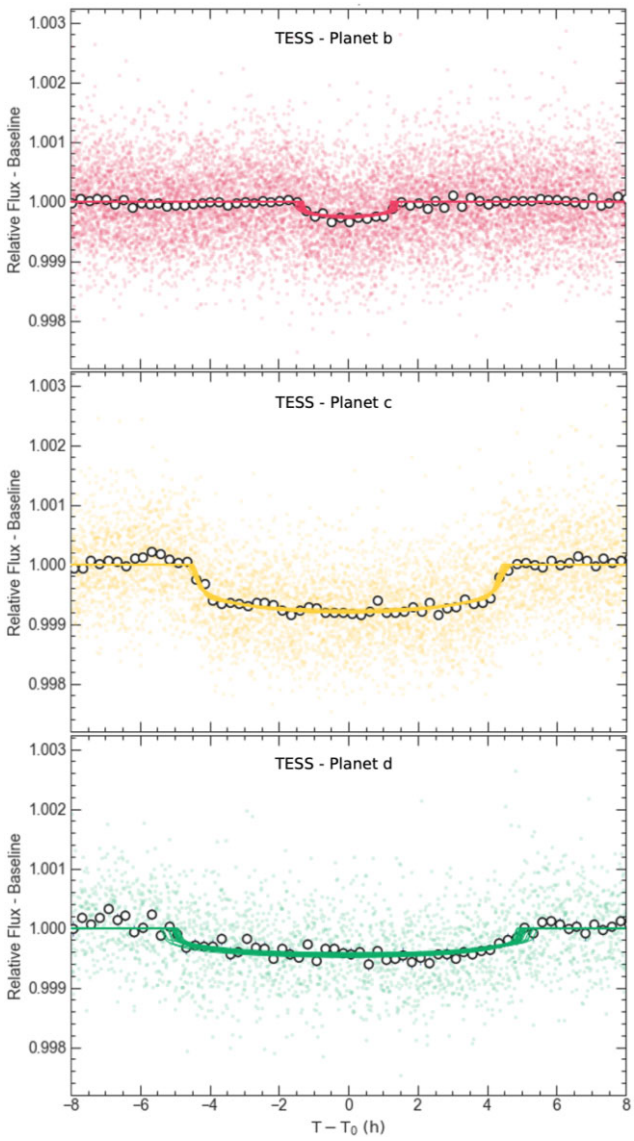


Figure 7. Global fit of the *TESS*photometric data for each of the planets of HD 28109. Points in the background are the phase-folded 2-min cadence data, while white circles are the binned points. Curves are 20 samples drawn from the posterior.

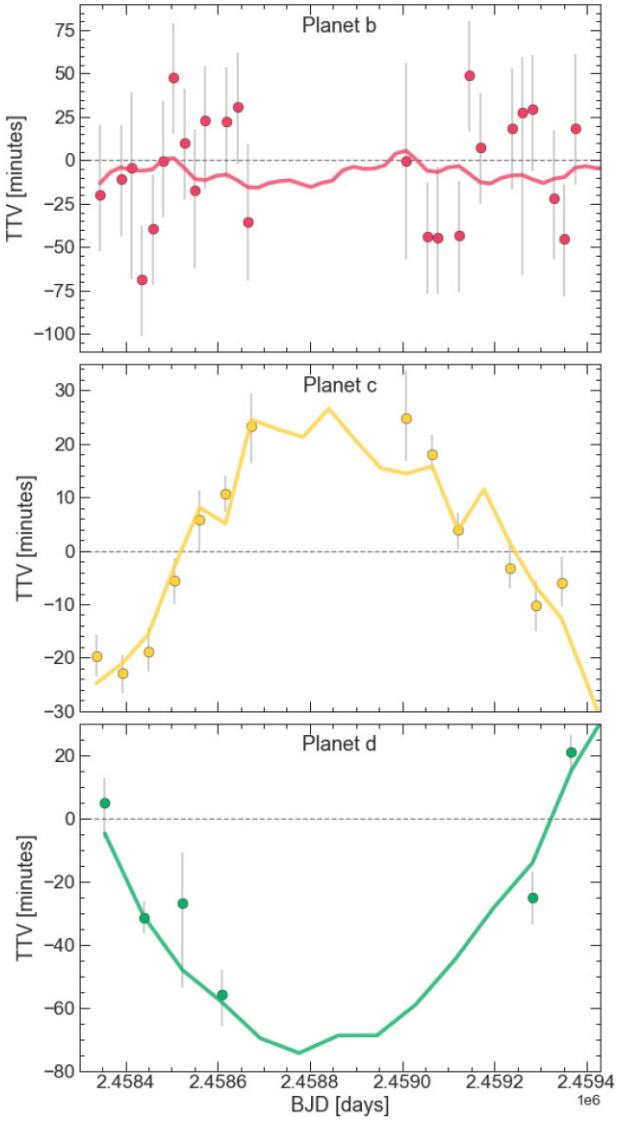


Figure 8. TTVs (in minutes) for each of the planets of HD 28109 spanning 2 yr of *TESS*data plus ground-based photometric monitoring of planet c. The points show the difference between the fitted midtimes and the linear predictions, while the lines show the model predictions from our dynamical analysis in Section 5.2.2.

the light curves. We therefore amplified the errors on all timings of planet b to be at least the mean timing uncertainty.

5.2.2 *Mass estimates From TTVs*

We perform dynamical analysis of the observed transit times with a symplectic *N*-body integrator code described in Nesvorný et al. (2012). We instruct the code to simultaneously fit all measured transit times, using MULTINEST (Feroz & Hobson 2008) to perform the regression, setting the integration time-step to 0.5 d, roughly 1/50 of the planet b's orbital period. We consider dynamical models with 2, 3, and 4 planets. The model with 3 planets has 20 parameters: planet-to-star mass ratios, orbital periods, eccentricities, longitudes of periapsis, impact parameters, difference in nodal longitudes, and reference epochs between a reference time (2458337 BJD UTC) and the first observed transit of each planet. The nodal longitude of the innermost planet in each fit is fixed at 270°, and therefore, the 2 and 4 planet models have 13 and 27 parameters, respectively. We use uniform priors for all parameters except for the impact parameter, since our light-curve fits provide strong constraints that are used here. The host star mass was fixed at $M_\star = 1.26\ \mathrm{M}_\odot$. The uncertainties discussed below therefore do not account for the uncertainty in the stellar mass.

We find that the existing measurements are not good enough to uniquely determine the planet properties. The first problem arises because there is a large radial separation between the inner planet b and the two outer planets: the measured TTVs of c and d thus most likely reflect their mutual interaction (rather than those of planet b). In addition, given the relatively large measurement errors of b's TTVs it is not clear whether b's TTVs contain any useful information about planets c and d. Thus, as b can be decoupled from the rest of the system it is difficult to meaningfully constrain its properties. Indeed, when we instruct MULTINEST to perform a three-planet fit, the mass of planet b always reaches to the upper edge of the mass

Downloaded from https://academic.oup.com/mnras/article/515/1/1328/6590833 by University of Birmingham user on 22 June 2023

prior even if this is clearly non-physical (i.e. mass exceeding that of Jupiter for the estimated radius $R_b = 2.199\,R_\oplus$). We therefore limit the uniform prior on the mass of planet b to $M_b = 11 M_\oplus$.

All fits performed here confirm that the masses of c and d are in the planetary range. Our best-fitting indicates $m_c/M_* = (1.9^{+1.0}_{-0.7}) \times 10^{-5}$ and $m_d/M_* = (1.4^{+0.6}_{-0.5}) \times 10^{-5}$, suggesting that both planets have low densities. The orbital eccentricities of c and d are most likely low ($e < 0.1$), but some two-planet fits identify modes with eccentric orbits ($e > 0.1$). In Table 3, we present the 2σ upper limits for the eccentricities of all three planets as this parameter remains poorly constrained; the mean values of the posterior distributions for the eccentricities are $e_b = 0.1519^{+0.0894}_{-0.0944}$, $e_c = 0.0391^{+0.0406}_{-0.0231}$, and $e_d = 0.0238^{+0.0313}_{-0.0157}$. The posteriors for the longitude of periastron are not included in Table 3, as they are unconstrained by our fits.

Given the wide orbital separation between planets b and c, we perform an additional fit including a putative fourth planet. This planet may be non-transiting or too small to be detected. We used a uniform prior between 28 d to 44 d for the fourth planet orbital period. The four-planet fits give masses of c and d that are consistent with the masses reported above (and low orbital eccentricities). The best parameters for the hypothetical fourth planet are $m_4/M_* \simeq 7.6 \times 10^{-6}$ and $P_4 \simeq 39.3$ d. With this orbit, the two inner planets would be wide of the 3:2 resonance. The Bayesian evidence for this fit is significantly lower than for the three-planet fit, indicating that the three-planet fit is preferred.

The eccentricities of planets c and d are low and when that is the case, the resonant and near-resonant dynamics can be studied analytically following Nesvorný & Vokrouhlický (2016). There are three variables to consider, each of them being a combination of orbital elements. Constant δ is an orbital invariant that defines the position of the system relative to the 3:2 resonance, the resonant angle ψ is a function of the usual 3:2 resonant angles σ_1 and σ_2, and variable Ψ is a combination of planetary masses, semimajor axes and eccentricities [see Nesvorný & Vokrouhlický (2016) for details]. The resonant librations of ψ can only happen for $\delta > 0.945$. Fig. 9 shows position of planets c and d in the terms of the dynamical variables δ, ψ, and Ψ. About two thirds of the posterior samples are non-resonant with the two orbits being slightly wide of the exact resonance. About one third of the sample, however, show resonant librations with a generally low libration amplitude. Additional observations will be needed to better constrain the location of the c and d planets relative to the 3:2 resonance.

We predict that the amplitudes of the TTVs will be very large ($\sim$ 1000 min for planet c and $\sim$ 2000 min for planet d) once one whole TTV period has been sampled. In Fig. 10, we present the predicted TTVs of the system for the next 11 000 d. Continued monitoring of the system will allow us to both improve timing predictions and refine the dynamical mass measurements of planets c and d.

5.3 Radial velocity analysis

The global photometric analysis yielded strong priors on all orbital parameters; additionally, we can place priors on the masses of the two outer planets from the dynamical fit. We therefore fit the radial velocity data set to gain an estimate on the mass of the innermost planet using ALLESFITTER. We adopt Gaussian priors on the all orbital parameters for the three planets (P, T_0, R_p/R_*, $(R_* + R_p)/a$, cos$i$), as well as the radial velocity semi-amplitudes of the outer planets (K). We place a wide uniform prior between 0.1 and 6.0 m s^{-1} (corresponding to 0.5–30 $M_\oplus$) on the semi-amplitude of the inner planet and fit for all three periods, reference times, and semi-amplitudes. In our models, we vary the RV offset and RV jitter for each individual data set. The jitter parameter appears as an additional

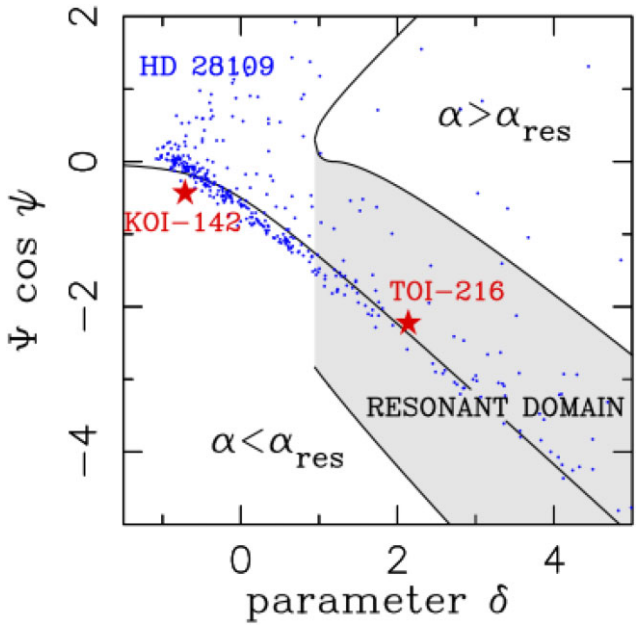


Figure 9. The 3:2 resonance structure diagram following Nesvorný & Vokrouhlický (2016). Systems with $\alpha = a_c/a_d < \alpha_{res}$ ($\alpha > \alpha_{res}$), where $\alpha = 0.763$ corresponds to the exact resonance, have orbits just wide (narrow) of the resonance. The resonance region where ψ librates is shaded. The separatrices and stable point are solid. Three planetary systems are plotted: HD 28109 (this work), TOI-216 (Dawson et al. 2021; Nesvorny, Chrenko & Flock 2021), and KOI-142 (Nesvorný et al. 2013). TOI-216 is firmly in the resonance and KOI-142 is firmly outside the resonance. For HD 28109, the blue dots show a sample of 500 posterior solutions from our dynamical three-planet fit, of which roughly two-thirds are non-resonant and roughly one-third are resonant.

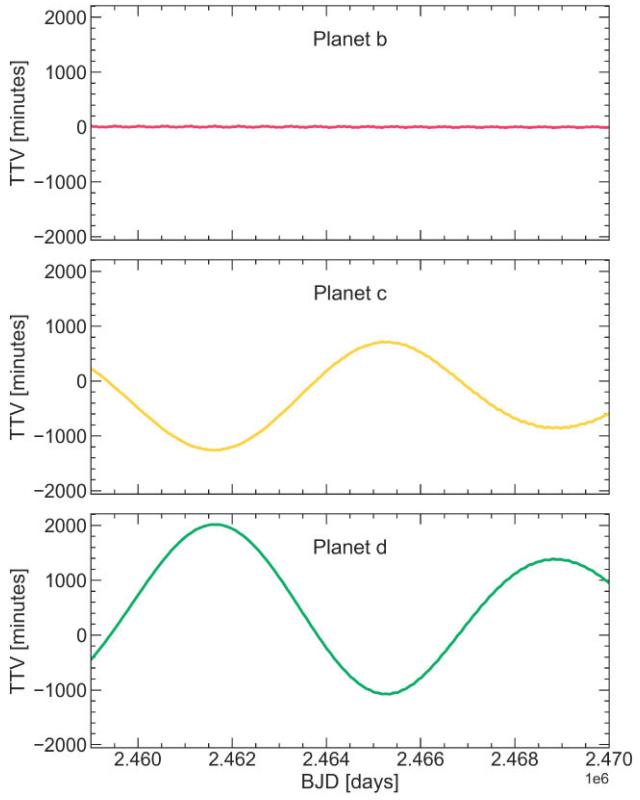


Figure 10. Model predictions of the transit timings variations for the planets of HD 28109 for the next 11 000 d, spanning more than one full TTV period for the two outer planets.

Downloaded from https://academic.oup.com/mnras/article/515/1/1328/6590833 by University of Birmingham user on 22 June 2023

RV noise term added in quadrature to the nominal RV uncertainties and subsums any instrumental or stellar effects (such as activity) not considered by the formal RV errors.

In Fig. 11, we present the phased radial velocity curves. The radial velocity semi-amplitude posterior for the inner planet yields a mass estimate of $M_{\rm b} = 18.50^{+9.12}_{-7.61}$ M$_\oplus$; for the outer planets, we find mass estimates consistent with the estimates from the dynamical analysis: $M_{\rm c} = 7.99^{+2.13}_{-2.03}$ M$_\oplus$ and $M_{\rm d} = 5.53^{+0.98}_{-0.94}$ M$_\oplus$. We do however note that to precisely constrain the masses of the system far more measurements are needed, and therefore, this result is just a first estimate.

6 SYSTEM DISCUSSION

HD 28109 is host to at least three planets, with two very close to a first-order mean-motion resonance. So far, this is the brightest *TESS*star, and the third brightest star overall, known to host TTV planets. In Fig. 12, we present the current sample of planets known to show TTVs in multiplanetary systems, plotted as planet radius and orbital period versus host V magnitude, highlighting the position of the three planets of the HD 28109 system.[6] Planets plotted as dark grey circles have measured masses (by RV or TTV), while grey circles have masses estimated by mass–radius relations. The only host brighter than HD 28109 known to host TTV planets with measured masses is WASP-18, but as the outer planet is non-transiting full characterization of the system is not yet possible (Pearson 2019).

In this section, we discuss the system in the context of other known exoplanetary systems, and current and near-future instrumentation capabilities.

6.1 The planets of HD 28109 on the mass–radius diagram

In Fig. 13, we present a mass–radius diagram showing the positions of HD 28109 b, c, and d in relation to other known exoplanets with masses measured using TTVs or precise radial velocities. The mean densities of Earth, Neptune, Saturn, and pure iron are also shown.

The masses of HD 28109 c and d estimated from TTVs indicate that they are underdense compared with most other sub-Neptunian mass planets. Given the paucity of planets in this size and mass regime with precisely constrained parameters at orbital separations comparable to HD 28109 b and c, we cannot determine at this time whether or not their densities are truly anomalous.

The mass estimate of HD 28109 b is rather more puzzling. First estimates from radial velocities in this work suggest that this planet is significantly denser than typical planets of its size. Atmospheric escape in sub-Neptunes is thought to be driven by photoevaporation (Owen & Wu 2013) and/or core-powered mass-loss (Ginzburg, Schlichting & Sari 2018). At its orbital separation, the gravity of planet b would be sufficient to retain a H/He dominated envelope if stellar irradiation is the main driver (Jin & Mordasini 2018). Should the large mass be confirmed with radial velocities, it could favour core-powered mass-loss as the main driver atmospheric escape in this scenario, as the heat source is the planet's own residual formation energy (Gupta & Schlichting 2020).

Given the two outer planets' relatively large orbital radii (>50 d), it is unlikely that they suffered major mass-loss (Gupta & Schlichting

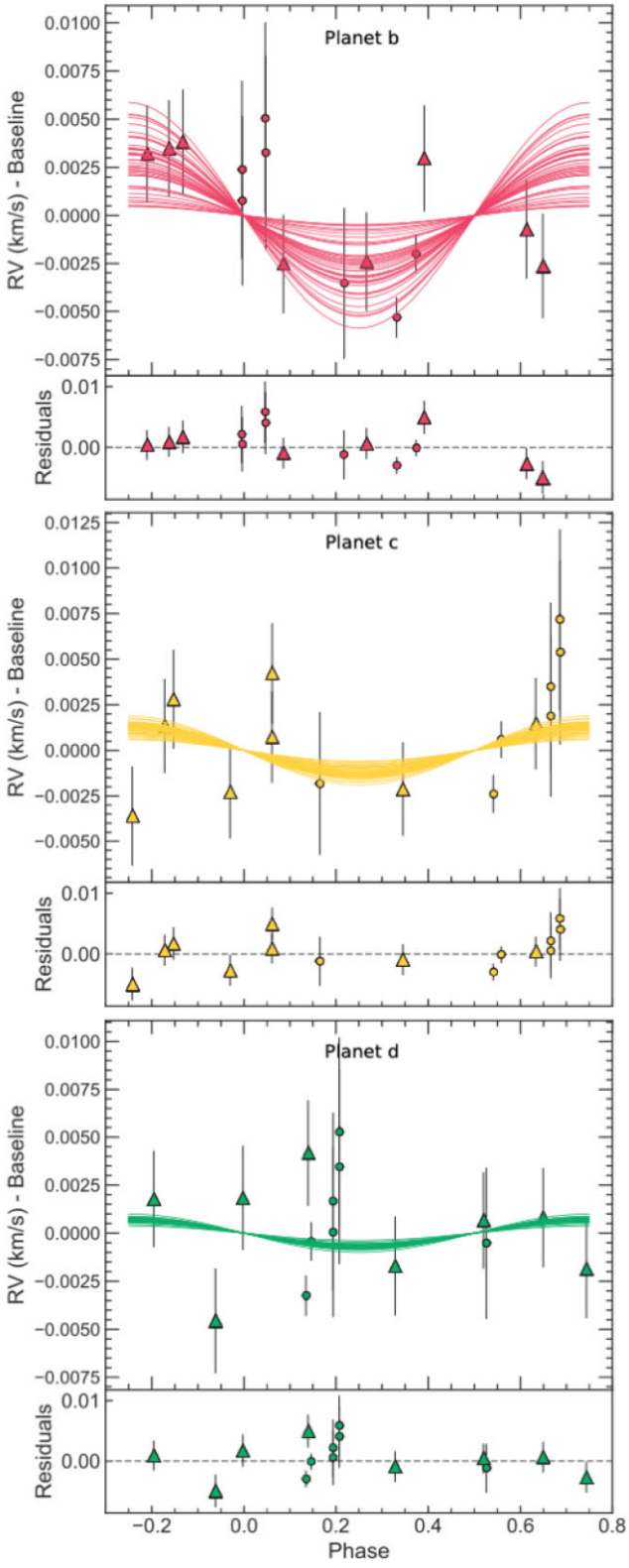


Figure 11. Phased radial velocity measurements for each of the three planets. Triangles are points from ESPRESSO, while circles are points from HARPS; the curves are 20 model samples from the posterior. The data uncertainties include the RV jitter.

[6]Data for this plot was retrieved from the NASA Exoplanet Archive (Akeson et al. 2013) on 2021 October 20: https://exoplanetarchive.ipac.caltech.edu/cgi-bin/TblView/nph-tblView?app = ExoTbls&config = PSCompPars.

Downloaded from https://academic.oup.com/mnras/article/515/1/1328/6590833 by University of Birmingham user on 22 June 2023

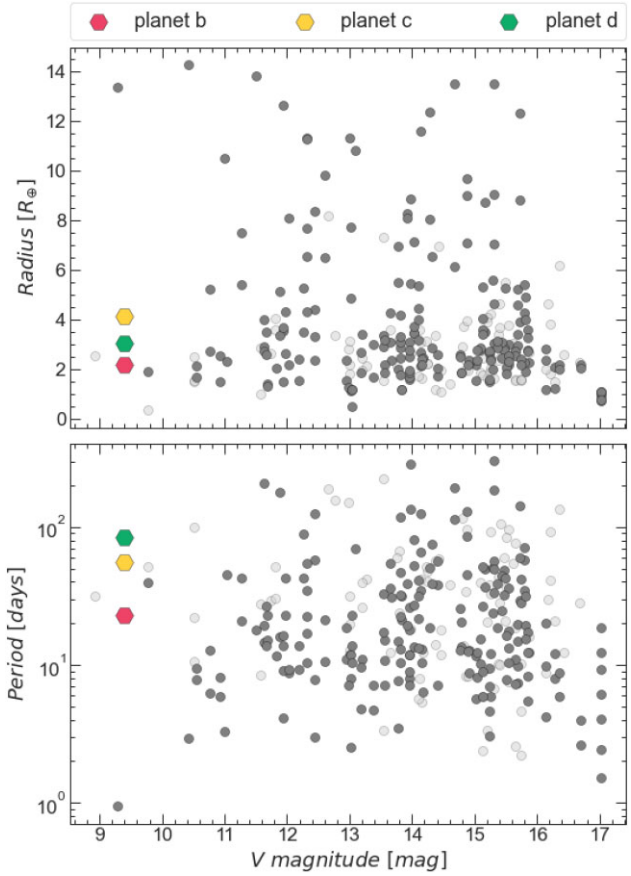


Figure 12. Distribution of known multiplanetary systems exhibiting TTVs. The planets of HD 28109 are shown as hexagons in violet (planet b), green (planet c), and pink (planet d); other planets are either shown in dark grey if they have a measured mass (by RV or TTV) or light grey if they do not. In the upper panel, we show the distribution in planet radius according to host star *V* mag, while in the bottom panel, we show the distribution in orbital period.

2020). Preliminary models of the contraction of the planetary envelope based on the approach used by Guillot et al. (2006) and Valencia et al. (2010) and neglecting the core luminosity indicate that matching their mass, radius, and age require a hydrogen–helium envelope which consists of 19 per cent of the planetary radius for planet c and 10 per cent for planet d. Such a relatively significant envelope mass fraction may result from a formation at large orbital distances (Lee & Chiang 2016). These values are to be considered with caution however because including core luminosity and tidal heating that may be caused by the resonances would yield smaller envelopes (Millholland 2019).

Planets with vastly different densities within the same system, which is likely to be the case for TOI-282, provide invaluable laboratories to explore the various outcomes of planet formation with the same conditions.

6.2 Prospects for precise mass measurements with radial velocities

Stellar activity in HD 28109 poses a challenge on RV follow-up observations, given the small RV semi-amplitudes of these planets. In our RV analysis, we find that the RV jitter terms in the HARPS and ESPRESSO measurements are on the order of 2.4 m s^{-1} and 0.4 m s^{-1}, respectively (Table 3). Given the TTV masses of planets c and d, their expected RV semi-amplitudes are $K_c \approx 1.14$ m s^{-1} and $K_d \approx 0.71$ m s^{-1}. For planet b, the range is broad, spanning from the Chen & Kipping (2017) estimate to the mass of a pure iron planet, $K \approx 0.91$–2.4 m s^{-1}. Given the length of the period of the outermost planet, sampling the full orbit will be a considerable undertaking.

With the goal to further characterize the system, we are currently conducting a radial velocity survey with ESPRESSO; once concluded, the results will be presented in a follow-up paper. These high-precision radial velocity measurements will help to disentangle the eccentricity of planet b, as well as shed light on the possible presence of additional non-transiting planets in the system. In addition, these measurements will finally put precise constraints on the masses of these planets, which will be crucial for atmospheric follow-up observations.

6.3 Dynamical exploration of planet b's parameters

Our dynamical and photometric fits provided us with TTV mass estimates for the two outermost planets, along with strong evidence for circular orbits. However, the mass and eccentricity of planet b remain largely unconstrained, and a dynamical analysis might be able to restrict plausible parameters of planet b. The first three-planet photometric fit in Section 5.1 found an eccentricity of ∼0.8, while the dynamical fits presented in Section 5.2.2 favour an eccentricity of ∼0.17.

We use the Mean Exponential Growth factor of Nearby Orbits chaos index ($Y(t)$, MEGNO; Cincotta & Simó 2000) to assess the stability of the HD 28109 system with the full range of eccentricity and mass estimates for planet b. MEGNO is used to evaluate whether a body's trajectory will be stable following perturbations of its initial conditions. The time-averaged MEGNO $\langle Y(t) \rangle$ will tend to 2 for $t \rightarrow \infty$ if the motion of the body is quasi-periodic, while chaotic behaviour will cause $\langle Y(t) \rangle$ to tend to infinity instead.

We made a 50 × 50 mass-eccentricity grid for planet b with eccentricity values evenly spaced between 0 and 0.8, and masses evenly spaced between 5 and 30 $M_\oplus$. We used the MEGNO implementation of the *N*-body integrator REBOUND (Rein & Liu 2012) which in turn uses the Wisdom–Holman WHFAST code (Rein & Tamayo 2015). We used steps of 1/50th of the period of planet b (0.5 d) and integrated for 10 000 orbits of the outermost planet (∼ 2300 yr) to construct a two-dimensional MEGNO map. We find that the full mass range is non-chaotic but only for eccentricities smaller than ∼0.4; eccentricities up to ∼0.5 can be stable but only for the largest masses in the range we tested. This indicates that a wide range of mass values are possible for planet b, in line with the wide mass prior used for our dynamical and RV fits.

6.4 Prospects For Atmospheric Characterization with *HST* and *JWST*

To assess the suitability of HD 28109 b, c, and d for atmospheric characterization using transmission and emission spectroscopy, we calculated for each planet the Transmission and Emission Spectroscopy Metrics following Kempton et al. (2018). The TSMs for each planet are 20, 64, and 38, respectively, while the ESMs are 1.08, 1.43, and 0.52. Given the brightness of the host and the long periods of the planets leading to equilibrium temperatures below 900K, the secondary eclipses would have very low SNR, making characterization with this method too challenging. However, their TSMs indicate that characterization with transmission spectroscopy is possible in principle.

Downloaded from https://academic.oup.com/mnras/article/515/1/1328/6590833 by University of Birmingham user on 22 June 2023

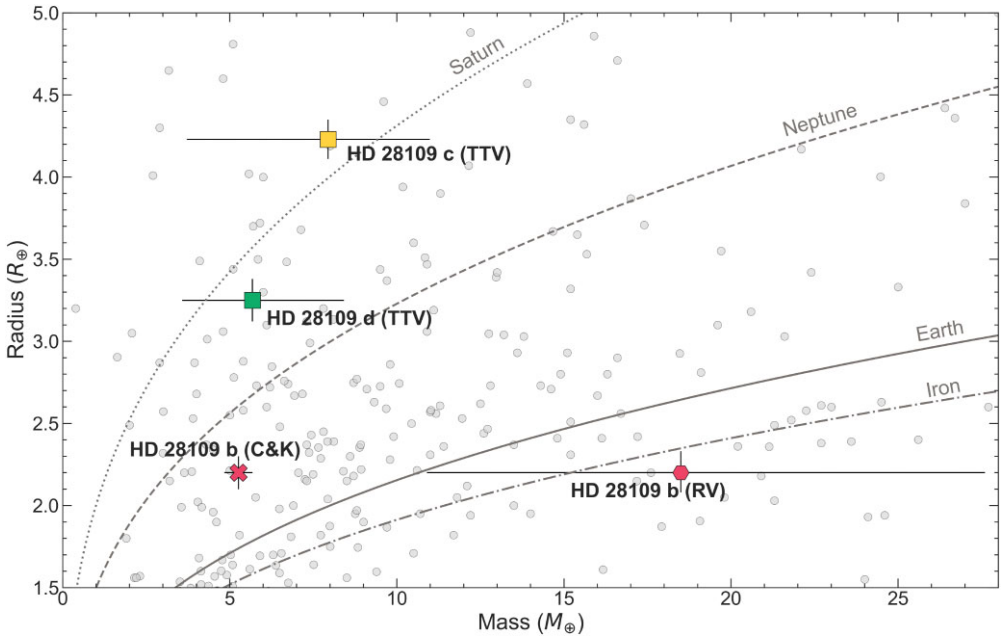


Figure 13. Mass–radius diagram showing the positions of HD 28109 b, c, and d. Planets c and d are plotted as squares with their masses are estimated from TTVs. As the mass of planet b is still poorly constrained, we plot its position using its RV estimated mass as a hexagon, while the average mass for planets of its radius [estimated mass following Chen & Kipping (2017)] is plotted as a cross.

We produced model transmission spectra for all three planets using EXO_TRANSMIT (Kempton et al. 2017) assuming solar metallicity and C/O ratio for the host, and cloud-free H_2 dominated atmospheres for the planets. Using these spectra we then used PANDEXO (Batalha et al. 2017) to simulate *Hubble Space Telescope* (*HST* hereafter) observations of their atmospheres using transmission spectroscopy. Our simulations indicate that for the two outermost planets a single *HST* transit would be sufficient to carry out reconnaissance spectroscopy (as in de Wit et al. 2018, 2016), to assess the presence of clouds in their atmospheres. In the event of a cloud-free atmosphere, we could detect the presence of water in transmission to 8σ and 3.5σ, respectively. To reach a 3.5σ detection for planet b could require a large number of transits, but with its mass unconstrained for the time being we cannot make a fair estimate. As an example, should the mass be consistent with the Chen & Kipping (2017) estimate, we would require 6 transits, each spanning 8 orbits of *HST* to reach a 3.5σ detection. We present the model spectra along with simulated *HST* observations in Fig. 14.

We do also note that the simulations described above assume the TTV masses for planets c and d, and the mass estimated from mass–radius relations for planet b. Should any mass be significantly larger the scale height of the atmosphere will decrease, leading to lower significance detections.

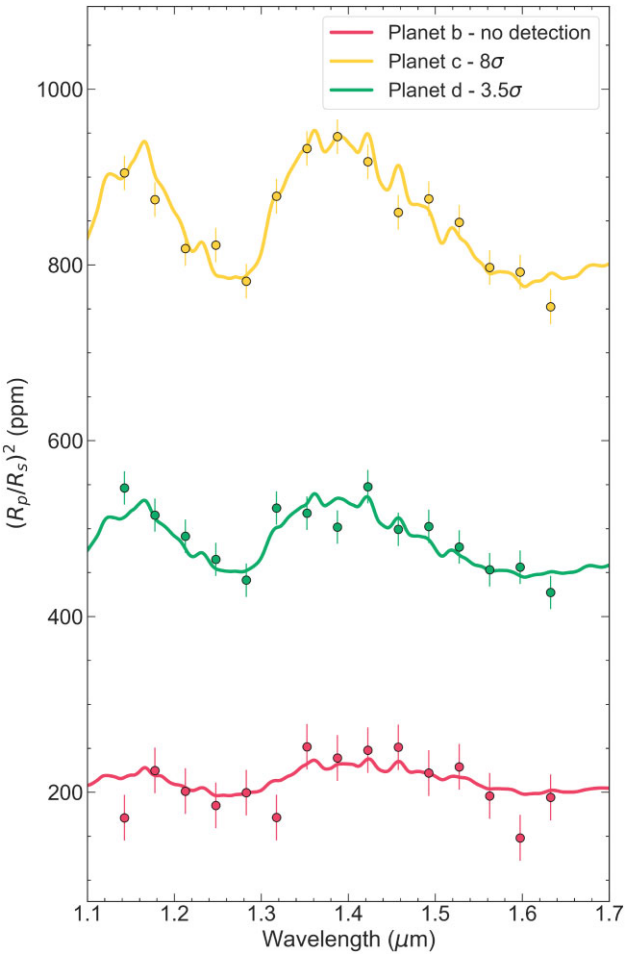


Figure 14. Model transmission spectra of HD 28109 b, c, and d with simulated *HST* observations. Each point corresponds to a single transit depth with no offset; the curves represent the simulated transmission spectra.

7 CONCLUSIONS

In this work, we have presented the discovery and confirmation of three sub-Neptune sized planets orbiting HD 28109. Given the brightness of the host, the planets are well-suited to precise radial velocity measurements, which will allow comparison of TTV masses with RV masses. This system is also the brightest *TESS*system discovered to date known to host TTV, making it an exquisite laboratory for planet formation theory. Additionally, we have shown that the outer two planets are well suited to atmospheric reconnaissance with current

Downloaded from https://academic.oup.com/mnras/article/515/1/1328/6590833 by University of Birmingham user on 22 June 2023

instrumentation, and they will be high-priority planets for follow-up with *JWST*and *Ariel*.

This work has also demonstrated the capabilities of *ASTEP*as an observatory specializing in planets with long periods, very long transits, and large TTVs. The uninterrupted night enjoyed from Antarctica during two months of the year enables observations of systems that cannot be feasibly followed from anywhere else in the world. Continued selection of these candidates for follow-up will help the community fill out the most sparsely populated parameter spaces in the ever-growing field of exoplanets.

ACKNOWLEDGEMENTS

The authors wish the thank the reviewer for their comments and feedback which helped to improve and clarify the manuscript. This work makes use of observations from the ASTEP telescope. ASTEP benefited from the support of the French and Italian polar agencies IPEV and PNRA in the framework of the Concordia station programme, from OCA, INSU, and Idex UCAJEDI (ANR-15-IDEX-01). The authors would also like the winterover staff of Concordia station; their work makes the continued operations of ASTEP possible. Some of the observations in the paper made use of the High-Resolution Imaging instrument Zorro obtained under Gemini LLP Proposal Number: GN/S-2021A-LP-105. Zorro was funded by the NASA Exoplanet Exploration Program and built at the NASA Ames Research Center by Steve B. Howell, Nic Scott, Elliott P. Horch, and Emmett Quigley. Zorro was mounted on the Gemini North (and/or South) telescope of the international Gemini Observatory, a programme of NSF's OIR Lab, which is managed by the Association of Universities for Research in Astronomy (AURA) under a cooperative agreement with the National Science Foundation on behalf of the Gemini partnership: the National Science Foundation (United States), National Research Council (Canada), Agencia Nacional de Investigación y Desarrollo (Chile), Ministerio de Ciencia, Tecnología e Innovación (Argentina), Ministério da Ciência, Tecnologia, Inovações e Comunicações (Brazil), and Korea Astronomy and Space Science Institute (Republic of Korea). This work has made use of data from the European Space Agency (ESA) mission *Gaia* (https://www.cosmos.esa.int/gaia), processed by the *Gaia* Data Processing and Analysis Consortium (DPAC, https://www.cosmos.esa.int/web/gaia/dpac/consortium). Funding for the DPAC has been provided by national institutions, in particular the institutions participating in the *Gaia* Multilateral Agreement. This paper includes data collected by the *TESS*mission. Funding for the *TESS*mission is provided by the NASA's Science Mission Directorate. Based in part on observations collected at the European Organisation for Astronomical Research in the Southern Hemisphere under ESO programme(s) 0102.C-0503(A). This work makes use of observations from the LCOGT network. Part of the LCOGT telescope time was granted by NOIRLab through the Mid-Scale Innovations Program (MSIP). MSIP is funded by NSF. MNG acknowledges support from the European Space Agency (ESA) as an ESA Research Fellow. Part of this work has been carried out within the framework of the NCCR PlanetS supported by the Swiss National Science Foundation. This research received funding from the European Research Council (ERC) under the European Union's Horizon 2020 research and innovation programme (grant agreement no. 803193/BEBOP), and from the Science and Technology Facilities Council (STFC; grant no. ST/S00193X/1). DG gratefully acknowledges financial support from the Cassa di Risparmio di Torino (CRT) foundation under grant no. 2018.2323 'Gaseous or rocky? Unveiling the nature of small worlds'. This research made use of LIGHTKURVE, a PYTHON package for *Kepler*and *TESS*data analysis (Lightkurve Collaboration et al. 2018), which in turn makes use of ASTROPY,[7] a community-developed core PYTHON package for Astronomy (Astropy Collaboration et al. 2013, 2018), ASTROQUERY (Ginsburg et al. 2019), and TESSCUT (Brasseur et al. 2019).

DATA AVAILABILITY

*TESS*data products are available via the MAST portal at https://mast.stsci.edu/portal/Mashup/Clients/Mast/Portal.html. Follow-up photometry and high-resolution imaging data for HD 28109 are available on ExoFOP at https://exofop.ipac.caltech.edu/tess/target.php?id = 29781292. These data are freely accessible to ExoFOP members immediately and are publicly available following a one-year proprietary period. The radial velocity data used in this paper are available via the ESO Public Archive at http://archive.eso.org/eso/eso_archive_main.html.

REFERENCES

Abe L. et al., 2013, A&A, 553, A49
Agol E., Steffen J., Sari R., Clarkson W., 2005, MNRAS, 359, 567
Akeson R. L. et al., 2013, PASP, 125, 989
Aller A., Lillo-Box J., Jones D., Miranda L. F., Barceló Forteza S., 2020, A&A, 635, A128
Astropy Collaboration et al., 2013, A&A, 558, A33
Astropy Collaboration et al., 2018, AJ, 156, 123
Bailer-Jones C. A. L., Rybizki J., Fouesneau M., Demleitner M., Andrae R., 2021, AJ, 161, 147
Baranne A. et al., 1996, A&AS, 119, 373
Batalha N. E. et al., 2017, PASP, 129, 064501
Bean J. L., Raymond S. N., Owen J. E., 2021, J. Geophys. Res. (Planets), 126, e06639
Borucki W. J. et al., 2010, Science, 327, 977
Brasseur C. E., Phillip C., Fleming S. W., Mullally S. E., White R. L., 2019, Astrocut: Tools for creating cutouts of TESS images. preprint (ascl:1905.007)
Broeg C. et al., 2013, CHEOPS: A transit photometry mission for ESA's small mission programme. Hot Planets and Cool Stars, Garching, Germany, p. 03005
Brown T. M. et al., 2013, Publ. Astron. Soc. Pac., 125, 1031
Buchhave L. A. et al., 2012, Nature, 486, 375
Chen J., Kipping D., 2017, ApJ, 834, 17
Ciardi D. R., Beichman C. A., Horch E. P., Howell S. B., 2015, ApJ, 805, 16
Cincotta P. M., Simó C., 2000, A&AS, 147, 205
Coleman G. A. L., Nelson R. P., 2016, MNRAS, 457, 2480
Collins K. A., Kielkopf J. F., Stassun K. G., Hessman F. V., 2017, AJ, 153, 77
Crouzet N. et al., 2010a, in Spinoglio L., Epchtein N., eds, EAS Publications Series, Vol. 40. 3rd ARENA Conference, Frascati, Italie, p. 367
Crouzet N. et al., 2010b, A&A, 511, A36
Crouzet N. et al., 2018, A&A, 619, A116
Cutri R. M. et al., 2003, VizieR Online Data Catalog, II/246
Dawson R. I. et al., 2021, AJ, 161, 161
de Wit J. et al., 2016, Nature, 537, 69
de Wit J. et al., 2018, Nature Astron., 2, 214
Deck K. M., Agol E., 2015, ApJ, 802, 116
Demory B. O. et al., 2020, A&A, 642, A49
Dietrich J., Apai D., 2020, AJ, 160, 107
Donati J. F., Semel M., Carter B. D., Rees D. E., Collier Cameron A., 1997, MNRAS, 291, 658
Eisner N., Lintott C., Aigrain S., 2020, J. Open Source Softw., 5, 2101
Fabrycky D. C. et al., 2014, ApJ, 790, 146

[7] http://www.astropy.org

Downloaded from https://academic.oup.com/mnras/article/515/1/1328/6590833 by University of Birmingham user on 22 June 2023

Feroz F., Hobson M. P., 2008, MNRAS, 384, 449
Findeisen K., Hillenbrand L., Soderblom D., 2011, AJ, 142, 23
Foreman-Mackey D., Hogg D. W., Lang D., Goodman J., 2013, PASP, 125, 306
Foreman-Mackey D., Agol E., Ambikasaran S., Angus R., 2017, Fast and Scalable Gaussian Process Modeling with Applications to Astronomical Time Series, The Astronomical Journal. Vol. 154 preprint (ascl:1709.008)
Fressin F. et al., 2013, ApJ, 766, 81
Fulton B. J. et al., 2017, AJ, 154, 109
Furlan E., Howell S. B., 2017, AJ, 154, 66
Gaia Collaboration et al., 2016, A&A, 595, A1
Gaia Collaboration et al., 2018, A&A, 616, A1
Gaia Collaboration et al., 2021, A&A, 649, A1
Giacalone S. et al., 2021, AJ, 161, 24
Ginsburg A. et al., 2019, AJ, 157, 98
Ginzburg S., Schlichting H. E., Sari R., 2018, MNRAS, 476, 759
Gray D. F., 2005, The Observation and Analysis of Stellar Photospheres. Cambridge Univ. Press, Cambridge
Guerrero N. M. et al., 2021, ApJS, 254, 39
Guillot T., Santos N. C., Pont F., Iro N., Melo C., Ribas I., 2006, A&A, 453, L21
Guillot T. et al., 2015, Astron. Nachr., 336, 638
Günther M. N., Daylan T., 2021, Allesfitter: Flexible Star and Exoplanet Inference from Photometry and Radial Velocity The Astrophysical Journal Supplement Series. Vol. 254, preprint (ascl:1903.003)
Günther M. N., Daylan T., 2021, ApJS, 254, 13
Gupta A., Schlichting H. E., 2020, MNRAS, 493, 792
Hadden S., Barclay T., Payne M. J., Holman M. J., 2019, AJ, 158, 146
Hippke M., Heller R., 2019, Optimized transit detection algorithm to search for periodic transits of small planets, A&A, 623
Hippke M., David T. J., Mulders G. D., Heller R., 2019, AJ, 158, 143
Holman M. J., Murray N. W., 2005, Science, 307, 1288
Holman M. J. et al., 2010, Science, 330, 51
Houk N., Cowley A. P., 1975, University of Michigan Catalogue of Two-Dimensional Spectral Types for the HD Stars. Volume I. Declinations -90_ to -53_f0. Department of Astronomy, University of Michigan, Ann Arbor, MI, USA
Howard A. W. et al., 2010a, Science, 330, 653
Howard A. W. et al., 2010b, ApJ, 721, 1467
Howell S. B., Everett M. E., Sherry W., Horch E., Ciardi D. R., 2011, AJ, 142, 19
Howell S. B., Matson R. A., Ciardi D. R., Everett M. E., Livingston J. H., Scott N. J., Horch E. P., Winn J. N., 2021, AJ, 161, 164
Husser T. O., Wende-von Berg S., Dreizler S., Homeier D., Reiners A., Barman T., Hauschildt P. H., 2013, A&A, 553, A6
Høg E. et al., 2000, A&A, 355, L27
Izidoro A., Bitsch B., Raymond S. N., Johansen A., Morbidelli A., Lambrechts M., Jacobson S. A., 2021, A&A, 650, A152
Jenkins J. M. et al., 2016, in Chiozzi G., Guzman J. C., eds, Proc. SPIE Conf. Ser. Vol. 9913, Software and Cyber Infrastructure for Astronomy IV. SPIE, Bellingham, p. 99133E
Jensen E., 2013, Tapir: A Web Interface for Transit/eclipse Observability. Astrophysics Source Code Library, preprint (ascl:1306.007)
Jin S., Mordasini C., 2018, ApJ, 853, 163
Johansen A., Lambrechts M., 2017, Ann. Rev. Earth Planet. Sci., 45, 359
Kass R. E., Raftery A. E., 1995, J. Am. Stat. Assoc., 90, 773
Kempton E. M. R., Lupu R., Owusu-Asare A., Slough P., Cale B., 2017, PASP, 129, 044402
Kempton E. M. R. et al., 2018, PASP, 130, 114401
Kipping D. M., 2013, MNRAS, 435, 2152
Kipping D. M., 2014, MNRAS, 440, 2164
Kurucz R. L., 1979, ApJS, 40, 1
Lambrechts M., Morbidelli A., Jacobson S. A., Johansen A., Bitsch B., Izidoro A., Raymond S. N., 2019, A&A, 627, A83
Lee E. J., Chiang E., 2015, ApJ, 811, 41
Lee E. J., Chiang E., 2016, ApJ, 817, 90
Lenzen R. et al., 2003, in Iye M., Moorwood A. F. M., eds, Proc. SPIE Conf. Ser. Vol. 4841, Instrument Design and Performance for Optical/Infrared Ground-based Telescopes. SPIE, Bellingham, p. 944
Lightkurve Collaboration et al., 2018, Astrophysics Source Code Library, record ascl:1812.013
Lissauer J. J. et al., 2012, ApJ, 750, 112
Lithwick Y., Xie J., Wu Y., 2012, ApJ, 761, 122
Lovis C., Pepe F., 2007, A&A, 468, 1115
Mamajek E. E., Hillenbrand L. A., 2008, ApJ, 687, 1264
Matson R. A., Howell S. B., Horch E. P., Everett M. E., 2018, AJ, 156, 31
Matsumura S., Thommes E. W., Chatterjee S., Rasio F. A., 2010, ApJ, 714, 194
Maxted P. F. L., 2016, A&A, 591, A111
Mayor M. et al., 2003, Messenger, 114, 20
Mayor M. et al., 2011, preprint (arXiv:1109.2497)
McCully C., Volgenau N. H., Harbeck D.-R., Lister T. A., Saunders E. S., Turner M. L., Siiverd R. J., Bowman M., 2018, Proc. SPIE, 10707, 107070K
Mékarnia D. et al., 2016, MNRAS, 463, 45
Millholland S., 2019, ApJ, 886, 72
Nesvorný D., Vokrouhlický D., 2016, ApJ, 823, 72
Nesvorný D., Kipping D. M., Buchhave L. A., Bakos G. Á., Hartman J., Schmitt A. R., 2012, Science, 336, 1133
Nesvorný D., Kipping D., Terrell D., Hartman J., Bakos G. Á., Buchhave L. A., 2013, ApJ, 777, 3
Nesvorny D., Chrenko O., Flock M., 2021, TOI-216: Resonant Constraints on Planet Migration. The Astrophysical Journal, Vol. 925, preprint(arXiv:2110.09577)
Owen J. E., Wu Y., 2013, ApJ, 775, 105
Paredes L. A., Henry T. J., Quinn S. N., Gies D. R., Hinojosa-Goñi R., James H.-S., Jao W.-C., White R. J., 2021, AJ, 162, 176
Parviainen H., Aigrain S., 2015, MNRAS, 453, 3821
Pearson K. A., 2019, AJ, 158, 243
Pepe F., Mayor M., Galland F., Naef D., Queloz D., Santos N. C., Udry S., Burnet M., 2002, A&A, 388, 632
Pepe F. et al., 2021, A&A, 645, A96
Pozuelos F. J. et al., 2020, A&A, 641, A23
Pu B., Wu Y., 2015, ApJ, 807, 44
Rein H., 2012, MNRAS, 427, L21
Rein H., Liu S. F., 2012, A&A, 537, A128
Rein H., Tamayo D., 2015, MNRAS, 452, 376
Ricker G. R. et al., 2015, J. Astron. Telesc. Instr. Syst., 1, 014003
Rousset G. et al., 2003, in Wizinowich P. L., Bonaccini D., eds, Proc. SPIE Conf. Ser. Vol. 4839, Adaptive Optical System Technologies II. SPIE, Bellingham, p. 140
Savitzky A., Golay M. J. E., 1964, Anal. Chem., 36, 1627
Schlegel D. J., Finkbeiner D. P., Davis M., 1998, ApJ, 500, 525
Seager S., Mallén-Ornelas G., 2003, ApJ, 585, 1038
Skilling J., 2004, in Fischer R., Preuss R., Toussaint U. V., eds, AIP Conf. Ser. Vol. 735, 24th International Workshop on Bayesian Inference and Maximum Entropy Methods in Science and Engineering. Am. Inst. Phys., New York, p. 395
Speagle J. S., 2020, MNRAS, 493, 3132
Stassun K. G., Torres G., 2016, AJ, 152, 180
Stassun K. G., Torres G., 2021, ApJ, 907, L33
Stassun K. G., Collins K. A., Gaudi B. S., 2017, AJ, 153, 136
Stassun K. G., Corsaro E., Pepper J. A., Gaudi B. S., 2018, AJ, 155, 22
Stassun K. G. et al., 2019, AJ, 158, 138
Tokovinin A., 2018, PASP, 130, 035002
Tokovinin A., Fischer D. A., Bonati M., Giguere M. J., Moore P., Schwab C., Spronck J. F. P., Szymkowiak A., 2013, PASP, 125, 1336
Torres G., Andersen J., Giménez A., 2010, A&AR, 18, 67
Twicken J. D. et al., 2018, PASP, 130, 064502
Valencia D., Ikoma M., Guillot T., Nettelmann N., 2010, A&A, 516, A20
Van Eylen V., Agentoft C., Lundkvist M. S., Kjeldsen H., Owen J. E., Fulton B. J., Petigura E., Snellen I., 2018, MNRAS, 479, 4786
Wright E. L. et al., 2010, AJ, 140, 1868

Downloaded from https://academic.oup.com/mnras/article/515/1/1328/6590833 by University of Birmingham user on 22 June 2023

York D. G. et al., 2000, AJ, 120, 1579
Zhou G. et al., 2018, AJ, 156, 93
Ziegler C., Tokovinin A., Briceño C., Mang J., Law N., Mann A. W., 2020, AJ, 159, 19

[1]*School of Physics & Astronomy, University of Birmingham, Edgbaston, Birmingham B15 2TT, UK*
[2]*Université Côte d'Azur, Observatoire de la Côte d'Azur, CNRS, Laboratoire Lagrange, Bd de l'Observatoire, CS 34229, F-06304 Nice cedex 4, France*
[3]*Southwest Research Institute, Department of Space Studies, 1050 Walnut St., Suite 400, Boulder, CO 80302, USA*
[4]*European Space Agency (ESA), European Space Research and Technology Centre (ESTEC), Keplerlaan 1, NL-2201 AZ Noordwijk, the Netherlands*
[5]*Leiden Observatory, Leiden University, Postbus 9513, NL-2300 RA, Leiden, the Netherlands*
[6]*INAF OAS, Osservatorio di Astrofisica e Scienza dello Spazio di Bologna via Piero Gobetti 93/3, Bologna, Italy*
[7]*Deutsches Zentrum für Luft- und Raumfahrt, Rutherfordstr. 2, D-12489 Berlin, Germany*
[8]*Dipartimento di Fisica, Università Degli Studi di Torino Via Pietro Giuria, 1, I-10125, Torino, Italy*
[9]*European Southern Observatory, Alonso de Cordova 3107, Vitacura, Santiago, Chile*
[10]*Center for Astrophysics | Harvard & Smithsonian, 60 Garden St, Cambridge, MA 02138, USA*
[11]*Dpto. Física Teórica y del Cosmos, Universidad de Granada, E-18071, Granada, Spain*
[12]*NASA Ames Research Center, Moffett Field, CA 94035, USA*
[13]*Geneva Observatory, University of Geneva, Chemin Pegasi 51, 1290 Versoix, Switzerland*
[14]*Department of Physics & Astronomy, Vanderbilt University, 6301 Stevenson Center Ln., Nashville, TN 37235, USA*
[15]*Hazelwood Observatory , Churchill, Victoria, Australia*
[16]*Department of Physics, Engineering and Astronomy, Stephen F. Austin State University, 1936 North Str, Nacogdoches, TX 75962, USA*
[17]*Department of Physics and Astronomy, University of Kansas, Lawrence, KS 66045, USA*
[18]*Department of Physics and Astronomy, The University of North Carolina at Chapel Hill, Chapel Hill, NC 27599, USA*
[19]*The United States Naval Observatory, 3450 Massachusetts Ave, NW, Washington, DC 20392, USA*
[20]*NASA Goddard Space Flight Center, 8800 Greenbelt Rd, Greenbelt, MD 20771, USA*
[21]*Centre for Astrophysics, University of Southern Queensland, West Street, Toowoomba, QLD 4350, Australia*

This paper has been typeset from a TEX/LATEX file prepared by the author.

Downloaded from https://academic.oup.com/mnras/article/515/1/1328/6590833 by University of Birmingham user on 22 June 2023

3.4 Paper: Validation of the TOI-715 system

During the first year of my PhD, I did for SPECULOOS some very similar work to what I did for ASTEP[a], in organising and managing observations. This was in the form of Google Sheets and a website to manage annex observations, as well as liaising with the person in charge of scheduling to ensure all annex observations were in the plans when needed.

TOI-715.01 was first proposed for observation by SPECULOOS by another PhD student and close collaborator of mine, Mathilde Timmermans. She and I worked together on SPECULOOS's *TESS* follow-up programme, and we both proposed many targets for observation. At the time, Mathilde was already busy preparing the validation of TOI-4336 b (Timmermans, in prep); as such, I was asked to lead the follow-up campaign for TOI-715. Once we had enough observations, I submitted an abstract to the *TESS* Wiki on behalf of the SPECULOOS team.

As the transits of the planet are very shallow, we continued to schedule as many transit observations as possible to build up the SNR over the course of the following year. This system was of interest to many teams due to the small size of the planet, and the fact that it is in its host's habitable zone; therefore there were also observations contributed by several other observatories. I liaised with the other teams, and had additional observations provided by Khalid Barkaoui (on behalf of LCO), Marion Cointepas (on behalf of ExTrA), and Franco Mallia (on behalf of OACC-CAO). SPECULOOS-South observations were also supplemented by TRAPPIST-South, as scheduled by Mathilde Timmermans. SPECULOOS and TRAPPIST observations were reduced by myself and Mathilde; photometry by other observatories was provided to us already reduced.

As with HD 28109/TOI-282, Keivan Stassun carried out the SED analysis and provided stellar parameters. The reconnaissance spectroscopy for this system was collected by Benjamin Rackham, reduced by Daniel Sebastian, and analysed by Adam Burgasser. The kinematic analysis to estimate the age of the system was done by Christian Aganze. High resolution imaging was provided once again by Steve Howell.

The vetting of the system was done by myself and Mathilde Timmermans, and the `SHERLOCK` search for additional candidates was conducted by Martín Devora-Pajares. The statistical validation using `TRICERATOPS` was done by me without the use of the `SHERLOCK` validation module on this occasion. I carried out the full global analysis of all the available photometry for both the validated planet and the newly identified candidate.

In the discussion section, Prajwal Niraula contributed the atmospheric simulations, while I calculated the transmission spectroscopy metrics. The section on the potential impact of flares on habitability was written by Maximilian Günther, and Daniel Sebastian wrote about the prospects for measuring the mass of TOI-715 b with ESPRESSO.

This work is published in MNRAS (Dransfield et al. 2023).

[a]The service work for ASTEP is documented in Chapter 2.6, but the similar service work done for SPECULOOS is not published).

Monthly Notices of the ROYAL ASTRONOMICAL SOCIETY

MNRAS **00,** 1–18 (2023) https://doi.org/10.1093/mnras/stad1439
Advance Access publication 2023 May 18

A 1.55 $R_\oplus$ habitable-zone planet hosted by TOI-715, an M4 star near the ecliptic South Pole

Georgina Dransfield [1★†‡§] Mathilde Timmermans,[2★] Amaury H. M. J. Triaud [1★] Martín Dévora-Pajares,[3] Christian Aganze,[4] Khalid Barkaoui [2,5,6] Adam J. Burgasser,[4] Karen A. Collins [7] Marion Cointepas,[8,9] Elsa Ducrot,[10] Maximilian N. Günther,[11] Steve B. Howell,[12] Catriona A. Murray,[13] Prajwal Niraula,[5] Benjamin V. Rackham [5] Daniel Sebastian [1] Keivan G. Stassun [14] Sebastián Zúñiga-Fernández,[2] José Manuel Almenara [8] Xavier Bonfils,[8] François Bouchy,[9] Christopher J. Burke,[15] David Charbonneau,[7] Jessie L. Christiansen,[16] Laetitia Delrez [2] Tianjun Gan,[17] Lionel J. García,[2] Michaël Gillon [2] Yilen Gómez Maqueo Chew,[18] Katharine M. Hesse,[15] Matthew J. Hooton [19] Giovanni Isopi,[20] Emmanuël Jehin,[21] Jon M. Jenkins,[12] David W. Latham,[7] Franco Mallia,[20] Felipe Murgas,[6,8,22] Peter P. Pedersen,[19] Francisco J. Pozuelos,[2,21,23] Didier Queloz,[19] David R. Rodriguez [24] Nicole Schanche [17,25,26] Sara Seager,[4,22,27] Gregor Srdoc,[28] Chris Stockdale,[29] Joseph D. Twicken,[12,30,31] Roland Vanderspek,[15] Robert Wells,[25] Joshua N. Winn,[32] Julien de Wit[5] and Aldo Zapparata [20]

Affiliations are listed at the end of the paper

Accepted 2023 May 9. Received 2023 May 9; in original form 2022 November 3

ABSTRACT

A new generation of observatories is enabling detailed study of exoplanetary atmospheres and the diversity of alien climates, allowing us to seek evidence for extraterrestrial biological and geological processes. Now is therefore the time to identify the most unique planets to be characterized with these instruments. In this context, we report on the discovery and validation of TOI-715 b, a $R_b = 1.55 \pm 0.06 R_\oplus$ planet orbiting its nearby (42 pc) M4 host (TOI-715/TIC 271971130) with a period $P_b = 19.288004^{+0.000027}_{-0.000024}$ d. TOI-715 b was first identified by *TESS* and validated using ground-based photometry, high-resolution imaging and statistical validation. The planet's orbital period combined with the stellar effective temperature $T_{eff} = 3075 \pm 75$ K give this planet an installation $S_b = 0.67^{+0.15}_{-0.20}$ $S_\oplus$, placing it within the most conservative definitions of the habitable zone for rocky planets. TOI-715 b's radius falls exactly between two measured locations of the M-dwarf radius valley; characterizing its mass and composition will help understand the true nature of the radius valley for low-mass stars. We demonstrate TOI-715 b is amenable for characterization using precise radial velocities and transmission spectroscopy. Additionally, we reveal a second candidate planet in the system, TIC 271971130.02, with a potential orbital period of $P_{02} = 25.60712^{+0.00031}_{-0.00036}$ d and a radius of $R_{02} = 1.066 \pm 0.092 R_\oplus$, just inside the outer boundary of the habitable zone, and near a 4:3 orbital period commensurability. Should this second planet be confirmed, it would represent the smallest habitable zone planet discovered by *TESS* to date.

Key words: planets and satellites: detection – planets and satellites: fundamental parameters – planets and satellites: terrestrial planets.

1 INTRODUCTION

At long last the era of *JWST* has arrived, and with it the age of detailed exoplanetary atmospheric characterization (The *JWST* Transiting Exoplanet Community Early Release Science Team 2023). This achievement was unlocked just as the community hit another significant milestone: the discovery of the 5000th planet beyond the solar system.[1] This ever-growing sample combined with the might of *JWST* is now set to deepen our understanding of planets, including those in our solar system, on a sub-population level.

★ E-mail: gxg831@student.bham.ac.uk (DG);
Mathilde.timmermans@uliege.be (MT); a.triaud@bham.ac.uk (AHMJT)
† Paris Region Fellow, Marie Sklodowska-Curie Action.
‡ ESA Research Fellow.
§ 51 Pegasi b Fellow.

[1] Reported on 2022 March 21: https://exoplanetarchive.ipac.caltech.edu/docs/exonews_archive.html.

© 2023 The Author(s).
Published by Oxford University Press on behalf of Royal Astronomical Society. This is an Open Access article distributed under the terms of the Creative Commons Attribution License (http://creativecommons.org/licenses/by/4.0/), which permits unrestricted reuse, distribution, and reproduction in any medium, provided the original work is properly cited.

One sub-population of particularly enduring interest consists of small, potentially habitable planets orbiting cool M-type stars. With current instrumentation, M dwarfs represent our best hope of finding temperate terrestrial planets, the best example being the seven Earth-sized planets of the TRAPPIST-1 system orbiting an M8V type star (Gillon et al. 2017). The reduced radii of M dwarfs enable small planets to produce large transit depths; this combined with the shorter orbital periods of these more compact systems makes photometric monitoring from ground and space-based facilities considerably more feasible (e.g. Nutzman & Charbonneau 2008; Reiners et al. 2018; Sebastian et al. 2021; Triaud 2021). In the context of atmospheric characterization by transmission spectroscopy, bright, nearby M dwarfs are ideal planetary hosts as small temperate planets will transit frequently, enabling high signal-to-noise detections of atmospheric features with fewer hours of telescope time (Charbonneau & Deming 2007; Dressing & Charbonneau 2015; Morley et al. 2017). Additionally, these low mass stars appear more likely to host small planets from a theoretical and observational point of view (Montgomery & Laughlin 2009; Bonfils et al. 2013; Dressing & Charbonneau 2013; Mulders, Pascucci & Apai 2015; Alibert & Benz 2017; He, Triaud & Gillon 2017; Sabotta et al. 2021).

The so-called 'habitable zone' is a circumstellar region where an Earth-like planet could sustain liquid water on its surface (Kasting, Whitmire & Reynolds 1993). With sometimes contradictory definitions of its boundaries, which depend on stellar spectral type, planetary albedo, mass and even cloud cover (Underwood, Jones & Sleep 2003; Kopparapu et al. 2014; Ramirez & Kaltenegger 2016), it can be challenging to categorise planets using this metric. However, the most widely applicable and conservative definition comes from Kopparapu et al. (2013), stating that rocky planets receiving between 0.42 and 0.842 $S_\oplus$ are in their star's HZ, irrespective of all other factors.

The activity of the M-dwarf host stars themselves is an additional factor to consider in the habitability of planets orbiting M dwarfs, as the effect of their frequent flaring is not fully known (O'Malley-James & Kaltenegger 2017). Stellar flares could destroy a nascent atmosphere entirely (Davenport et al. 2016; Dong et al. 2017), or they might provide the energy needed to catalyse biological processes (Buccino, Lemarchand & Mauas 2007; Patel et al. 2015; Lingam & Loeb 2017; Rimmer et al. 2018). Additionally, we must look beyond our own terrestrial version of habitability, by exploring the possibility that biology might arise on water-worlds (Madhusudhan, Piette & Constantinou 2021) or temperate sub-Neptunes (Seager et al. 2021), as both of these may have different HZ boundaries.

We owe much of our current understanding of exoplanetary demographics to the *Kepler* mission (Borucki et al. 2010), and one of the most influential results to come out of statistical studies of the *Kepler* sample was the bimodal radius distribution of sub-Neptune sized planets, with a gap between 1.5 and 2 $R_\oplus$ (Fulton et al. 2017; Van Eylen et al. 2018). The current best explanations for this bimodality are core-powered mass loss (Lopez & Fortney 2013; Ginzburg, Schlichting & Sari 2018; Gupta & Schlichting 2019), photo-evaporation (Owen & Wu 2013, 2017) and volatile-poor formation (Lee, Chiang & Ormel 2014; Venturini & Helled 2017). While the exact location of this so-called 'radius valley' depends on stellar mass among other things (Wu 2019; Gupta & Schlichting 2020), it is still unclear whether it is present around M dwarfs or not (Cloutier & Menou 2020). Therefore, planets with sizes within the radius valley (e.g. Cloutier et al. 2020, 2021; Luque et al. 2022) help us to understand the shape and depth of this gap around M dwarfs. A recent study by Luque & Pallé (2022), however, indicates that M-dwarf planets may have a density gap rather than a radius gap separating two populations of small planets (rocky and water worlds), and that these observations are also well explained by formation pathways that include disc-driven migration (Venturini et al. 2020).

At present *TESS* (Ricker et al. 2015) is providing the community with ample new planets to improve our understanding of exoplanetary demographics, including by populating the habitable zone. Notably, while several 'habitable zone' planets discovered by *TESS* have been confirmed (e.g. Gilbert et al. 2020; Vach et al. 2022), none yet have fallen within the conservative habitable zone as described by Kopparapu et al. (2013) – until now.

In this context, we report on the discovery of TOI-715 b, a small planet orbiting a nearby M4 star (TOI-715/TIC 271971130). The planet's relatively long orbital period and cool host provide it with a mild installation, placing TOI-715 b comfortably within its star's conservative habitable zone. We additionally find a second candidate in the system that, if confirmed, could be *TESS*'s smallest habitable zone planet discovered to date.

Our paper is organised as follows: we begin by characterizing the host star using its spectral energy distribution and reconnaissance spectroscopy in Section 2. We then describe the identification of planetary candidates in the data, first by *TESS* followed by our own search, in Section 3. In Section 4, we describe our ground-based follow-up campaign and our procedures to validate the system, and in Section 5 we detail our global analysis of all available data. Finally, we contextualize our results in Section 6 and conclude in Section 7.

2 STELLAR CHARACTERIZATION

TOI-715 (TIC 271971130) is a nearby (42 pc; Bailer-Jones et al. 2021) M dwarf of spectral type M4. It is a high-proper-motion target with right ascension 07:35:24.56 hms and declination −73:34:38.67 dms (J2000, epoch 2015.5), placing it within *TESS*'s continuous viewing zone (CVZ). As all our planetary information will be derived using the host star's parameters, we begin in the section that follows by characterizing TOI-715. All photometry and stellar parameters adopted for this work can be found in Table 1.

2.1 Reconnaissance spectroscopy

We collected an optical spectrum of TOI-715 on 2022 January 7 (UT) using the Low Dispersion Survey Spectrograph on the 6.5-m *Magellan* II (Clay) Telescope at Las Campanas Observatory in Chile. With its upgraded red-sensitive CCD (Stevenson et al. 2016), this instrument is now known as 'LDSS-3C'. We used LDSS-3C in long-slit mode with the standard setup (fast readout speed, low gain, and 1 × 1 binning) and the VPH-Red grism, OG-590 blocking filter, and the 0.″75 × 0.′4 center slit. This setup provides spectra covering 6000–10 000 Å with a resolution of $R \sim 1810$, which is insufficient to produce a notable constraint on $v \sin i_\star$.

We observed TOI-715 during clear conditions with seeing of 0.″5. We collected six exposures of 300 s each, totaling 30 min on-source, at an average airmass of 1.445. Afterwards, we collected three 1-s exposures of the nearby F8 V standard star HR 2283 (Maiolino, Rieke & Rieke 1996) at an average airmass of 1.360. At each pointing, we collected a 1-s HeNeAr arc lamp exposure and three, 10-s flat fields with the 'quartz high' lamp. We reduced the data with a custom, PYTHON-based pipeline, which includes bias removal, flat field correction, and spectral extraction. For wavelength calibration, the HeNeAr arc exposure was used, which was extracted similarly to the science spectrum. For flux calibration, we used the ratio of the spectrum of the flux standard HR 2283 with an F8 V template from

Table 1. Stellar parameters adopted for this work.

Designations	TOI-715, TIC 271971130, 2MASS J07352425−7334388, APASS 33649915, Gaia DR2 5262666416118954368, UCAC4 083–012601, *WISE* J073524.46−733438.7	
Parameter	Value	Source
α	07:35:24.56	Gaia Collaboration (2022)
δ	−73:34:38.67	Gaia Collaboration (2022)
Distance	42.46 ± 0.03 pc	Bailer-Jones et al. (2021)
μ_α	82.67 ± 0.02 mas yr^{-1}	Gaia Collaboration (2022)
μ_δ	9.92 ± 0.02 mas yr^{-1}	Gaia Collaboration (2022)
RV	$+55.8 \pm 2.7$ km s^{-1}	Gaia Collaboration (2022)
U	$+29.7 \pm 0.6$ km s^{-1}	This work
V	-54.8 ± 2.1 km s^{-1}	This work
W	$+0.7 \pm 0.9$ km s^{-1}	This work
SpT	M4	This work
$R_\star$	$0.240 \pm 0.012 R_\odot$	This work
$M_\star$	$0.225 \pm 0.012 M_\odot$	This work
$T_{\rm eff}$	3075 ± 75 K	This work
$\log g_\star$	5.0 ± 0.2	This work
[Fe/H]	$+0.09 \pm 0.20$ dex	This work (spectroscopy)
	-0.25 ± 0.25 dex	This work (SED)
Age	$6.2^{+3.2}_{-2.2}$ Gyr	This work
T mag	13.5308 ± 0.0073	Stassun et al. (2019)
B mag	18.14 ± 0.16	Zacharias et al. (2013)
V mag	16.24 ± 0.01	Zacharias et al. (2013)
G mag	14.8940 ± 0.0007	Gaia Collaboration (2022)
J mag	11.808 ± 0.024	Cutri et al. (2003)
H mag	11.264 ± 0.026	Cutri et al. (2003)
K mag	10.917 ± 0.019	Cutri et al. (2003)
$W1$ mag	10.753 ± 0.023	Cutri et al. (2021)
$W2$ mag	10.571 ± 0.020	Cutri et al. (2021)
$W3$ mag	10.387 ± 0.049	Cutri et al. (2021)
$W4$ mag	> 8.92	Cutri et al. (2021)

Pickles (1998) to compute a relative flux correction; no correction was made to address telluric absorption. The final science spectrum has a maximum SNR per resolution element of 193 at 9202 Å and a mean SNR per resolution element of 124 in the 6000–10 000 Å range.

The reduced spectrum (Fig. 1) was analysed using KASTREDUX.[2] We compared the spectrum to Sloan Digital Sky Survey templates from Kesseli et al. (2017), finding a best match to an M4 dwarf. This classification was verified through spectral classification indices from Reid, Hawley & Gizis (1995), Lépine, Rich & Shara (2003), and Riddick, Roche & Lucas (2007), all of which measure consistent spectral classifications of M4. We evaluated the ζ metallicity index (Lépine, Rich & Shara 2007; Lépine et al. 2013), determining a value of 1.066 ± 0.002 which corresponds to a metallicity [Fe/H] $= +0.09 \pm 0.20$ dex based on the empirical calibration of Mann et al. (2013). There is no significant evidence of Hα emission, with an equivalent width limit $|EW| < 1.2$ Å corresponding to $\log_{10} L_{\rm H\alpha}/L_{\rm bol} < -6.5$ (Douglas et al. 2014). We also find no evidence of Li I absorption at 6708 Å ($EW < 0.7$ Å), ruling out a young age and substellar mass (Magazzu, Martin & Rebolo 1993).

2.2 Spectral energy distribution

As an independent determination of the basic stellar parameters, we performed an analysis of the broadband spectral energy distribution

[2] https://github.com/aburgasser/kastredux.

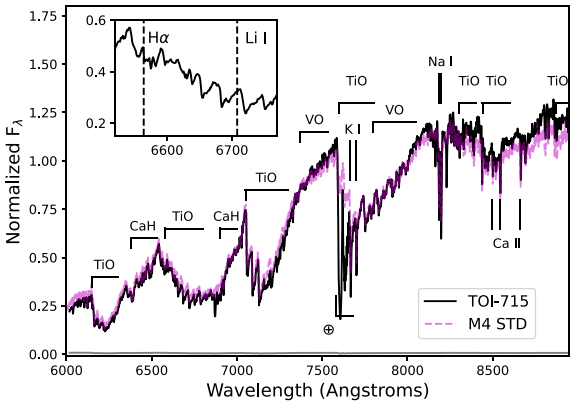


Figure 1. LDSS-3C red optical spectrum of TOI-715 (black line), compared to its best-fitting M4 template (Kesseli et al. 2017, magenta line). Spectra are normalized in the 7400–7500 Å region, and major absorption features are labeled, including regions of strong telluric absorption (⊕). The inset box shows a close-up of the region encompassing H α (6563 Å) and Li I (6708 Å) features, neither of which is detected in the data.

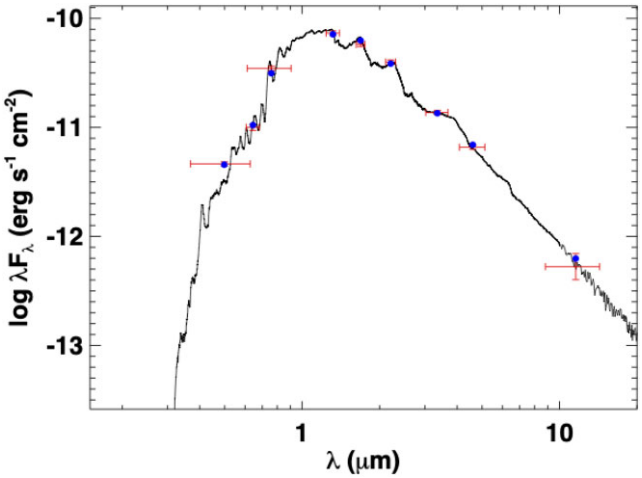


Figure 2. Spectral energy distribution of TOI-715. Red symbols represent the observed photometric measurements, where the horizontal bars represent the effective width of the passband. Blue symbols are the model fluxes from the best-fit NextGen atmosphere model (black).

(SED) of the star together with the *Gaia* DR3 parallax (with no systematic offset applied; see e.g. Stassun & Torres 2021), to determine an empirical measurement of the stellar radius, following the procedures described in Stassun & Torres (2016) and Stassun, Collins & Gaudi (2017); Stassun et al. (2018). We utilized the highest quality broadband photometry available, which were the JHK_S magnitudes from *2MASS*, the $W1$–$W3$ magnitudes from *WISE*, and the $GG_{\rm BP}G_{\rm RP}$ magnitudes from *Gaia*. Together, the available photometry spans the full stellar SED over the wavelength range 0.4–10 μm (see Fig. 2).

We performed a fit using NextGen stellar atmosphere models (Hauschildt, Allard & Baron 1999), with the free parameters being the effective temperature ($T_{\rm eff}$), surface gravity ($\log g$), and metallicity ([Fe/H]). The remaining free parameter is the extinction A_V, which we fixed at zero due to the star's proximity. The resulting fit (Fig. 2) has a reduced χ^2 of 1.3, with best-fitting $T_{\rm eff} = 3075 \pm 75$ K, $\log g = 5.0 \pm 0.2$, [Fe/H] $= -0.25 \pm 0.25$. Integrating the

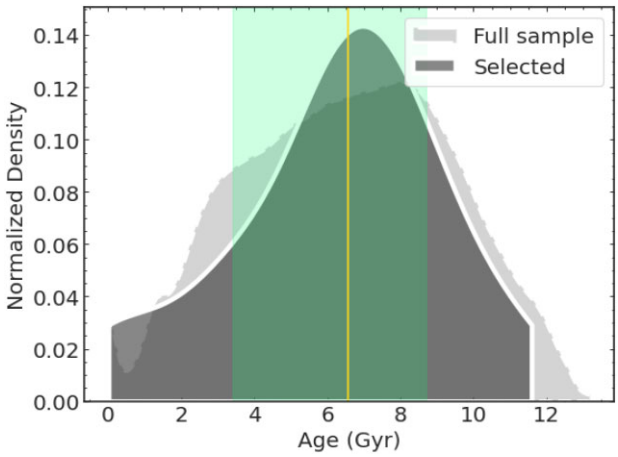


Figure 3. Distribution of ages for all sources in GALAH Data Release 3 (light grey histogram) and those GALAH sources that match the *UVW* velocities and metallicity of TOI-715. (dark grey histogram). The latter distribution is consistent with a median age of $6.6^{+3.2}_{-2.2}$ Gyr (green shaded region, 25 and 75 per cent quantiles), which we adopt as the age of TOI-715.

(unreddened) model SED gives the bolometric flux at Earth, $F_{\rm bol} = 8.21 \pm 0.19 \times 10^{-11}$ erg s^{-1} cm^{-2}. Taking the $F_{\rm bol}$ and $T_{\rm eff}$ together with the *Gaia* parallax, gives the stellar radius, $R_\star = 0.240 \pm 0.012$ R$_\odot$. In addition, we can estimate the stellar mass from the empirical relations of Mann et al. (2019), giving $M_\star = 0.225 \pm 0.012$ M$_\odot$, which is consistent with the value of 0.21 ± 0.05 M$_\odot$ determined via $\log g$ and $R_\star$.

2.3 Estimated age

The lack of detectable Hα emission in its optical spectrum, and absence of any significant flaring activity in its *TESS* light curve, both suggest a relatively old age for TOI-715 given the persistent emission of most mid-type M dwarfs (Newton et al. 2017; Kiman et al. 2019). We estimated the age of TOI-715 by comparing its *UVW* velocities and metallicity to local stars with previously determined ages from isochrone fitting and metallicities from high resolution spectroscopy (cf. Burgasser & Mamajek 2017; Delrez et al. 2022). Our comparison sample was drawn from the GALAH Data Release 3 catalogue (Buder et al. 2021), for which ages are estimated using the Bayesian Stellar Parameter Estimation (BSTEP) code (Sharma et al. 2018). A matched GALAH sample was selected by requiring a distance $\leq$200 pc, and agreement with TOI-715 in individual *UVW* velocities to within 10 km s^{-1} and metallicity to within 0.20 dex. The age distributions of the full GALAH sample and matched stars are shown in Fig. 3. The latter shows a broad peak with a maximum probability at 7 Gyr; the median age of the distribution and 25 and 75 per cent quantiles yields an age estimate of $6.6^{+3.2}_{-2.2}$ Gyr. TOI-715 is likely to be as old or older than the Sun, consistent with its low degree of magnetic activity.

Analyses of ground-based and Kepler photometry by Newton et al. (2016) and McQuillan, Mazeh & Aigrain (2014), respectively, show that typical rotational periods of old M4 dwarfs (0.4–0.5 M$_\odot$) are roughly 15–50 d, most likely at the longer end of this range (and possibly beyond; longer periods in Newton et al. (2016) are 'grade B' detections due to low amplitude variations). This range falls within the detectable period range for the full *TESS* data set; however, the absence of detectable Hα emission suggests a lack of significant spotting, so even if the period were within this range *TESS* measurements may not be sufficient to detect variability. In either case, the lack of Hα emission and rotationally induced variability on a time-scale $\leq$50 d are both consistent with an old age.

3 IDENTIFICATION OF PLANETARY CANDIDATES

TOI-715 is in *TESS*'s southern CVZ, meaning that in principle, it would be observed in all southern sectors. In practice, it was not optimally placed on the CCD during sectors 28 and 38, so at the time of writing, there are 24 sectors of short-cadence (2 min) data for this target.[3]

In the following sections, we describe first the initial candidate identification in the *TESS* data, followed by our own search for further candidates.

3.1 *TESS* Candidate Identification

All *TESS* 2-minute cadence data are processed in the first instance by the SPOC (Science Processing Operations Center) pipeline, presented in Jenkins et al. (2016). Data products are then available to the community in the form of Simple Aperture Photometry (SAP; Twicken et al. 2010; Morris et al. 2020) or Presearch Data Conditioning Simple Aperture Photometry (PDCSAP; Smith et al. 2012; Stumpe et al. 2012, 2014), the latter having been corrected for instrument systematics and for crowding effects. Data products are downloadable from the NASA Mikulski Archive for Space Telescopes (MAST) and available via the LIGHTKURVE package (Lightkurve Collaboration 2018). All light curves are additionally searched by SPOC for periodic transit-like signals and candidates with SNR $>$ 7.1 are reported as threshold crossing events (TCEs).

TOI-715.01 was first reported as a candidate on 2019 May 24 (Guerrero et al. 2021) following a multisector transit search (Jenkins 2002; Jenkins et al. 2010, 2020) conducted on 2019 May 5 for sectors 1–9. The candidate was already identified in the multi-sector search of Sectors 1–6 conducted on 2019 April 18, but did not at this time pass the necessary tests to be reported as a TOI. The transit signal was fitted with an initial limb-darkened transit model (Li et al. 2019) and subjected to a suite of diagnostic tests (Twicken et al. 2018) to help determine whether the signature is from an exoplanet. The transit signature passed all of the tests reported in the Data Validation report for Sectors 1–9[4], and the difference image centroiding test located the source of the transit signal to within $3\farcs7 \pm 3\farcs5$ in the subsequent data validation reports for the multisector searches of Sectors 1–13 and 27–39.

At the time of the first reported TCE[5], the *TESS* Input Catalog (TIC) in use was version 7, which had not yet incorporated the *Gaia*-DR2 data; as such, TOI-715 did not have a stellar radius and the planet candidate was reported as a 7.1 R$_\oplus$ object with a period of $\sim$ 19.2 d. Following the update to the TICv8 (Stassun et al. 2019) the planet candidate's radius estimate was revised, demonstrating that TOI-715.01 was likely a super-Earth and thus a high priority target.

[3]There are additionally two sectors of fast cadence (20 s) data available for TIC 271 971 130 (27 and 28). Observations at 2-min cadence were requested by two General Observer programs: G011180 (PI: Dressing) and G03278 (PI: Mayo).
[4]All data validation reports (Twicken et al. 2018) referred to in this section are downloadable at https://tev.mit.edu/data/search/?q = 271971130.
[5]Multi-sector TCE statistics available at https://archive.stsci.edu/missions/tess/catalogs/tce/tess2018206190142-s0001-s0006_dvr-tcestats.csv.

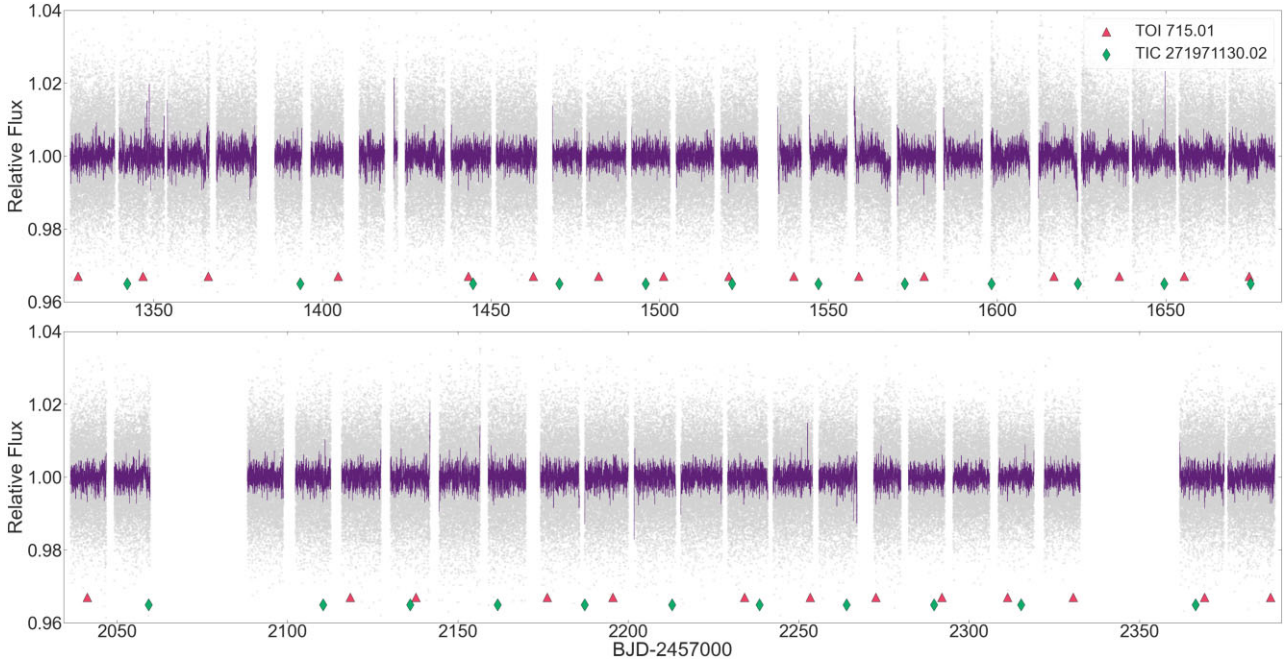


Figure 4. PDCSAP flux extracted from the short (2 min) cadence data of the 24 sectors (1–13, 27, 29–37, 39) in which TOI-715 was observed. Light grey point show the 120 s exposures and the purple line shows the flux in 3 min bins. The transit events of TOI-715.01 are shown with the dark pink arrows and the locations of possible transits of TIC 271971130.02 are indicated with green arrows; we note that individual transits are not readily apparent by eye.

SPOC TCEs are subject to the TESS-ExoClass[6] automated classifier that reduces the number of TCEs that undergo the manual TOI vetting procedure. TESS-ExoClass applies a series of tests that are similar to the *Kepler* Robovetter (Coughlin et al. 2016; Thompson et al. 2018). TOI 715.01 passes all the tests of TESS-ExoClass and has been placed in the Tier 1 (highest quality candidate) category, and has been classified as a Tier 1 candidate in the subsequent SPOC multi-sector 1–13, 1–36, and 1–39 searches. Further details for the TOI assignment process are available in Guerrero et al. (2021).

We present the PDCSAP *TESS* light curves for all 24 sectors of 2-min cadence data in Fig. 4; the timings of the 29 transits are indicated with dark pink arrows.

3.2 Search for additional candidates

We make use of the custom pipeline sherlock[7], presented in Pozuelos et al. (2020) and Demory et al. (2020), to search the *TESS* data for additional transiting candidates, as was done in Dransfield et al. (2022a). sherlock downloads all light curves from MAST and, using Wotan (Hippke et al. 2019), applies a bi-weight function with varying window sizes to detrend the data. Each detrended light curve and the original PDCSAP light curve are then searched for transit-like signals using Transit Least Squares (Hippke & Heller 2019). We use only the 2-min cadence in our candidate search, applying a Savitzky–Golay (SG) digital filter (Savitzky & Golay 1964) previously following the strategy described in Delrez et al. (2022)[8] and we test 11 window sizes between 0.19 and 1.9 d when detrending with the bi-weight filter. We thus carry out our transit search on the PDCSAP light curve and the 11 detrended light curves and only consider signals with SNR > 7 for further investigation.

We recover TOI-715.01 at a period of 19.29 d in the first instance in all 12 light curves, and we find that the highest SNR and SDE are achieved in the PDCSAP flux without any detrending with Wotan.

We additionally find two other periodic signals in the data. Of these, the signal with highest SNR is at a period of 25.61 d, putting it within 0.4 per cent of the first order 4:3 commensurability. The signal is detected in nine of the searched light curves with a maximum SNR of 13.81 and SDE of 11.6; it has a depth of $\sim$ 1 ppt, making this a $\sim 1.16\,R_\oplus$ candidate. In order to ensure this signal is not an artefact produced by the SG filter, we additionally search the untreated PDCSAP light curve and recover the signal with an SNR of 6.81. We adopt this candidate as TIC 271971130.02[9] and highlight the positions of transit events on Fig. 4 with dark green arrows. In Fig. 5, we present the *TESS* light curve folded on this signal, along with the Lomb–Scargle periodogram.

Given the large amount of data in Fig. 4, it is not apparent by eye how much pre- and post-transit baseline each transit has. We therefore note that the total number of in-transit points for TIC 271971130.02 is 1371, while the total number of points before and after the transits are 1349 and 1369 respectively (counted up to 1 transit duration). Thus on average the pre-transit baseline is 98.4 per cent of a transit duration, while the post-transit baseline is 99.9 per cent.

The SPOC ran the Data Validation module at the ephemeris for the second signal and obtained an SNR of 5.5σ, and additionally identified other sub-threshold transit-like signals at higher SNR.

The second signal we recover has a period of 7.17 d and a depth of $<$ 1 ppt; it has a maximum SNR of 9.63 and SDE of 8.17. The

[6] https://github.com/christopherburke/TESS-ExoClass
[7] sherlock is publicly available at https://github.com/franpoz/SHERLOCK.
[8] We use SciPy's implementation of the SG filter, using a 3rd order polynomial and a window size of 11 points.
[9] This candidate has been submitted as a Community TESS Object of Interest (CTOI): https://exofop.ipac.caltech.edu/tess/target.php?id = 271971130.

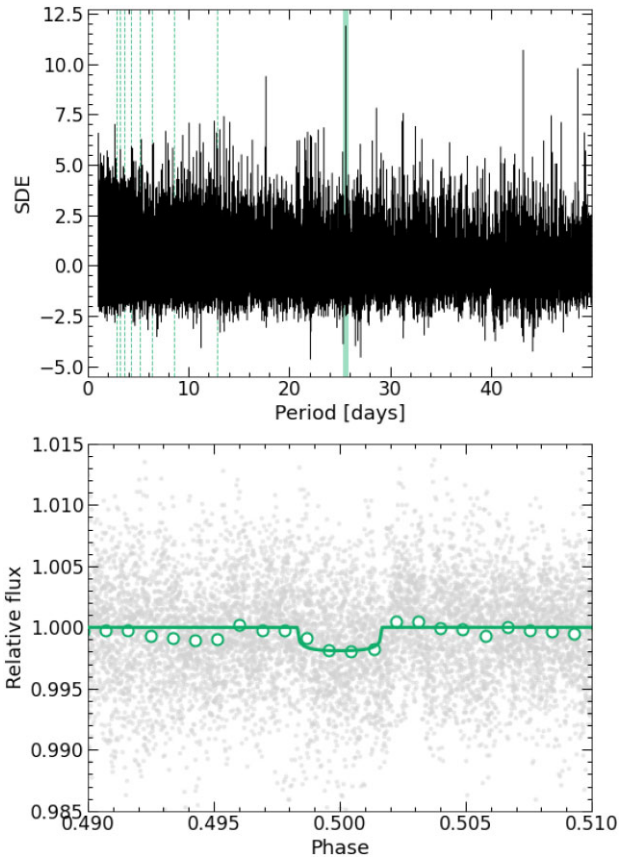


Figure 5. Results of our search for additional candidates in the data, using TRANSIT LEAST SQUARES as implemented by SHERLOCK. **Upper panel:** TLS periodogram showing the detected 25.61-d period of TIC 271971130.02 and its harmonics. **Lower panel:** *TESS* PDCSAP light curve phase-folded on this period, with a transit model overplotted. We note that the errorbars on the binned points are smaller than the markers, and that the light curve shown here is the one treated with the SG Filter.

very low SNR of the signal makes it challenging to discern by eye whether or not the shape is consistent with that of a planetary transit. We also note that this signal is only found in four of the detrended light curves (with window sizes between 0.38–0.65 d, but not the PDCSAP light curve, indicating that the signal could be dependent on detrending. The duration of a transit at this period on a circular orbit is should be of order 0.065 d, and all tested windows are at least 3 × this duration. We therefore do not believe the detrending will have suppressed the transit in other light curves if it is real. When *TESS* returns to the southern skies in its second extended mission, the additional photometry will provide further insight into the nature of this signal.

It is important to note that the SNR and SDE yielded by SHERLOCK are inherited from the TRANSIT LEAST SQUARES algorithm, which uses a simple estimation that cannot be compared with values provided by other pipelines, such as SPOC. Instead, these values are used internally in SHERLOCK to compare the signals found and select the most prominent among them.

4 VETTING AND VALIDATION

In this section we describe the results of the multifacility follow-up campaign conducted between May 2020 and April 2022. We begin with the high-resolution imaging observations, and then outline the photometric observations collected from five southern observatories. Finally, we describe how all our follow-up observations were used to validate the planetary nature of TOI-715.01 and TIC 271971130.02.

All follow-up observations are summarized in Table 2.

4.1 High resolution imaging

Close stellar companions (bound or in the line of sight) can confound derived exoplanet properties in a number of ways. The detected transit signal might be a false positive due to a background eclipsing binary and even real planet discoveries will yield incorrect stellar and exoplanet parameters if a close companion exists and is unaccounted for (e.g. Ciardi et al. 2015; Furlan & Howell 2017, 2020). Additionally, the presence of a close companion star leads to the non-detection of small planets residing within the same exoplanetary system (Lester et al. 2021). Approximately 25 per cent of M dwarfs are part of binary or multiple star systems (e.g. Cortes Contreras et al. 2015; Winters et al. 2019), though fewer than 5 per cent of known spectroscopic binaries include an M-dwarf primary star (Pourbaix et al. 2004).[10] None the less, high resolution imaging provides crucial information towards our understanding of exoplanetary formation, dynamics, and evolution (Howell et al. 2021).

TOI-715 was observed on 2020 December 26 UT using the Zorro speckle instrument on the Gemini South 8-m telescope (Scott et al. 2021). Zorro provides simultaneous speckle imaging in two bands (562 nm and 832 nm) with output data products including a reconstructed image with robust contrast limits on companion detection (see Howell & Furlan 2022). TOI-715 was found to be a single star to within the angular and brightness contrast levels achieved. Eight sets of 1000 × 0.06 s images were obtained and processed by our standard reduction pipeline (Howell et al. 2011). Fig. 6 shows our final contrast curves and the 832 nm reconstructed speckle image. These high-resolution observations revealed no companion star brighter than 5 magnitudes below that of the target star from the 8-m telescope diffraction limit (20 mas) out to 1.2 arcsec. At the distance of TOI-715 (42.4 pc) these angular limits correspond to spatial limits of 0.84 to 50.9 au.

4.2 Photometric follow-up

4.2.1 Las Cumbres Observatory

We used the Las Cumbres Observatory Global Telescopes (LCOGT; Brown et al. 2013) 1.0-m network nodes at South Africa Astronomical Observatory (SAAO) and Cerro Tololo Inter-American Observatory to observe three transits of TOI-715.01. First and second transits were observed with LCO-SAAO on 2020 May 13 and 2020 October 15, and third was observed with LCO-CTIO on 2021 April 25. All observations were carried out with the Sloan-i' and an exposure time of 180 s.

Photometric brightness was measured using an uncontaminated target aperture of 4.3 arcsec (11 pixels). We used the *TESS* TRANSIT FINDER, which is a customized version of the TAPIR software package (Jensen 2013), to schedule our photometric time series. The 1.0-m telescopes are equipped with 4096 × 4096 SINISTRO cameras with an image scale of 0.″389 per pixel, resulting in a 26 arcmin × 26 arcmin field of view. The raw images were calibrated with the standard LCO BANZAI pipeline (McCully et al. 2018), and

[10] https://sb9.astro.ulb.ac.be

Table 2. Summary of ground-based follow-up observations carried out for the validation of TOI-715.01 and TIC 271971130.02.

Observatory	Filter	Date	Sensitivity limit	Result
			Follow-up Observations	
			High resolution imaging	
Gemini South	562 nm	2020 December 26	$\Delta m = 4.69$ at $0.5''$	No sources detected
Gemini South	832 nm	2020 December 26	$\Delta m = 5.07$ at $0.5''$	No sources detected
			Photometric Follow-up	
LCO-SAAO	*Sloan-i'*	2020 May 13	Ingress	Transit ruled out on or off target during the time covered
LCO-SAAO	*Sloan-i'*	2020 October 15	(.01) Ingress	Transit detected on target
ExTrA	1.21 µm	2021 February 26	(.01) Full	Detection
ExTrA	1.21 µm	2021 April 25	(.01) Full	Detection
TRAPPIST-South	$I+z'$	2021 April 25	(.01) Full	Detection
LCO-CTIO	*Sloan-i'*	2021 April 25	(.01) Full	Detection
SSO-Callisto	*Sloan-r'*	2021 September 26	(.01) Full	Detection
SSO-Io	*Sloan-r'*	2021 September 26	(.01) Full	Detection
SSO-Europa	*Sloan-r'*	2021 September 26	(.01) Full	Detection
SSO-Ganymede	*Sloan-r'*	2021 September 26	(.01) Gapped	Interruption due to weather – ingress detected
TRAPPIST-South	$I+z'$	2021 September 26	(.01) Full	Detection
OACC-CAO	*Sloan-i'2*	2021 November 24	(.01) Full	Detection
SSO-Callisto	$I+z'$	2021 November 24	(.01) Full	Detection
SSO-Io	$I+z'$	2021 November 24	(.01) Full	Detection
SSO-Ganymede	$I+z'$	2021 November 24	(.01) Full	Detection
TRAPPIST-South	$I+z'$	2021 November 24	(.01) Full	Detection
ExTrA	1.21 µm	2022 February 08	(.01) Full	Detection
TRAPPIST-South	$I+z'$	2022 April 07	(.01) Full	Detection
ExTrA	1.21 µm	2022 April 07	(.01) Full	Detection
TRAPPIST-South	$I+z'$	2022 October 25	(.02) Egress	Inconclusive (high airmass)
			Spectroscopic Observations	
Instrument	Wavelength range	Date	Number of spectra	Use
Magellan/LDSS3	380–1000 nm	2022 January 06	1	Stellar characterization

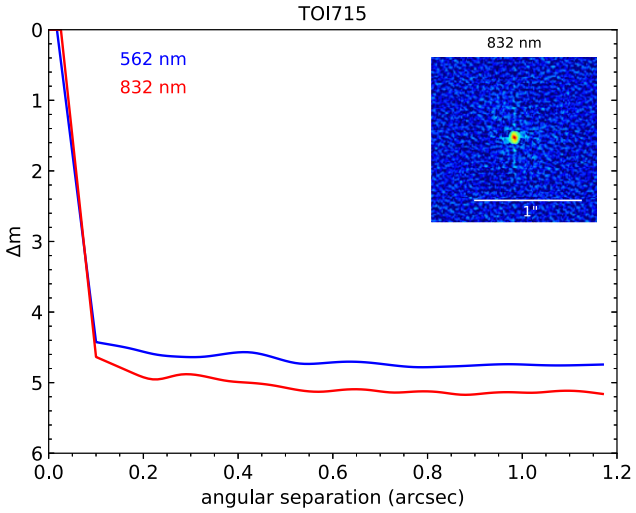


Figure 6. Plot showing the 5σ speckle imaging contrast curves in both filters as a function of the angular separation out to 1.2 arcsec, the end of speckle coherence. The inset shows the reconstructed 832 nm image with a 1 arcsec scale bar. The star, TOI-715, was found to have no close companions to within the angular and brightness contrast levels achieved.

photometric data were extracted with ASTROIMAGEJ (Collins et al. 2017).

The observation of 2020 May 13 only provided ~ 20 per cent in-transit coverage as well as 1.2 h of pre-transit baseline. The transit was ruled out on or off target during the window covered by this observation.[11] The subsequent observation of 2020 October 15 confirmed the transit event on target with the detection of an ingress that was 29 min late relative to the ephemeris. The observation of 2021 April 25 resulted in the detection of a ful transit.

4.2.2 *SPECULOOS-Southern Observatory*

The SPECULOOS Southern Observatory (SSO) is comprised of four Ritchey-Chrétien 1.0 m-class telescopes installed at ESO Paranal in the Atacama desert (Delrez et al. 2018). Designed to hunt for small, habitable-zone planets orbiting ultra-cool stars (Sebastian et al. 2021), all four telescopes are equipped with a deep-depletion Andor CCD camera with 2048 × 2048 13-µm pixels. Each telescope therefore has a field of view of 12 arcmin × 12 arcmin and a pixel scale of $0''.35$ (Burdanov et al. 2018).

All SPECULOOS observations are scheduled using the PYTHON package SPOCK.[12] (Sebastian et al. 2021), and processed in the first instance by an automatic data reduction pipeline, described in detail in Murray et al. (2020). Successful observations of *TESS* targets are then reprocessed using PROSE, a publicly available PYTHON framework for processing astronomical images[13] as described in Garcia et al. (2021, 2022). Images are calibrated and aligned before performing aperture photometry on the 500 brightest sources detected; PROSE then performs differential photometry (Broeg, Fernández &

[11] With the updated ephemeris we confirm that transit would have started just after the end of the window covered by this observation.
[12] https://github.com/educrot/SPOCK
[13] https://github.com/lgrcia/prose

Neuhäuser 2005) on the target star to extract the light curve. Individual light curves are detrended for airmass, sky background and FWHM (full width at half maximum) using second order polynomials in time, and they are then modelled using EXOPLANET (Foreman-Mackey et al. 2021b).

We observed TOI-715.01 for the first time on the night of 2021 September 26 with all four telescopes simultaneously (Io, Europa, Ganymede, Callisto) using the *Sloan-r′* filter and 120-s exposures. Cloudy skies during the transit caused some large systematics in three out of four telescopes, although this did not prevent the transit from being detected. The fourth telescope, Ganymede, closed during the weather alert, causing only the ingress to be detected.

We re-observed TOI-715.01 on the night of 2021 November 24 with three of our telescopes. We collected 13-s exposures using the custom filter $I + z'$ (Sebastian et al. 2021). Observations were once again hampered by the untimely appearance of clouds, which affected the in-transit precision of our observations. Fortunately, the transit was still detected with all three instruments despite the overcast conditions.

4.2.3 TRAPPIST-South

We observed four transits of TOI-715.01 with TRAPPIST-South (TS; Gillon et al. 2011; Jehin et al. 2011), located in ESO La Silla Observatory in Chile. This 0.6-m telescope is equipped with a FLI ProLine PL3041-BB camera and a back-illuminated CCD with a pixel size of 0.″64, providing a total field of view of 22 arcmin × 22 arcmin for an array of 2048 × 2048 pixels. TS is a Ritchey–Chrétien telescope with F/8 and is equipped with a German equatorial mount.

All four transits were observed with the custom $I + z'$ filter to maximize the photometric precision. The observations took place on 2021 April 25, 2021 September 26, 2021 November 24, and 2022 April 7, with exposure times of 50s, 70s, 120s, and 90s, respectively. We reduced the images using PROSE pipeline (Garcia et al. 2021, 2022) to extract optimal light curves. Individual light curves were then modeled using the EXOPLANET (Foreman-Mackey et al. 2021b) package and detrended using a second order polynomial of airmass, FWHM and sky background. None of the observations suffered weather losses.

We additionally observed TOI-715 on 2022 October 25 during a partial transit of the second candidate (.02) but the target was too low during the event. The observation was therefore inconclusive.

4.2.4 ExTrA

ExTrA (Bonfils et al. 2015) is a near-infrared (0.85–1.55 μm) multi-object spectrograph fed by three 0.6 m telescopes located at La Silla observatory. We observed four full transits of TOI 715.01 on 2021 February 26, 2021 April 25, 2022 February 8, and 2022 April 7. We observed the first three transits using two telescopes, and the fourth using three; all observations were carried out with 8 arcsec aperture fibers. For both nights, we used the spectrograph's low resolution mode ($R \sim 20$) and 60s exposures. Five fibre positioners are used at the focal plane of each telescope to collect light from the target and four comparison stars. As comparison stars, we also observed 2MASS J07381369−7347351, 2MASS J07410628−7341297, 2MASS J07393394−7330535, and 2MASS J07372328−7321411 with *J*-magnitude (Skrutskie et al. 2006) and $T_{\rm eff}$ (Gaia Collaboration 2021) similar to TOI-715. The resulting ExTrA data were analyzed with custom data reduction software, detailed in Cointepas et al. (2021).

4.2.5 OACC-CAO

We observed a transit of TOI-715.01 with Campo Catino Austral Observatory (OACC-CAO), located in El Sauce Observatory in the Atacama desert in Chile, on the night of 2021 November 24. The telescope is a 0.6 m Planewave CDK 24 arcsec with a Planewave L600 mount, equipped with an FLI filter wheel with *Sloan* filters and an FLI PL16803 camera with 4096 × 4096 9 μm pixels. It has a field of view of 32 arcmin and a pixel scale of 0.″48.

TOI-715.01 was observed with the *Sloan-i'2* filter using 180s exposures. The images were reduced using ASTROIMAGEJ (Collins et al. 2017) and we detect the full transit in an uncontaminated aperture.

4.3 Statistical validation

We make use of the statistical validation package TRICERATOPS[14] (Giacalone & Dressing 2020; Giacalone et al. 2021) to assess the probability of the planet hypothesis for TOI-715.01 and TIC 271971130.02. TRICERATOPS calculates the flux contribution from nearby stars to check if any could be responsible for the transit signal. It then calculates the relative probabilities of a range of transiting planet (TP) and eclipsing binary (EB) scenarios using light curve models fitted to the phase-folded photometry. In the first instance we find that the false positive probabilities (FPP) are 0.403 and 0.592 for candidates .01 and .02, respectively when examining the *TESS* data, while the threshold for validation is 0.015. For candidate .01, we make use of our follow-up photometry by folding in the four TRAPPIST-South light curves. We choose these as they were observed with the custom $I + z$' filter (which is very similar to the *TESS* bandpass) and all four are at different epochs.

With this phase-folded subset of our follow-up photometry, we find that the false positive probability reduces to 0.0107, placing it below the threshold for statistical validation. To similarly reduce the FPP for TIC 271971130.02, we will need to collect ground-based photometry to confirm the event on-target or rule out events on nearby stars (such an observation was scheduled from Hazelwood Observatory but cancelled due to bad weather).

4.3.1 Statistical validation conclusions

With a FPP of 0.0107 TOI-715.01 is now below the customary threshold for statistical validation (0.015; Giacalone et al. 2021); we therefore consider the planet validated and refer to it as TOI-715 b. TIC 271971130.02 does not yet meet the criterion for statistical validation, and is therefore classified as a 'likely transiting planet' until more evidence such as ground-based photometry is collected.

5 GLOBAL PHOTOMETRIC ANALYSIS

We carried out a global photometric analysis of the *TESS* photometry and the data sets described in Section 4.3 using ALLESFITTER (Günther & Daylan 2019, 2021), a flexible and publicly available PYTHON-based inference package. We exclude all partial transits, as well as the transit obtained from OACC (due to large scatter in the data) from our analysis, leaving 15 full transits from our

[14] Version 1.0.17.

Table 3. Priors used in our fit, along with fitted and derived parameters. Uniform priors are indicated as $\mathcal{U}$(lower bound, upper bound) and normal priors are indicated as $\mathcal{N}$(mean, standard deviation). ⋆Equillibrium temperature is calculated assuming an albedo of 0.3 and emissivity of 1.

	TOI-715 b	TIC 271971130.02	
Fit parametrization and priors			
Transit depth; $R_p/R_\star$	$\mathcal{U}(0.01, 0.1)$	$\mathcal{U}(0.01, 0.1)$	
Inverse scaled semimajor axis; $(R_\star + R_p)/a$	$\mathcal{U}(0.01, 0.05)$	$\mathcal{U}(0.008, 0.04)$	
Orbital inclination; cos i	$\mathcal{U}(0.000, 0.04)$	$\mathcal{U}(0.000, 0.04)$	
Transit epoch; T_0 (BJD)	$\mathcal{U}(2\,458\,327.3, 2\,458\,327.7)$	$\mathcal{U}(2\,458\,342.0, 2\,458\,342.4)$	
Period; P (d)	$\mathcal{U}(19.0, 19.4)$	$\mathcal{U}(25.4, 25.8)$	
Limb-darkening coefficients			
TESS u_1	0.3322 ± 0.0013	*TESS* q_1	$\mathcal{N}(0.413, 0.050)$
TESS u_2	0.3103 ± 0.0047	*TESS* q_2	$\mathcal{N}(0.259, 0.050)$
$I + z$ u_1	0.2942 ± 0.0014	$I + z$ q_1	$\mathcal{N}(0.453, 0.050)$
$I + z$ u_2	0.3791 ± 0.0052	$I + z$ q_2	$\mathcal{N}(0.218, 0.050)$
Sloan-i' u_1	0.3863 ± 0.0018	*Sloan-i'* q_1	$\mathcal{N}(0.532, 0.050)$
Sloan-i' u_2	0.3431 ± 0.0060	*Sloan-i'* q_2	$\mathcal{N}(0.265, 0.050)$
Sloan-r' u_1	0.6408 ± 0.0032	*Sloan-r'* q_1	$\mathcal{N}(0.768, 0.050)$
Sloan-r' u_2	0.2273 ± 0.0079	*Sloan-r'* q_2	$\mathcal{N}(0.218, 0.050)$
ExTra (1.2 μm) u_1	0.2058 ± 0.0007	*ExTra (1.2μm)* q_1	$\mathcal{N}(0.142, 0.050)$
ExTra (1.2 μm) u_2	0.1708 ± 0.0028	*ExTra (1.2μm)* q_2	$\mathcal{N}(0.273, 0.050)$
External priors		**GP priors**	
Stellar Mass; $M_\star$ ($M_\odot$)	$\mathcal{N}(0.225, 0.012)$	Amplitude scale GP ln σ(flux)	$\mathcal{U}(-7, -7)$
Stellar Radius; $R_\star$ ($R_\odot$)	$\mathcal{N}(0.240, 0.012)$	Length scale GP ln ρ(flux)	$\mathcal{U}(-7, 2)$
Stellar Effective Temperature; $T_{\rm eff}$ (K)	$\mathcal{N}(3075, 75)$		
Fitted parameters			**Source**
$R_p/R_\star$	0.0618 ± 0.0017	0.0425 ± 0.0034	2-planet linear fit
$(R_\star + R_p)/a$	0.01367 ± 0.00017	$0.01129^{+0.00055}_{-0.00047}$	2-planet linear fit
cos i	$0.00252^{+0.00030}_{-0.00032}$	$0.0048^{+0.0021}_{-0.0024}$	2-planet linear fit
T_0 (BJD)	$2\,459\,002.63051^{+0.00070}_{-0.00074}$	$2\,459\,007.9879^{+0.0045}_{-0.0041}$	2-planet linear fit
P (d)	$19.288004^{+0.000027}_{-0.000024}$	$25.60712^{+0.00031}_{-0.00036}$	2-planet linear fit
Fitted GP hyperparameters			**Source**
ExTrA 2	gp ln σ $-3.77^{+0.24}_{-0.19}$	gp ln ρ $-2.73^{+0.26}_{-0.17}$	2-planet linear fit
ExTrA 3	gp ln σ $-4.60^{+0.22}_{-0.19}$	gp ln ρ $-2.77^{+0.24}_{-0.15}$	2-planet linear fit
Derived parameters			**Source**
Companion radius; R_p ($R_\oplus$)	1.550 ± 0.064	1.066 ± 0.092	2-planet linear fit
Instellation; S_p ($S_\oplus$)	$0.67^{+0.15}_{-0.20}$	$0.48^{+0.12}_{-0.17}$	2-planet linear fit
Semi-major axis; a (au)	0.0830 ± 0.0027	0.0986 ± 0.0054	2-planet linear fit
Inclination; i (deg)	$89.856^{+0.018}_{-0.017}$	$89.72^{+0.14}_{-0.12}$	2-planet linear fit
Impact parameter; b	$0.195^{+0.023}_{-0.024}$	$0.44^{+0.18}_{-0.22}$	2-planet linear fit
Total transit duration; $T_{\rm tot}$ (h)	1.980 ± 0.025	$1.99^{+0.14}_{-0.21}$	2-planet linear fit
Full-transit duration; $T_{\rm full}$ (h)	1.741 ± 0.022	$1.79^{+0.15}_{-0.25}$	2-planet linear fit
Equilibrium temperature⋆; $T_{\rm eq}$ (K)	234 ± 12	215 ± 12	2-planet linear fit
Transit depth *TESS*; $\delta_{\rm tr;\,TESS}$ (ppt)	$4.48^{+0.26}_{-0.23}$	$2.03^{+0.31}_{-0.27}$	2-planet linear fit
Transit depth $i + z$; $\delta_{\rm tr;\,i+z}$ (ppt)	$4.48^{+0.54}_{-0.48}$	-	2-planet linear fit
Transit depth *Sloan-i'*; $\delta_{\rm tr;Sloan-i'}$ (ppt)	$4.60^{+1.50}_{-1.20}$	-	2-planet linear fit
Transit depth *Sloan-r'*; $\delta_{\rm tr;Sloan-r'}$ (ppt)	$4.81^{+0.78}_{-0.90}$	-	2-planet linear fit
Transit depth *ExTra* (1.2 μm); $\delta_{\rm tr;\,ExTra(1.2\mu m)}$ (ppt)	$4.20^{+1.10}_{-0.96}$	-	2-planet linear fit

ground-based facilities. ALLESFITTER generates light curve models using ELLC (Maxted 2016), and Gaussian Process (GP) models using CELERITE (Foreman-Mackey et al. 2017). The best fitting models are then chosen using either a nested sampling algorithm via DYNESTY (Speagle 2020), or MCMC sampling with EMCEE (Foreman-Mackey et al. 2013). For all modeling in this paper, we make use of the nested sampling algorithm as it calculates the Bayesian evidence at each step in the sampling; this allows us to compare the Bayesian evidence for different models by calculating the Bayes Factor (Kass & Raftery 1995). All prior distributions and their bounds can be found in Table 3.

We adopt the signal parameters from Section 3 as uniform priors, and the stellar parameters from Section 2 as normal priors and fit for all planetary parameters ($R_p/R_\star$, $(R_\star + R_p)/a$, cos i, T_0, and P). We fit two models in the first instance: one where eccentricity is constrained to zero and another where eccentricity is allowed to vary, parametrized as $\sqrt{e_b}\cos\omega_b$ and $\sqrt{e_b}\sin\omega_b$ (as in Triaud et al. 2011).

The observations described in Section 4.3 span several photometric filters from the blue to the near-infrared ends of the spectrum. To allow the colour-dependent transit depth to be a free parameter in our models, we also fit each light curve for a dilution parameter (D)

which we give a uniform prior between −1 and 1. We fix the dilution of the *TESS* observations at 0 as the PDCSAP light curve is already corrected for crowding (Stumpe et al. 2012), and use the transit depth as the reference depth; we then use ALLESFITTER's 'coupled_with' functionality to ensure that the dilution and quadratic limb-darkening coefficients are fitted together for all observations taken in the same photometric band.

We use the PYTHON package PYLDTK (Parviainen & Aigrain 2015) and the PHOENIX stellar atmosphere library (Husser et al. 2013) to calculate quadratic limb-darkening coefficients for each photometric band. These are also adopted as normal priors in our models after we reparameterise them in the Kipping (2013) parametrization by converting from u_1, u_2 to q_1, q_2.

Finally, due to the complex instrument systematics present in the data obtained with the ExTrA telescopes, we model the correlated 'red' noise in these observations using a GP. We select the *Matérn 3/2* kernel as implemented by CELERITE due to its versatility and its ability to model both long and short term trends. We fit for two GP hyperparameters for each ExTrA telescope: the amplitude scale, σ, and the length scale, ρ. We place wide uniform priors on these terms. For all other telescopes, we make use of a hybrid spline to model the baseline. ALLESFITTER also fits an 'error scaling' term to account for white noise in the data.

The initial fits (1-planet circular, and 1-planet eccentric) both confirm that TOI-715 b is a 1.550 ± 0.061 $R_\oplus$ planet with an equilibrium temperature of 234 ± 12 K. We find that the eccentric model has slightly higher evidence, with a logged Bayes Factor of $\sim 6.5 \pm 1.1$, although the eccentricity derived from this more complex model, $e = 0.31^{+0.38}_{-0.20}$, is consistent with zero at the 2σ level, and we do not consider this a detection of orbital eccentricity. All modelled ground-based transits of TOI-715 b, as well as the phase-folded *TESS* photometry, can be found in Figs 7 and 8. In Fig. 9 we present the averaged depths, in each photometric band, demonstrating the achromaticity of the observed transits.

We remind the reader that in Section 3, we identified a second transiting planet candidate in the *TESS* data, which we now incorporate into the model, and test this two-planet hypothesis. We test two further models to seek evidence of a second planet in the system, starting by fixing the linear ephemerides of planet b and allowing the mid-time of each individual transit to vary. This model is motivated by the second candidate's proximity to a 1st order 4:3 mean-motion resonance with the first planet. If the second candidate is real, we might expect for these planets to experience mutual gravitational interactions exciting transit timing variations (TTVs).

We place a wide uniform prior on each transit mid-time, corresponding to the linear predicted mid-time ± 60 min. We find that due to the low SNR of individual transits in the *TESS* data, the transit mid-times are not well constrained for events observed only by *TESS*. However, transits observed simultaneously by several ground-based observatories have significantly less scatter and smaller error bars. In these events, we see evidence suggesting TTVs of up to 5 min, although the Bayesian evidence for this model is lower than for the two linear models tested. Models with linear ephemerides are preferred, with Bayes Factors of ∼9.5 and ∼16 for the circular and eccentric models respectively. We note that we did not test a fixed linear ephemerides fit with a 2-planet model as the individual transits in *TESS* for the second candidate have even lower SNR and we have no ground-based transits at the time of writing.

The final model we test is a 2-planet circular Keplerian model. We fit for all the same parameters as before, but now additionally include the transit parameters for the second candidate. The phase-folded *TESS* photometry for the second candidate is presented in Fig. 10; the fitted and derived parameters for planet b resulting from the 2-planet model are consistent with those emerging from all previous models. Also noteworthy is that the host density as calculated by ALLESFITTER following Seager & Mallén-Ornelas (2003) with the transit parameters of the second candidate is 22.7 ± 3.0 g cm^{-3}, which is within 1σ of the stellar density prior of 23.1 ± 3.2 g cm^{-3}, suggesting that both signals are produced over the same star. The results of this fit indicate that if TIC 271971130.02 is confirmed, it is likely a 1.066 ± 0.092 $R_\oplus$ planet with an orbital period of $25.60712^{+0.00031}_{-0.00036}$ and an equilibrium temperature of 215 ± 12 K.

All fitted and derived parameters from the linear 2-planet circular model are presented in Table 3.

6 DISCUSSION

TOI-715 is host to at least one planet (TOI-715 b), with $R_b = 1.550 \pm 0.064$ $R_\oplus$, receiving an installation $S_b = 0.67^{+0.15}_{-0.20}$ $S_\oplus$, which places it within the 'conservative habitable zone' defined by Kopparapu et al. (2013) as the circumstellar region where a rocky planet receives and installation flux of $0.42 - 0.842$ $S_\oplus$. Our model suggests that there is also a possibly second, smaller planet in the system, with size $R_{02} = 1.066 \pm 0.092$ $R_\oplus$, just within the outer edge of the host's habitable zone, at an installation $S_{02} = 0.48^{+0.12}_{-0.17}$ $S_\oplus$.

Expectation of planet yield by *TESS* prior to launch showed *TESS* would detect of order 70 ± 9 Earth-sized planets (< 1.25 $R_\oplus$) and 14 ± 4 conservative 'habitable zone' planets < 2 $R_\oplus$ (as in Kopparapu et al. 2013), but that *TESS* would identify of order 0 Earth-sized (< 1.25 $R_\oplus$) 'conservative habitable zone planets' (Sullivan et al. 2015). More recent yield estimates (post-launch) by Kunimoto et al. (2022) appear more pessimistic, however, finding only 5 ± 2 'conservative habitable zone planets' < 2 $R_\oplus$ would be detected within the primary mission and first extended mission of *TESS*, a factor nearly three times lower than Sullivan et al. (2015). Should the second planet candidate, TIC 271971130.02 be fully confirmed, its existence would thus represent an unexpectedly important discovery made possible by the *TESS* mission, with the contributions of many ground-based facilities.

In this section, we contextualize the system by examining other factors required for habitability, and assessing its suitability for further in-depth characterization. We begin by revisiting the radius valley to understand what can be learned about the mass of TOI-715 b from current mass–radius relations. We then explore the prospects for a precise mass measurement of this planet with current spectroscopic instrumentation, followed by a discussion of the potential for atmospheric characterization with *HST* and *JWST*.

6.1 TOI-715 b and the radius valley

The radius valley, as identified in the *Kepler* sample by Fulton et al. (2017), shows a lack of close-in ($P < 100$ d) planets with sizes between $1.5 - 2$ $R_\oplus$; TOI-715 b's 1.55 $R_\oplus$ appears just inside this underpopulated region of parameter space. The importance of the radius valley lies in its potential to teach us about planetary formation and post-formation evolution (e.g. Owen & Wu 2017; Ginzburg et al. 2018; Venturini et al. 2020), and hence planets inside this gap are crucial in furthering our understanding of the factors that sculpt it.

The location and slope of the radius valley has been shown to depend on the properties of the host star (e.g. Fulton & Petigura 2018; Gupta & Schlichting 2019; Berger et al. 2020), and Cloutier & Menou (2020) and Van Eylen et al. (2021) recently re-examined this for low-mass stars. Cloutier & Menou (2020) looked at the small, close-in planet distribution around stars cooler than 4700 K and found

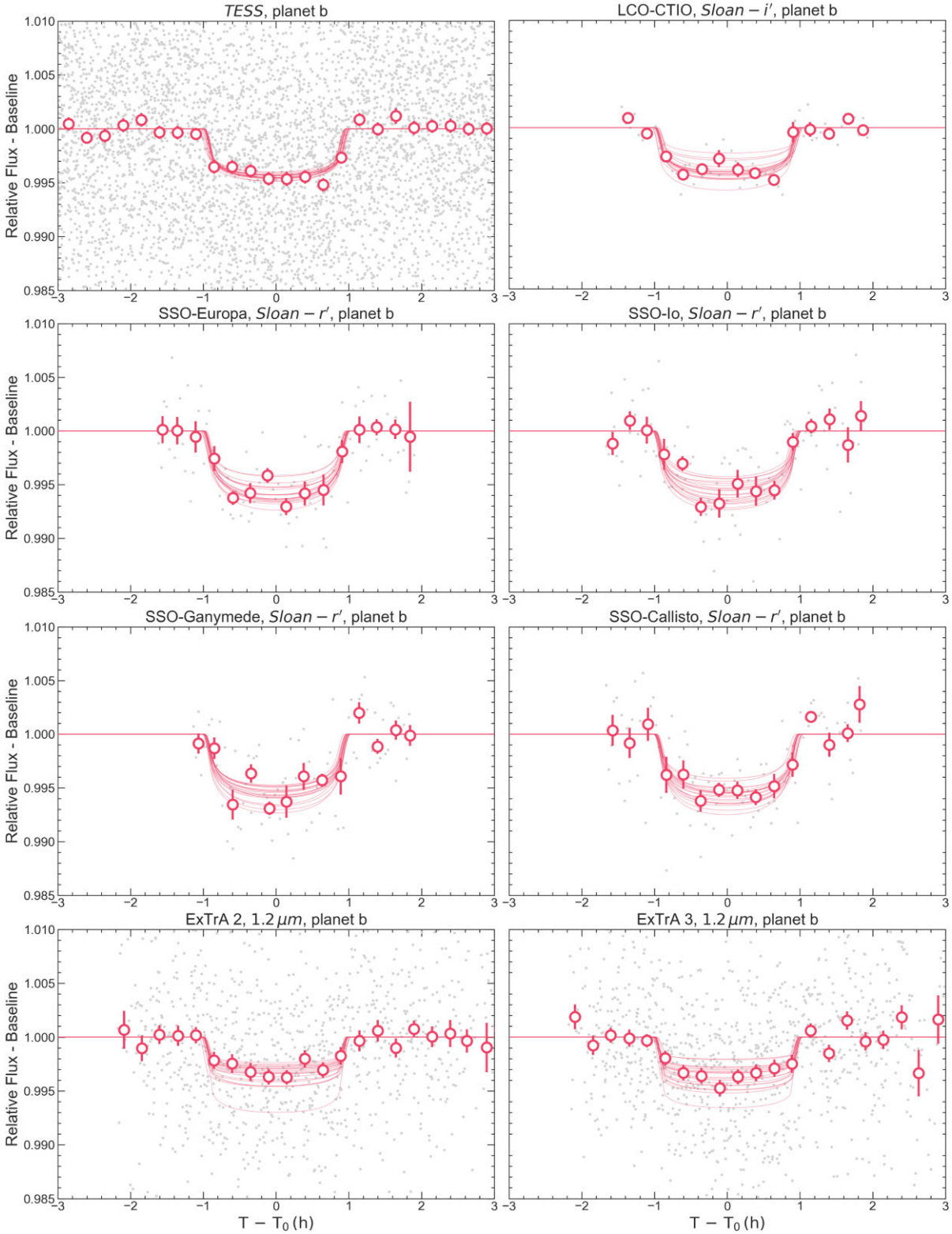


Figure 7. Photometry of TOI-715 b along with best fitting models. Grey points are raw flux and dark pink circles are 15-min binned points. The dark pink lines are 20 fair draws from the posterior transit model. The flux and the transit models have been corrected by subtracting the baseline models. The *TESS*, ExTrA 2 and ExTrA 3 photometry are phase-folded, while the others are single transits.

that the slope is opposite in sign compared with FGK stars, and also that the peaks of the planet radius distributions are shifted toward smaller planets. According to this, the center of the radius valley also shifts towards smaller radii. The sample examined in this study contained planets discovered by *Kepler* and *K2*, and was corrected for completeness. This work states that planets falling between their

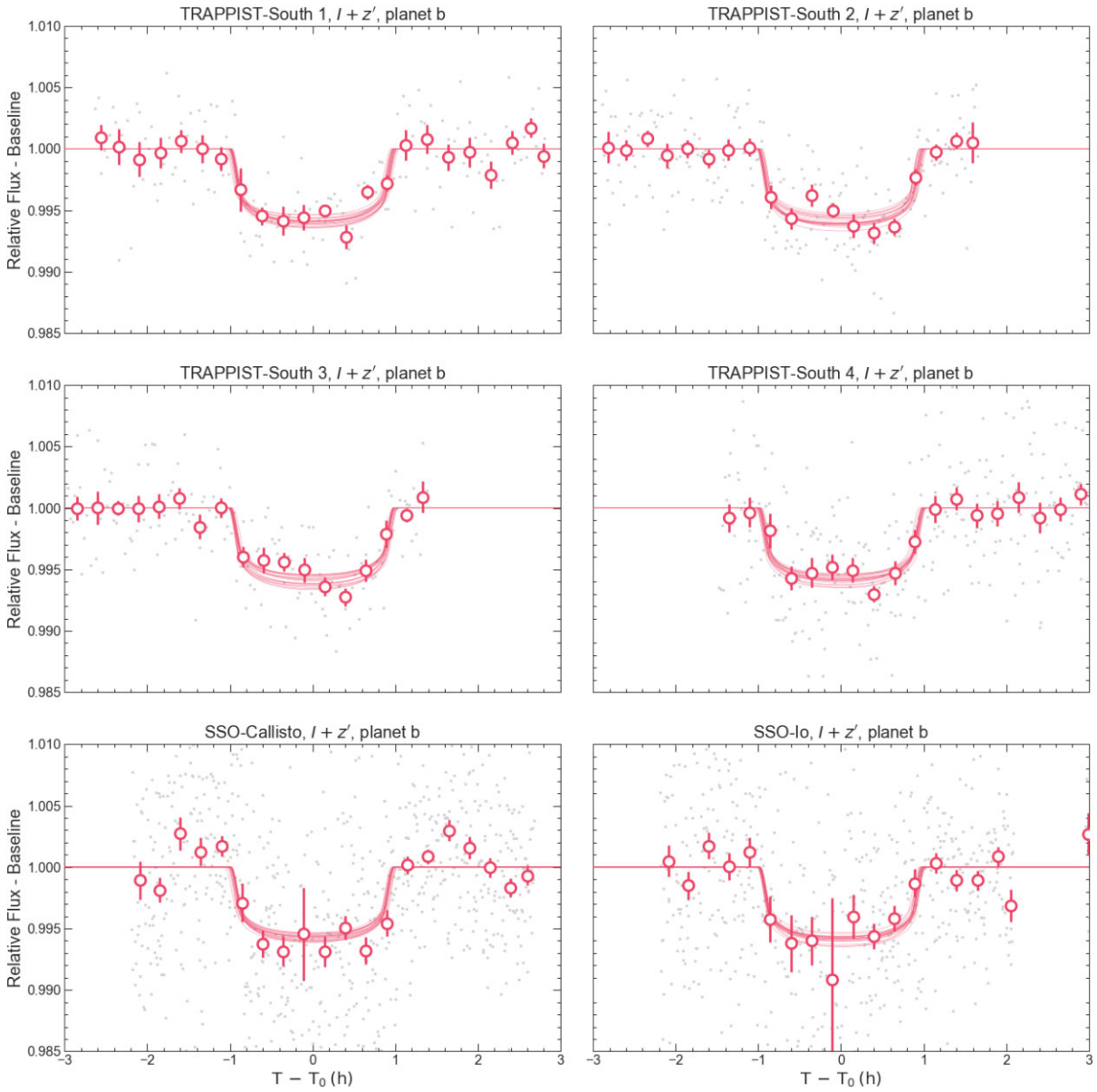


Figure 8. Photometry of TOI-715 b along with best-fitting models. Grey points are raw flux and dark pink circles are 15-min binned points. The dark pink lines are 20 fair draws from the posterior transit model. The flux and the transit models have been corrected by subtracting the baseline models. All transits shown here are single transits. For the TRAPPIST light curves, the number in the figure titles denotes the visit number. These are treated as single transits due to the different exposure times of each visit. Increased scatter during the transit observed by SSO-Io (bottom right panel) cause the middle binned point to have a large errorbar.

measured radius valley and the one measured by Martinez et al. (2019) for Sun-like stars are so-called 'keystone planets', crucial for further understanding the radius valley around low-mass stars. By this metric TOI-715 b's radius of 1.55 $R_\oplus$ is just below the boundary of 1.66 $R_\oplus$ for a period of 19.288 d, falling within the super-Earth category.

Van Eylen et al. (2021), however, used a significantly smaller sample, restricted to confirmed and well-characterized planets, with masses and radii measured to at least 20 per cent precision, orbiting stars cooler than 4000 K. They found a slope in radius-period space opposite in sign compared with Cloutier & Menou (2020), and therefore consistent in sign with FGK stars as measured by, for instance, Martinez et al. (2019). They do, however, find that the valley shifts towards smaller radii for later spectral types. Contrary to the work of Cloutier & Menou (2020), the functional form of the radius valley derived in this study places TOI-715 b above the radius valley and with the population of sub-Neptunes.

In Fig. 11 we present the current sample of exoplanets orbiting stars cooler than $T_{\rm eff} = 4000$ K with planetary radii measured to better than 10 per cent precision[15] in radius-period space. We highlight the positions of the radius valleys as measured by Martinez et al. (2019); Cloutier & Menou (2020) and Van Eylen et al. (2021) and

[15]Retrieved from the NASA Exoplanet Archive on 2022 October 05, https://exoplanetarchive.ipac.caltech.edu/cgi-bin/TblView/nph-tblView?app=ExoTbls&config = PSCompPars.

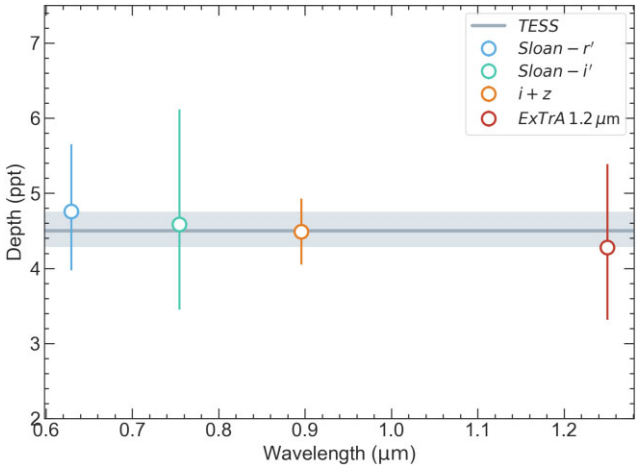


Figure 9. Measured transit depths versus wavelength. The dark grey horizontal line indicates the depth of the *TESS* transits, while other depths are highlighted with circles for comparison.

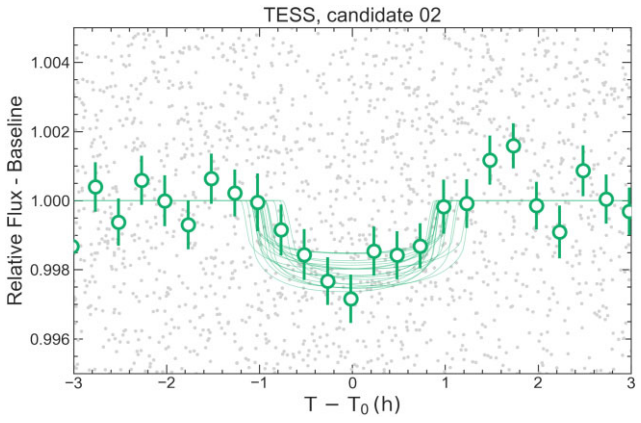


Figure 10. Phase folded *TESS* photometry of TIC 271971130.02. Grey points are raw flux and green circles are 15-min binned points. The green lines are 20 fair draws from the posterior transit model. The flux and the transit models have been corrected by subtracting the baseline models.

the positions of TOI-715 b and TIC 271971130.02. In this sample, a clear radius bimodality for planets orbiting M dwarfs is not visible. What is evident is that precise characterization of planets such as TOI-715 b that fall *between* the various definitions of the low-mass star radius valley is essential to understand whether or not this bimodality will eventually be borne out by the data.

6.2 TOI-715 b and the density gap

Luque & Pallé (2022) recently demonstrated using a sample of planets with precisely measured radii (to at least <8 per cent) and masses (to at least <25 per cent) that small planets orbiting low-mass stars in fact likely have a density gap rather than a radius valley. The results of that study indicate that small planets come in three flavours: rocky, water-worlds and gassy. For planets smaller than 2 $R_\oplus$ they find a clear bi-modality in density which allow us to estimate the mass of TOI-715 b in both the rocky ($\sim$ 7$M_\oplus$) and water-world ($\sim$ 2$M_\oplus$) scenarios; both different from the Chen & Kipping (2017) estimate of $\sim$ 3.5$M_\oplus$ and the rocky and volatile-rich predictions from Otegi, Bouchy & Helled (2020) ($\sim$ 4.1$M_\oplus$ and $\sim$ 3.5$M_\oplus$ respectively). While this result is very promising for our understanding of the composition of small planets around low-mass stars, their sample contained only 34 planets; therefore continued systematic characterization of these systems with consistent sample selection criteria remains crucial to understand this distribution and ultimately the composition of planets around M dwarfs.

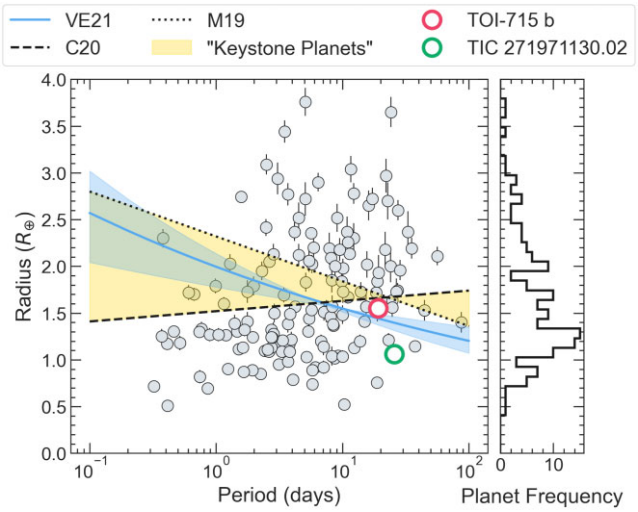


Figure 11. Plot of the current sample of planets orbiting hosts cooler than 4000 K in radius-period space. The grey circles are confirmed planets with radii measured to better than 10 per cent precision, and the dark pink and green circles are TOI-715 b and TIC 271971130.02, respectively. We note that some errorbars are smaller than the markers. The blue line indicates the measured radius valley according to Van Eylen et al. (2021) for hosts cooler than 4000 K. The black dashed line is the low-mass star radius valley as measured by Cloutier & Menou (2020) for hosts cooler than 4700 K, while the dotted black line indicated the radius valley for Sun-like stars as measured by Martinez et al. (2019). The yellow shaded area indicates where planets referred to as 'keystone planets' can be found. The histogram in the right-hand panel does not include TOI-715 b or TIC 271971130.02.

6.3 Prospects for a mass measurement of TOI-715 b

Given the faintness of TOI-715, the only southern hemisphere instrument currently capable of the precision required to measure the mass of planet b is ESPRESSO at the VLT (Very Large Telescope Pepe et al. 2010). If the planet is rocky and has a mass of $\sim$ 7 $M_\oplus$, then we calculate a predicted RV semi-amplitude of 4.5 m s^{-1}. From ESPRESSO's exposure time calculator (ETC) we find that we could achieve a precision of 7.4 m s^{-1} per measurement, meaning that for a 25 per cent precision on the mass of the planet, 44 spectra need to be collected, with 1800 s exposures and SNR $\sim$ 14. For this, we assume that TOI-715 is a relatively slow rotator (vsini $\lesssim$ 2 km s^{-1}) which is not unusual for old M dwarfs that do not show significant stellar activity (Moutou et al. 2017; Reiners et al. 2022).

However the ETC is usually pessimistic. Based on observed radial-velocity precision of mid-M type planet-host stars obtained with ESPRESSO we expect a slightly better performance for this instrument. Observations of Proxima Cen (M5V) resulted in a mean precision of 0.6 m s^{-1} (Suárez Mascareño et al. 2020), which is about 40 per cent better than the ETC predicts. A similar case is LHS 1140 (M3V), for which a mean precision of 0.8 m s^{-1} has been achieved (Lillo-Box et al. 2020), which is a precision twice better than expected. Empirical results[16] for M dwarfs using the MAROON-

[16]Empirical RV Uncertainties – MAROON-X.

X spectrograph at Gemini North (Seifahrt et al. 2020) found a more than 40 per cent increase in precision between M0 and M6 dwarf stars. The ESPRESSO ETC assumes an M2 spectral type to predict the RV precision. Thus, this apparent increase in RV precision for mid-M dwarfs, compared to early M dwarfs can explain the observed difference in performance.

Since TOI-715 is an M4 dwarf, we can conservatively expect a 20 per cent better RV precision compared to the ETC (thus a precision of $\sim 5.9\,\mathrm{m\,s^{-1}}$). This means a 25 per cent precision on the mass of the planet can be reached with only ~ 30 spectra (1800 s exposures; SNR ~ 14). This amounts to 15 h of telescope time, which is not unrealistic for a planet of this importance.

If however, TOI-715 b is in fact a 'water world', then a mass of $\sim 2\,\mathrm{M_\oplus}$ would produce an RV semi-amplitude of just $1.3\,\mathrm{m\,s^{-1}}$. In this case 150 h of telescope time are needed to constrain the mass with 25 per cent precision. Should the density bi-modality for small planets around M dwarfs suggested by Luque & Pallé (2022) be confirmed, a non-detection might enable us to infer the planet's mass.

In Section 5, we found that there were small hints of transit timing variations (TTVs) in the ground-based transits of TOI-715 b. If the second planet is confirmed and the orbits are commensurate, the masses of both planets could be suitable for characterization using dynamical modelling. Given the low SNR of individual transits and the long orbital periods, such a campaign would be well suited to ASTEP (Antarctic Search for Transiting Exoplanets, Daban et al. 2010; Schmider et al. 2022), given its convenient Antarctic location (Dransfield et al. 2022b).

6.4 Prospects for detailed atmospheric characterization of TOI-715 b

The Transmission Spectroscopy Metric (TSM) as established by Kempton et al. (2018) is often used to quantify the suitability of planets for atmospheric characterization via transmission spectroscopy. We calculate the TSM for TOI-715 b in both mass limits[17] and for TIC 271971130.02, as well as the published sample of planets with $R_p < 2\,\mathrm{R_\oplus}$ and $S_p < 1.6\,\mathrm{S_\oplus}$[18] The comparison sample contained 34 planets initially; we then removed the seven planets discovered via radial velocity as these are not known to transit. In Fig. 12, we present this sample of small habitable zone and temperate exoplanets, highlighting the location of the conservative habitable zone (Kopparapu et al. 2013). We also highlight the positions of the five TRAPPIST-1 planets that fall in this parameter space (d-h) (Gillon et al. 2017), the recently discovered LP 890–9 c (SPECULOOS-2 c/TOI-4306 c; Delrez et al. 2022), K2-3 d (Crossfield et al. 2015), and the well characterized mini-Neptune, LHS 1140 b (Dittmann et al. 2017).

In the case of a 'water world' composition, TOI-715 b could have a transmission signal comparable to LHS-1140 b if it does indeed have detectable atmospheric features. In the higher mass limit we find that TOI-715 b has a TSM of approximately 1.9, below the suggested cutoff of 12 for follow-up of terrestrial planets.

[17]The formula for TSM calculations includes a planetary radius-dependent scale factor, with the cutoff for 'terrestrial planets' at $1.5\,\mathrm{R_\oplus}$. As the radius of TOI-715 b is $1.55\,\mathrm{R_\oplus}$ we use the terrestrial scale factor (0.190) for the 'rocky world' TSM, and the 'sub-Neptune' scale factor (1.26) for the 'water world' TSM to enable a fair comparison.

[18]Retrieved from the NASA Exoplanet Archive on 2022 September 14, https://exoplanetarchive.ipac.caltech.edu/cgi-bin/TblView/nph-tblView?app=ExoTbls&config = PSCompPars.

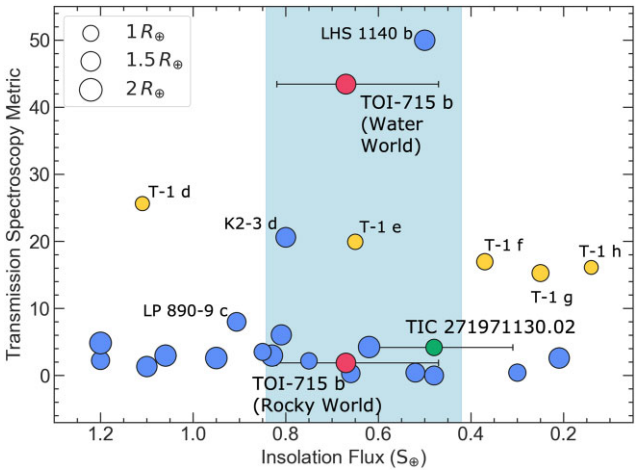


Figure 12. Transmission spectroscopy metric verus installation for transiting planets orbiting hosts cooler than 4000 K. The blue shaded area shows the conservative habitable zone as defined by Kopparapu et al. (2013). The two dark pink circles highlight the positions of TOI-715 b in the rocky and water world scenarios, while the green circle indicates the position of TIC 271971130.02. We highlight in yellow the positions of the seven planets of TRAPPIST-1. The sizes of the circles are scaled with planetary radius.

We use TIERRA (Niraula et al. 2022) to calculate simulated transmission spectra for TOI-715 b in the 'rocky' ($\sim 7\,\mathrm{M_\oplus}$) and 'water-world' ($\sim 2\,\mathrm{M_\oplus}$) mass scenarios in the case of a primordial hydrogen/helium-dominated atmosphere. We then use PANDEXO (Batalha et al. 2017) to simulate *JWST* observations in both cases to assess the detectability of atmospheric features. We find that in the low-mass case atmospheric features could be detectable with a single *JWST* transit if the atmosphere is cloudless. In the higher mass case, we find that extracting meaningful features would require at least five transits, also in the cloud-free case. A secondary atmosphere with higher mean molecular mass could suppress the scale height by more than an order of magnitude, in turn making it challenging to detect atmospheric features of these planets (de Wit et al. 2016).

In both mass cases, the carbon dioxide feature centered on 4.5 μm, the methane feature at 3.3 μm and multiple water bands are some of the most accessible atmospheric features with the NIRSpec PRISM, the most suitable instrument for *JWST* follow-up given the similar brightness of TOI-715 compared to TRAPPIST-1. Detection of these features will constrain the metallicity of the putative planetary atmospheres, providing first hints of the carbon-chemistry of the atmosphere itself (Madhusudhan 2012), and insights into their formation history (Öberg, Murray-Clay & Bergin 2011).

6.5 Flares and habitability

Both TOI-715 b and the candidate TIC 271971130.02 lie in an interesting location of the parameter space with regard to insolation, radius, and potential rocky composition, naturally posing questions of their habitability. Many recent prebiotic chemistry and astrobiology studies investigated how life may have originated on Earth and other planets (see e.g. Patel et al. 2015; Airapetian et al. 2016; Xu et al. 2018 and reviews by Sutherland 2017; Kitadai & Maruyama 2018). The first processes leading from inorganic compounds towards RNA precursors likely require a liquid solution (e.g. liquid surface water) and an energy source. For the latter, the host star's flaring may provide the necessary UV radiation (in the 200–280 nm range) to

trigger these early steps (e.g. Rimmer et al. 2018; Todd et al. 2018; Rimmer et al. 2021).

On the other hand, stellar activity can also pose a significant danger to exoplanets. Strong stellar winds and XUV outbursts can contribute to atmospheric loss (e.g. Atri & Mogan 2020). Even if the atmosphere prevails, coronal mass ejections (charged particle streams) may interact with and dissociate atmospheric ozone (e.g. Tilley et al. 2019). Without the major atmospheric absorber of harmful UV radiation, the next flares might sterilize existing surface biology.

We investigate TOI-715's 24 sectors of TESS data for signs of stellar flaring. We find an average rate of 7 flares per 100 d of observations, with a maximum flare amplitude of 5 per cent in relative flux over nearly 2 yr of data. This analysis was performed using the STELLA neural network (Feinstein et al. 2020) and as part of the TESS flare catalog (Günther et al., in preparation), building on (Günther et al. 2020). We also compare this flare frequency distribution with the theoretical potential for ozone sterilization (Tilley et al. 2019) and laboratory thresholds for prebiotic chemistry (Rimmer et al. 2018). We find that the flaring is likely too rare and not energetic enough to influence either of these effects.

As TOI-715 is an older star ($6.6^{+3.2}_{-2.2}$ Gyr), its flaring is likely not as prominent as in younger years, when its planets were forming and prebiotic chemistry steps might have been triggered. Demographic studies of young (<100 Myr) and older M dwarfs show that flaring activity decreases with stellar age, likely due to spin-down and a decreasing stellar dynamo (e.g. Feinstein et al. 2020; Günther et al. 2020). Thus, one could carefully speculate: if stronger flaring or other processes (volcanoes, impacts, or lightning) had led to astrobiology on TOI-715 b or TIC 271971130.02 several Gyr ago, there might be a chance it could still exist (pending, of course, all other criteria such as atmospheric composition, liquid water, etc. are fulfilled).

7 CONCLUSIONS

In this work, we have presented the discovery, validation and characterization of TOI-715 b, a $R_b = 1.550 \pm 0.064\,R_\oplus$ habitable zone planet orbiting an M4 star with a period of $19.288004^{+0.000027}_{-0.000024}$ d. We also demonstrated that there is possibly a second, smaller planet with radius $R_{02} = 1.066 \pm 0.092\,R_\oplus$ at a period of $25.60712^{+0.00031}_{-0.00036}$ d, placing it just inside the outer edge of the circumstellar habitable zone. This system represents the first *TESS* discovery to fall within this most conservative and widely applicable 'habitable zone'.

We have also demonstrated that TOI-715 b is amenable to further characterization with precise radial velocities and transmission spectroscopy; detailed follow-up of this planet is crucial to further our understanding of the formation and evolution of small, close-in planets. Given its location in radius-installation space, TOI-715 b could also help us understand the characteristics of the M-dwarf radius valley.

Confirmation of the existence of the TIC 271971130.02 in the coming months will also be crucial in planning further characterization of planet b, as disentangling the two planets in a putative radial velocity campaign could prove challenging if the orbit of a second planet is not well known.

ACKNOWLEDGEMENTS

We thank the reviewer for their comments and feedback as these helped clarify and streamline the manuscript significantly. Funding for the *TESS* mission is provided by NASA's Science Mission Directorate. We acknowledge the use of public *TESS* data from pipelines at the *TESS* Science Office and at the *TESS* Science Processing Operations Center. This research has made use of the Exoplanet Follow-up Observation Program website, which is operated by the California Institute of Technology, under contract with the National Aeronautics and Space Administration under the Exoplanet Exploration Program. This paper includes data collected by the *TESS* mission that are publicly available from the Mikulski Archive for Space Telescopes (MAST). Based on data collected by the SPECULOOS-South Observatory at the ESO Paranal Observatory in Chile.The ULiege's contribution to SPECULOOS has received funding from the European Research Council under the European Union's Seventh Framework Programme (FP/2007-2013) (grant agreement no. 336480/SPECULOOS), from the Balzan Prize and Francqui Foundations, from the Belgian Scientific Research Foundation (F.R.S.-FNRS; grant no. T.0109.20), from the University of Liege, and from the ARC grant for Concerted Research Actions financed by the Wallonia–Brussels Federation. This work is supported by a grant from the Simons Foundation (PI Queloz, grant number 327127). This research is in part funded by the European Union's Horizon 2020 research and innovation programme (grants agreements no. 803193/BEBOP), and from the Science and Technology Facilities Council (STFC; grant no. ST/S00193X/1 and ST/W000385/1). The material is based upon work supported by NASA under award number 80GSFC21M0002 Based on data collected by the TRAPPIST-South telescope at the ESO La Silla Observatory. TRAPPIST is funded by the Belgian Fund for Scientific Research (Fond National de la Recherche Scientifique, FNRS) under the grant FRFC 2.5.594.09.F, with the participation of the Swiss National Science Fundation (SNF). Based on data collected under the ExTrA project at the ESO La Silla Paranal Observatory. ExTrA is a project of Institut de Planétologie et d'Astrophysique de Grenoble (IPAG/CNRS/UGA), funded by the European Research Council under the ERC Grant Agreement n. 337591-ExTrA. This work has been supported by a grant from Labex OSUG@2020 (Investissements d'avenir – ANR10 LABX56). This work has been carried out within the framework of the NCCR PlanetS supported by the Swiss National Science Foundation. Some of the observations in the paper made use of the High-Resolution Imaging instrument Zorro obtained under Gemini LLP Proposal Number: GN/S-2021A-LP-105. Zorro was funded by the NASA Exoplanet Exploration Program and built at the NASA Ames Research Center by Steve B. Howell, Nic Scott, Elliott P. Horch, and Emmett Quigley. Zorro was mounted on the Gemini South telescope of the international Gemini Observatory, a program of NSF's OIR Lab, which is managed by the Association of Universities for Research in Astronomy (AURA) under a cooperative agreement with the National Science Foundation on behalf of the Gemini partnership: the National Science Foundation (United States), National Research Council (Canada), Agencia Nacional de Investigación y Desarrollo (Chile), Ministerio de Ciencia, Tecnología e Innovación (Argentina), Ministério da Ciencia, Tecnología, Inovações e Comunicações (Brazil), and Korea Astronomy and Space Science Institute (Republic of Korea). The Digitized Sky Surveys were produced at the Space Telescope Science Institute under U.S. Government grant NAG W-2166. The images of these surveys are based on photographic data obtained using the Oschin Schmidt Telescope on Palomar Mountain and the UK Schmidt Telescope. The plates were processed into the present compressed digital form with the permission of these institutions. This work makes use of observations from the LCOGT network. Part of the LCOGT telescope time was granted by NOIRLab through the Mid-Scale Innovations Program (MSIP). MSIP is funded by NSF. This publication benefits from the support of the French Community

of Belgium in the context of the FRIA Doctoral Grant awarded to MT. MNG acknowledges support from the European Space Agency (ESA) as an ESA Research Fellow. BVR thanks the Heising–Simons Foundation for support. MG is F.R.S.-FBRS Research Director. YGMC acknowledges support from UNAM-PAPIIT-IG101321 FJP acknowledges financial support from the grant CEX2021-001131-S funded by MCIN/AEI/10.13039/501100011033. This research made use of Lightkurve, a Python package for Kepler and *TESS* data analysis (Lightkurve Collaboration, 2018). This work made use of ASTROPY:[19] a community-developed core Python package and an ecosystem of tools and resources for astronomy (Astropy Collaboration 2013, 2018, 2022). This research has made use of the NASA Exoplanet Archive, which is operated by the California Institute of Technology, under contract with the National Aeronautics and Space Administration under the Exoplanet Exploration Program. This research made use of `exoplanet` (Foreman-Mackey et al. 2021a) and its dependencies (Astropy Collaboration 2013, 2018; Salvatier, Wiecki & Fonnesbeck 2016; Theano Development Team 2016; Kumar et al. 2019; Luger et al. 2019; Agol, Luger & Foreman-Mackey 2020). Resources supporting this work were provided by the NASA High-End Computing (HEC) Program through the NASA Advanced Supercomputing (NAS) Division at Ames Research Center for the production of the SPOC data products.

DATA AVAILABILITY

TESS data products are available via the MAST portal at https://mast.stsci.edu/portal/Mashup/Clients/Mast/Portal.html. Follow-up photometry and high resolution imaging data for TOI-715 are available on ExoFOP at https://exofop.ipac.caltech.edu/tess/target.php?id = 271971130. These data are freely accessible to ExoFOP members immediately and are publicly available following a one-year proprietary period.

REFERENCES

Agol E., Luger R., Foreman-Mackey D., 2020, AJ, 159, 123
Airapetian V. S., Glocer A., Gronoff G., Hébrard E., Danchi W., 2016, Nat. Geosci., 9, 452
Alibert Y., Benz W., 2017, A&A, 598, L5
Astropy Collaboration, 2013, A&A, 558, A33
Astropy Collaboration, 2018, AJ, 156, 123
Astropy Collaboration, 2022, ApJ, 935, 167
Atri D., Mogan S. R. C., 2020, MNRAS, 500, L1
Bailer-Jones C. A. L., Rybizki J., Fouesneau M., Demleitner M., Andrae R., 2021, AJ, 161, 147
Batalha N. E. et al., 2017, PASP, 129, 064501
Berger T. A., Huber D., Gaidos E., van Saders J. L., Weiss L. M., 2020, AJ, 160, 108
Bonfils X. et al., 2013, A&A, 549, A109
Bonfils X. et al., 2015, in Shaklan S.ed., Proc. SPIE Conf. Ser. Vol. 9605, Techniques and Instrumentation for Detection of Exoplanets VII. SPIE, Bellingham, p. 96051L
Borucki W. J. et al., 2010, Science, 327, 977
Broeg C., Fernández M., Neuhäuser R., 2005, Astron. Nachr., 326, 134
Brown T. M. et al., 2013, PASP, 125, 1031
Buccino A. P., Lemarchand G. A., Mauas P. J. D., 2007, Icarus, 192, 582
Buder S. et al., 2021, MNRAS, 506, 150
Burdanov A., Delrez L., Gillon M., Jehin E., 2018, in Deeg H. J., Belmonte J. A., eds, Handbook of Exoplanets. Springer Cham, New York, p. 130
Burgasser A. J., Mamajek E. E., 2017, ApJ, 845, 110
Charbonneau D., Deming D., 2007, preprint (arXiv:0706.1047)
Chen J., Kipping D., 2017, ApJ, 834, 17
Ciardi D. R., Beichman C. A., Horch E. P., Howell S. B., 2015, ApJ, 805, 16
Cloutier R., Menou K., 2020, AJ, 159, 211
Cloutier R. et al., 2020, AJ, 160, 22
Cloutier R. et al., 2021, AJ, 162, 79
Cointepas M. et al., 2021, A&A, 650, A145
Collins K. A., Kielkopf J. F., Stassun K. G., Hessman F. V., 2017, AJ, 153, 77
Cortes Contreras M. et al., 2015, 18th Cambridge Workshop on Cool Stars, Stellar Systems, and the Sun. Lowell Observatory, p. 805
Coughlin J. L. et al., 2016, ApJS, 224, 12
Crossfield I. J. M. et al., 2015, ApJ, 804, 10
Cutri R. M. et al., 2003, VizieR Online Data Catalog, p. II/246
Cutri R. M. et al., 2021, VizieR Online Data Catalog, p. II/328
Daban J.-B. et al., 2010, in Stepp L. M., Gilmozzi R., Hall H. J., eds, Proc. SPIE Conf. Ser. Vol. 7733, Ground-based and Airborne Telescopes III. SPIE, Bellingham, p. 77334T
Davenport J. R. A., Kipping D. M., Sasselov D., Matthews J. M., Cameron C., 2016, ApJ, 829, L31
de Wit J. et al., 2016, Nature, 537, 69
Delrez L. et al., 2018, in Marshall H. K., Spyromilio J., eds, Proc. SPIE Conf. Ser. Vol. 10700, Ground-based and Airborne Telescopes VII. SPIE, Bellingham, p. 107001I
Delrez L. et al., 2022, A&A, 667, A59
Demory B. O. et al., 2020, A&A, 642, A49
Dittmann J. A. et al., 2017, Nature, 544, 333
Dong C., Lingam M., Ma Y., Cohen O., 2017, ApJ, 837, L26
Douglas S. T. et al., 2014, ApJ, 795, 161
Dransfield G. et al., 2022a, MNRAS, 515, 1328
Dransfield G. et al., 2022b, in Adler D. S., Seaman R. L., Benn C. R., eds, Proc. SPIE Conf. Ser. Vol. 12186, Observatory Operations: Strategies, Processes, and Systems IX. SPIE, Bellingham, p. 121861F
Dressing C. D., Charbonneau D., 2013, ApJ, 767, 95
Dressing C. D., Charbonneau D., 2015, ApJ, 807, 45
Feinstein A. D., Montet B. T., Ansdell M., Nord B., Bean J. L., Günther M. N., Gully-Santiago M. A., Schlieder J. E., 2020, AJ, 160, 219
Foreman-Mackey D., Hogg D. W., Lang D., Goodman J., 2013, PASP, 125, 306
Foreman-Mackey D., Agol E., Ambikasaran S., Angus R., 2017, Astrophysics Source Code Library, record ascl:1709.008
Foreman-Mackey D. et al., 2021a, exoplanet-dev/exoplanet v0.5.0
Foreman-Mackey D. et al., 2021b, JOSS, 6, 3285
Fulton B. J., Petigura E. A., 2018, AJ, 156, 264
Fulton B. J. et al., 2017, AJ, 154, 109
Furlan E., Howell S. B., 2017, AJ, 154, 66
Furlan E., Howell S. B., 2020, ApJ, 898, 47
Gaia Collaboration, 2022, preprint (arXiv:2208.00211)
Gaia Collaboration, 2021, A&A, 650, C3
Garcia L. J., Timmermans M., Pozuelos F. J., Ducrot E., Gillon M., Delrez L., Wells R. D., Jehin E., 2021, Astrophysics Source Code Library, recordascl:2111.006
Garcia L. J., Timmermans M., Pozuelos F. J., Ducrot E., Gillon M., Delrez L., Wells R. D., Jehin E., 2022, MNRAS, 509, 4817
Giacalone S., Dressing C. D., 2020, Astrophysics Source Code Library, record ascl:2002.004
Giacalone S. et al., 2021, AJ, 161, 24
Gilbert E. A. et al., 2020, AJ, 160, 116
Gillon M., Jehin E., Magain P., Chantry V., Hutsemékers D., Manfroid J., Queloz D., Udry S., 2011, EPJ Web Conf., 11, 06002
Gillon M. et al., 2017, Nature, 542, 456
Ginzburg S., Schlichting H. E., Sari R., 2018, MNRAS, 476, 759
Guerrero N. M. et al., 2021, ApJS, 254, 39
Günther M. N., Daylan T., 2019, Astrophysics Source Code Library, recordascl:1903.003
Günther M. N., Daylan T., 2021, ApJS, 254, 13
Günther M. N. et al., 2020, AJ, 159, 60

[19] http://www.astropy.org

Gupta A., Schlichting H. E., 2019, MNRAS, 487, 24
Gupta A., Schlichting H. E., 2020, MNRAS, 493, 792
Hauschildt P. H., Allard F., Baron E., 1999, ApJ, 512, 377
He M. Y., Triaud A. H. M. J., Gillon M., 2017, MNRAS, 464, 2687
Hippke M., Heller R., 2019, Astrophysics Source Code Library, record-dascl:1910.007
Hippke M., David T. J., Mulders G. D., Heller R., 2019, AJ, 158, 143
Howell S. B., Furlan E., 2022, Front. Astron. Space Sci., 9, 871163
Howell S. B., Everett M. E., Sherry W., Horch E., Ciardi D. R., 2011, AJ, 142, 19
Howell S. B., Scott N. J., Matson R. A., Everett M. E., Furlan E., Gnilka C. L., Ciardi D. R., Lester K. V., 2021, Front. Astron. Space Sci., 8, 10
Husser T. O., Wende-von Berg S., Dreizler S., Homeier D., Reiners A., Barman T., Hauschildt P. H., 2013, A&A, 553, A6
Jehin E. et al., 2011, The Messenger, 145, 2
Jenkins J. M., 2002, ApJ, 575, 493
Jenkins J. M. et al., 2010, in Radziwill N. M., Bridger A., eds, Proc. SPIE Conf. Ser. Vol. 7740, Software and Cyberinfrastructure for Astronomy. SPIE, Bellingham, p. 77400D
Jenkins J. M. et al., 2016, in Chiozzi G., Guzman J. C., eds, Proc. SPIE Conf. Ser. Vol. 9913, Software and Cyberinfrastructure for Astronomy IV. SPIE, Bellingham, p. 99133E
Jenkins J. M., Tenenbaum P., Seader S., Burke C. J., McCauliff S. D., Smith J. C., Twicken J. D., Chandrasekaran H., 2020, Kepler Data Processing Handbook: Transiting Planet Search, Kepler Science Document KSCI-19081-003
Jensen E., 2013, Astrophysics Source Code Library , recordascl:1306.007
Kass R. E., Raftery A. E., 1995, J. Am. Stat. Assoc., 90, 773
Kasting J. F., Whitmire D. P., Reynolds R. T., 1993, Icarus, 101, 108
Kempton E. M. R. et al., 2018, PASP, 130, 114401
Kesseli A. Y., West A. A., Veyette M., Harrison B., Feldman D., Bochanski J. J., 2017, ApJS, 230, 16
Kiman R., Schmidt S. J., Angus R., Cruz K. L., Faherty J. K., Rice E., 2019, AJ, 157, 231
Kipping D. M., 2013, MNRAS, 435, 2152
Kitadai N., Maruyama S., 2018, Geosci. Front., 9, 1117
Kopparapu R. K. et al., 2013, ApJ, 765, 131
Kopparapu R. K., Ramirez R. M., SchottelKotte J., Kasting J. F., Domagal-Goldman S., Eymet V., 2014, ApJ, 787, L29
Kumar R., Carroll C., Hartikainen A., Martin O. A., 2019, J. Open Source Softw., 4, 1143
Kunimoto M., Winn J., Ricker G. R., Vanderspek R. K., 2022, AJ, 163, 290
Lee E. J., Chiang E., Ormel C. W., 2014, ApJ, 797, 95
Lépine S., Rich R. M., Shara M. M., 2003, AJ, 125, 1598
Lépine S., Rich R. M., Shara M. M., 2007, ApJ, 669, 1235
Lépine S., Hilton E. J., Mann A. W., Wilde M., Rojas-Ayala B., Cruz K. L., Gaidos E., 2013, AJ, 145, 102
Lester K. V. et al., 2021, AJ, 162, 75
Li J., Tenenbaum P., Twicken J. D., Burke C. J., Jenkins J. M., Quintana E. V., Rowe J. F., Seader S. E., 2019, PASP, 131, 024506
Lightkurve Collaboration, 2018, Astrophysics Source Code Library , recordascl:1812.013
Lillo-Box J. et al., 2020, A&A, 642, A121
Lingam M., Loeb A., 2017, ApJ, 848, 41
Lopez E. D., Fortney J. J., 2013, ApJ, 776, 2
Luger R., Agol E., Foreman-Mackey D., Fleming D. P., Lustig-Yaeger J., Deitrick R., 2019, AJ, 157, 64
Luque R., Pallé E., 2022, Science, 377, 1211
Luque R. et al., 2022, A&A, 666, A154
Madhusudhan N., 2012, ApJ, 758, 36
Madhusudhan N., Piette A. A. A., Constantinou S., 2021, ApJ, 918, 1
Magazzu A., Martin E. L., Rebolo R., 1993, ApJ, 404, L17
Maiolino R., Rieke G. H., Rieke M. J., 1996, AJ, 111, 537
Mann A. W., Brewer J. M., Gaidos E., Lépine S., Hilton E. J., 2013, AJ, 145, 52
Mann A. W. et al., 2019, ApJ, 871, 63
Martinez C. F., Cunha K., Ghezzi L., Smith V. V., 2019, ApJ, 875, 29
Maxted P. F. L., 2016, A&A, 591, A111
McCully C., Volgenau N. H., Harbeck D.-R., Lister T. A., Saunders E. S., Turner M. L., Siiverd R. J., Bowman M., 2018, in Guzman J. C., Ibsen J., eds, Proc. SPIE Conf. Ser. Vol. 10707, Software and Cyberinfrastructure for Astronomy V. SPIE, Bellingham, p. 107070K
McQuillan A., Mazeh T., Aigrain S., 2014, ApJS, 211, 24
Montgomery R., Laughlin G., 2009, Icarus, 202, 1
Morley C. V., Kreidberg L., Rustamkulov Z., Robinson T., Fortney J. J., 2017, ApJ, 850, 121
Morris R. L., Twicken J. D., Smith J. C., Clarke B. D., Jenkins J. M., Bryson S. T., Girouard F., Klaus T. C., 2020, Kepler Data Processing Handbook: Photometric Analysis, Kepler Science Document KSCI-19081-003
Moutou C. et al., 2017, MNRAS, 472, 4563
Mulders G. D., Pascucci I., Apai D., 2015, ApJ, 814, 130
Murray C. A. et al., 2020, MNRAS, 495, 2446
Newton E. R., Irwin J., Charbonneau D., Berta-Thompson Z. K., Dittmann J. A., West A. A., 2016, ApJ, 821, 93
Newton E. R., Irwin J., Charbonneau D., Berlind P., Calkins M. L., Mink J., 2017, ApJ, 834, 85
Niraula P., de Wit J., Gordon I. E., Hargreaves R. J., Sousa-Silva C., Kochanov R. V., 2022, Nat. Astron., 6, 1287
Nutzman P., Charbonneau D., 2008, PASP, 120, 317
Öberg K. I., Murray-Clay R., Bergin E. A., 2011, ApJ, 743, L16
O'Malley-James J. T., Kaltenegger L., 2017, MNRAS, 469, L26
Otegi J. F., Bouchy F., Helled R., 2020, A&A, 634, A43
Owen J. E., Wu Y., 2013, ApJ, 775, 105
Owen J. E., Wu Y., 2017, ApJ, 847, 29
Parviainen H., Aigrain S., 2015, MNRAS, 453, 3821
Patel B. H., Percivalle C., Ritson D. J., Duffy C. D., Sutherland J. D., 2015, Nat. Chem., 7, 301
Pepe F. A. et al., 2010, in McLean I. S., Ramsay S. K., Takami H., eds, Proc. SPIE Conf. Ser. Vol. 7735, Ground-based and Airborne Instrumentation for Astronomy III. SPIE, Bellingham, p. 77350F
Pickles A. J., 1998, PASP, 110, 863
Pourbaix D. et al., 2004, A&A, 424, 727
Pozuelos F. J. et al., 2020, A&A, 641, A23
Ramirez R. M., Kaltenegger L., 2016, ApJ, 823, 6
Reid I. N., Hawley S. L., Gizis J. E., 1995, AJ, 110, 1838
Reiners A. et al., 2018, A&A, 609, L5
Reiners A. et al., 2022, A&A, 662, A41
Ricker G. R. et al., 2015, J. Astron. Telesc. Instrum. Syst., 1, 014003
Riddick F. C., Roche P. F., Lucas P. W., 2007, MNRAS, 381, 1067
Rimmer P. B., Xu J., Thompson S. J., Gillen E., Sutherland J. D., Queloz D., 2018, Sci. Adv., 4, eaar3302
Rimmer P. B., Thompson S. J., Xu J., Russell D. A., Green N. J., Ritson D. J., Sutherland J. D., Queloz D. P., 2021, Astrobiology, 21, 1099
Sabotta S. et al., 2021, A&A, 653, A114
Salvatier J., Wiecki T. V., Fonnesbeck C., 2016, PeerJ Comput. Sci., 2, e55
Savitzky A., Golay M. J. E., 1964, Anal. Chem., 36, 1627
Schmider F.-X. et al., 2022, in Marshall H. K., Spyromilio J., Usuda T., eds, Proc. SPIE Conf. Ser. Vol. 12182, Ground-based and Airborne Telescopes IX. SPIE, Bellingham, p. 121822O
Scott N. J. et al., 2021, Front. Astron. Space Sci., 8, 138
Seager S., Mallén-Ornelas G., 2003, ApJ, 585, 1038
Seager S., Petkowski J. J., Günther M. N., Bains W., Mikal-Evans T., Deming D., 2021, Universe, 7, 172
Sebastian D. et al., 2021, A&A, 645, A100
Seifahrt A. et al., 2020, in Evans C. J., Bryant J. J., Motohara K., eds, Proc. SPIE Conf. Ser. Vol. 11447, Ground-based and Airborne Instrumentation for Astronomy VIII. SPIE, Bellingham, p. 114471F
Sharma S. et al., 2018, MNRAS, 473, 2004
Skrutskie M. F. et al., 2006, AJ, 131, 1163
Smith J. C. et al., 2012, PASP, 124, 1000
Speagle J. S., 2020, MNRAS, 493, 3132
Stassun K. G., Torres G., 2016, AJ, 152, 180
Stassun K. G., Torres G., 2021, ApJ, 907, L33
Stassun K. G., Collins K. A., Gaudi B. S., 2017, AJ, 153, 136
Stassun K. G., Corsaro E., Pepper J. A., Gaudi B. S., 2018, AJ, 155, 22
Stassun K. G. et al., 2019, AJ, 158, 138

Stevenson K. B., Bean J. L., Seifahrt A., Gilbert G. J., Line M. R., Désert J.-M., Fortney J. J., 2016, ApJ, 817, 141
Stumpe M. C. et al., 2012, PASP, 124, 985
Stumpe M. C., Smith J. C., Catanzarite J. H., Van Cleve J. E., Jenkins J. M., Twicken J. D., Girouard F. R., 2014, PASP, 126, 100
Suárez Mascareño A. et al., 2020, A&A, 639, A77
Sullivan P. W. et al., 2015, ApJ, 809, 77
Sutherland J. D., 2017, Nat. Rev. Chem., 1, 1
The JWST Transiting Exoplanet Community Early Release Science Team, 2023, Nature, 614, 649
Theano Development Team, 2016, preprint (arXiv:1605.02688)
Thompson S. E. et al., 2018, ApJS, 235, 38
Tilley M. A., Segura A., Meadows V., Hawley S., Davenport J., 2019, Astrobiology, 19, 64
Todd Z. R., Fahrenbach A. C., Magnani C. J., Ranjan S., Björkbom A., Szostak J. W., Sasselov D. D., 2018, Chem. Commun., 54, 1121
Triaud A. H. M. J., 2021, in Madhusudhan N.ed., ExoFrontiers; Big Questions in Exoplanetary Science. IOP Publishing, Bristol, p. 6
Triaud A. H. M. J. et al., 2011, A&A, 531, A24
Twicken J. D., Clarke B. D., Bryson S. T., Tenenbaum P., Wu H., Jenkins J. M., Girouard F., Klaus T. C., 2010, in Radziwill N. M., Bridger A., eds, Proc. SPIE Conf. Ser. Vol. 7740, Software and Cyberinfrastructure for Astronomy. SPIE, Bellingham, p. 774023
Twicken J. D. et al., 2018, PASP, 130, 064502
Underwood D. R., Jones B. W., Sleep P. N., 2003, Int. J. Astrobiol., 2, 289
Vach S. et al., 2022, AJ, 164, 71
Van Eylen V., Agentoft C., Lundkvist M. S., Kjeldsen H., Owen J. E., Fulton B. J., Petigura E., Snellen I., 2018, MNRAS, 479, 4786
Van Eylen V. et al., 2021, MNRAS, 507, 2154
Venturini J., Helled R., 2017, ApJ, 848, 95
Venturini J., Guilera O. M., Haldemann J., Ronco M. P., Mordasini C., 2020, A&A, 643, L1
Winters J. G. et al., 2019, AJ, 157, 216
Wu Y., 2019, ApJ, 874, 91
Xu J., Ritson D. J., Ranjan S., Todd Z. R., Sasselov D. D., Sutherland J. D., 2018, Chem. Commun., 54, 5566
Zacharias N., Finch C. T., Girard T. M., Henden A., Bartlett J. L., Monet D. G., Zacharias M. I., 2013, AJ, 145, 44

[1]*School of Physics & Astronomy, University of Birmingham, Edgbaston, Birmingham B15 2TT, UK*
[2]*Astrobiology Research Unit, University of Liège, Allée du 6 août, 19, Sart-Tilman, B-4000 Liège, Belgium*
[3]*Departamento de Física Teórica y del Cosmos, Universidad de Granada, E-18071 Granada, Spain*
[4]*Center for Astrophysics and Space Sciences, UC San Diego, UCSD Mail Code 0424, 9500 Gilman Drive, La Jolla, CA 92093-0424, USA*
[5]*Department of Earth, Atmospheric and Planetary Sciences, MIT, 77 Massachusetts Avenue, Cambridge, MA 02139, USA*
[6]*Instituto de Astrofísica de Canarias (IAC), Calle Vía Láctea s/n, E-38200 La Laguna, Tenerife, Spain*
[7]*Center for Astrophysics | Harvard & Smithsonian, 60 Garden St, Cambridge, MA 02138, USA*
[8]*CNRS, Université Grenoble Alpes, IPAG, F-38000 Grenoble, France*
[9]*Observatoire de Genève, Département d'Astronomie, Université de Genève, Chemin Pegasi 51b, CH-1290 Versoix, Switzerland*
[10]*AIM, CEA, CNRS, Université Paris-Saclay, Université de Paris, F-91191 Gif-sur-Yvette, France*
[11]*European Space Agency (ESA), European Space Research and Technology Centre (ESTEC), Keplerlaan 1, NL-2201 AZ Noordwijk, the Netherlands*
[12]*NASA Ames Research Center, Moffett Field, CA 94035, USA*
[13]*Department of Astrophysical and Planetary Sciences, University of Colorado Boulder, Boulder, CO 80309, USA*
[14]*Department of Physics & Astronomy, Vanderbilt University, 6301 Stevenson Center Ln., Nashville, TN 37235, USA*
[15]*Department of Physics and Kavli Institute for Astrophysics and Space Research, Massachusetts Institute of Technology, Cambridge, MA 02139, USA*
[16]*NASA Exoplanet Science Institute, Caltech/IPAC, Mail Code 100-22, 1200 E. California Blvd., Pasadena, CA 91125, USA*
[17]*Department of Astronomy and Tsinghua Centre for Astrophysics, Tsinghua University, Beijing 100084, China*
[18]*Instituto de Astronomía, Universidad Nacional Autónoma de México, Ciudad Universitaria, Ciudad de México 04510, México*
[19]*Cavendish Laboratory, JJ Thomson Avenue, Cambridge CB3 0HE, UK*
[20]*Campo Catino Astronomical Observatory, Regione Lazio, I-03010 Guarcino (FR), Italy*
[21]*Space Sciences, Technologies and Astrophysics Research (STAR) Institute, Université de Liège, Allée du 6 Août 19C, B-4000 Liège, Belgium*
[22]*Departamento de Astrofísica, Universidad de La Laguna (ULL), E-38206 La Laguna, Tenerife, Spain*
[23]*Instituto de Astrofísica de Andalucía (IAA-CSIC), Glorieta de la Astronomía s/n, E-18008 Granada, Spain*
[24]*Space Telescope Science Institute, 3700 San Martin Drive, Baltimore, MD 21218, USA*
[25]*Center for Space and Habitability, University of Bern, Gesellschaftsstrasse 6, CH-3012 Bern, Switzerland*
[26]*Department of Astronomy, University of Maryland, College Park, MD 20742, USA*
[27]*Department of Aeronautics and Astronautics, Massachusetts Institute of Technology, Cambridge, MA 02139, USA*
[28]*NASA Goddard Space Flight Center, 8800 Greenbelt Road, Greenbelt, MD 20771, USA*
[29]*Kotizarovci Observatory, Sarsoni 90, 51216 Viskovo, Croatia*
[30]*Hazelwood Observatory, Australia*
[31]*SETI Institute, Mountain View, CA 94043, USA*
[32]*Department of Astrophysical Sciences, Princeton University, Princeton, NJ 08544, USA*

This paper has been typeset from a TEX/LATEX file prepared by the author.

© 2023 The Author(s).
Published by Oxford University Press on behalf of Royal Astronomical Society. This is an Open Access article distributed under the terms of the Creative Commons Attribution License (http://creativecommons.org/licenses/by/4.0/), which permits unrestricted reuse, distribution, and reproduction in any medium, provided the original work is properly cited.

3.6 Work in progress: Validation of the Nemesis-12/AMY-1 system

In this section I present a portion of the work done so far on the validation of the Nemesis-12/AMY-1 system. While I have been following this system for over a year and a half, I have not yet had the time to write up the manuscript. Some of the text below is taken from the manuscript draft which is currently in prep.

The NEMESIS (Exoplanet Tra**N**sit Survey of N**E**arby **M**-Dwarfs in ***TESS*** FF**Is**) pipeline, presented in Feliz et al. (2021), was designed to produce detrended photometry of M Dwarfs visible in *TESS* full frame images (FFIs), and conduct a transit search on the resulting lightcurves. In the first release the pipeline analysed data from Sectors 1–5, which included 33,054 M Dwarfs within $100\,\mathrm{pc}$, and produced 29 planet candidates. Of these, 5 matched known *TESS* Objects of Interest (TOIs) and the remaining 24 were new detections.

I selected the 12 candidates found orbiting the hosts with effective temperatures $< 3300\,\mathrm{K}$ as these align the best with the existing SPECULOOS target list. These were TIC 139456051, TIC 143996634, TIC 281461138, TIC 389662862, TIC 9632592, TIC 101991992, TIC 183231138, TIC 408038524, TIC 161478895, TIC 406478079, TIC 7688647, and TIC 192833836 and they were given internal designations of Nemesis 1–12 for the purpose of our follow-up campaign.

All 12 candidates were observed over the course of a few months; of these, 11 were false alarms and one, Nemesis-12, was found to have transits on target at the period reported by the NEMESIS pipeline. The candidate, Nemesis-12.01, has a period of 6.23 days and a depth of ~ 11 ppt.

Shortly after the release of the NEMESIS pipeline, *TESS*'s SPOC (Science Processing Operations Centre) pipeline began to produce lightcurves for up to 160,000 FFI sources per sectors. As this photometry is of slightly higher quality and the transits are easily visible by eye, I present in Figure 3.27 the TESS-SPOC photometry for the sectors where Nemesis-12 was observed (Sectors 5, 6, 32, and 33). During the prime mission, FFIs were taken at 30 min cadence (1800s) but for the first extended mission this was changed to a 10 min cadence (600s). In the second extended mission, FFIs will be taken with 200s cadence.

From May 2021 onwards, the TESS-SPOC pipeline began to search for candidate planets in the FFI lightcurves. Despite this, the candidate around TIC 192833836 has not yet been identified and as such there is no corresponding TOI. As the star is not yet named, and Nemesis-12 is an internal designation, we designated the star AMY-1, where AMY stands for **A**n **M**-dwarf budd**Y**[b].

We characterised the host star using spectral energy distribution analysis (SED, done by Keivan Stassun) and reconnaissance spectroscopy (spectrum collected by Benjamin Rackham, reduced by Daniel Sebastian and analysed by Adam Burgasser). The SED is presented in Figure 3.28 and the spectrum is presented in Figure 3.29. The host star parameters adopted for this work can be found in Table 3.7.

We collected high-resolution imaging using the Zorro speckle instrument on the Gemini-South 8-m

[b] Amy also happens to, very coincidentally, be the name of my dog.

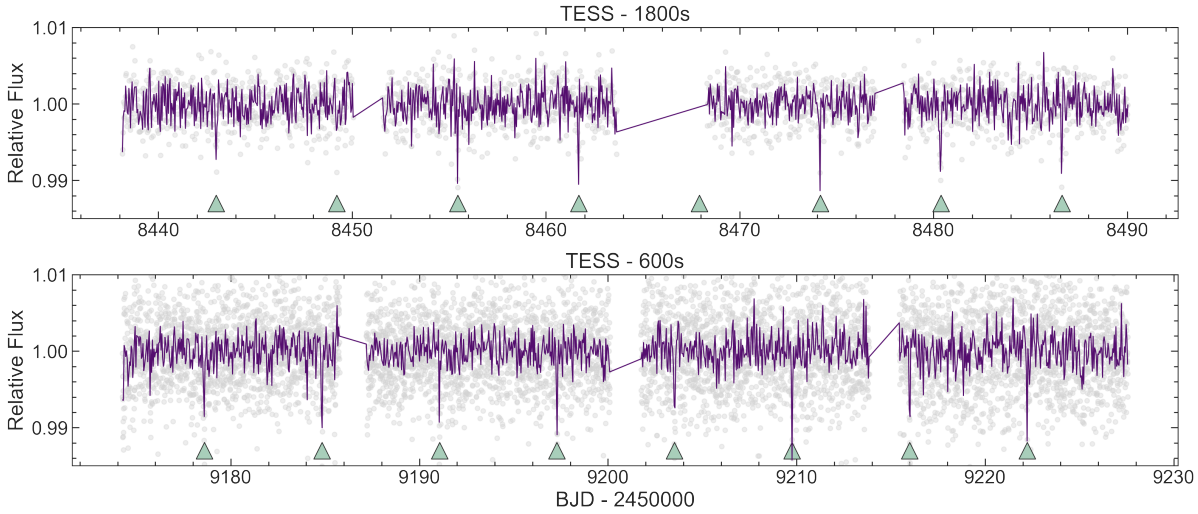


Figure 3.27: TESS-SPOC photometry of Nemesis-12/AMY-1. The light grey points are raw while the purple line indicates the 5min binned points. The transit times are indicated with light green arrows. The upper panel contains the 1800s photometry from sectors 5 and 6, and the lower panel has the 600s photometry from sectors 32 and 33.

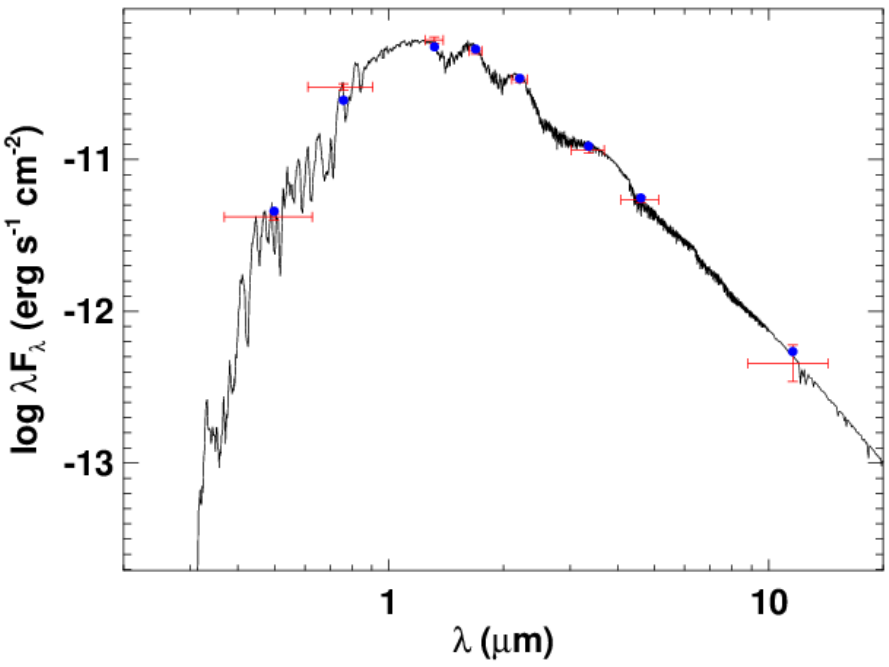


Figure 3.28: Spectral energy distribution of Nemesis-12/AMY-1. Red symbols are observed photometric measurements, with the horizontal bars representing the width of the bandpasses. The blue points are the model fluxes from the best-fit NextGen atmosphere model (black line). (Caption adapted from previous captions provided by Keivan Stassun.)

Table 3.7: Stellar parameters adopted for this work.

Designations	AMY-1, TIC 192833836, 2MASS J05322483-3950016, Gaia DR2 4808732662634331520, UCAC4 251-006761, WISE J053224.78-395002.7	
Parameter	**Value**	**Source**
T mag	13.694±0.008	Stassun et al. (2019)
B mag	17.63±0.17	Zacharias et al. (2013)
V mag	16.704±0.206	Zacharias et al. (2013)
G mag	15.04560±0.0008	Gaia Collaboration (2022)
J mag	12.001±0.026	Cutri et al. (2003)
H mag	11.382±0.026	Cutri et al. (2003)
K mag	11.096±0.023	Cutri et al. (2003)
W1 mag	10.942±0.023	Cutri et al. (2021)
W2 mag	10.779±0.021	Cutri et al. (2021)
W3 mag	10.551±0.064	Cutri et al. (2021)
W4 mag	> 8.92	Cutri et al. (2021)
Distance	66.79±0.20 pc	Bailer-Jones et al. (2021)
α	05:32:24.76	Gaia Collaboration (2022)
δ	-39:50:03.3	Gaia Collaboration (2022)
μ_α	$-46.0\,\mathrm{mas\,yr^{-1}}$	Gaia Collaboration (2022)
μ_δ	$-101.8\,\mathrm{mas\,yr^{-1}}$	Gaia Collaboration (2022)
SpT	M4	This work
$R_\star$	$0.314\pm0.009 R_\odot$	This work
$M_\star$	$0.292 \pm 0.020 M_\odot$	This work
$\mathrm{T_{eff}}$	3211±157 K	This work
$\log g_\star$	4.911±0.004	This work
[Fe/H]	+0.15±0.20 dex	This work (spectroscopy)

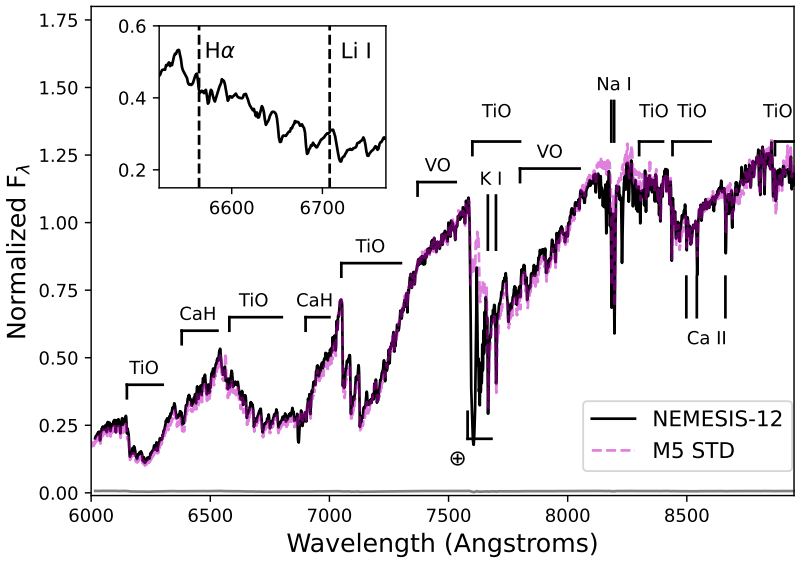


Figure 3.29: LDSS-3C red optical spectrum of Nemesis-12/AMY-1 compared to its best fitting M5 template. (Caption adapted from previous captions provided by Adam Burgasser.)

telescope (Scott et al. 2021) and ruled out any bound or line-of-sight blended companions brighter than 5 magnitudes fainter than AMY-1 within 0.5"[c]. The contrast curves and the reconstructed speckle image are both presented in Figure 3.30.

We collected multi-colour photometry of AMY-1 between October 2021 and February 2023, spanning the blue to the near-infrared (NIR), by making use of SPECULOOS's NIR camera, SPIRIT (Pedersen, in prep) which was temporarily mounted on one of the telescopes of the SPECULOOS Southern Observatory. In total, our ground-based photometry includes six photometric filters which allowed us to confirm the lack of chromatic depth variations of the transits. We then used the statistical validation software `TRICERATOPS` (Giacalone et al. 2021) to validate the planetary nature of AMY-1.01 by calculating the false positive probability (FPP). The threshold for validation is set at < 0.015, and for our candidate we find it to be 0.000664, placing well below the the threshold. We therefore consider the planet validated and refer to it as AMY-1 b.

For the global analysis of all available photometry, we made use of `allesfitter` following the methods described in Chapter 2.4.3. We find it to be a 3.50 ± 0.11 $R_\oplus$ planet with an equilibrium temperature of 378 ± 19 K. All fitted parameters can be found in Table 3.8, and derived parameters are in Table 3.9.

All detrended ground- and space-based photometry is presented in Figure 3.31 along with best-fitting models.

[c]High resolution imaging was provided by Steve Howell and his team.

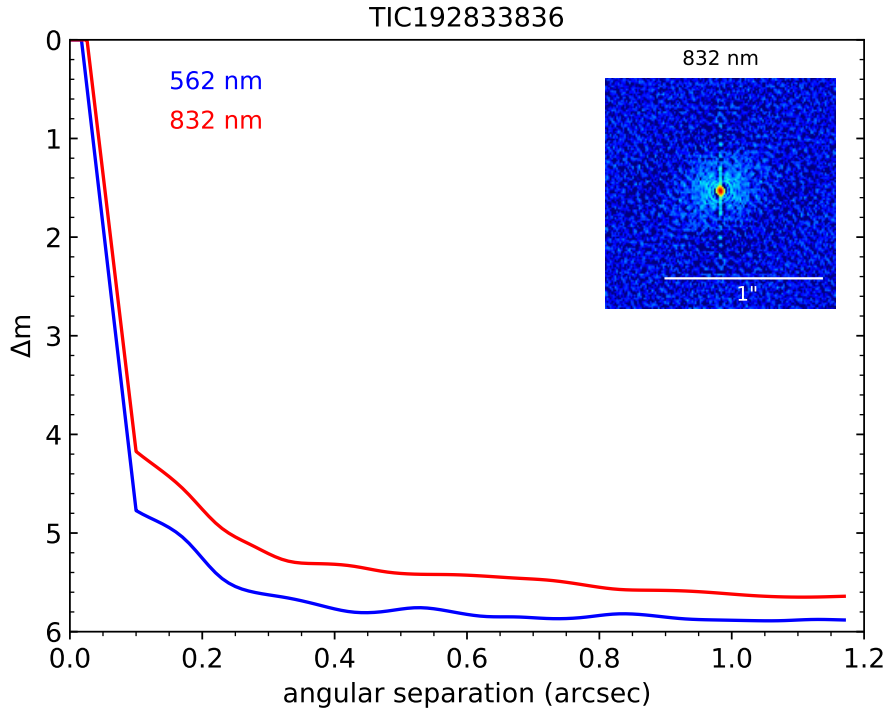


Figure 3.30: Plot showing the $5-\sigma$ speckly imaging contrast curve in the blue and red filters as a function of angular separation. The inset image shows the reconstructed speckle image. (Caption adapted from other captions provided by Steve Howell).

parameter	value	unit	fit/fixed
	Fitted parameters		
$R_b/R_\star$	0.10230 ± 0.00072		fit
$(R_\star + R_b)/a_b$	0.03657 ± 0.00097		fit
$\cos i_b$	0.0202 ± 0.0014		fit
$T_{0;b}$	$2459197.29370^{+0.00040}_{-0.00037}$	BJD	fit
P_b	$6.2340250^{+0.0000036}_{-0.0000039}$	d	fit

Table 3.8: Fitted parameters from AMY-1 b.

Parameter	Value	Source
Derived parameters		
Host radius over semi-major axis b; $R_\star/a_\mathrm{b}$	0.03318 ± 0.00087	derived
Semi-major axis b over host radius; $a_\mathrm{b}/R_\star$	30.14 ± 0.78	derived
Companion radius b over semi-major axis b; $R_\mathrm{b}/a_\mathrm{b}$	0.00339 ± 0.00011	derived
Companion radius b; R_b ($\mathrm{R}_\oplus$)	3.50 ± 0.11	derived
Companion radius b; R_b (R_jup)	0.3124 ± 0.0098	derived
Semi-major axis b; a_b ($\mathrm{R}_\odot$)	9.46 ± 0.38	derived
Semi-major axis b; a_b (AU)	0.0440 ± 0.0018	derived
Inclination b; i_b (deg)	88.840 ± 0.081	derived
Impact parameter b; $b_\mathrm{tra;b}$	$0.610^{+0.026}_{-0.028}$	derived
Total transit duration b; $T_\mathrm{tot;b}$ (h)	1.451 ± 0.012	derived
Full-transit duration b; $T_\mathrm{full;b}$ (h)	$1.041^{+0.014}_{-0.015}$	derived
Host density from orbit b; $\rho_{\star;\mathrm{b}}$ (cgs)	$13.33^{+1.1}_{-1.00}$	derived
Equilibrium temperature b; $T_\mathrm{eq;b}$ (K)	378 ± 19	derived
Transit depth b; $\delta_\mathrm{tr;dil;b;TESS}$ (ppt)	11.21 ± 0.011	derived
Transit depth b; $\delta_\mathrm{tr;dil;b;TS}$ (ppt)	11.18 ± 0.011	derived
Transit depth b; $\delta_\mathrm{tr;dil;b;Callisto}$ (ppt)	$11.17^{+0.12}_{-0.11}$	derived
Transit depth b; $\delta_\mathrm{tr;dil;b;spirit}$ (ppt)	$10.95^{+0.12}_{-0.11}$	derived
Transit depth b; $\delta_\mathrm{tr;dil;b;ganymede_g}$ (ppt)	$11.79^{+0.13}_{-0.15}$	derived
Transit depth b; $\delta_\mathrm{tr;dil;b;Io_i+z}$ (ppt)	$11.19^{+0.11}_{-0.12}$	derived
Transit depth b; $\delta_\mathrm{tr;dil;b;europa_z}$ (ppt)	$10.94^{+0.10}_{-0.12}$	derived
Transit depth b; $\delta_\mathrm{tr;dil;b;io_g}$ (ppt)	$11.77^{+0.15}_{-0.13}$	derived
Transit depth b; $\delta_\mathrm{tr;dil;b;europa_r}$ (ppt)	$11.67^{+0.14}_{-0.13}$	derived
Transit depth b; $\delta_\mathrm{tr;dil;b;ganymede_i}$ (ppt)	11.31 ± 0.11	derived
Transit depth b; $\delta_\mathrm{tr;dil;b;TESS_2}$ (ppt)	11.21 ± 0.11	derived
Limb darkening; $u_\mathrm{1;Sloan-g'}$	0.5959 ± 0.0078	derived
Limb darkening; $u_\mathrm{2;Sloan-g'}$	0.2339 ± 0.0075	derived
Limb darkening; $u_\mathrm{1;Sloan-r'}$	0.5820 ± 0.0072	derived
Limb darkening; $u_\mathrm{2;Sloan-r'}$	0.1907 ± 0.0068	derived
Limb darkening; $u_\mathrm{1;Sloan-i'}$	0.3621 ± 0.0058	derived
Limb darkening; $u_\mathrm{2;Sloan-i'}$	0.2234 ± 0.0054	derived
Limb darkening; $u_\mathrm{1;TESS}$	0.3246 ± 0.0054	derived
Limb darkening; $u_\mathrm{2;TESS}$	0.2088 ± 0.0050	derived
Limb darkening; $u_\mathrm{1;i+z'}$	0.2969 ± 0.0052	derived
Limb darkening; $u_\mathrm{2;i+z'}$	0.2182 ± 0.0049	derived
Limb darkening; $u_\mathrm{1;Sloan-z'}$	0.2059 ± 0.0048	derived
Limb darkening; $u_\mathrm{2;Sloan-z'}$	0.1527 ± 0.0042	derived
Limb darkening; $u_\mathrm{1;SPIRIT}$	0.2105 ± 0.0048	derived
Limb darkening; $u_\mathrm{2;SPIRIT}$	0.1553 ± 0.0042	derived

Table 3.9: Derived parameters for AMY-1 b.

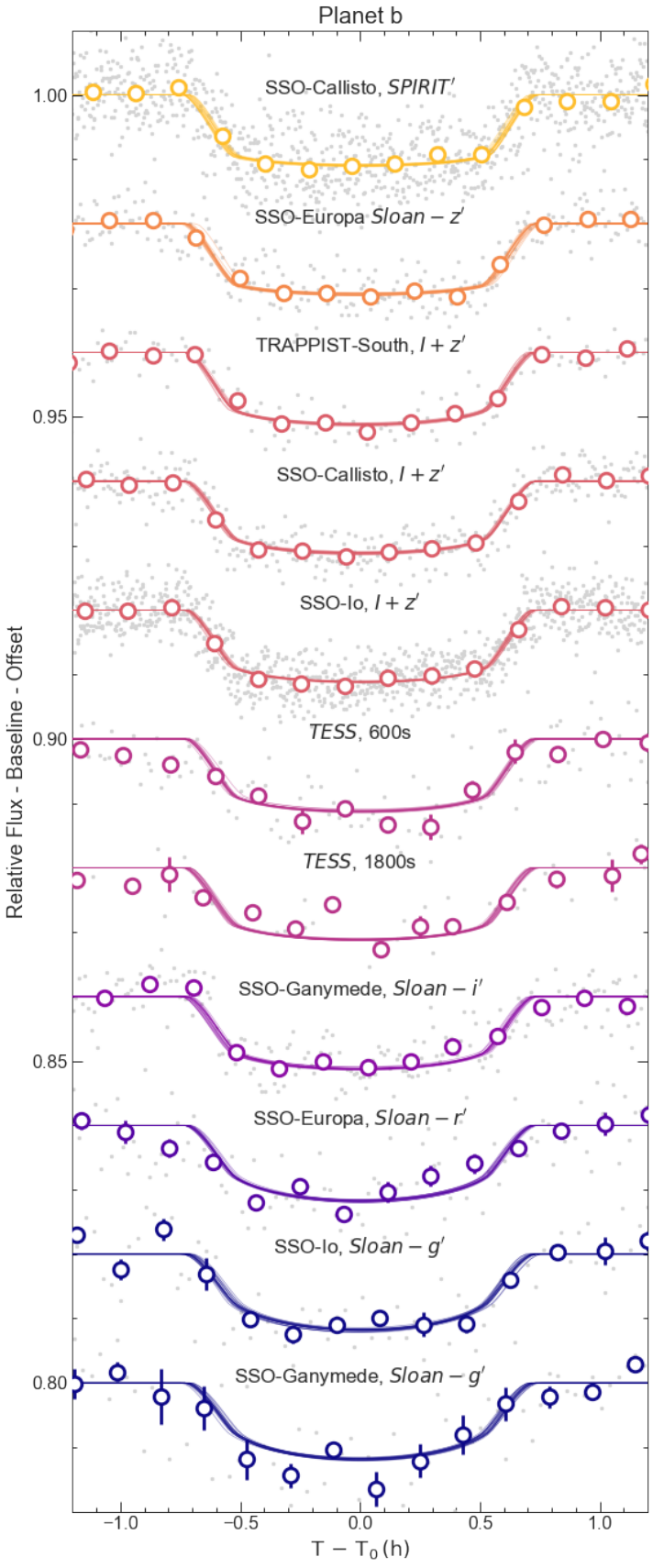


Figure 3.31: Phase-folded and detrended ground- and space-based photometry for AMY-1 b. Overplotted on each lightcurve are 20 models randomly drawn from the posterior distribution.

4

MANGOs in Space

4.1 World: meet MANGOs

This chapter presents a project that I have led within SPECULOOS since its inception, one that was born out of sheer curiosity. While searching for new candidates to observe with ASTEP, I came across a handful of Hot Jupiter-like candidates around M dwarfs. The notes in the *TESS* SG1 Google Sheet mentioned that these objects are rare, which led to a fair bit of reading on the subject. I then proposed them for observation with ASTEP just before the start of the 2022 observing season, but it was decided they were not the best way to exploit the observatory's unique capabilities.

Some weeks later, during late night discussions about potential ESO radial velocity proposals with my SPECULOOS colleague Mathilde Timmermans, I brought up the possibility of observing these rare candidates. I shared with her all I had learned about these objects and we agreed that we would initially pursue validations of some of the most promising systems.

In the months that followed, we scheduled dozens of transits for many systems. Some showed clear chromaticity indicative of binarity, but we soon realised that even the systems composed of Brown Dwarf - M-dwarf or M-dwarf - M-dwarf binaries are of high scientific value. It became evident that other teams were also pursuing validation and confirmation of Hot Jupiter-like planets around low-mass stars, so we chose to make our programme more holistic by systematically following up on all three flavours of close-in giant objects orbiting M dwarfs: giant planets, Brown Dwarfs, and M dwarfs.

And like any good astronomical observing programme, we needed a name: MANGOs are **M**-dwarfs **A**ccompanied by close-i**N** **G**iant **O**rbiter**s**[a].

The goals of the MANGOs programme are as follows:

- To understand the mechanism by which Hot Jupiters form around low-mass stars. As described in Chapter 1, the leading theory for giant planet formation, namely core accretion, does not predict their existence. And yet, they exist. By systematically working on detection of these systems we aim to build up a statistically significant sample with measured masses in order to uncover their formation histories.

[a] This acronym may be the achievement I am most proud of from my whole thesis.

- Brown Dwarfs around low-mass stars are equally rare, and the question of the boundary between Brown Dwarfs and giant planets is as yet unclear. We seek to carry out a census of these systems and characterise their densities, to uncover whether their formation mechanisms distinguishes them from giant planets, and indeed from Brown Dwarfs around FGK stars.
- M-dwarf masses and radii are known to deviate significantly from model predictions (Parsons et al. 2018), more so than other spectral types. These models can only be improved with precise measurements of masses and radii of low-mass stars, and the only way to gain these measurements is by identifying double-lined binary systems containing M dwarfs. Therefore, we hope to gain precise spectroscopic masses for the M-M binaries we uncover, in order to improve the mass-radius relation for low-mass stars. Only by improving our understanding of the masses and radii of M-dwarf hosts can we gain precisely derived measurements of masses and radii for the planets orbiting them.

This programme has been running within the SPECULOOS consortium for approximately one year at the time of writing. In that time we have observed dozens of MANGOs candidates and validated 19 new planets by collecting multi-colour ground-based photometry. We have also identified several new binaries to be classified.

In this Chapter, I present the current status of the MANGOs project. The first paper in the series is presented below in Section 4.2, and the second paper is currently in the preparatory stages. I present some of the work done so far on MANGOs II in Section 4.4.

4.2 Paper: MANGOs I - Validation of the TOI-4860 system

TOI-4860 b was one of the first MANGOs added to our target list back in March 2022. We initially scheduled it on TRAPPIST-South to confirm there were transits on the correct target, but the star vanished from the sky before we could conduct further follow-up that season. As soon as it reappeared in the sky at the start of 2023, we began to collect transits in all available photometric bands to carry out a chromaticity check. We also observed at phase 0.5 to check for signs of a secondary eclipse.

It soon became evident that this was indeed a planet, and one not to be missed. For many of our early systems, we were beaten to a validation paper by other teams and instead contributed our data to their publications where possible. But for TOI-4860 b, we did not want to miss the boat.

The team rapidly began to prepare a validation paper to be led by Amaury Triaud. However, when we requested to put an abstract on the *TESS* Wiki, we were notified that other teams also had photometry and that two teams had collected radial velocity observations. One other photometric team was preparing a confirmation paper, so we reached out to one of the RV teams inviting them to collaborate. They generously provided their high-resolution spectra and joined our publication. This upgraded our paper from a validation to a confirmation, and meant that two parallel papers were prepared using independent data sets for the same system[b].

[b] At the time of writing, the other team's paper is yet to be submitted.

As one of the leaders of the MANGOs project, I was involved in the scheduling, reduction, modeling and reporting of ground based transits taken with the SPECULOOS Southern Observatory. For the paper I also carried out the global analysis using `allesfitter`, produced the plots in Figures 1 and 2, and the results tables found in Table 1 and Table A4. I also wrote up the analysis in Section 1.3. Finally, I retrieved the field images and made Figure A4, and calculated the transmission spectroscopy metric for the system discussion.

All other sections of the paper were contributed by other team members.

MNRAS **000**, 1–8 (2023) Preprint 29 June 2023 Compiled using MNRAS LATEX style file v3.0

An M-dwarf accompanied by a close-in giant orbiter

Amaury H.M.J. Triaud,[1]* Georgina Dransfield,[1] Taiki Kagetani,[2] Mathilde Timmermans,[3] Norio Narita,[4,5,6] Khalid Barkaoui,[3,6,7] Teruyuki Hirano,[5,8] Benjamin V. Rackham,[7,9]† Mayuko Mori,[2] Thomas Baycroft,[1] Zouhair Benkhaldoun,[10] Adam J. Burgasser,[11] Douglas A. Caldwell, [12,13] Karen A. Collins,[14] Yasmin T. Davis,[1] Laetitia Delrez,[3,15] Brice-Oliver Demory,[16] Elsa Ducrot,[17] Akihiko Fukui,[4,6] Clàudia Jano Muñoz,[18] Emmanuël Jehin,[15] Lionel J. García,[3] Mourad Ghachoui,[3,10] Michaël Gillon,[3] Yilen Gómez Maqueo Chew,[19] Matthew J. Hooton,[18] Masahiro Ikoma,[8] Kiyoe Kawauchi,[20] Takayuki Kotani,[21,8,22] Alan M. Levine,[9] Enric Pallé,[6] Peter P. Pedersen,[23] Francisco J. Pozuelos, [24,3] Didier Queloz,[18,23] Owen J. Scutt,[1] Sara Seager,[7] Daniel Sebastian,[1] Motohide Tamura,[25,21,8] Samantha Thompson,[18] Noriharu Watanabe,[2] Julien de Wit,[7] Joshua N. Winn,[26] Sebastián Zúñiga-Fernández[3]
A list of affiliations is given at the end of the paper

Accepted XXX. Received YYY; in original form ZZZ

ABSTRACT

In the last decade a dozen close-in giant planets have been discovered orbiting stars with spectral types ranging from M0 to M4, a mystery since known formation pathways do not predict the existence of such systems. Here, we confirm TOI-4860 b, a Jupiter-sized planet orbiting an M4.5 host, a star at the transition between fully and partially convective interiors. First identified with *TESS* data, we validate the transiting companion's planetary nature through multi-colour photometry from the TRAPPIST-South/North, SPECULOOS and MuSCAT3 facilities. Our analysis yields a radius of 0.76 ± 0.02 R_{Jup} for the planet, a mass of 0.34 $M_{\odot}$ for the star, and an orbital period of 1.52 days. Using the newly commissioned SPIRIT InGaAs camera at the SPECULOOS South Observatory, we collect infrared photometry in zYJ that spans the time of secondary eclipse. These observations do not detect a secondary eclipse, placing an upper limit on the brightness of the companion. The planetary nature of the companion is further confirmed through high-resolution spectroscopy obtained with the IRD spectrograph at Subaru Telescope, from which we measure a mass of 0.67 ± 0.14 M_{Jup}. Based on its overall density, TOI-4860 b appears to be rich in heavy elements, like its host star.

Key words: exoplanets – infrared: planetary systems – techniques: photometric – techniques: radial velocities

Protoplanetary disc mass scales with stellar mass (e.g. Andrews et al. 2013). It is therefore expected that the lowest-mass stars have less material available to form exoplanets with masses similar to Jupiter's. Many formation models confirm this (e.g. Laughlin et al. 2004; Ida & Lin 2005; Alibert et al. 2011; Burn et al. 2021). However, this does not mean gas-giant planet formation is totally impossible, and several examples have been identified with almost every detection method, including GJ 876 by radial velocities (Delfosse et al. 1998; Marcy et al. 1998; Correia et al. 2010), MOA 2003-BLG-53 by microlensing (Bond et al. 2004), and WASP-80 (Triaud et al. 2013) and HATS-6 (Hartman et al. 2015) by transits. The accumulation of these detections is being used to compute occurrence rates (e.g. Bryant et al. 2023) that suggest a small reduction in giant planet frequency compared to Sun-like stars, which will eventually feed into and calibrate population synthesis models (e.g. Burn et al. 2021) and improve our understanding of planetary formation and orbital evolution.

∗E-mail: a.triaud@bham.ac.uk
†51 Pegasi b Fellow

Of particular interest amongst all exoplanets are those in a transiting geometry. Wavelength-dependent transit observations obtained with high- and low-resolution spectra produce transmission spectra (Seager & Sasselov 2000). These are analysed to study exoplanets' atmospheric structure (Knutson et al. 2012), their chemical composition (Madhusudhan & Seager 2009) and even their wind speed (Snellen et al. 2010). Giant planets transiting M dwarfs are beneficial with respect to such planets transiting Sun-like stars in two main ways. First, the fractional amplitude of features within a planet's transmission spectrum scales with $R_{\star}^{-2}$, making a planet's atmospheric signature easier to measure. Second, M dwarfs' cooler effective temperatures allow short-period gas giants to have temperate equilibrium temperatures (e.g. Triaud 2021).

Calibrating stellar evolution models for fully convective stars is important since the vast majority of exoplanets have physical parameters that depend on the assumed stellar parameters. The only practical way to obtain absolute stellar masses and radii is to model double-lined eclipsing binaries (e.g. Triaud et al. 2020). However, there are very few such systems among fully convective stars (< 0.3 $M_{\odot}$; Baraffe et al. 2015). Such systems are intrinsically faint, short period bina-

© 2023 The Authors

ries are rare (Duquennoy & Mayor 1991), and the occurrence rate of binary stars decreases with the primary star's mass (Burgasser 2007). There is currently only one known double-lined, fully-evolved eclipsing binary on the Main Sequence where the primary has a mass < 0.2 M$_\odot$ (Casewell et al. 2018).

To address these and closely related science topics, the SPECULOOS consortium launched an internal project code-named MANGOs (M-dwarfs Accompanied by close-iN Giant Orbiters; Dransfield in prep) whose purpose is to confirm and study all transiting/eclipsing companions to late-M dwarfs. This confirmation of TOI-4860 b is the MANGO project's first publication, for which we joined forces with the MuSCAT3 and IRD teams. TOI-4860 (2MASS J12141555-1310290, TIC 335590096, Gaia DR2 3571038605366263424) is a $V = 16.47$, $J = 12.06$ M star at a distance of 80 pc (Stassun et al. 2019). This system contains a transiting/eclipsing object for which our analysis of all collected observations indicates a planetary companion. The system was first observed by *TESS* (Ricker et al. 2014) where a threshold crossing event was detected. It is at that moment that TIC 335590096 received the TOI-4860 designation, with the planet candidate being referred to as TOI-4860.01. Several ground-based photometric observatories later confirmed the existence of periodic transit-like features. All photometric data are described in Sec 1.1. In addition, spectra were collected to determine the stellar parameters and measure radial velocities (Sec 1.2). We describe our analysis of all data in Sec. 1.3. Our results are detailed and discussed in Sec. 2.

1 OBSERVATIONS COLLECTED AND THEIR ANALYSIS

Another team has also confirmed this planetary system (Bonfils et al. in prep). Through communications with them, we agreed they would report an analysis of both their data and the *TESS* data, and that the present paper would report a fully independent analysis that does not cover *TESS* photometry. However we do use *TESS* data to produce validation tests and search for transit timing variations.

1.1 Description of the photometric data

TOI-4860 was observed with *TESS* in sector 10 with 30-min cadence spanning 2019 March 26 to 2019 April 22 and sectors 36 and 46 with 10-min cadence respectively spanning the periods 2021 March 07 to 2021 April 02 and 2021 December 02 to 2021 December 30. The Full Frame Images were first processed by the Quick Look Pipeline (Huang et al. 2020) resulting in the detection of a threshold crossing event and the assignment of a *TESS* Object of Interest (TOI) number on 2021 December 21. The data were later reprocessed by the TESS-SPOC pipeline (Jenkins et al. 2016) and we make use of these to search for transit timing variations (TTVs). We retrieved these data from the NASA Mikulski Archive for Space Telescopes (MAST) with the Lightkurve package (Lightkurve Collaboration et al. 2018).

We obtained ground-based seeing-limited photometric data with the TRAPPIST-South/North (Jehin et al. 2011; Gillon et al. 2011; Barkaoui et al. 2019), SPECULOOS (Delrez et al. 2018; Burdanov et al. 2018; Sebastian et al. 2021), and MuSCAT3 (Narita et al. 2020) facilities. Two transits were obtained with TRAPPIST-South on 2022 March 27 and 2022 April 22 in a custom blue-blocking band and the *Sloan-z'*-band respectively, and we obtained one transit with TRAPPIST-North in the *I+z*-band on 2023 January 21. We observed one transit simultaneously in the *Sloan-g'*, *Sloan-i'*, and *Sloan-r'*-bands, as well as using the SPIRIT camera (SPeculoos' Infra-Red photometric Imager for Transits), which is an InGaAs-based instrument, with a custom wide-pass filter called *zYJ* (Pedersen et al. in prep) using all four SPECULOOS-South telescopes on 2023 January 27, and one transit in the *Sloan-z'*-band on 2023 January 30. The data reduction and photometric measurements of the TRAPPIST and SPECULOOS data were done with a custom pipeline built with prose (Garcia et al. 2021), a Python framework designed for image processing. MuSCAT3 observed one transit epoch on 2023 April 18 in four photometric bands simultaneously (*Sloan-g'*, *Sloan-i'*, *Sloan-r'*, and *Sloan-z_s*). All observations are reported in the journal of observations in Table A1.

1.2 Spectroscopic data & stellar parameter determination

We collected an optical spectrum of TOI-4860 with the MagE spectrograph (Marshall et al. 2008) on the 6.5-m Magellan Baade Telescope on 2023 Feb 03 (UT) under clear and stable conditions. We used the 0.″7 slit to gather a 3500–10 000 Å spectrum with R~4100. We collected two exposures of 530 s each, totaling 17.7 min on source, followed by a 2-s ThAr exposure. We observed the spectrophotometric standard LTT 3218 (Hamuy et al. 1994; Vernet et al. 2010; Moehler et al. 2014) earlier that night for flux calibration and did not apply any telluric correction. Relying on a standard set of afternoon MagE calibrations, we reduced the data with `PypeIt` (Prochaska et al. 2020b; Prochaska et al. 2020a). The final spectrum has a maximum SNR of 149 at 7584 Å and a median SNR of 61 over the full 3500–10 000 Å range.

The optical spectrum of TOI-4860 is best matched to M4 and M5 templates from Bochanski et al. (2007) (across the 4500-8900 Å range) so we adopt a mean classification of M4.5±0.5. This classification is confirmed by spectral index/classification relations from Reid et al. (1995), Gizis (1997), and Lépine et al. (2003). The optical spectrum shows no indication of significant subsolar metallicity features, and measurement of the zeta metallicity index of Lépine et al. (2013), $\zeta = 1.113 \pm 0.003$, implies [Fe/H] = +0.15 ± 0.20 based on the calibration of Mann et al. (2013). None of the H I Balmer features are seen in emission or absorption, indicating weak magnetic activity, and we infer an upper limit of $\log_{10}(L_{\mathrm{H}\alpha}/L_{\mathrm{bol}}) \lesssim -5.4$ based on the χ relation of Douglas et al. (2014). The absence of magnetic emission suggests an age $\gtrsim$ 4.5 Gyr (West et al. 2008). We also see no evidence of Li I absorption, consistent with an evolved low-mass star.

We collected a near-infrared spectrum of TOI-4860 with the SpeX spectrograph (Rayner et al. 2003) on the 3.2-m NASA Infrared Telescope Facility (IRTF) on 2022 April 19 (UT) in clear conditions with seeing of 1.″5. We used the short-wavelength cross-dispersed (SXD) mode with the $0.3'' \times 15''$ slit aligned to the parallactic angle, yielding spectra that cover 0.75–2.42 μm with R~2000. We nodded in an ABBA pattern and collected 10 exposures of 179.8 s each, totaling 30 min on source. We collected the standard set of SXD flat-field and arc-lamp exposures immediately after the science frames, followed by an A0 V telluric standard. We reduced the data with Spextool v4.1 (Cushing et al. 2004), following the standard approach.

We use the SpeX Prism Library Analysis Toolkit (SPLAT, Burgasser & Splat Development Team 2017) to compare the spectrum to that of single-star spectral standards in the IRTF Spectral Library (Cushing et al. 2005; Rayner et al. 2009), finding the M5 standard Wolf 47 to be the best single match. The M4 standard Ross 47 only provides a marginally poorer fit, and so we adopt a spectral type of M4.5 ± 0.5, consistent with the optical classification. Following Delrez et al. (2022), we use index measurements across the SpeX spectrum defined by Mann et al. (2014) to derive a metallicity estimate of [Fe/H] = +0.45 ± 0.15.

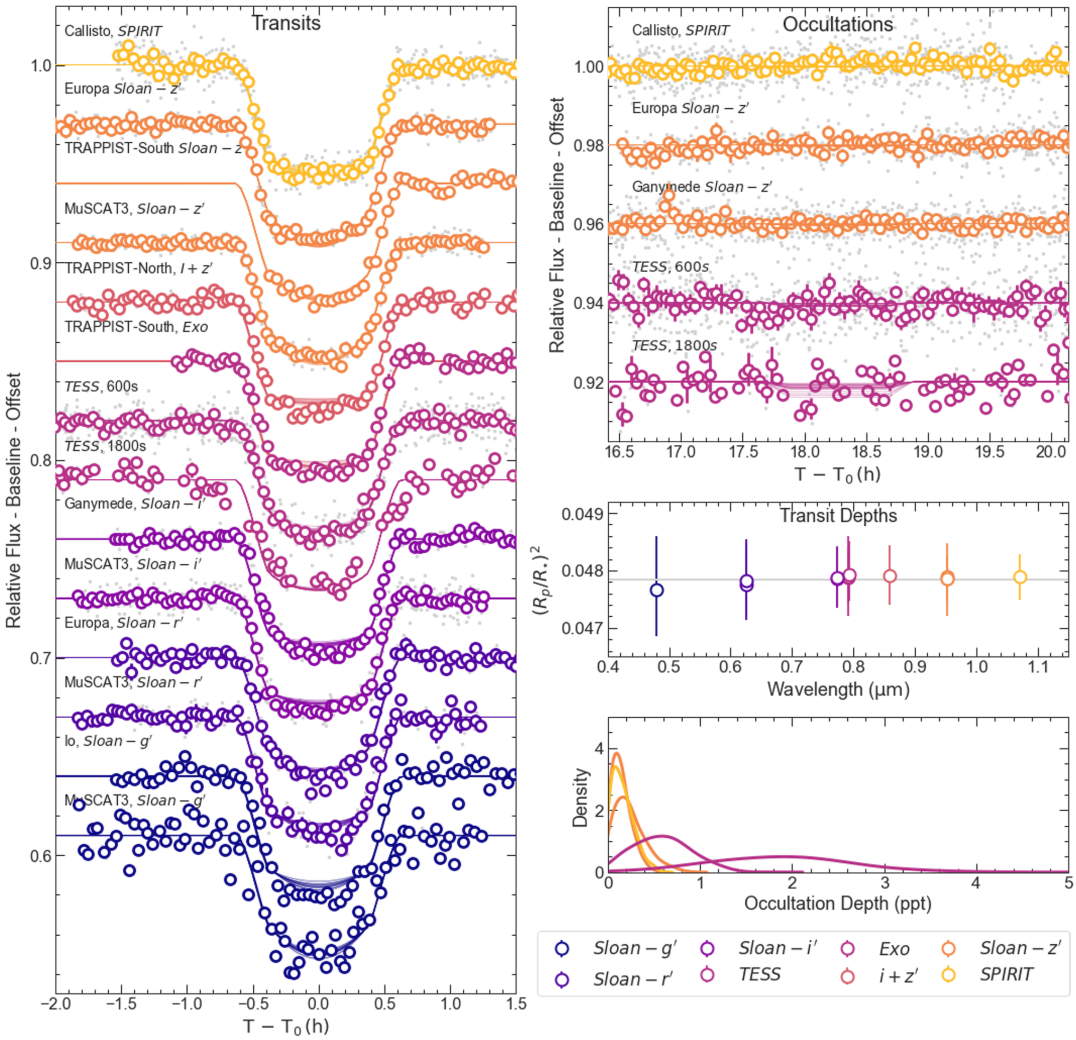


Figure 1. This figure shows all of the photometric data we use in this paper. On the left hand side we show each lightcurve and 20 models obtained from the posterior. On the top right, we plot photometry obtained around the time of secondary eclipse and 20 models from the posterior for each of the 14 lightcurves. The *TESS* data are not used to determine planetary parameters in this paper. Instead, they were used to corroborate the other observations we obtained. The middle right panels shows that when transit depths $R_b^2/R_\star^2$ are fitted independently in each wavelength, they demonstrate that the transit signal is achromatic. The bottom right panel draws the density of posterior samples for solutions including secondary eclipse depths parameters (arbitrary unit), assuming the orbit of the planet is circular. All are consistent with no loss of light. All colours are chosen to depict the wavelength of the observations.

We use the infrared metallicity along with the *Gaia* DR3 distance and *BP–RP* color (Gaia Collaboration et al. 2016, 2022), and the 2MASS Ks-band apparent magnitude (m_{Ks}; Skrutskie et al. 2006) to derive the fundamental parameters of TOI-4860. With the *Gaia* distance and m_{Ks} we calculate the absolute Ks-band magnitude (M_{Ks}). We then use the empirical relation between M_{Ks}, [Fe/H], stellar mass ($M_\star$; Mann et al. 2019, Eq. 5) and radius ($R_\star$; Mann et al. 2015, Eq. 5) to estimate $M_\star$ and $R_\star$. We estimate the stellar effective temperature ($T_{\rm eff}$) using the empirical relation between *Gaia* *BP–RP* color, [Fe/H], and this parameter (Mann et al. 2015, Eq. 6). These and derivative parameters are given in Table A2.

In addition, seven high-resolution spectra were obtained with IRD (Tamura et al. 2012; Kotani et al. 2018), at Subaru, between 2023 January 08 and 2023 February 03. These data are reduced as described in Hirano et al. (2020) to obtain precision radial-velocities with a mean precision of 23 m s^{-1}. Three of these were affected by poor weather, and two from technical issues, but we use all in our analysis and absorb their scatter with a jitter term. All measurements are listed in Table A3. Comparison of cross-correlation profiles of TOI-4860 with those of the reference star TOI-1634 (Hirano et al. 2021), also known to host a transiting planet (Cloutier et al. 2021; Hirano et al. 2021), show that TOI-4860 is a single-lined system (Fig. A3). TOI-4860's line profile is similar to TOI-1634 implying a similarly slow rotating star. Based on the spectroscopic resolution of IRD, we can place a limit on the projected rotational velocity, $v \sin i_\star < 5$ km s^{-1}.

1.3 Joint analysis of all the data

We analyse the ground-based photometric and high-resolution radial-velocity data described in Sections 1.1 and 1.2 using Allesfitter (Günther & Daylan 2019, 2021, and references therein), making use of the nested sampling algorithm Dynesty (Speagle 2020).

We adopt the signal parameters reported by SPOC (Jenkins et al. 2016; Caldwell et al. 2020) as uniform priors and the stellar parameters derived in Section 1.2 as normal priors. We additionally make

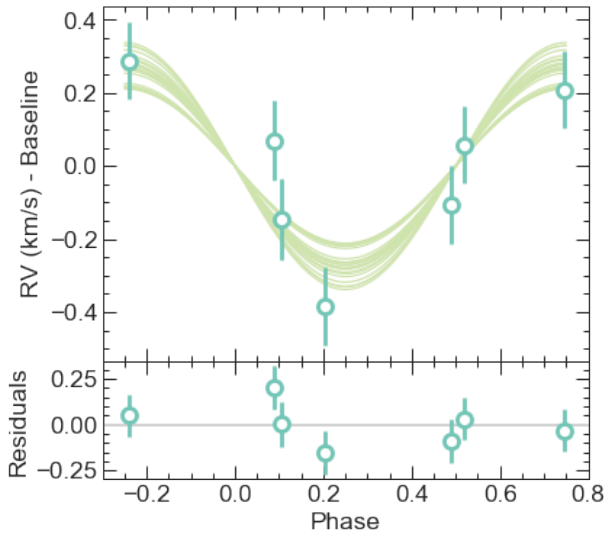


Figure 2. Radial-velocities measured by IRD as a function of orbital phase. We show 20 models randomly drawn from the posterior.

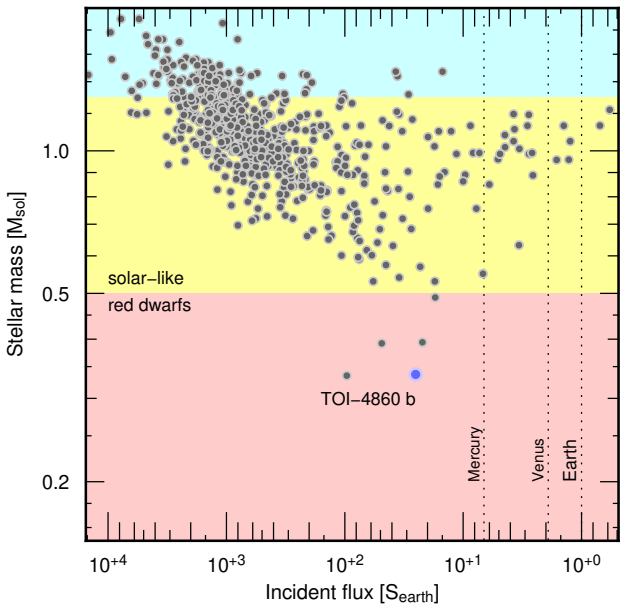


Figure 3. This diagram highlights TOI-4860 b's uniqueness amongst transiting giant exoplanets as being hosted by the lowest mass star yet. The purple dot corresponds to TOI-4860 b. All other grey dots correspond to planets with radius > 0.6 R$_{Jup}$ and a measured mass < 25 M$_{Jup}$. Data from TEPCAT (Southworth 2011).

Table 1. Fitted and derived parameters after performing a global analysis of the data. *TESS* photometry is not included in the analysis. Parameters denoted with * were estimated by letting the eccentricity to be set by two free parameters. All other parameters assume a circular orbit. The equilibrium temperature is calculated assuming an albedo of 0.3 and emissivity of 1.

Fitted parameters	
$R_b/R_\star$	0.22009 ± 0.00070
$(R_\star + R_b)/a_b$	0.10848 ± 0.00085
$\cos i_b$	0.0197 ± 0.0030
$T_{0;b}$ (BJD)	$2\,459\,832.641439 \pm 0.000032$
P_b (d)	$1.52275959^{+0.00000032}_{-0.00000035}$
K_b (km/s)	0.250 ± 0.049
$^*\sqrt{e_b}\cos\omega_b$	$0.11^{+0.17}_{-0.24}$
$^*\sqrt{e_b}\sin\omega_b$	$0.056^{+0.10}_{-0.094}$
$\ln\sigma_{\rm jitter;ird}$ (ln km/s)	$-2.16^{+0.27}_{-0.25}$
Derived parameters	
Host radius over semi-major axis; $R_\star/a_b$	0.08891 ± 0.00066
Semi-major axis ; a_b (AU)	0.01845 ± 0.00059
Inclination; i_b (deg)	88.87 ± 0.18
Impact parameter; $b_{tra;b}$	0.221 ± 0.033
Full-transit duration; $T_{full;b}$ (h)	$0.7742^{+0.0050}_{-0.0060}$
Total transit duration; $T_{tot;b}$ (h)	1.2435 ± 0.0041
Epoch occultation; $T_{0;occ;b}$	$2\,459\,833.402819 \pm 0.000033$
*Eccentricity; e_b	$0.047^{+0.053}_{-0.035}$
*Argument of periastron; w_b (deg)	98^{+210}_{-82}
Companion mass; M_b (M$_{Jup}$)	0.67 ± 0.14
Companion radius ; R_b (R$_{Jup}$)	0.756 ± 0.024
Companion density; ρ_b (g cm^{-3})	$1.92^{+0.50}_{-0.44}$
Companion surface gravity; g_b (cm s^{-2})	3090 ± 610
Equilibrium temperature; $T_{eq;b}$ (K)	624 ± 30

use of PyLDTK (Parviainen & Aigrain 2015) and the Phoenix stellar atmosphere models (Husser et al. 2013) to calculate quadratic limb darkening coefficients for each photometric band used, and adopt these as normal priors.

We run two fits in the first instance: one with a circular orbit and the second where eccentricity is allowed to vary, parameterised as $\sqrt{e_b}\cos\omega_b$ and $\sqrt{e_b}\sin\omega_b$ (Triaud et al. 2011). We fit for all transit parameters ($R_p/R_\star$, $(R_\star + R_p)/a$, $\cos i$, T_0, and P) in both fits, as well as for the surface brightness ratio in the two photometric bands where we observed near phase 0.5, to search for the signal produced by a secondary eclipse. By doing so, we can derive an upper limit on the occultation depths and therefore on the brightness temperature of the planet. Such short orbits are likely to be circularised (e.g. Guillot et al. 1996), so we do not expect to find significant eccentricity in our model. We additionally fit for a radial velocity jitter term which is added in quadrature to the input RV errors.

Finally, to assess the presence of additional perturbing bodies in the system, we ran a third fit as in Dransfield et al. (2022), with each transit mid-times being a free parameter. We find all transit mid-times measured from ground-based follow-up are consistent with no transit timing variations.

2 RESULTS & DISCUSSION

Our joint analysis of the ground based photometry and radial velocities confirms that candidate TOI-4860.01 is consistent with a transiting exoplanet. All transits we collected have similar depths, and the depths of odd transits are similar to those of even transits. All transits are consistent with the *TESS* transits as well (Fig. 1). To further confirm the planetary nature of this signal, we searched for contaminating light. *Gaia* measurements demonstrate that TOI-4860 is a high proper-motion system. A search of the Digitised Sky Survey database[1] shows there are no known contaminating background source near the target at the moment (Fig. A4). In addition, mid to late M dwarfs suffer less from this kind of false positives on account of their spectral types. The IRD spectra also show the system is single-lined, removing most gravitationally-bound sources of contamination.

[1] Retrieved from https://irsa.ipac.caltech.edu/applications/finderchart on 2023 May 11.

We find TOI-4860 b to be a 0.67 M_{Jup}, 0.76 R_{Jup} planet on a P_{orb} = 1.522 day transiting orbit. The host star has an M4.5 spectral type (T_{eff} = 3390 K, $M_\star$ = 0.34 $M_\odot$). As expected, measurements are compatible with a circular orbit, and we place a 95% confidence upper limit at $e_b < 0.15$. All results are presented in Table 1, with complementary information in Table A4. These fitted and derived values were not obtained using any *TESS* data and are entirely independent of the parallel analysis by Bonfils et al. (in prep). The IRD radial-velocities were mostly taken under adverse conditions, and we expect the mass to be the weakly determined by our analysis (Fig. 2). TOI-4860 b's density of 1.55 ρ_{Jup} implies the planet is particularly enriched with heavy elements (e.g. Thorngren et al. 2016; Thorngren & Fortney 2019), which appears consistent with indications the star is also enriched in metals (with a mean [Fe/H] = +0.30 ± 0.13; Tab. A2). Gas giants with large metal mass fractions are not rare, and TOI-4860 b likely fall in that category. Such systems are important to refine our understanding of the planet formation process (e.g. Morbidelli et al. 2023)

TOI 4860 b sits in a part of the parameter space that is very sparsely populated (Fig. 3). Restricting known transiting exoplanets to those where $R_p > 0.6\,R_{Jup}$ and their host has $M_\star < 0.5\,M_\odot$, there are seven objects listed on TEPCAT (`https://www.astro.keele.ac.uk/jkt/tepcat/`; Southworth 2011). LHS 6343 (Johnson et al. 2011; Montet et al. 2015) and TOI-263 (Palle et al. 2021) both host a transiting brown dwarf. TOI-1227 b (Mann et al. 2022) does not have measured masses. TOI-1227 is an 11 Myr old system and its transiting object is suspected to have a mass in the range of Neptune's and still be contracting (Mann et al. 2022). Of the objects that remain, those most similar to TOI-4860 b are the very recently identified planets TOI-519 b (Parviainen et al. 2021; Kagetani et al. 2023), TOI-3984 b (Cañas et al. 2023), TOI-3235 b (Hobson et al. 2023) and TOI-5205 b (Kanodia et al. 2023). All four orbit higher mass stars than TOI-4860, and receive similar irradiation. Thanks to its very short orbital period, TOI-4860 b provides a convenient opportunity to study the atmospheric properties of a warm Jupiter. We calculate the Transmission Spectroscopy Metric (TSM; Kempton et al. 2018) to gauge how well this particular planet's atmosphere can be studied. Based on our fitted parameters, we find TSM = 67, a good score for this planet's equilibrium temperature.

Warm Jupiters have traditionally been defined as having orbital periods > 10 days (e.g. Huang et al. 2016). This worked for Sun-like stars, but a more judicious definition would be to use the scaled distance $a_b/R_\star$ instead, which makes TOI-4860 b dynamically and irradiatively similar to other warm Jupiters. Warm Jupiters are expected to have followed a different migratory pathway from hot Jupiters, and a large fraction (> 50%) of them host additional planets in their system (Huang et al. 2016; Wu et al. 2023). They also tend to occupy orbits that are aligned with the stellar equator (Triaud 2018; Albrecht et al. 2022; Rice et al. 2022; Attia et al. 2023).

LIST OF AFFILIATIONS

[1]School of Physics & Astronomy, University of Birmingham, Edgbaston, Birmingham B15 2TT, United Kingdom
[2]Department of Multi-Disciplinary Sciences, Graduate School of Arts and Sciences, The University of Tokyo, 3-8-1 Komaba, Meguro, Tokyo 153-8902, Japan
[3]Astrobiology Research Unit, University of Liège, Allée du 6 août, 19, 4000 Liège (Sart-Tilman), Belgium
[4]Komaba Institute for Science, The University of Tokyo, 3-8-1 Komaba, Meguro, Tokyo 153-8902, Japan
[5]Astrobiology Center, 2-21-1 Osawa, Mitaka, Tokyo 181-8588, Japan
[6]Instituto de Astrofísica de Canarias (IAC), Calle Vía Láctea s/n, 38200, La Laguna, Tenerife, Spain
[7]Department of Earth, Atmospheric and Planetary Sciences, MIT, 77 Massachusetts Avenue, Cambridge, MA 02139, USA
[8]National Astronomical Observatory of Japan, 2-21-1 Osawa, Mitaka, Tokyo 181-8588, Japan
[9]Department of Physics and Kavli Institute for Astrophysics and Space Research, Massachusetts Institute of Technology, Cambridge, MA 02139, USA
[10] Oukaimeden Observatory, High Energy Physics and Astrophysics Laboratory, Faculty of sciences Semlalia, Cadi Ayyad University, Marrakech, Morocco
[11]Department of Astronomy and Astrophysics, UC San Diego, 9500 Gilman Drive, La Jolla, CA 92093, USA
[12]NASA Ames Research Center, Moffett Field, CA 94035, USA
[13]SETI Institute, 339 Bernardo Ave, Suite 200, Mountain View, CA 94043, USA
[14]Center for Astrophysics | Harvard & Smithsonian, 60 Garden Street, Cambridge, MA 02138, USA
[15]Space Sciences, Technologies and Astrophysics Research (STAR) Institute, Université de Liège, Allée du 6 Août 19C, B-4000 Liège, Belgium
[16]University of Bern, Center for Space and Habitability, Gesellschaftsstrasse 6, 3012 Bern, Switzerland
[17]AIM, CEA, CNRS, Université Paris-Saclay, Université de Paris, F-91191 Gif-sur-Yvette, France
[18]Cavendish Laboratory, JJ Thomson Avenue, Cambridge CB3 0HE, UK
[19]Instituto de Astronomía, Universidad Nacional Autónoma de México, Ciudad Universitaria, Ciudad de México, 04510, México
[20]Department of Physical Sciences, Ritsumeikan University, Kusatsu, Shiga 525-8577, Japan
[21]Astrobiology Center, NINS, 2-21-1 Osawa, Mitaka, Tokyo 181-8588, Japan
[22]Department of Astronomy, School of Science, The Graduate University for Advanced Studies (SOKENDAI), 2-21-1 Osawa, Mitaka, Tokyo, Japan
[23]ETH Zurich, Department of Physics, Wolfgang-Pauli-Strasse 2, CH-8093 Zurich, Switzerland
[24]Instituto de Astrofísica de Andalucía (IAA-CSIC), Glorieta de la Astronomía s/n, 18008 Granada, Spain
[25]Department of Astronomy, University of Tokyo, 7-3-1 Hongo, Bunkyo-ku, Tokyo 113-0033, Japan
[26]Department of Astrophysical Sciences, Princeton University, Princeton, NJ 08544, USA

ACKNOWLEDGEMENTS

Funding for the *TESS* mission is provided by NASA's Science Mission Directorate. We acknowledge the use of public *TESS* data from pipelines at the *TESS* Science Office and at the *TESS* Science Processing Operations Center. This research has made use of the Exoplanet Follow-up Observation Program website, which is operated by the California Institute of Technology, under contract with the National Aeronautics and Space Administration under the Exoplanet Exploration Program. This paper includes data collected by the *TESS* mission that are publicly available from the Mikulski Archive for Space Telescopes (MAST). Based on data collected

by the SPECULOOS-South Observatory at the ESO Paranal Observatory in Chile. ULiège's contribution to SPECULOOS received funding from the European Research Council under the European Union's Seventh Framework Programme (FP/2007-2013) (grant Agreement n° 336480/SPECULOOS), from the Balzan Prize and Francqui Foundations, from the Belgian Scientific Research Foundation (F.R.S.-FNRS; grant n° T.0109.20), from the University of Liège, and from the ARC grant for Concerted Research Actions financed by the Wallonia-Brussels Federation. This work is supported by a grant from the Simons Foundation (PI Queloz, grant number 327127). This research is in part funded by the European Union's Horizon 2020 research and innovation programme (grants agreements n° 803193/BEBOP), and from the Science and Technology Facilities Council (STFC; grant n° ST/S00193X/1, and ST/W000385/1). The material is based upon work supported by NASA under award number 80GSFC21M0002. The postdoctoral fellowship of KB is funded by F.R.S.-FNRS grant T.0109.20 and by the Francqui Foundation. B.V.R. thanks the Heising-Simons Foundation for support. YGMC acknowledges support from UNAM PAPIIT-IG101321. F.J.P. acknowledges financial support from the grant CEX2021-001131-S funded by MCIN/AEI/10.13039/501100011033. This publication benefits from the support of the French Community of Belgium in the context of the FRIA Doctoral Grant awarded to MT. L.D. is an F.R.S.-FNRS Postdoctoral Researcher. Based on data collected by the TRAPPIST-South telescope at the ESO La Silla Observatory. TRAPPIST is funded by the Belgian Fund for Scientific Research (Fond National de la Recherche Scientifique, FNRS) under the grant FRFC 2.5.594.09.F, with the participation of the Swiss National Science Fundation (SNF). This work is partly supported by MEXT/JSPS KAKENHI Grant Numbers JP15H02063, JP17H04574, JP18H05439, JP18H05442, JP19K14783, JP21H00035, JP21K13955, JP21K20376, JP22000005, and JST CREST Grant Number JPMJCR1761. This paper is based on observations made with the MuSCAT3 instrument, developed by the Astrobiology Center and under financial supports by JSPS KAKENHI (JP18H05439) and JST PRESTO (JPMJPR1775), at Faulkes Telescope North on Maui, HI, operated by the Las Cumbres Observatory.

DATA AVAILABILITY

TESS data products are available via the MAST portal at https://mast.stsci.edu/portal/Mashup/Clients/Mast/Portal.html. Follow-up photometry and high resolution imaging data for TOI-4860 are available on ExoFOP at https://exofop.ipac.caltech.edu/tess/target.php?id=335590096. These data are freely accessible to ExoFOP members immediately and are publicly available following a one-year proprietary period. SPECULOOS and TRAPPIST data are also publicly available at the ESO archive a year after obtention.

The MagE Spectrograph User Manual is available at https://www.lco.cl/technical-documentation/the-mage-spectrograph-user-manual/. The Spextool User's Manual can obtained here: http://irtfweb.ifa.hawaii.edu/~spex/observer/.

APPENDIX A

Additional figures can be found in the online supplementary material.

REFERENCES

Albrecht S. H., Dawson R. I., Winn J. N., 2022, PASP, 134, 082001
Alibert Y., Mordasini C., Benz W., 2011, A&A, 526, A63
Andrews S. M., Rosenfeld K. A., Kraus A. L., Wilner D. J., 2013, ApJ, 771, 129
Attia O., Bourrier V., Delisle J. B., Eggenberger P., 2023, arXiv e-prints, p. arXiv:2305.00829
Baraffe I., Homeier D., Allard F., Chabrier G., 2015, A&A, 577, A42
Barkaoui K., et al., 2019, AJ, 157, 43
Bochanski J. J., West A. A., Hawley S. L., Covey K. R., 2007, AJ, 133, 531
Bond I. A., et al., 2004, ApJ, 606, L155
Bryant E. M., Bayliss D., Van Eylen V., 2023, MNRAS,
Burdanov A., Delrez L., Gillon M., Jehin E., 2018, in Deeg H. J., Belmonte J. A., eds, , Handbook of Exoplanets. p. 130, doi:10.1007/978-3-319-55333-7_130
Burgasser A. J., 2007, ApJ, 659, 655
Burgasser A. J., Splat Development Team 2017, in Astronomical Society of India Conference Series. pp 7–12 (arXiv:1707.00062)
Burn R., Schlecker M., Mordasini C., Emsenhuber A., Alibert Y., Henning T., Klahr H., Benz W., 2021, A&A, 656, A72
Cañas C. I., et al., 2023, arXiv e-prints, p. arXiv:2302.07714
Caldwell D. A., et al., 2020, Research Notes of the American Astronomical Society, 4, 201
Casewell S. L., et al., 2018, MNRAS, 481, 1897
Cloutier R., et al., 2021, AJ, 162, 79
Correia A. C. M., et al., 2010, A&A, 511, A21
Cushing M. C., Vacca W. D., Rayner J. T., 2004, PASP, 116, 362
Cushing M. C., Rayner J. T., Vacca W. D., 2005, ApJ, 623, 1115
Delfosse X., Forveille T., Mayor M., Perrier C., Naef D., Queloz D., 1998, A&A, 338, L67
Delrez L., et al., 2018, in Marshall H. K., Spyromilio J., eds, Society of Photo-Optical Instrumentation Engineers (SPIE) Conference Series Vol. 10700, Ground-based and Airborne Telescopes VII. p. 107001I (arXiv:1806.11205), doi:10.1117/12.2312475
Delrez L., et al., 2022, A&A, 667, A59
Douglas S. T., et al., 2014, ApJ, 795, 161
Dransfield G., et al., 2022, MNRAS, 515, 1328
Duquennoy A., Mayor M., 1991, A&A, 248, 485
Gaia Collaboration et al., 2016, A&A, 595, A1
Gaia Collaboration et al., 2022, arXiv e-prints, p. arXiv:2208.00211
Garcia L. J., Timmermans M., Pozuelos F. J., Ducrot E., Gillon M., Delrez L., Wells R. D., Jehin E., 2021, MNRAS,
Gillon M., Jehin E., Magain P., Chantry V., Hutsemékers D., Manfroid J., Queloz D., Udry S., 2011, EPJ Web of Conferences, 11, 06002
Gizis J. E., 1997, AJ, 113, 806
Guillot T., Burrows A., Hubbard W. B., Lunine J. I., Saumon D., 1996, ApJ, 459, L35
Günther M. N., Daylan T., 2019, allesfitter: Flexible star and exoplanet inference from photometry and radial velocity (ascl:1903.003)
Günther M. N., Daylan T., 2021, ApJS, 254, 13
Hamuy M., Suntzeff N. B., Heathcote S. R., Walker A. R., Gigoux P., Phillips M. M., 1994, PASP, 106, 566
Hartman J. D., et al., 2015, AJ, 149, 166
Hirano T., et al., 2020, PASJ, 72, 93
Hirano T., et al., 2021, AJ, 162, 161
Hobson M. J., et al., 2023, ApJ, 946, L4
Huang C., Wu Y., Triaud A. H. M. J., 2016, ApJ, 825, 98
Huang C. X., et al., 2020, Research Notes of the American Astronomical Society, 4, 204
Husser T. O., Wende-von Berg S., Dreizler S., Homeier D., Reiners A., Barman T., Hauschildt P. H., 2013, A&A, 553, A6
Ida S., Lin D. N. C., 2005, ApJ, 626, 1045
Jehin E., et al., 2011, The Messenger, 145, 2
Jenkins J. M., et al., 2016, in Chiozzi G., Guzman J. C., eds, Society of Photo-Optical Instrumentation Engineers (SPIE) Conference Series Vol. 9913, Software and Cyberinfrastructure for Astronomy IV. p. 99133E, doi:10.1117/12.2233418

Johnson J. A., et al., 2011, ApJ, 730, 79
Kagetani T., et al., 2023, arXiv e-prints, p. arXiv:2304.14703
Kanodia S., et al., 2023, AJ, 165, 120
Kempton E. M. R., et al., 2018, PASP, 130, 114401
Knutson H. A., et al., 2012, ApJ, 754, 22
Kotani T., et al., 2018, in Evans C. J., Simard L., Takami H., eds, Society of Photo-Optical Instrumentation Engineers (SPIE) Conference Series Vol. 10702, Ground-based and Airborne Instrumentation for Astronomy VII. p. 1070211, doi:10.1117/12.2311836
Laughlin G., Bodenheimer P., Adams F. C., 2004, ApJ, 612, L73
Lépine S., Rich R. M., Shara M. M., 2003, AJ, 125, 1598
Lépine S., Hilton E. J., Mann A. W., Wilde M., Rojas-Ayala B., Cruz K. L., Gaidos E., 2013, AJ, 145, 102
Lightkurve Collaboration et al., 2018, Lightkurve: Kepler and TESS time series analysis in Python, Astrophysics Source Code Library (ascl:1812.013)
Madhusudhan N., Seager S., 2009, ApJ, 707, 24
Mann A. W., Brewer J. M., Gaidos E., Lépine S., Hilton E. J., 2013, AJ, 145, 52
Mann A. W., Deacon N. R., Gaidos E., Ansdell M., Brewer J. M., Liu M. C., Magnier E. A., Aller K. M., 2014, AJ, 147, 160
Mann A. W., Feiden G. A., Gaidos E., Boyajian T., von Braun K., 2015, ApJ, 804, 64
Mann A. W., et al., 2019, ApJ, 871, 63
Mann A. W., et al., 2022, AJ, 163, 156
Marcy G. W., Butler R. P., Vogt S. S., Fischer D., Lissauer J. J., 1998, ApJ, 505, L147
Marshall J. L., et al., 2008, in McLean I. S., Casali M. M., eds, Society of Photo-Optical Instrumentation Engineers (SPIE) Conference Series Vol. 7014, Ground-based and Airborne Instrumentation for Astronomy II. p. 701454 (arXiv:0807.3774), doi:10.1117/12.789972
Moehler S., et al., 2014, A&A, 568, A9
Montet B. T., et al., 2015, ApJ, 800, 134
Morbidelli A., Batygin K., Lega E., 2023, arXiv e-prints, p. arXiv:2306.01653
Narita N., et al., 2020, in Evans C. J., Bryant J. J., Motohara K., eds, Society of Photo-Optical Instrumentation Engineers (SPIE) Conference Series Vol. 11447, Ground-based and Airborne Instrumentation for Astronomy VIII. p. 114475K, doi:10.1117/12.2559947
Palle E., et al., 2021, A&A, 650, A55
Parviainen H., Aigrain S., 2015, MNRAS, 453, 3821
Parviainen H., et al., 2021, A&A, 645, A16
Prochaska J. X., et al., 2020a, pypeit/PypeIt: Release 1.0.0, doi:10.5281/zenodo.3743493
Prochaska J. X., et al., 2020b, Journal of Open Source Software, 5, 2308
Rayner J. T., Toomey D. W., Onaka P. M., Denault A. J., Stahlberger W. E., Vacca W. D., Cushing M. C., Wang S., 2003, PASP, 115, 362
Rayner J. T., Cushing M. C., Vacca W. D., 2009, ApJS, 185, 289
Reid I. N., Hawley S. L., Gizis J. E., 1995, AJ, 110, 1838
Rice M., et al., 2022, AJ, 164, 104
Ricker G. R., et al., 2014, in Oschmann Jacobus M. J., Clampin M., Fazio G. G., MacEwen H. A., eds, Society of Photo-Optical Instrumentation Engineers (SPIE) Conference Series Vol. 9143, Space Telescopes and Instrumentation 2014: Optical, Infrared, and Millimeter Wave. p. 914320 (arXiv:1406.0151), doi:10.1117/12.2063489
Seager S., Sasselov D. D., 2000, ApJ, 537, 916
Sebastian D., et al., 2021, A&A, 645, A100
Skrutskie M. F., et al., 2006, AJ, 131, 1163
Snellen I. A. G., de Kok R. J., de Mooij E. J. W., Albrecht S., 2010, Nature, 465, 1049
Southworth J., 2011, MNRAS, 417, 2166
Speagle J. S., 2020, MNRAS, 493, 3132
Stassun K. G., et al., 2019, AJ, 158, 138
Tamura M., et al., 2012, in McLean I. S., Ramsay S. K., Takami H., eds, Society of Photo-Optical Instrumentation Engineers (SPIE) Conference Series Vol. 8446, Ground-based and Airborne Instrumentation for Astronomy IV. p. 84461T, doi:10.1117/12.925885
Thorngren D., Fortney J. J., 2019, ApJ, 874, L31
Thorngren D. P., Fortney J. J., Murray-Clay R. A., Lopez E. D., 2016, ApJ, 831, 64
Triaud A. H. M. J., 2018, in Deeg H. J., Belmonte J. A., eds, , Handbook of Exoplanets. p. 2, doi:10.1007/978-3-319-55333-7_2
Triaud A. H. M. J., 2021, in Madhusudhan N., ed., , ExoFrontiers. pp 6–1, doi:10.1088/2514-3433/abfa8fch6
Triaud A. H. M. J., et al., 2011, A&A, 531, A24
Triaud A. H. M. J., et al., 2013, A&A, 551, A80
Triaud A. H. M. J., et al., 2020, Nature Astronomy, 4, 650
Vernet J., et al., 2010, Highlights of Astronomy, 15, 535
West A. A., Hawley S. L., Bochanski J. J., Covey K. R., Reid I. N., Dhital S., Hilton E. J., Masuda M., 2008, AJ, 135, 785
Wu D.-H., Rice M., Wang S., 2023, AJ, 165, 171

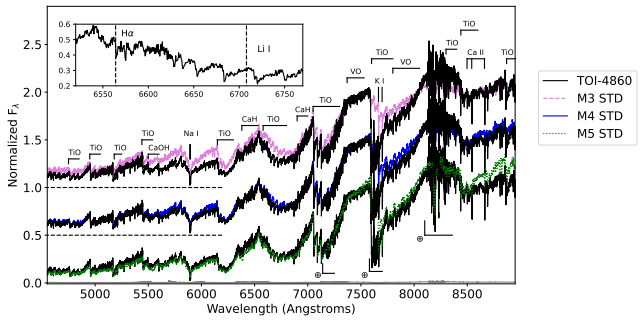


Figure A1. MagE optical spectrum of TOI-4860 (black lines) compared to M3, M4, and M5 spectral templates (colored lines from top to bottom) from Bochanski et al. (2007). All spectra are normalized at 7400–7500 Å. Primary atomic and molecular absorption features in the 4500-9000 Å spectra of M dwarfs are labeled, as are regions of strong telluric absorption (⊕). The inset box displays a close-up of the 6500–6800 Å region that hosts the 6563 Å Hα and 6708 Å Li I lines (vertical dashed lines), neither of which are detected.

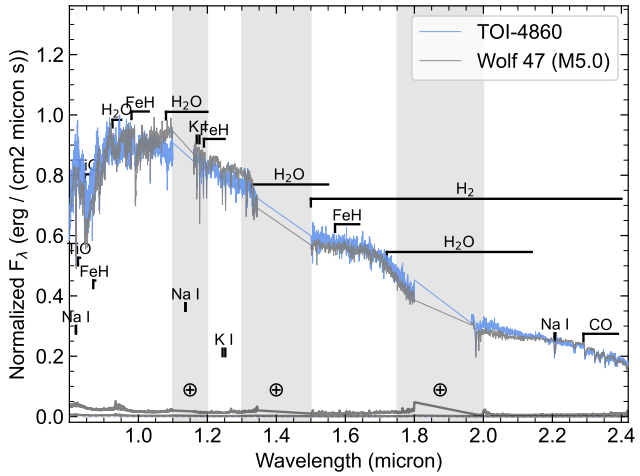


Figure A2. SpeX SXD spectrum of TOI-4860 (blue) and the M5 standard Wolf 47 (grey). Prominent M-dwarf spectral features are highlighted, and regions of strong telluric absorption are shaded in grey. The grey lines at the bottom of the plot show the measurement uncertainties for the target and comparison star (higher and lower, respectively).

APPENDIX A: ONLINE SUPPLEMENTARY MATERIAL

Table A2 provides the estimates of the stellar parameters of TOI-4860 derived in this work. Figure A1 and Figure A2 illustrate the Magellen/MagE optical and IRTF/SpeX near-infrared spectra of TOI-4860.

This paper has been typeset from a TEX/LATEX file prepared by the author.

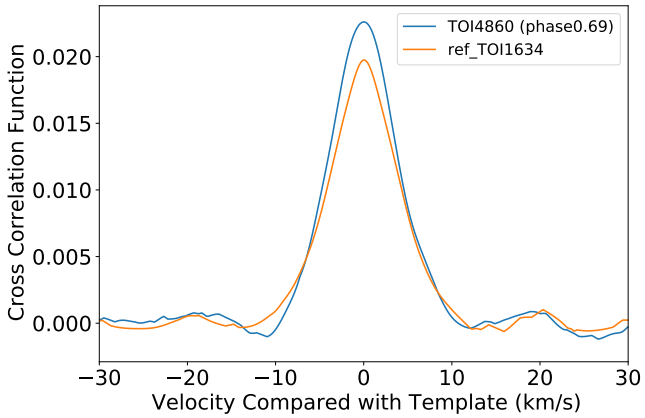


Figure A3. Cross-correlated IRD spectrum for on 2023-02-01, when TOI-4860 b was at orbital phase 0.69 (i.e. close to maximum velocity). This profile shows TOI-4860 is a single-lined system and unlikely to be an unresolved binary.

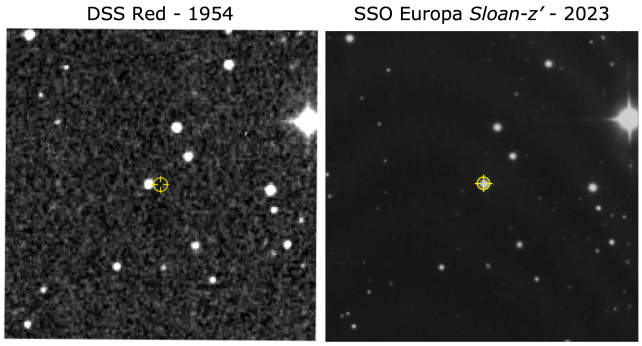


Figure A4. Images of the field of TOI-4860. In both images, the yellow cross-hairs are positioned on the current location of the target. **Left panel:** 1954 red image from the Digitised Sky Survey (DSS). **Right panel:** *Sloan-z'* image taken by SSO Europa in 2023.

Table A1. Summary of photometric ground-based observations table for TOI-4860.01.

Date (UT)	Filter	Telescope	Exptime [second]	Aperture size [arcsec]	FWHM [arcsec]	Coverage
		Transit				
2022 March 27	Exo	TRAPPIST-South-0.6m	120	3.9	2.1	Full
2022 April 18	*Sloan*-g'	MUSCAT3	120	2.2	1.8	Full
2022 April 18	*Sloan*-r'	MUSCAT3	50	2.2	1.7	Full
2022 April 18	*Sloan*-i'	MUSCAT3	20	2.7	1.5	Full
2022 April 18	*Sloan*-z_s	MUSCAT3	30	3.2	1.3	Full
2022 April 22	Sloan-z'	TRAPPIST-South-0.6m	160	5.1	3.0	Egress
2023 January 21	$I+z'$	TRAPPIST-North-0.6m	100	3.0	2.6	Full
2023 January 27	zYJ	SPECULOOS-South/Calisto	22	2.4	2.8	Full
2023 January 27	Sloan-i'	SPECULOOS-South/Ganymede	38	2.9	1.6	Full
2023 January 27	Sloan-r'	SPECULOOS-South/Europa	75	2.8	1.4	Full
2023 January 27	Sloan-g'	SPECULOOS-South/Io	160	2.9	2.2	Full
2023 January 30	Sloan-z'	SPECULOOS-South/Europa	27	3.4	1.5	Full
		Occultation				
2023 February 12	Sloan-z'	SPECULOOS-South/Ganymede	27	3.1	1.9	Full
2023 February 15	Sloan-z'	SPECULOOS-South/Europa	27	2.6	1.0	Full
2023 February 15	Sloan-z'	SPECULOOS-South/Ganymede	27	3.0	1.4	Full
2023 February 21	zYJ	SPECULOOS-South/Calisto	22	2.1	1.9	Full

Table A2. Stellar parameter estimates.

Parameter	Value	Source
SpType	M4.5 ± 0.5	Magellan/MagE
	M4.5 ± 0.5	IRTF/SpeX
$T_{\rm eff}$ (K)	3390 ± 120	BP–RP, [Fe/H], Mann et al. (2015)
[Fe/H]	+0.15 ± 0.20	Magellan/MagE, Mann et al. (2013)
	+0.45 ± 0.15	IRTF/SpeX, Mann et al. (2014)
	+0.30 ± 0.13	adopted, mean
Age (Gyr)	≳4.5	Magellan/MagE, West et al. (2008)
$M_\star$ ($M_\odot$)	0.3357 ± 0.0081	M_{Ks}, [Fe/H], Mann et al. (2019)
$R_\star$ ($R_\odot$)	0.348 ± 0.011	M_{Ks}, [Fe/H], Mann et al. (2015)
$L_\star$ ($L_\odot$)	0.0146 ± 0.0023	$T_{\rm eff}$, $R_\star$
log $g_\star$ (cgs)	4.880 ± 0.029	$M_\star$, $R_\star$
$\rho_\star$ (g cm^{-3})	11.3 ± 1.1	$M_\star$, $R_\star$

Table A3. Radial velocity measurements with IRD at Subaru Telescope.

Julian Date day	Radial velocity m s^{-1}	Uncertainty m s^{-1}	notes –
2 459 953.07655	-9.18	32.77	poor seeing
2 459 953.09783	-223.97	36.38	poor seeing
2 459 954.07577	130.09	10.26	
2 459 954.09705	209.56	12.25	
2 459 978.04964	-184.08	30.78	exposure interrupted in the middle
2 459 978.09204	-20.63	21.17	cloud passed
2 459 979.13594	-462.39	20.33	AO lost

Table A4. Table containing other fitted and derived parameters from our analysis and complementing Table 1

Parameter	Value
Transit depth b; $\delta_{\mathrm{tr;b;}}$ Callisto, *SPIRIT* (ppt)	47.88 ± 0.40
Transit depth b; $\delta_{\mathrm{tr;b;}}$ Europa, *Sloan* $- z'$ (ppt)	47.85 ± 0.37
Transit depth b; $\delta_{\mathrm{tr;b;}}$ TRAPPIST-South *Sloan* $- z'$ (ppt)	$47.89^{+0.58}_{-0.67}$
Transit depth b; $\delta_{\mathrm{tr;b;}}$ MuSCAT3, *Sloan* $- z'$ (ppt)	47.86 ± 0.40
Transit depth b; $\delta_{\mathrm{tr;b;}}$ TRAPPIST-North, $I + z'$ (ppt)	47.91 ± 0.52
Transit depth b; $\delta_{\mathrm{tr;b;}}$ TRAPPIST-South, *Exo* (ppt)	$47.93^{+0.57}_{-0.47}$
Transit depth b; $\delta_{\mathrm{tr;b;}}$ Ganymede, *Sloan* $- i'$ (ppt)	$47.86^{+0.55}_{-0.51}$
Transit depth b; $\delta_{\mathrm{tr;b;}}$ MuSCAT3, *Sloan* $- i'$ (ppt)	$47.87^{+0.51}_{-0.48}$
Transit depth b; $\delta_{\mathrm{tr;b;}}$ Europa, *Sloan* $- r'$ (ppt)	$47.58^{+0.68}_{-0.62}$
Transit depth b; $\delta_{\mathrm{tr;b;}}$ MuSCAT3, *Sloan* $- r'$ (ppt)	$47.83^{+0.71}_{-0.62}$
Transit depth b; $\delta_{\mathrm{tr;b;}}$ Io, *Sloan* $- g'$ (ppt)	$47.67^{+0.92}_{-0.80}$
Transit depth b; $\delta_{\mathrm{tr;b;}}$ MuSCAT3, *Sloan* $- g'$ (ppt)	47.71 ± 0.89
Occultation depth b; $\delta_{\mathrm{occ;b;}}$ Callisto, *SPIRIT* (ppt)	$0.139^{+0.14}_{-0.094}$
Occultation depth b; $\delta_{\mathrm{occ;b;}}$ Europa, *Sloan* $- z'$ (ppt)	$0.20^{+0.20}_{-0.14}$
Occultation depth b; $\delta_{\mathrm{occ;b;}}$ Ganymede, *Sloan* $- z'$ (ppt)	$0.128^{+0.12}_{-0.085}$
Limb darkening; $u_{1;\mathrm{europa_r p}}$	$0.654^{+0.054}_{-0.046}$
Limb darkening; $u_{2;\mathrm{europa_r p}}$	$0.143^{+0.052}_{-0.059}$
Limb darkening; $u_{1;\mathrm{europa_z p}}$	$0.127^{+0.037}_{-0.045}$
Limb darkening; $u_{2;\mathrm{europa_z p}}$	$0.696^{+0.055}_{-0.048}$
Limb darkening; $u_{1;\mathrm{ganymede_i p}}$	$0.438^{+0.052}_{-0.044}$
Limb darkening; $u_{2;\mathrm{ganymede_i p}}$	$0.318^{+0.055}_{-0.062}$
Limb darkening; $u_{1;\mathrm{ganymede_z p}}$	0.195 ± 0.072
Limb darkening; $u_{2;\mathrm{ganymede_z p}}$	0.632 ± 0.074
Limb darkening; $u_{1;\mathrm{io_g p}}$	$0.612^{+0.066}_{-0.059}$
Limb darkening; $u_{2;\mathrm{io_g p}}$	$0.300^{+0.061}_{-0.068}$
Limb darkening; $u_{1;\mathrm{spirit}}$	$0.040^{+0.035}_{-0.027}$
Limb darkening; $u_{2;\mathrm{spirit}}$	$0.803^{+0.038}_{-0.048}$
Limb darkening; $u_{1;\mathrm{TN_i+z}}$	$0.182^{+0.050}_{-0.054}$
Limb darkening; $u_{2;\mathrm{TN_i+z}}$	$0.554^{+0.068}_{-0.062}$
Limb darkening; $u_{1;\mathrm{TS_e xo}}$	$0.322^{+0.047}_{-0.041}$
Limb darkening; $u_{2;\mathrm{TS_e xo}}$	$0.347^{+0.051}_{-0.056}$
Limb darkening; $u_{1;\mathrm{TS_z p}}$	$0.236^{+0.066}_{-0.054}$
Limb darkening; $u_{2;\mathrm{TS_z p}}$	$0.591^{+0.061}_{-0.071}$
Limb darkening; $u_{1;\mathrm{muscat_g}}$	0.524 ± 0.065
Limb darkening; $u_{2;\mathrm{muscat_g}}$	0.375 ± 0.066
Limb darkening; $u_{1;\mathrm{muscat_r}}$	$0.542^{+0.052}_{-0.048}$
Limb darkening; $u_{2;\mathrm{muscat_r}}$	0.239 ± 0.056
Limb darkening; $u_{1;\mathrm{muscat_i}}$	0.366 ± 0.046
Limb darkening; $u_{2;\mathrm{muscat_i}}$	0.379 ± 0.057
Limb darkening; $u_{1;\mathrm{muscat_z}}$	$0.162^{+0.046}_{-0.048}$
Limb darkening; $u_{2;\mathrm{muscat_z}}$	0.641 ± 0.062

4.4 Work in progress: MANGOs II - Programme introduction and multi-flavour validation

Had it not been for the urgency to publish TOI-4860 b, this would have been the first paper in the MANGOs series. MANGOs II will present the full programme and our aims, as well as the methods we are currently using. Additionally, I have selected eight new MANGOs to present as a way of exemplifying the methods.

At present, we do not count on access to a spectrograph capable of precise radial velocities[c], and as such we cannot readily carry out confirmations of our systems. Therefore, our strategy is to use our network of telescopes to collect simultaneous multi-colour photometry to check for chromaticity in the transits. We additionally collect photometry at phase 0.5 to check for the presence of secondary eclipses, and use `TRICERATOPS` to carry out statistical validations. We are also using the evolutionary models presented in Baraffe et al. (2015) to develop a toolkit to determine the most likely nature of a companion in cases where we clearly detect the telltale signs of binarity (chromaticity and/or secondary eclipses). Finally, we are collecting low resolution spectra to characterise the host stars in our systems; in some cases this can also reveal binarity in the form of a second set of spectral lines.

The MANGOs programme is currently organised via a Google Sheet where we keep track of targets and observations. Table 4.6 lists the dispositions we use to classify objects in our target list before and after follow-up observations. Following each observation, a member of the team reduces and models the data, and prepares a report to submit to TFOP (*TESS* Follow-up Observing Program); the results and actions from these reports are tracked within our Google Sheet, as shown in Figure 4.8.

Disposition	Meaning
PC	Planet Candidate (If no follow-up)
VPC	Validated Planet Candidate (If 2 colours)
VPC+	Validated Planet Candidate Plus (If 3+ colours)
CP	Confirmed Planet (If mass measured)
EBC	Eclipsing Binary Canidate (No longer a PC, M or BD)
MBC	M-M binary candidate
BMBC	BD-M binary candidate
NPC	Nearby planet candidate
NEB	Nearby eclipsing binary

Table 4.6: Dispositions used to classify MANGOs in our target list.

Figure 4.9 shows the progress made so far on the systems that will be included in the paper. Reconnaissance spectroscopy and multi-colour photometry has been collected for all targets, and most systems have had a secondary eclipse check performed. What is missing for most systems is

[c] Although we have submitted proposals for time on ESO spectrographs and are seeking collaborations with teams that have access to RV facilities.

Observatory	Target	Filter	Observation date	Apparent depth	Contact	Comments	Spot	Submission date
SSO Io	2415.11	gp	8/11/2022		George			
SSO (SPIRIT)	4666.01	zYJ	11/11/2022	-	Mathilde	Bad weather		22/11/2022
SSO (Io)	4666.01	g'	11/11/2022	-	Mathilde	Bad weather - out of transit		-
SSO (Ganymede)	4666.01	r'	11/11/2022	-	Mathilde	Bad weather - out of transit		-
SSO SPIRIT	3288.01	zYJ	12/11/2022					
SSO Io	3288.01	gp	12/11/2022		George			
TS	4666.01	z'	14/11/2022	-	Mathilde	Astrometry issue		-
SSO Ganymede	5315.01	rp	14/11/2022	~38ppt	khalid	Just egress (weather loss?)		01/12/2022
SSO Europa	5315.01	zp	14/11/2022	~48ppt	khalid			01/12/2022
SSO SPIRIT	5315.01	zYJ	14/11/2022	~40ppt	khalid			01/12/2022
SNO	5315.01	I+z	14/11/2022	~50ppt	khalid			01/12/2022
SSO SPIRIT	4506.01	zYJ	15/11/2022		khalid	EB		
SSO Io	4506.01	gp	15/11/2022		khalid	EB		
SSO Europa	4506.01	zp	15/11/2022		khalid	EB		
TS	5873.01	I+z	15/11/2022	~25ppt	Mathilde/Khalid			19/12/2022
SSO Io	234.01	gp	16/11/2022		George			
SSO Europa	234.01	zp	16/11/2022		George			
SSO SPIRIT	234.01	zYJ	16/11/2022		George			
TS	4666.01	I+z	17/11/2022	-	Mathilde	Astrometry issue		-
TS	4988.01	I+z	18/11/2022	-	Mathilde	Technical issue		-
SNO	5375.01	z'	18/11/2022	30 ppt	Khalid			22/10/2022
SSO SPIRIT	2415.01	zYJ	19/11/2022		George			
SSO Ganymede	2415.01	zp	19/11/2022		George			
SSO Europa	2415.01	gp	19/11/2022		George			
SSO Io	2415.01	rp	19/11/2022		George			
TS	5349.01	I+z	22/11/2022	23 ppt	Khalid			28/11/2022
SSO Europa	5349.01	g'	22/11/2022	23ppt	khalid			15/01/2023
SSO Ganymede	5349.01	r'	22/11/2022	24ppt	khalid	Next observation in ZYJ		15/01/2023
SSO Io	2496.01	g'	23/11/2022	60-80 ppt	Mathilde	Detrending affects the depth a lot		13/01/2023
SSO Europa	2496.01	r'	23/11/2022		Mathilde			13/01/2023
SSO Ganymede	2496.01	z'	23/11/2022		Mathilde			13/01/2023
SNO	5375.01	rp	25/11/2022	~30ppt	Khalid	Shows a deep feature in the mid-of-transit		no yet on ExoFOP
SSO Europa	4858.01	r'	26/11/2022		Mathilde			
SNO	5916.01	g'	28/11/2022	45 ppt	Khalid			29/11/2022
TN	5916.01	I+z	28/11/2022	48 ppt	Khalid			29/11/2022

Figure 4.8: View of the Google Sheet used to track observations and reports submitted to TFOP.

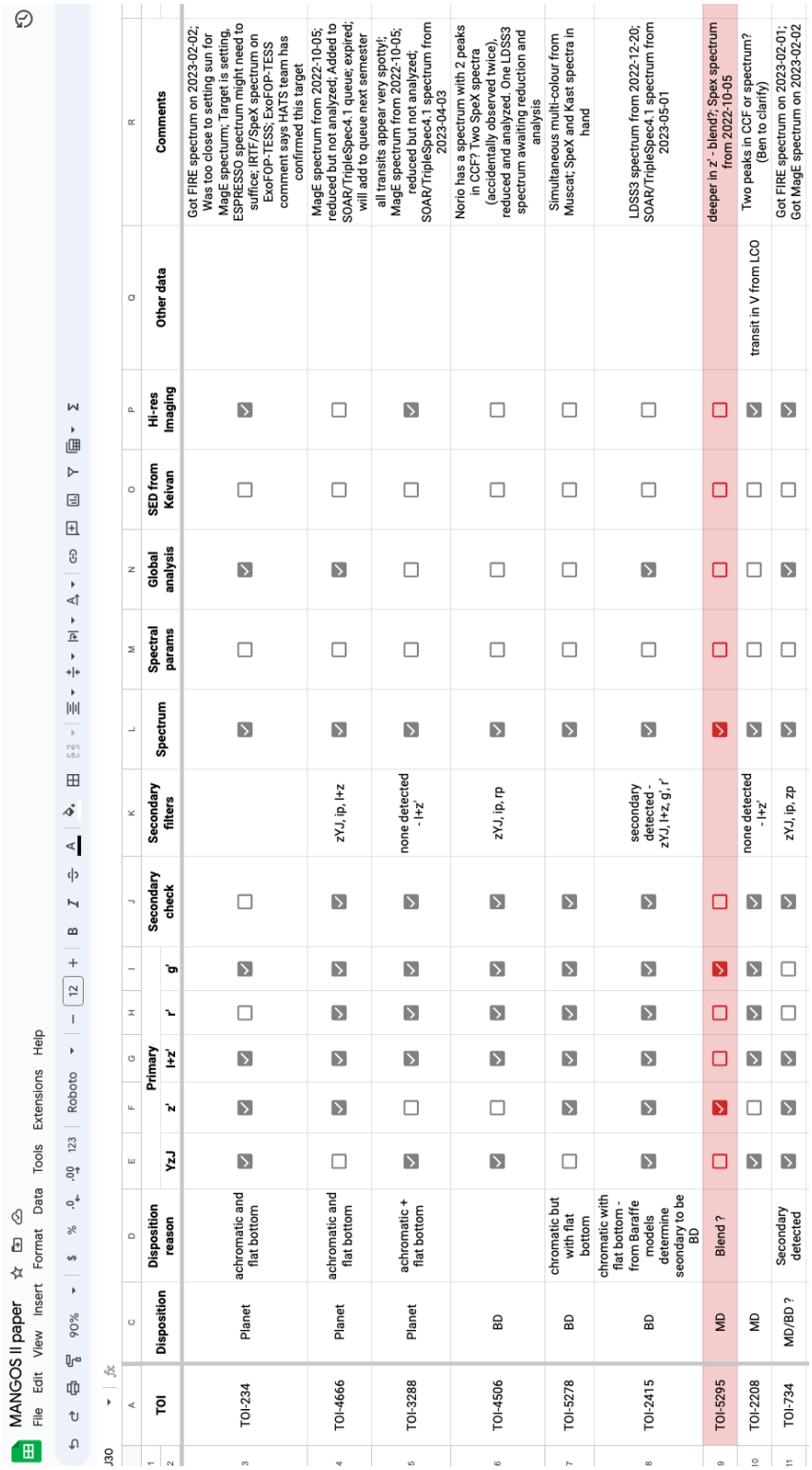


Figure 4.9: View of the Google Sheet used for tracking progress on the MANGOs II paper.

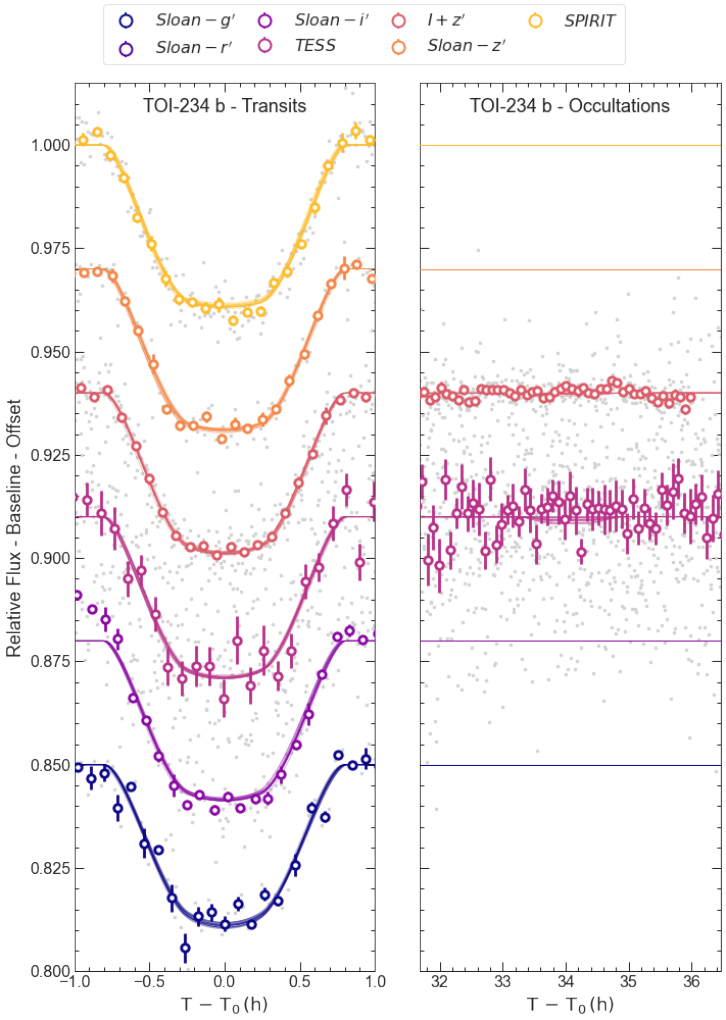


Figure 4.10: Photometric observations of TOI-234 b. Plotted on each lightcurve there 20 models randomly drawn from the posterior.

high-resolution imaging and spectral energy distribution analysis. Global analysis of all available photometry has been performed for half of the systems so far using `allesfitter`, following the methods described in Chapter 2, and Sections 3.2, 3.4 and 4.2.

TOI-234 is a 0.54 ± 0.02 $M_\odot$, 0.55 ± 0.02 $R_\odot$ star, with an effective temperature of 3628 ± 157 K. Given its size and effective temperature, this host is likely an early M dwarf. TOI-234 was observed by *TESS* in two sectors (2 and 29) at 2-minute cadence.

In Figure 4.10 I present the results of the global photometric fit for TOI-234 b. The achromatic flat bottomed transits reveal this to be a 1.053 ± 0.037 R_J object with an equilibrium temperature of 656 ± 29 K. We collected photometry at the expected epoch of a secondary eclipse and none was detected; we therefore classify this system as a likely planet[d]. Fitted and derived parameters for this system are presented in Table 4.7

[d]We are also aware that another team has collected ESPRESSO radial velocity measurements and have noted on the *TESS* Wiki that the mass of TOI-234 b is in the planetary range.

Parameter	Value
Fitted parameters	
$R_b/R_\star$	0.1970 ± 0.0011
$(R_\star + R_b)/a_b$	0.0935 ± 0.0010
$\cos i_b$	0.0580 ± 0.0012
$T_{0;b}$ (BJD)	$2459596.85298^{+0.00026}_{-0.00028}$
P_b (d)	$2.8392740^{+0.0000026}_{-0.0000024}$
Fitted parameters	
Companion radius b; R_b ($\mathrm{R}_\oplus$)	11.80 ± 0.42
Companion radius b; R_b (R_jup)	1.053 ± 0.037
Semi-major axis b; a_b (AU)	0.0327 ± 0.0012
Inclination b; i_b (deg)	86.674 ± 0.068
Impact parameter b; $b_\mathrm{tra;b}$	0.7424 ± 0.0076
Equilibrium temperature b; $T_\mathrm{eq;b}$ (K)	656 ± 29

Table 4.7: Fitted and derived parameters for TOI-234 b.

Parameter	Value
Fitted parameters	
$R_b/R_\star$	$0.19418^{+0.00083}_{-0.00078}$
$(R_\star + R_b)/a_b$	$0.09676^{+0.00094}_{-0.00071}$
$\cos i_b$	0.0120 ± 0.0047
$T_{0;b}$ (BJD)	$2459555.35974 \pm 0.00045$
P_b (d)	2.9089214 ± 0.0000034
Fitted parameters	
Companion radius b; R_b ($\mathrm{R}_\oplus$)	12.43 ± 0.39
Companion radius b; R_b (R_jup)	1.109 ± 0.035
Semi-major axis b; a_b (AU)	0.0336 ± 0.0011
Inclination b; i_b (deg)	89.31 ± 0.27
Impact parameter b; $b_\mathrm{tra;b}$	0.148 ± 0.056
Equilibrium temperature b; $T_\mathrm{eq;b}$ (K)	675 ± 29

Table 4.8: Fitted and derived parameters for TOI-4666 b.

TOI-4666 is a 0.58 ± 0.02 $\mathrm{M}_\odot$, 0.59 ± 0.02 $\mathrm{R}_\odot$ star, with an effective temperature of 3666 ± 157 K. Given its size and effective temperature, this host is also likely an early M dwarf. TOI-4666 was observed by *TESS* in one sector (31) in full frame images at 10-minute cadence.

In Figure 4.11 I present the results of the global photometric fit for TOI-4666 b. The achromatic flat bottomed transits reveal this to be a 1.109 ± 0.035 $\mathrm{R_J}$ object with an equilibrium temperature of 675 ± 29 K. We collected photometry at the expected epoch of a secondary eclipse and none was detected; we therefore classify this system as a likely planet. In the $I+z'$ lightcurve taken at phase 0.5 for TOI-4666 b, there does appear to be a small dip. However, as no corresponding dip was detected in the near infrared with SPIRIT, this is likely down to instrument systematics. Before publication of the full manuscript, we will repeat these observations to confirm the lack of a detectable occultation in this band. Fitted and derived parameters for this system are presented in Table 4.8

TOI-734 is a 0.17 ± 0.02 $\mathrm{M}_\odot$, 0.201 ± 0.006 $\mathrm{R}_\odot$ star, with an effective temperature of 2868 ± 157 K.

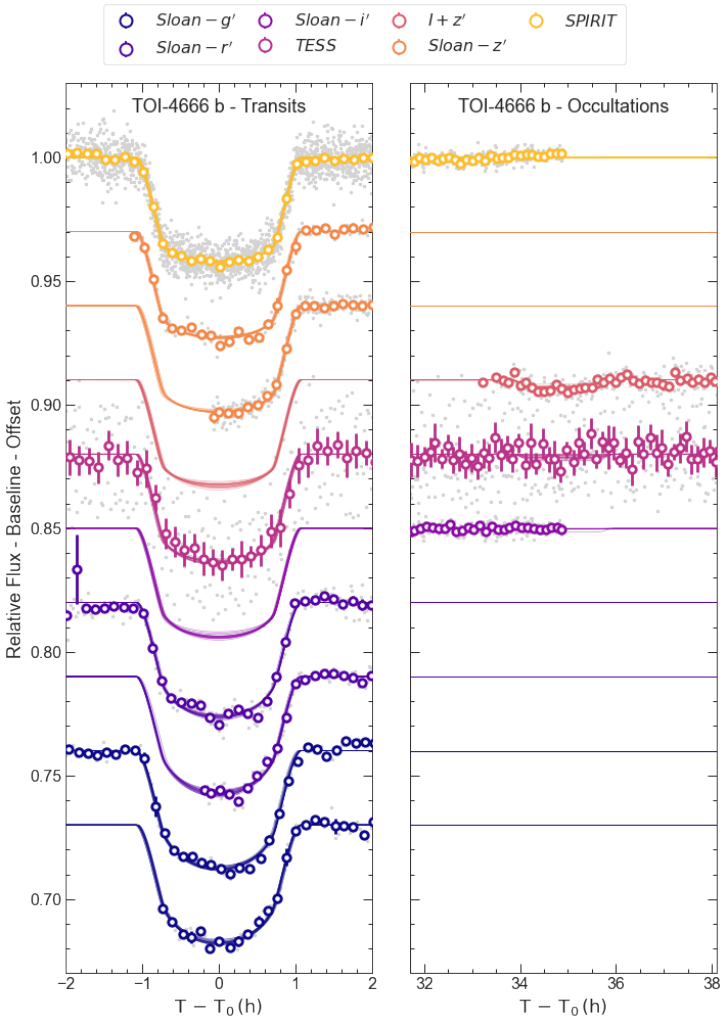


Figure 4.11: Photometric observations of TOI-4666 b. Plotted on each lightcurve there 20 models randomly drawn from the posterior.

Given its size and effective temperature, this host is likely a very late M dwarf. TOI-734 was observed by *TESS* in four sectors (9, 10, 36, 63) at 2-minute cadence.

In Figure 4.12 I present the results of the global photometric fit for TOI-734 B. The chromatic, grazing eclipses constrain this to be a $1.09^{+0.22}_{-0.14}$ R_J object; given the detected chromaticity and the presence of a secondary eclipse, we classify this object as an eclipsing binary. The secondary is likely a Brown Dwarf given its size, although there is a large uncertainty due to the grazing geometry. The occultation detected in *TESS* is not exactly at phase 0.5, which allowed us to measure a small eccentricity of $0.072^{+0.020}_{-0.018}$. The measured surface brightness ratio in this band is $0.145^{+0.014}_{-0.016}$; before publication we will seek to observe more occultations in different bands to better characterise the secondary object in the system. We also detected some ETVs (eclipse timing variations) both in *TESS* and in the ground-based follow-up; a fixed-linear ephemeris fit will be necessary to determine whether the timing discrepancy might be caused by an additional body in the system. Fitted and derived parameters for TOI-734 B are presented in Table 4.9.

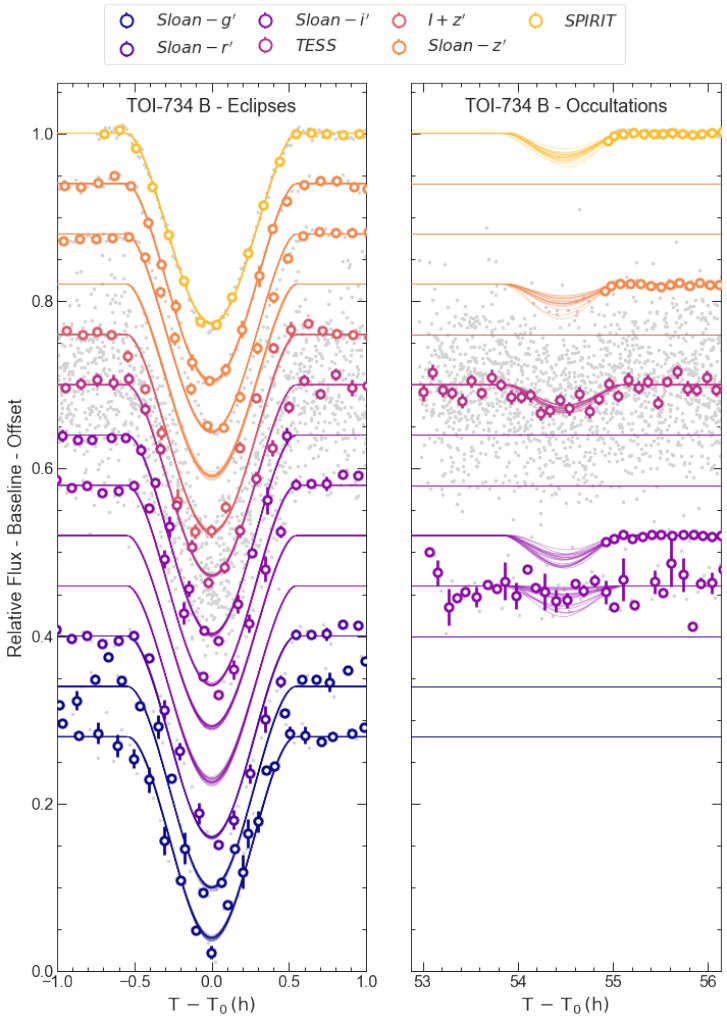


Figure 4.12: Photometric observations of TOI-734 B. Plotted on each lightcurve there 20 models randomly drawn from the posterior.

TOI-2415 is a 0.60 ± 0.02 $M_\odot$, 0.62 ± 0.02 $R_\odot$ star, with an effective temperature of 3558 ± 157 K. Given its size and effective temperature, this host is likely an early M dwarf. TOI-2415 was observed by *TESS* in one sector (28) at 2-minute cadence.

In Figure 4.13 I present the results of the global photometric fit for TOI-2415 B. The chromatic, flat-bottomed eclipses constrain this to be a 1.233 ± 0.041 object; given the detected chromaticity and the presence of a secondary eclipse, we classify this object as an eclipsing binary. The secondary is either a Brown Dwarf or an M dwarf. The occultations were detected in three bands (*TESS*, SPIRIT's custom filter zYJ, and $Sloan - z'$), and the measured depths increased with wavelength. We also observed in two bluer bands ($Sloan - g'$ and $Sloan - r'$) but did not detect the occultation. As occultations were detected at phase 0.5 we determine that the orbit is circular. Our observations may allow for characterisation of the secondary object with spectral energy distribution analysis prior to publication of the paper. Fitted and derived parameters for TOI-2415 B are presented in Table 4.10.

Over the coming months, I aim to gather the remaining observations where necessary and com-

Parameter	Value
Fitted parameters	
$R_B/R_\star$	0.5194 ± 0.0086
$(R_\star + R_B)/a_b$	0.03526 ± 0.00076
$\cos i_B$	$0.01615^{+0.00080}_{-0.00076}$
$T_{0;B}$ (BJD)	$2459296.506676 \pm 0.000049$
P_B (d)	$4.75354432 \pm 0.00000041$
$\sqrt{e_B}\cos\omega_b$	$-0.131^{+0.015}_{-0.019}$
$\sqrt{e_B}\sin\omega_b$	$0.234^{+0.045}_{-0.056}$
$J_{B;\mathrm{TESS}}$	$0.145^{+0.014}_{-0.016}$
Fitted parameters	
Companion radius B; R_B ($\mathrm{R}_\oplus$)	$12.2^{+2.5}_{-1.6}$
Companion radius B; R_B (R_jup)	$1.09^{+0.22}_{-0.14}$
Semi-major axis B; a_B (AU)	$0.0431^{+0.0087}_{-0.0057}$
Inclination B; i_B (deg)	89.074 ± 0.046
Impact parameter B; $b_\mathrm{tra;B}$	0.652 ± 0.017
Epoch occultation B; $T_\mathrm{0;occ;B}$	$2459298.77717 \pm 0.00082$
Impact parameter occultation B; $b_\mathrm{occ;B}$	$0.739^{+0.036}_{-0.034}$
Eccentricity B; e_B	$0.072^{+0.020}_{-0.018}$
Argument of periastron B; w_B (deg)	$119.2^{+11}_{-6.6}$
Equilibrium temperature B; $T_\mathrm{eq;B}$ (K)	282 ± 16

Table 4.9: Fitted and derived parameters for TOI-734 B.

Parameter	Value
Fitted parameters	
$R_B/R_\star$	0.2053 ± 0.0013
$(R_\star + R_B)/a_B$	$0.2925^{+0.0010}_{-0.0017}$
$\cos i_B$	$0.0755^{+0.0074}_{-0.0088}$
$T_{0;B}$ (BJD)	$2459499.05393 \pm 0.00011$
P_B (d)	$0.51536507 \pm 0.00000016$
$J_{b;\mathrm{TESS}}$	0.212 ± 0.025
$J_{B;\mathrm{Sloan-g'}}$	$0.082^{+0.040}_{-0.043}$
$J_{B;\mathrm{zYJ}}$	0.429 ± 0.016
$J_{B;\mathrm{Sloan-z'}}$	0.360 ± 0.058
Fitted parameters	
Companion radius b; R_b ($\mathrm{R}_\oplus$)	13.82 ± 0.46
Companion radius b; R_b (R_jup)	1.233 ± 0.041
Semi-major axis b; a_b (AU)	0.01185 ± 0.00039
Inclination b; i_b (deg)	$85.67^{+0.51}_{-0.43}$
Impact parameter b; $0.307^{+0.033}_{-0.038}$	
Epoch occultation b; $T_\mathrm{0;occ;b}$	$2459499.31236^{+0.00040}_{-0.00036}$
Impact parameter occultation b; $b_\mathrm{occ;b}$	$0.315^{+0.028}_{-0.034}$
Equilibrium temperature b; $T_\mathrm{eq;b}$ (K)	$1132 \pm 50.$

Table 4.10: Fitted and derived parameters for TOI-2415 B.

plete the global fits for all systems in the MANGOs II paper. The goal is to have the manuscript submitted by the end of the year. There are two other MANGOs papers also in the pipeline, to be

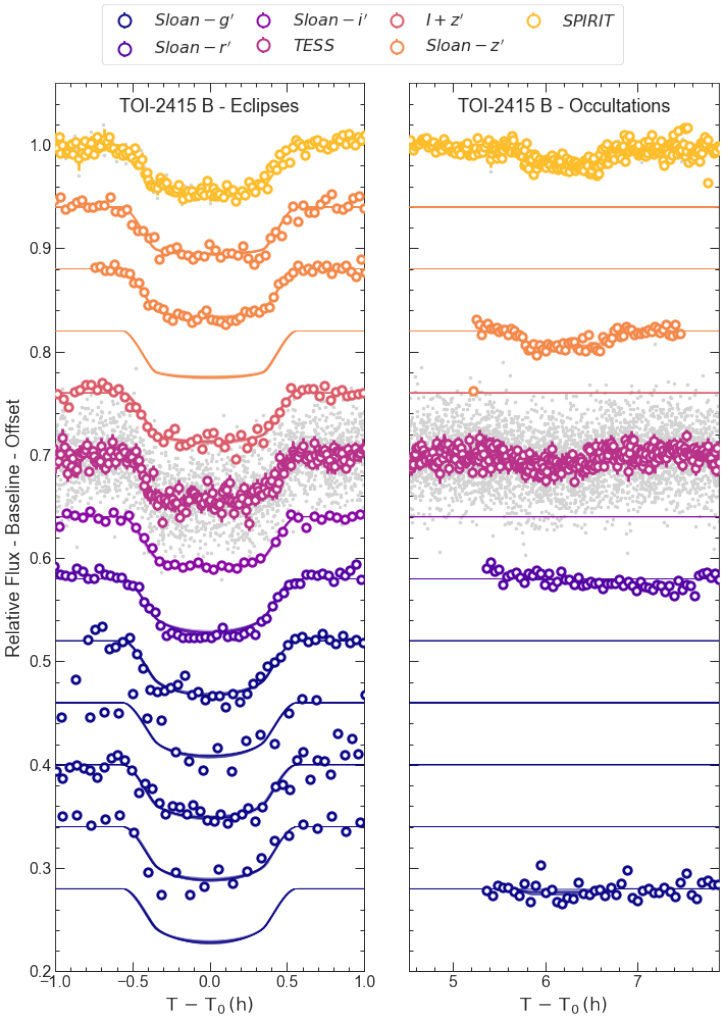


Figure 4.13: Photometric observations of TOI-2415 B. Plotted on each lightcurve there 20 models randomly drawn from the posterior.

authored by other team members. Khalid Barkaoui will be preparing MANGOs III, presenting validations of several more planets; and Lionel García will be leading MANGOs IV, where we will present the various MANGOs where the transits present spot crossings.

We estimate that a sample of 30 planets will be needed to begin to find statistical patterns; given the current rate of discovery from various teams, this should be achievable in the next 5-7 years.

5

In Conclusion

This chapter is where I conclude. I will be following in the rich tradition of all the conclusions chapters written before this one, by reminding you of what you have just read. But summarised, of course. The hope is that by presenting three and a half years' of work condensed into just a few pages, you will get a clear idea of the impact my work has had on the field.

5.1 Concluding remarks

Before that, however, I would like to present a visual aid for the task of 'impact assessment'. In Figure 5.1, all known exoplanets are presented in radius-instellation space. The grey planets in the background are the bulk of the known sample, but the planets in the foreground are the ones where I directly contributed to the system's discovery. Yellow stars are the four planets where I have led the discovery (HD 28109 b,c,d and TOI-715 b), while orange stars are systems in prep. that I will lead (AMY-1 b and TOI-791 b[a]). The purple hexagons are systems I co-authored as part of my work with ASTEP (TOI-836, TOI-4406, TOI-2338, TOI-2589, TOI-2525, TOI-2136, TOI-712, TOI-1064, TOI-3362, TOI-1231, and TOI-837), and red triangles are the systems I co-authored with SPECULOOS (TOI-2096, LP 890-9, TOI-2257, TOI-2406, TOI-2084, and TOI-4184). The crosses are planet-flavoured MANGOs that have already been validated by our project.

In Chapter 1, while setting the scene for this work, I introduced the three telescopes that have provided me with the data for my research: *TESS*, SPECULOOS and ASTEP. I also teased some of the exciting open questions in Exoplanetology that need further discoveries to be answered. For instance, are short-period giant planets around M dwarfs truly rare? Does the M-dwarf radius valley exist? Do Hot and Warm Jupiters form in the same way? Are planets in multi-planetary systems truly like 'peas in a pod'? Let us take a trip down the lane of very recent memory to see if we are any closer to answering these questions.

[a] This is a glorious long-period planet validated by ASTEP. There was no time or space to write about it in the body, but it is a Warm Jupiter with a 139 day period and we observed a full > 12 hr transit from the ground. It is magnificent.

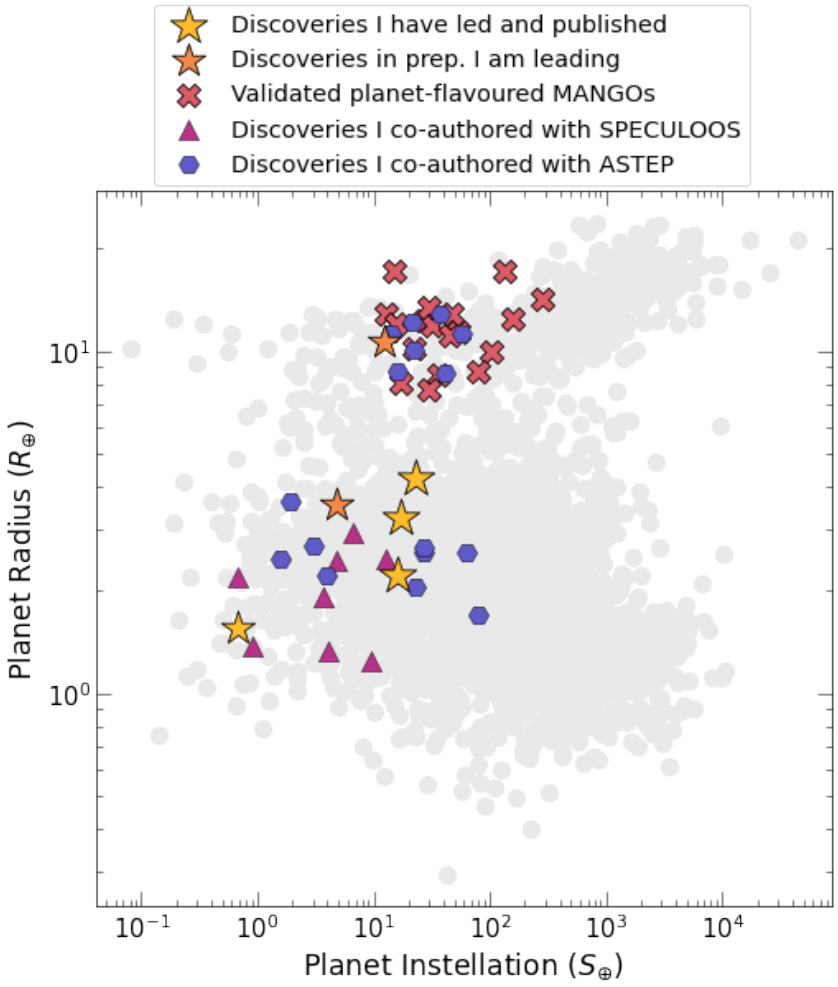


Figure 5.1: The impact of my thesis on the field of exoplanets. The yellow and orange stars are planet discoveries published or in preparation, led by me. Purple hexagons are discoveries that made use of ASTEP photometry, to which I contributed. Dark pink triangles are SPECULOOS-led discoveries which I co-authored. The large collection of crosses at the top are all validated MANGOs.

5.1.1 The conundrum of Hot and Warm Jupiter formation

We saw in Figure 1.13 in Chapter 1 that the population of Warm Jupiters is largely absent from transit detections. This is down to low transit probabilities caused by very large orbital separations. *TESS* is detecting several new candidates, but RV confirmations are pricey, and transit validations from the ground are challenging for most telescopes. Although not so for ASTEP, the 40 cm telescope on the Antarctic plateau, wielding its 3-month-long night to detect transiting planets from the ground.

I have not led any discoveries of Hot or Warm Jupiters in this thesis[b], but my work for ASTEP certainly contributed to the seven Warm Jupiters at the top of Figure 5.1. My paper in Section 2.6 (Dransfield et al. 2022b) details the transformative work I did designing new scheduling systems for the observatory, which allowed available telescope time to be allocated to those planets where ASTEP could have the most significant impact. By ensuring that long-period, long-transit-duration systems

[b] Although TOI-791 b is coming soon!



Figure 5.2: Four of us travelled to Concordia for our 2021/22 summer service mission; pictured here from left to right are Djamel Mekarnia, myself, Olivier Lai, and Karim Agabi. Behind us is ASTEP in its new dome, and in the background are the two towers that make up the main quarters of the station.

were scheduled ahead of time, crucial transits were not missed. The graphical interface on the website also meant that the team could fill gaps in the schedule with the most favourable opportunistic observations, allowing us to select those systems clearly out of reach to telescopes limited by the tyranny of the day-night cycle.

I also presented the new `python`-based automatic pipeline I wrote for ASTEP, which incidentally I installed in-person in Antarctica (see Figure 5.2 for receipts). The new pipeline allows ASTEP's results to come through far quicker and in a more flexible format so the data can be shared with collaborators. Having the pipeline built around open-source software like `prose` means that the principle data products can be manipulated by anyone with a `python` installation. The increase in precision of the lightcurves is a nice bonus too.

So what more do we know about Warm and Hot Jupiter formation from the discoveries shown in Figure 5.1? One stand-out system ASTEP contributed to was TOI-2525 (Trifonov et al. 2023), which hosts two warm Jupiters close to a 2:1 mean-motion resonance. Their long periods (23 and 49 days) and large-amplitude TTVs (transit timing variations) made these planets ideal candidates for ASTEP to follow up on. In fact, ASTEP was the only ground-based observatory to contribute full transits, which were crucial for the TTV monitoring. Simulations presented in the discovery paper indicate that the two planets simultaneously migrated and underwent gravitational interactions, which resulted in their current configuration. The authors also report that formation via core accretion would be challenging but not impossible.

TOI-3362 b (Dong et al. 2021b) is another exciting find, as it appears to have been caught in the act of high-eccentricity tidal migration, and ASTEP contributed two out of the three ground-based transits for this discovery. TOI-3362 b's exceptionally high eccentricity ($e \approx 0.815$) and current semi-major axis of 0.153 are consistent with ongoing tidal circularisation, indicating that this planet will eventually become a Hot Jupiter with a much shorter orbital period.

Finally, the three new Warm Jupiters presented in Brahm et al. (2023) do not appear to be Hot Jupiter progenitors, despite two of them having moderate eccentricities. However, the authors do believe that the planets migrated to their present positions. All three are amenable for further characterisation using the Rossiter-McLaughlin effect (Triaud 2018), which might reveal the mechanism responsible for their migrations. With periods between 22 and 62 days, it was natural for ASTEP to contribute full transits for these discoveries.

5.1.2 Peas in a pod: yay or nay?

An interesting pattern was spotted by Weiss et al. (2018) when studying multi-planetary systems from the *Kepler* sample: they appear to have intra-system size uniformity. However, the effect of planets potentially lurking undetected in the system is as yet unknown. So the question is, have I anything to add to the puzzle?

In Chapter 3 I presented two published discovery papers and another system in preparation. The first of these systems consists of three transiting planets orbiting the Solar-like star HD 28109, with the outer two planets very close to a 3:2 mean-motion resonance. I used ground- and space-based photometry combined with high- and low-resolution spectroscopy, high-resolution imaging and dynamical analysis to characterise the system in collaboration with my colleagues. The long periods, long transits and TTVs made this system an almost tailor-made opportunity for ASTEP to flex.

Curiously, the three planets found to be orbiting HD 28109 are all slightly different sizes (Section 3.2, Dransfield et al. 2022a): $R_\mathrm{b} = 2.199^{+0.098}_{-0.10}$ $\mathrm{R}_\oplus$, $R_\mathrm{c} = 4.23 \pm 0.11$ $\mathrm{R}_\oplus$ and $R_\mathrm{d} = 3.25 \pm 0.11$ $\mathrm{R}_\oplus$. The uniformity is said to also extend to planetary masses in multi-planetary systems, and the inferred masses for the three planets are also dissimilar: $M_\mathrm{b} = 18.5^{+9.1}_{-7.6}$ $\mathrm{M}_\oplus$, $M_\mathrm{c} = 7.9^{+4.2}_{-3.0}$ $\mathrm{M}_\oplus$ and $M_\mathrm{d} = 5.7^{+2.7}_{-2.1}$ $\mathrm{M}_\oplus$. I will note that the mass for the innermost planet is poorly constrained as yet, however it does appear to differ from its siblings.

Another noteworthy point about these planets is that there is a large gap between planets b and c, with semimajor axes of 0.1357 ± 0.0034 AU and 0.308 ± 0.011 AU respectively. For context, planet d is at 0.411 ± 0.016 AU. In the paper, we investigated the possibility of an additional non-transiting planet in this gap and found the best fit 4-planet model suggested a possible orbital period of 39 days and a mass of 3.2 $\mathrm{M}_\oplus$ for a putative fourth planet. Even if that planet exists, its mass is less than half that of each of its neighbours, making this system an interesting exception to the 'peas in a pod' pattern. Further monitoring of the system, both photometrically and spectroscopically may reveal whether there are truly more than three planets in the system.

I won't discuss TOI-715 (Section 3.4 Dransfield et al. 2023) too much here as it fits better else-

where, but the second (as yet unconfirmed) candidate in the system is very close in size to the first planet, in good agreement with the pattern presented in Weiss et al. (2018). Additionally, the two planets of LP 890-9/SPECULOOS-2 (Delrez et al. 2022), a SPECULOOS led discovery, are almost identical in size ($1.32\ \mathrm{R}_\oplus$ and $1.37\ \mathrm{M}_\oplus$) making them perfect peas in a pod.

This highlights how crucial ongoing discovery and characterisation is to continue to understand planetary system diversity.

5.1.3 The M-dwarf radius valley... or not

In Section 3.4 (Dransfield et al. 2023) I presented the discovery of TOI-715 b, a small habitable zone planet orbiting a nearby M dwarf. The planet may or may not be in the radius valley, which may or may not exist around low-mass stars.

Upon first posting an abstract on TOI-715 b to the *TESS* Wiki, I dubbed it 'a planet in the radius valley'. By the original standard of $1.5 - 2\ \mathrm{R}_\oplus$ presented in Fulton et al. (2017), its radius of $1.550 \pm 0.064\ \mathrm{R}_\oplus$ places it just inside that underpopulated region. However, as is so often the case, there turned out to be a bit more to the story. The M-dwarf radius valley remains contested, with differing selection methods for studies of its location and slope producing opposite results (e.g. Cloutier & Menou 2020; Van Eylen et al. 2021). In fact, the sample I chose for Figure 3.25 (hosts $< 4000\ \mathrm{K}$ and planet radii measured to 10% or better) shows no sign of a radius valley around low-mass stars. This isn't to say there isn't one, but further investigation is needed.

Systematically seeking out planets like TOI-715 b that lie close to the 'contested zone', and characterising them as fully as possible, is what will allow us to understand the full story of atmospheric loss in planets around M dwarfs. TOI-715 b is a particularly good target for this, as according to Martinez et al. (2019) and Cloutier & Menou (2020), it is below the radius valley and therefore a Super-Earth; however the definition from Van Eylen et al. (2021) places it above the radius valley, making it a Mini-Neptune. I demonstrated in Section 3.5.6 of the discovery paper that TOI-715 b is amenable to mass characterisation using precise radial velocities; this investigation would add a further crucial piece to the puzzle. I also raised in the paper that Luque & Pallé (2022) proposes a density gap for small planets around M dwarfs rather than a radius gap - characterising the densities of these small planets will reveal whether or not this is the case.

As part of my work with SPECULOOS, I also contributed to the discovery of the two planets orbiting TOI-2096 (Pozuelos et al. 2023). These charming planets have radii of $1.243\ \mathrm{R}_\oplus$ and $1.914\ \mathrm{R}_\oplus$, meaning that together they straddle the M-dwarf radius valley as defined by Cloutier & Menou (2020). The 'low-mass star radius valley' plot in the discovery paper (their Figure 17) *does* show a clear bimodality, but their sample includes hosts up to $0.7\ \mathrm{M}_\odot$, which again shows the effects of differing selection methods.

Once again, continued discovery of small planets around low-mass stars is the only route to resolving the mystery of the M-dwarf radius valley. SPECULOOS is ideally placed to hunt these down, with its vast (and growing) telescope network in the northern and southern hemispheres. Throughout my



Figure 5.3: Photos from my 2022 service mission to the SPECULOOS Southern Observatory at ESO Paranal in Chile. **Left panel:** here I am preparing to dismount the camera from one of the telescopes for cleaning. **Right panel:** sitting comfortably in the slit of one of the domes. My colleagues preferred not having to touch the chain grease for the slit motors if they could avoid it - I had no such reservations which meant I got to climb up and enjoy the views.

PhD I have done essential work to manage our follow-up observations, from organising and scheduling, to writing a website to allow consortium members to keep track of our efforts. In fact, I even travelled to Chile on a telescope service mission to help keep things running smoothly, as evidenced by Figure 5.3.

5.1.4 How common are MANGOs in space?

MANGOs (**M**-dwarfs **A**ccompanied by close-i**N** **G**iant **O**rbiter**s**) is my newest project, and possibly the one I'm the most proud of. This is a project I instigated in the consortium, and have led from the start along with another PhD student (Mathilde Timmermans from the University of Liège). Prior to the start of MANGOs, we were struggling to fill the 20% of SPECULOOS's telescope time allocated for annex observations. Since we began observing these objects, over 100 candidates have been added to our target list. We have completed over 300 photometric observations spanning more than 1000 hours of telescope time. Additionally, we have collected spectra for a quarter of the candidates on our target list to precisely characterise the hosts. All these efforts have resulted in the validation of 19 new planet-flavoured MANGOs.

In Chapter 4, I presented the project and its aims. Unlike several other teams working on validation

and confirmation of Hot Jupiters hosted by low-mass stars, MANGOs takes a more holistic approach by including Brown Dwarf and M-dwarf companions. This broader scope will allow us to learn crucial lessons about the differences between Brown Dwarf and giant planet formation, as well as improving models of M-dwarf mass-radius relations.

The project is still in its infancy, having been going for approximately a year so far. In Section 4.2, I presented the first paper in the MANGOs series, with the confirmation of TOI-4860 b (Triaud et al., submitted). In this work, we used ground- and space-based photometry combined with precise radial velocities to characterise this new MANGO, a planet with mass and radius 67% and 75% that of Jupiter respectively. This collaborative effort allowed us to raise the number of known close-in giant planets around M dwarfs to 13.

In Section 4.4 I laid out the foundations for our next paper in the series, which I will lead. This work will present the programme in its entirety and map out our plans for the next few years. Additionally, it will include eight new systems of which three are planets and the remaining five are binaries. There are further papers in the pipeline too, with other MANGOs team members preparing validation papers presenting some of the other objects we have observed so far.

We don't yet know quite how rare these objects are, but occurrence rates studies such as the one presented by Bryant et al. (2023) demonstrate that they are less common than giant orbiters hosted by FGK stars, as predicted by formation models. There is a vast amount of work to be done to grow this sample to a well-characterised, statistically significant one. Only then will we truly understand whether or not the formation of MANGOs is unique.

5.2 Future work

There are plenty of loose ends to tie up here, leaving vast scope for future work.

The HD 28109 system has unanswered questions still. Are there more planets in there? And, is the inner planet really that massive? With ASTEP, we are also continuing to monitor the TTVs in the system to support the ongoing ESPRESSO RV effort. Our new ground-based transits from last season, together with the incoming *TESS* data will make for a lovely photodynamical paper in the near future.

TOI-715 is also a work in progress. I have continued to monitor the system in an attempt to confirm the existence of the second candidate (hampered by weather so far), and I am hoping to submit a proposal to ESO to measure the first planet's mass with ESPRESSO next season. I also demonstrated in the paper that the system is amenable for atmospheric characterisation, and the hope is to prepare a proposal for *JWST* for Cycle 3 observations.

Throughout the next year, I will also put some time into finishing up AMY-1. I strongly suspect there are more planets in there[c] but more monitoring of the system is needed to confirm its architecture. It should be back in the sky in the Autumn, and I'll be scheduling it on SPECULOOS then.

[c] Mostly because I detected an additional random transit simultaneously in three colours.

There is so much more I want to achieve with ASTEP - I have been incredibly fortunate to gain access to such a unique instrument, and I do not think it is yet being exploited to its fullest capability. The future for ASTEP will likely involve monitoring of TTV systems as our main focus, as this will allow us to gain dynamical masses for systems out of reach to current spectrographs.

And finally, MANGOs. I've created a beast of a project here and it's allowed for new collaborations to emerge. There is so much science to do with MANGOs, and the hope is that in the coming years we will do it justice. I am waiting on the results of my second ESO proposal[d] to measure the masses of validated MANGOs. Should it be unsuccessful again, I will reassess and resubmit. The masses of these objects are crucial to unravel their origins, as well as to take the next steps into atmospheric investigations. I believe that MANGOs will keep me busy for a good long while yet.

And what of the future of the field of exoplanets? As described previously, the field is moving in the direction of in-depth characterisation of known exoplanets, with instruments such as *JWST* and the upcoming ground-based ELTs (Extremely Large Telescopes). However, we can also look forward to a vast influx of new planets as well. *Gaia*, the European Space Agency's (ESA) current astrometric mission is expected to discover $\sim 21,000 \pm 6000$ new planets via astrometry during its five-year nominal mission (Perryman et al. 2014). Additionally, ESA is set to launch *Plato* in 2026, and this instrument is set to detect several thousand new planets (Matuszewski et al. 2023). In particular, *Plato* is expected to discover ~ 500 Earth-sized planets orbiting Sun-like stars. Therefore, we may yet enter a new golden age of planetary discovery.

5.3 The End

This is the end of the thesis. But hopefully, it's just the beginning of my journey through Exoplanetology. We'll see.

[d] The first was rejected.

Bibliography

Agol E., Fabrycky D. C., 2018, Transit-Timing and Duration Variations for the Discovery and Characterization of Exoplanets. p. 7, doi:10.1007/978-3-319-55333-7_7

Agol E., et al., 2021, Planetary Science Journal, 2, 1

Aller A., Lillo-Box J., Jones D., Miranda L. F., Barceló Forteza S., 2020, A&A, 635, A128

Alonso R., 2018, in Deeg H. J., Belmonte J. A., eds, , Handbook of Exoplanets. p. 40, doi:10.1007/978-3-319-55333-7_40

Aristidi E., et al., 2005, A&A, 430, 739

Astropy Collaboration et al., 2013, A&A, 558, A33

Astropy Collaboration et al., 2018, AJ, 156, 123

Astropy Collaboration et al., 2022, apj, 935, 167

Baglin A., 2003, Advances in Space Research, 31, 345

Baglin A., Lebreton Y., Auvergne M., 1993, in Ecole de Printemps d'Astrophysique de Goutelas: HIPPARCOS. pp 299–366

Bailer-Jones C. A. L., Rybizki J., Fouesneau M., Demleitner M., Andrae R., 2021, AJ, 161, 147

Bakos G. Á., 2018, in Deeg H. J., Belmonte J. A., eds, , Handbook of Exoplanets. p. 111, doi:10.1007/978-3-319-55333-7_111

Bakos G., Noyes R. W., Kovács G., Stanek K. Z., Sasselov D. D., Domsa I., 2004, PASP, 116, 266

Bakos G. Á., et al., 2007, ApJ, 656, 552

Baraffe I., Homeier D., Allard F., Chabrier G., 2015, A&A, 577, A42

Barclay T., et al., 2013, Nature, 494, 452

Barclay T., Pepper J., Quintana E. V., 2018, ApJS, 239, 2

Barge P., et al., 2008, A&A, 482, L17

Barnes R., Jackson B., Raymond S. N., West A. A., Greenberg R., 2009, ApJ, 695, 1006

Baruteau C., et al., 2014, in Beuther H., Klessen R. S., Dullemond C. P., Henning T., eds, Protostars and Planets VI. pp 667–689 (arXiv:1312.4293), doi:10.2458/azu_uapress_9780816531240-ch029

Batalha N. E., et al., 2017, PASP, 129, 064501

Batygin K., Bodenheimer P. H., Laughlin G. P., 2016, ApJ, 829, 114

Bean J. L., Raymond S. N., Owen J. E., 2021, Journal of Geophysical Research (Planets), 126, e06639

Berger T. A., Huber D., Gaidos E., van Saders J. L., Weiss L. M., 2020, AJ, 160, 108

Bochanski J. J., West A. A., Hawley S. L., Covey K. R., 2007, AJ, 133, 531

Boley A. C., Granados Contreras A. P., Gladman B., 2016, ApJ, 817, L17

Bonfils X., et al., 2013, A&A, 549, A109

Bonomo A. S., et al., 2023, arXiv e-prints, p. arXiv:2304.05773

Borucki W. J., 2016, Reports on Progress in Physics, 79, 036901

Borucki W. J., Summers A. L., 1984, Icarus, 58, 121

Borucki W. J., Koch D. G., Dunham E. W., Jenkins J. M., 1997, in Soderblom D., ed., Astronomical Society of the Pacific Conference Series Vol. 119, Planets Beyond the Solar System and the Next Generation of Space Missions. p. 153

Borucki W. J., et al., 2003, in Blades J. C., Siegmund O. H. W., eds, Society of Photo-Optical Instrumentation Engineers (SPIE) Conference Series Vol. 4854, Future EUV/UV and Visible Space Astrophysics Missions and Instrumentation.. pp 129–140, doi:10.1117/12.460266

Borucki W., et al., 2008, in Sun Y.-S., Ferraz-Mello S., Zhou J.-L., eds, Proceedings of the International Astronomical Union, IAU Symposium Vol. 249, Exoplanets: Detection, Formation and Dynamics. pp 17–24, doi:10.1017/S174392130801630X

Borucki W., et al., 2009, in Pont F., Sasselov D., Holman M. J., eds, Proceedings of the International Astronomical Union, IAU Symposium Vol. 253, Transiting Planets. pp 289–299, doi:10.1017/S1743921308026513

Borucki W. J., et al., 2010, Science, 327, 977

Bradley L., et al., 2016, Photutils: Photometry tools, Astrophysics Source Code Library, record ascl:1609.011 (ascl:1609.011)

Brahm R., et al., 2023, AJ, 165, 227

Broeg C., Fernández M., Neuhäuser R., 2005, Astronomische Nachrichten, 326, 134

Bryant E. M., Bayliss D., Van Eylen V., 2023, MNRAS, 521, 3663

Bryson S., et al., 2021, AJ, 161, 36

Burdanov A., Delrez L., Gillon M., Jehin E., 2018, in Deeg H. J., Belmonte J. A., eds, , Handbook of Exoplanets. p. 130, doi:10.1007/978-3-319-55333-7_130

Burn R., Schlecker M., Mordasini C., Emsenhuber A., Alibert Y., Henning T., Klahr H., Benz W., 2021, A&A, 656, A72

Butler R. P., M G., Williams E., Hauser H., Shirts P., 1997, ApJ, 474, L115

Butters O. W., et al., 2010, A&A, 520, L10

Chabrier G., Baraffe I., Allard F., Hauschildt P., 2000, ApJ, 542, 464

Chakrabarty A., Sengupta S., 2019, AJ, 158, 39

Charbonneau D., Brown T. M., Latham D. W., Mayor M., 2000, ApJ, 529, L45

Charbonneau D., Brown T. M., Noyes R. W., Gilliland R. L., 2002, ApJ, 568, 377

Charbonneau D., et al., 2009, Nature, 462, 891

Chen J., Kipping D., 2017, ApJ, 834, 17

Christian D. J., et al., 2006, MNRAS, 372, 1117

Clarkson W. I., et al., 2007, MNRAS, 381, 851

Cloutier R., Menou K., 2020, AJ, 159, 211

Cochran W. D., Hatzes A. P., Butler R. P., M G., 1997, ApJ, 483, 457

Collier Cameron A., et al., 2007, MNRAS, 375, 951

Collier Cameron A., et al., 2010, MNRAS, 407, 507

Collins K., 2019, in American Astronomical Society Meeting Abstracts #233. p. 140.05

Collins K. A., Kielkopf J. F., Stassun K. G., Hessman F. V., 2017, AJ, 153, 77

Crouzet N., et al., 2010a, in Spinoglio L., Epchtein N., eds, EAS Publications Series Vol. 40, EAS Publications Series. pp 367–373 (arXiv:1002.2898), doi:10.1051/eas/1040051

Crouzet N., et al., 2010b, A&A, 511, A36

Crouzet N., et al., 2018, A&A, 619, A116

Crouzet N., et al., 2020, in Society of Photo-Optical Instrumentation Engineers (SPIE) Conference Series. p. 114470O, doi:10.1117/12.2562550

Csizmadia S., Pasternacki T., Dreyer C., Cabrera J., Erikson A., Rauer H., 2013, A&A, 549, A9

Cumming A., Butler R. P., M G., Vogt S. S., Wright J. T., Fischer D. A., 2008, PASP, 120, 531

Cutri R. M., et al., 2003, VizieR Online Data Catalog, p. II/246

Cutri R. M., et al., 2021, VizieR Online Data Catalog, p. II/328

D'Angelo G., Lissauer J. J., 2018, in Deeg H. J., Belmonte J. A., eds, , Handbook of Exoplanets. p. 140, doi:10.1007/978-3-319-55333-7_140

Daban J.-B., et al., 2010, in Stepp L. M., Gilmozzi R., Hall H. J., eds, Society of Photo-Optical Instrumentation Engineers (SPIE) Conference Series Vol. 7733, Ground-based and Airborne Telescopes III. p. 77334T, doi:10.1117/12.854946

Dawson R. I., Johnson J. A., 2018, ARA&A, 56, 175

Dawson R. I., et al., 2021, AJ, 161, 161

Deeg H. J., Alonso R., 2018, in Deeg H. J., Belmonte J. A., eds, , Handbook of Exoplanets. p. 117, doi:10.1007/978-3-319-55333-7_117

Delrez L., et al., 2022, arXiv e-prints, p. arXiv:2209.02831

Demory B. O., et al., 2020, A&A, 642, A49

Díaz R. F., Almenara J. M., Santerne A., Moutou C., Lethuillier A., Deleuil M., 2014, MNRAS, 441, 983

Dong J., et al., 2021a, ApJS, 255, 6

Dong J., et al., 2021b, ApJ, 920, L16

Dransfield G., Timmermans M., Gillon M., Niraula P., Triaud A., de Wit J., 2021, Reconnaissance Transmission Spectroscopy of The BEST Temperate Mini-Neptune for Atmospheric Characterisationround, HST Proposal. Cycle 29, ID. #16875

Dransfield G., et al., 2022a, MNRAS,

Dransfield G., et al., 2022b, in Adler D. S., Seaman R. L., Benn C. R., eds, Society of Photo-Optical Instrumentation Engineers (SPIE) Conference Series Vol. 12186, Observatory Operations: Strategies, Processes, and Systems IX. p. 121861F (arXiv:2208.04501), doi:10.1117/12.2629920

Dransfield G., et al., 2023, MNRAS,

Dressing C. D., Charbonneau D., 2015, ApJ, 807, 45

Eisner N., Lintott C., Aigrain S., 2020, The Journal of Open Source Software, 5, 2101

Endl M., Cochran W. D., Kürster M., Paulson D. B., Wittenmyer R. A., MacQueen P. J., Tull R. G., 2006, ApJ, 649, 436

Faria J. P., et al., 2022, A&A, 658, A115

Feliz D. L., Plavchan P., Bianco S. N., Jimenez M., Collins K. I., Villarreal Alvarado B., Stassun K. G., 2021, AJ, 161, 247

Fischer D. A., M G., Butler R. P., Vogt S. S., Apps K., 1999, PASP, 111, 50

Foreman-Mackey D., Hogg D. W., Lang D., Goodman J., 2013, PASP, 125, 306

Foreman-Mackey D., Agol E., Ambikasaran S., Angus R., 2017, celerite: Scalable 1D Gaussian Processes in C++, Python, and Julia (ascl:1709.008)

Foreman-Mackey D., et al., 2021, arXiv e-prints, p. arXiv:2105.01994

Fressin F., et al., 2006, in Fridlund M., Baglin A., Lochard J., Conroy L., eds, ESA Special Publication Vol. 1306, The CoRoT Mission Pre-Launch Status - Stellar Seismology and Planet Finding. p. 513

Fulton B. J., Petigura E. A., 2018, AJ, 156, 264

Fulton B. J., et al., 2017, AJ, 154, 109

Gaia Collaboration 2022, VizieR Online Data Catalog, p. I/355

Gaia Collaboration et al., 2018, A&A, 616, A1

Gaidos E., Mann A. W., Kraus A. L., Ireland M., 2016, MNRAS, 457, 2877

Gan T., et al., 2023, AJ, 165, 17

Garcia L. J., Timmermans M., Pozuelos F. J., Ducrot E., Gillon M., Delrez L., Wells R. D., Jehin E., 2022, MNRAS, 509, 4817

Gardner J. P., et al., 2006, Space Sci. Rev., 123, 485

Gaudi B. S., 2010, in Seager S., ed., , Exoplanets. pp 79–110

Gaudi B. S., 2012, ARA&A, 50, 411

Gaudi B. S., Meyer M., Christiansen J., 2021, in Madhusudhan N., ed., , ExoFrontiers; Big Questions in Exoplanetary Science. pp 2–1, doi:10.1088/2514-3433/abfa8fch2

Giacalone S., et al., 2021, AJ, 161, 24

Gillon M., Jehin E., Magain P., Chantry V., Hutsemékers D., Manfroid J., Queloz D., Udry S., 2011, in European Physical Journal Web of Conferences. p. 06002 (arXiv:1101.5807), doi:10.1051/epjconf/20101106002

Gillon M., et al., 2017, Nature, 542, 456

Gilmozzi R., Spyromilio J., 2008, in Stepp L. M., Gilmozzi R., eds, Society of Photo-Optical Instrument-

ation Engineers (SPIE) Conference Series Vol. 7012, Ground-based and Airborne Telescopes II. p. 701219, doi:10.1117/12.790801

Ginzburg S., Schlichting H. E., Sari R., 2018, MNRAS, 476, 759

Goyal A. V., Wang S., 2022, ApJ, 933, 162

Greklek-McKeon M., Knutson H. A., Vissapragada S., Jontof-Hutter D., Chachan Y., Thorngren D., Vasisht G., 2023, AJ, 165, 48

Griest K., Safizadeh N., 1998, ApJ, 500, 37

Grieves N., et al., 2022, A&A, 668, A29

Günther M. N., Daylan T., 2019, allesfitter: Flexible star and exoplanet inference from photometry and radial velocity (ascl:1903.003)

Günther M. N., Daylan T., 2021, ApJS, 254, 13

Gupta A., Schlichting H. E., 2019, MNRAS, 487, 24

Habets G. M. H. J., Heintze J. R. W., 1981, A&AS, 46, 193

Hadden S., Lithwick Y., 2014, ApJ, 787, 80

Hadden S., Lithwick Y., 2017, AJ, 154, 5

Hebb L., et al., 2009, ApJ, 693, 1920

Heber U., 2009, ARA&A, 47, 211

Heller R., 2019, A&A, 623, A137

Hippke M., Heller R., 2019, TLS: Transit Least Squares (ascl:1910.007)

Hippke M., David T. J., Mulders G. D., Heller R., 2019, AJ, 158, 143

Hobson M. J., et al., 2023, ApJ, 946, L4

Horne K., 2003, in Deming D., Seager S., eds, Astronomical Society of the Pacific Conference Series Vol. 294, Scientific Frontiers in Research on Extrasolar Planets. pp 361–370 (arXiv:astro-ph/0301249), doi:10.48550/arXiv.astro-ph/0301249

Howard A. W., et al., 2009, ApJ, 696, 75

Howell S. B., et al., 2014, PASP, 126, 398

Hsu D. C., Ford E. B., Terrien R., 2020, MNRAS, 498, 2249

Huang C., Wu Y., Triaud A. H. M. J., 2016, ApJ, 825, 98

Huang C. X., et al., 2018, ApJ, 868, L39

Husser T. O., Wende-von Berg S., Dreizler S., Homeier D., Reiners A., Barman T., Hauschildt P. H., 2013, A&A, 553, A6

JWST Transiting Exoplanet Community Early Release Science Team et al., 2023, Nature, 614, 649

Jenkins J. M., et al., 2016, in Chiozzi G., Guzman J. C., eds, Society of Photo-Optical Instrumentation Engineers (SPIE) Conference Series Vol. 9913, Software and Cyberinfrastructure for Astronomy IV. p. 99133E, doi:10.1117/12.2233418

Johnson J. A., et al., 2010, ApJ, 721, L153

Jones A., 2000, in Murdin P., ed., , Encyclopedia of Astronomy and Astrophysics. p. 1918, doi:10.1888/0333750888/1918

Kagetani T., et al., 2023, arXiv e-prints, p. arXiv:2304.14703

Kane S. R., Collier Cameron A., Horne K., James D., Lister T. A., Pollacco D. L., Street R. A., Tsapras Y., 2004, MNRAS, 353, 689

Kane S. R., Lister T. A., Collier Cameron A., Horne K., James D., Pollacco D. L., Street R. A., Tsapras Y., 2005a, MNRAS, 362, 117

Kane S. R., Collier Cameron A., Horne K., James D., Lister T. A., Pollacco D. L., Street R. A., Tsapras Y., 2005b, MNRAS, 364, 1091

Kass R. E., Raftery A. E., 1995, Journal of the American Statistical Association, 90, 773

Kempton E. M. R., Lupu R., Owusu-Asare A., Slough P., Cale B., 2017, PASP, 129, 044402

Kempton E. M. R., et al., 2018, PASP, 130, 114401

Kepler J., 1609, Astronomia nova ..., seu physica coelestis, tradita commentariis de motibus stellae martis, doi:10.3931/e-rara-558.

Kesseli A. Y., West A. A., Veyette M., Harrison B., Feldman D., Bochanski J. J., 2017, ApJS, 230, 16

Kipping D. M., 2010, Monthly Notices of the Royal Astronomical Society, 407, 301

Kipping D. M., 2013, MNRAS, 435, 2152

Kipping D. M., 2014, MNRAS, 440, 2164

Kirkpatrick J. D., 2005, ARA&A, 43, 195

Knutson H. A., Charbonneau D., Noyes R. W., Brown T. M., Gilliland R. L., 2007, ApJ, 655, 564

Koch D. G., et al., 2010, ApJ, 713, L79

Konacki M., Torres G., Jha S., Sasselov D. D., 2003, Nature, 421, 507

Kopparapu R. K., et al., 2013, ApJ, 765, 131

Kopparapu R. K., Ramirez R. M., SchottelKotte J., Kasting J. F., Domagal-Goldman S., Eymet V., 2014, ApJ, 787, L29

Kovács G., Zucker S., Mazeh T., 2002, A&A, 391, 369

Kovács G., Zucker S., Mazeh T., 2016, BLS: Box-fitting Least Squares, Astrophysics Source Code Library, record ascl:1607.008 (ascl:1607.008)

Kramer M., 2018, Pulsar Timing as an Exoplanet Discovery Method. p. 5, doi:10.1007/978-3-319-55333-7_5

Kreidberg L., 2018, in Deeg H. J., Belmonte J. A., eds, , Handbook of Exoplanets. p. 100, doi:10.1007/978-3-319-55333-7_100

Kumar S. S., 1963, ApJ, 137, 1121

Kurtovic N. T., et al., 2021, A&A, 645, A139

Laughlin G., Bodenheimer P., Adams F. C., 1997, ApJ, 482, 420

Laughlin G., Bodenheimer P., Adams F. C., 2004, ApJ, 612, L73

Lawrence J. S., Ashley M. C. B., Tokovinin A., Travouillon T., 2004, Nature, 431, 278

Lee E. J., Chiang E., Ormel C. W., 2014, ApJ, 797, 95

Léger A., et al., 2004, Icarus, 169, 499

Léger A., et al., 2009, A&A, 506, 287

Lightkurve Collaboration et al., 2018, Lightkurve: Kepler and TESS time series analysis in Python, Astrophysics Source Code Library (ascl:1812.013)

Lithwick Y., Xie J., Wu Y., 2012, ApJ, 761, 122

Lopez E. D., Fortney J. J., 2013, ApJ, 776, 2

Lopez T. A., et al., 2019, A&A, 631, A90

Luque R., Pallé E., 2022, arXiv e-prints, p. arXiv:2209.03871

Macintosh B., et al., 2015, Science, 350, 64

Mackay D. J. C., 2003, Information Theory, Inference and Learning Algorithms

Madhusudhan N., 2021, in Madhusudhan N., ed., , ExoFrontiers; Big Questions in Exoplanetary Science. pp 1–1, doi:10.1088/2514-3433/abfa8fch1

Madhusudhan N., Piette A. A. A., Constantinou S., 2021, ApJ, 918, 1

Mann A. W., Feiden G. A., Gaidos E., Boyajian T., von Braun K., 2015, ApJ, 804, 64

Marois C., Macintosh B., Barman T., Zuckerman B., Song I., Patience J., Lafrenière D., Doyon R., 2008, Science, 322, 1348

Martin D. V., Fitzmaurice E., 2022, MNRAS, 512, 602

Martinez C. F., Cunha K., Ghezzi L., Smith V. V., 2019, ApJ, 875, 29

Matuszewski F., Nettelmann N., Cabrera J., Börner A., Rauer H., 2023, arXiv e-prints, p. arXiv:2307.12163

Maxted P. F. L., 2016, A&A, 591, A111

Mayor M., Queloz D., 1995, Nature, 378, 355

Mayor M., et al., 2011, arXiv e-prints, p. arXiv:1109.2497

Mayor M., Lovis C., Santos N. C., 2014, Nature, 513, 328

Mazeh T., et al., 2000, ApJ, 532, L55

Mékarnia D., et al., 2016, MNRAS, 463, 45

Mékarnia D., et al., 2017, A&A, 608, L6

Millholland S., Wang S., Laughlin G., 2017, ApJ, 849, L33

Moffat A. F. J., 1969, A&A, 3, 455

Mollière P., Wardenier J. P., van Boekel R., Henning T., Molaverdikhani K., Snellen I. A. G., 2019, A&A, 627, A67

Montet B. T., et al., 2015, ApJ, 809, 25

Mordasini C., 2018, in Deeg H. J., Belmonte J. A., eds, , Handbook of Exoplanets. p. 143, doi:10.1007/978-3-319-55333-7_143

Mortier A., Collier Cameron A., 2017, A&A, 601, A110

Morton T. D., 2012, ApJ, 761, 6

Morton T. D., Swift J., 2014, ApJ, 791, 10

Mulders G. D., Pascucci I., Apai D., 2015a, ApJ, 798, 112

Mulders G. D., Pascucci I., Apai D., 2015b, ApJ, 814, 130

Murray C. D., Correia A. C. M., 2010, in Seager S., ed., , Exoplanets. pp 15–23,

doi:10.48550/arXiv.1009.1738

Murray C. A., et al., 2020, MNRAS, 495, 2446

Naef D., Mayor M., Beuzit J. L., Perrier C., Queloz D., Sivan J. P., Udry S., 2004, A&A, 414, 351

Nesvorný D., Vokrouhlický D., 2016, ApJ, 823, 72

Nesvorný D., Kipping D., Terrell D., Hartman J., Bakos G. Á., Buchhave L. A., 2013, ApJ, 777, 3

Nesvorny D., Chrenko O., Flock M., 2021, arXiv e-prints, p. arXiv:2110.09577

Niraula P., et al., 2020, AJ, 160, 172

Otegi J. F., Helled R., Bouchy F., 2022, A&A, 658, A107

Owen J. E., Wu Y., 2013, ApJ, 775, 105

Owen J. E., Wu Y., 2017, ApJ, 847, 29

Parsons S. G., et al., 2018, arXiv e-prints, p. arXiv:1808.07780

Parviainen H., 2018, in Deeg H. J., Belmonte J. A., eds, , Handbook of Exoplanets. p. 149, doi:10.1007/978-3-319-55333-7_149

Parviainen H., Aigrain S., 2015, MNRAS, 453, 3821

Pascucci I., et al., 2016, ApJ, 831, 125

Pepe F. A., et al., 2010a, in McLean I. S., Ramsay S. K., Takami H., eds, Society of Photo-Optical Instrumentation Engineers (SPIE) Conference Series Vol. 7735, Ground-based and Airborne Instrumentation for Astronomy III. p. 77350F, doi:10.1117/12.857122

Pepe F. A., et al., 2010b, in McLean I. S., Ramsay S. K., Takami H., eds, Society of Photo-Optical Instrumentation Engineers (SPIE) Conference Series Vol. 7735, Ground-based and Airborne Instrumentation for Astronomy III. p. 77350F, doi:10.1117/12.857122

Pepe F., Ehrenreich D., Meyer M. R., 2014, Nature, 513, 358

Perryman M., 2018, The Exoplanet Handbook

Perryman M., Hartman J., Bakos G. Á., Lindegren L., 2014, ApJ, 797, 14

Petrovich C., 2015, ApJ, 805, 75

Pollacco D. L., et al., 2006, PASP, 118, 1407

Pozuelos F. J., et al., 2020, A&A, 641, A23

Pozuelos F. J., et al., 2023, A&A, 672, A70

Pueyo L., 2018, Direct Imaging as a Detection Technique for Exoplanets. p. 10, doi:10.1007/978-3-319-55333-7_10

Queloz D., et al., 2001, The Messenger, 105, 1

Queloz D., et al., 2009, A&A, 506, 303

Rasio F. A., Ford E. B., 1996, Science, 274, 954

Rasmussen C. E., Williams C. K. I., 2006, Gaussian Processes for Machine Learning

Rauer H., et al., 2014, Experimental Astronomy, 38, 249

Reiner E., Pingree D., 1985, Babylonian Planetary Omens. Part Two. Enuma Anu Enlil Tablets 50-51. No. 2 in Bibliotheca Mesopotamica, Undena Publications

Ricker G. R., et al., 2009, in American Astronomical Society Meeting Abstracts #213. p. 403.01

Ricker G. R., et al., 2015, Journal of Astronomical Telescopes, Instruments, and Systems, 1, 014003

Ricker G. R., et al., 2016, in MacEwen H. A., Fazio G. G., Lystrup M., Batalha N., Siegler N., Tong E. C., eds, Society of Photo-Optical Instrumentation Engineers (SPIE) Conference Series Vol. 9904, Space Telescopes and Instrumentation 2016: Optical, Infrared, and Millimeter Wave. p. 99042B, doi:10.1117/12.2232071

Rivera E. J., et al., 2005, ApJ, 634, 625

Rodrigo C., Solano E., 2020, in XIV.0 Scientific Meeting (virtual) of the Spanish Astronomical Society. p. 182

Rodrigo C., Solano E., Bayo A., 2012, SVO Filter Profile Service Version 1.0, IVOA Working Draft 15 October 2012, doi:10.5479/ADS/bib/2012ivoa.rept.1015R

Sabotta S., et al., 2021, A&A, 653, A114

Sackett P. D., 1999, in Mariotti J. M., Alloin D., eds, NATO Advanced Study Institute (ASI) Series C Vol. 532, Planets Outside the Solar System: Theory and Observations. p. 189 (arXiv:astro-ph/9811269), doi:10.48550/arXiv.astro-ph/9811269

Salvatier J., Wiecki T. V., Fonnesbeck C., 2016, PeerJ Computer Science, 2, e55

Santerne A., Díaz R. F., Almenara J. M., Lethuillier A., Deleuil M., Moutou C., 2013a, in Cambresy L., Martins F., Nuss E., Palacios A., eds, SF2A-2013: Proceedings of the Annual meeting of the French Society of Astronomy and Astrophysics. pp 555–560 (arXiv:1310.2133)

Santerne A., Fressin F., Díaz R. F., Figueira P., Almenara J. M., Santos N. C., 2013b, A&A, 557, A139

Santerne A., et al., 2016, A&A, 587, A64

Savitzky A., Golay M. J. E., 1964, Analytical Chemistry, 36, 1627

Schanche N., et al., 2022, A&A, 657, A45

Schlecker M., et al., 2022, A&A, 664, A180

Schmider F.-X., et al., 2022, in Marshall H. K., Spyromilio J., Usuda T., eds, Society of Photo-Optical Instrumentation Engineers (SPIE) Conference Series Vol. 12182, Ground-based and Airborne Telescopes IX. p. 121822O (arXiv:2305.08454), doi:10.1117/12.2628952

Scott N. J., et al., 2021, Frontiers in Astronomy and Space Sciences, 8, 138

Seager S., Mallén-Ornelas G., 2003, ApJ, 585, 1038

Sebastian D., et al., 2020, in Society of Photo-Optical Instrumentation Engineers (SPIE) Conference Series. p. 1144521 (arXiv:2101.10970), doi:10.1117/12.2563563

Sebastian D., et al., 2021, A&A, 645, A100

Showman A. P., Tan X., Parmentier V., 2020, Space Sci. Rev., 216, 139

Skilling J., 2004, in Fischer R., Preuss R., Toussaint U. V., eds, American Institute of Physics Conference Series Vol. 735, Bayesian Inference and Maximum Entropy Methods in Science and Engineering: 24th International Workshop on Bayesian Inference and Maximum Entropy Methods in Science and Engineering. pp 395–405, doi:10.1063/1.1835238

Sotin C., Grasset O., Mocquet A., 2007, Icarus, 191, 337

Southworth J., 2011, MNRAS, 417, 2166

Speagle J. S., 2020, MNRAS, 493, 3132

Stapelfeldt K., Rauer H., Roberge A., Mandell A., 2021, in Madhusudhan N., ed., , ExoFrontiers; Big Questions in Exoplanetary Science. pp 9–1, doi:10.1088/2514-3433/abfa8fch9

Stassun K. G., Corsaro E., Pepper J. A., Gaudi B. S., 2018, AJ, 155, 22

Stassun K. G., et al., 2019, AJ, 158, 138

Stetson P. B., 1987, PASP, 99, 191

Stevens D. J., Gaudi B. S., 2013, PASP, 125, 933

Struve O., 1952, The Observatory, 72, 199

Sullivan P. W., et al., 2015, ApJ, 809, 77

Thuillier A., Van Grootel V., Dévora-Pajares M., Pozuelos F. J., Charpinet S., Siess L., 2022, A&A, 664, A113

Tinetti G., et al., 2018, Experimental Astronomy, 46, 135

Torres G., et al., 2011, ApJ, 727, 24

Traub W. A., Oppenheimer B. R., 2010, in Seager S., ed., , Exoplanets. pp 111–156

Triaud A. H. M. J., 2018, in Deeg H. J., Belmonte J. A., eds, , Handbook of Exoplanets. p. 2, doi:10.1007/978-3-319-55333-7_2

Trifonov T., et al., 2023, AJ, 165, 179

Trotta R., 2008, Contemporary Physics, 49, 71

Tsai S.-M., et al., 2023, Nature, 617, 483

Twicken J. D., et al., 2018, PASP, 130, 064502

Van Eylen V., Agentoft C., Lundkvist M. S., Kjeldsen H., Owen J. E., Fulton B. J., Petigura E., Snellen I., 2018, MNRAS, 479, 4786

Van Eylen V., et al., 2021, MNRAS, 507, 2154

Vanderburg A., et al., 2020, Nature, 585, 363

Venturini J., Helled R., 2017, ApJ, 848, 95

Vogel H. C., 1890, Astronomische Nachrichten, 123, 289

Weiss L. M., Petigura E. A., 2020, ApJ, 893, L1

Weiss L. M., et al., 2018, AJ, 155, 48

Wilson D. M., et al., 2008, ApJ, 675, L113

Winn J. N., 2010, Exoplanet Transits and Occultations. pp 55–77

Winn J. N., 2018, in Deeg H. J., Belmonte J. A., eds, , Handbook of Exoplanets. p. 195, doi:10.1007/978-3-319-55333-7_195

Winters J. G., et al., 2015, AJ, 149, 5

Wittenmyer R. A., O'Toole S. J., Jones H. R. A., Tinney C. G., Butler R. P., Carter B. D., Bailey J., 2010, ApJ, 722, 1854

Wolszczan A., 1994, Science, 264, 538

Wolszczan A., Frail D. A., 1992, Nature, 355, 145

Wright J. T., 2018, Radial Velocities as an Exoplanet Discovery Method. p. 4, doi:10.1007/978-3-319-

55333-7_4

York D. G., et al., 2000, AJ, 120, 1579

Zacharias N., Finch C. T., Girard T. M., Henden A., Bartlett J. L., Monet D. G., Zacharias M. I., 2013, AJ, 145, 44

Zhu W., 2020, AJ, 159, 188

Zhu W., Dong S., 2021, ARA&A, 59, 291

de Mooij E. J. W., et al., 2012, A&A, 538, A46